Modelling the Effects of High-Luminosity Optics in the Upgrades of the Large Hadron Collider

Thesis submitted in accordance with the requirements of
the University of Liverpool for the degree of Doctor in Philosophy by

Emilia Cruz Alaniz

June 2016

Contents

List of Figures

List of Tables

Abstract

The High-Luminosity Large Hadron Collider (HL-LHC) and the Large Hadron electron Collider (LHeC) are two proposed upgrades to build on the success of the Large Hadron Collider (LHC). This thesis considers some of the challenges of increasing the luminosity of the collisions in both of these upgrades.

The LHeC aims to make use of the LHC infrastructure to take electron-proton collisions into the TeV era. This work aims to explore the feasibility of the extension of a novel optical technique called the Achromatic Telescopic Squeezing scheme and the flexibility of the interaction region design, in order to find the optimal solution that would produce the highest luminosity while controlling the chromaticity, minimizing the synchrotron radiation power and maintaining the dynamic aperture required for stability.

The HL-LHC aims to increase the luminosity of the proton-proton collisions by an order of magnitude. To achieve this, new quadrupoles with larger apertures and higher gradients are to be implemented. The effects of fringe fields in these quadrupoles is expected to increase in comparison with the LHC. This work explores the possible effects that fringe fields may have on the machine, specifically on the dynamic aperture.

Introduction

The Large Hadron Collider (LHC) has been providing different kinds of hadron collisions since it started operations in 2009. Thanks to the data collected by the experiments several contributions have been made to particle physics. Most importantly, the Higgs boson was discovered in 2012, reaching a milestone in the understanding of nature.

Several upgrade options have been planned to build on the success of this machine. Among them, the High-Luminosity-LHC (HL-LHC) project aims to increase the luminosity of the LHC by an order of magnitude. Another upgrade of the LHC is the Large Hadron electron Collider (LHeC) aiming to make use of the LHC infrastructure to also take electron-proton collisions into the TeV era. Particle physics in the past has profited from having different types of collisions. The LHeC would ideally run synchronously with the HL-LHC, substantially extending and complementing the physics research at the TeV energy scale.

This thesis addresses challenges arising from having high-luminosity collisions in both of these upgrades. First, the flexibility of the design of the interaction region for the LHeC is studied to find the optimal design that will achieve the highest luminosity with the least impact on the machine. Secondly, the impact of the fringe fields of the new quadrupoles to be implemented in the HL-LHC insertions, is studied in terms of the stability of the beam.

Chapter 1 introduces the basic concepts of beam dynamics. Particular focus is given to providing equations of motion of particles passing through the main components of a beamline: drifts, dipoles and quadrupoles. Also given is the description of different concepts that will be used throughout this thesis. These include the Courant-Snyder parameters, chromaticity, dispersion and synchrotron radiation as well as the description of different tools generally used for lattice design: chromaticity correction, dynamic aperture and frequency map analysis.

In order to find transfer matrices for the basic elements of an accelerator described in Chapter 1 the use of a linear approximation is used; however, a real life accelerator requires the use of elements for which a linear approximation will no longer hold. The main focus of Chapter 2 is the description of techniques to obtain transfer maps for the nonlinear elements in a symplectic and explicit form.

Chapter 3 presents an overview of the history of particle accelerators; the developments in particle physics that motivated the construction of high energy accelerators, and the advances in technology that allowed their evolution, is presented in this chapter.

At the end of this development is the LHC, the largest experiment ever built. A description of this accelerator will be presented as well as the description of the proposed upgrades used in this thesis: the HL-LHC and the LHeC. Particular focus will be given to the challenges encountered to increase the luminosity in both of these experiments.

The interaction region is a challenging part of any accelerator. The complexity of the interaction region design is increased for the LHeC, given that this experiment is expected to work alongside the HL-LHC to allow simultaneous proton-proton and electron-proton collisions. Chapter 4 explores the flexibility of the integration of the LHeC interaction region into the HL-LHC lattice; in particular, this flexibility is explored in terms of increasing L^* (the distance between the interaction point and the first quadrupole), to minimize the synchrotron radiation, and minimizing β^* (the β function in the interaction point), to find the upper limits on luminosity. The competing criteria are evaluated to find the right balance between achieving the luminosity goals while controlling the impact that having high-luminosity collisions may have on the machine. Particular focus is given to controlling the chromatic aberrations and finding the means to minimize the synchrotron radiation.

To complement the previous studies, Chapter 5 presents particle tracking studies performed for the different LHeC lattice configurations found in Chapter 4. By calculating the dynamic aperture and performing frequency map analysis, further information is obtained to evaluate the feasibility of the LHeC lattice configurations and proposed chromaticity corrections schemes in terms of the stability of particle orbits.

In order to achieve the luminosity goals of the HL-LHC, new quadrupoles with higher gradients will have to be implemented in the HL-LHC insertions; furthermore, the β function at the location of the quadrupoles is much larger, requiring larger quadrupole apertures. Therefore, the effect of the fringe fields of these quadrupoles is expected to increase in comparison with the LHC. Chapter 6 presents the studies performed to study the impact that these fringe fields may have on the performance of the machine, particularly in the dynamic aperture.

In conclusion, the necessary increase in luminosity for the upgrades of the LHC, both in proton-proton and electron-proton collisions, comes with great challenges. This thesis makes use of particle beam dynamics theory, optical techniques and different computer tracking codes to analyze the feasibility of achieving the required luminosity while maintaining the dynamic aperture necessary to ensure the long term stability of the beam.

Chapter 1

Beam Dynamics

When designing a particle accelerator, it is necessary to have elements to guide and accelerate the beam. These tasks can be performed with electromagnetic fields. Electric fields can be used to accelerate the particles, and both electric and magnetic fields can be used to bend and focus the beam. However, as it will be shown, bending and focusing are better performed with magnetic fields.

A beamline is designed in such a way that a particle beam is accelerated to a particular energy and also optimized for the experiments in which they will be used, for example, producing a small beam at the interaction point of a collider. To achieve this a variety of electromagnetic elements are used which will be covered in the following sections.

The goal of this chapter is to provide a description of the fields used to guide a beam around an accelerator and to describe the motion of the particles passing through them. Particular attention will be given to multipole magnets which are the most common means to steer the beam (dipoles), focus the beam (quadrupoles) and to correct effects such as chromaticity (sextupoles).

Following on from this, the equations of motion of a beam in an accelerator will then be presented with an emphasis on the considerations required for circular accelerators.

1.1 Fields in Accelerator Magnets

A beam of particles in a circular particle accelerator is expected to follow a prescribed path, this trajectory is known as the "closed orbit" since it repeats (closes on) itself after exactly one turn. A particle following the exact closed orbit may or not exist, but the aim of the accelerator is to steer and focus the whole beam of particles such that it adheres as closely as possible to that design path. The components of the accelerator that perform this task make use of the Lorentz force which is experienced by a charged particle in an electromagnetic field.

The Lorentz force is given by [2]:

$$\vec{F} = q\vec{E} + q(\vec{v} \times \vec{B}), \tag{1.1}$$

where q is the basic unit of electric charge, the vectors $\vec{E}$ and $\vec{B}$ represent the electrical and magnetic field vectors respectively and $\vec{v}$ is the velocity vector of the particle. The study of "beam dynamics" involves the analysis of particle motion in the electromagnetic fields produced by accelerator components.

The Lorentz force given in Eq. 1.1 shows that with the proper arrangement of fields the force derived from them can be used to steer the beam. This can be done by both electric and magnetic forces, however for relativistic particles travelling at velocities $|\vec{v}| \approx c$, an electric field and a magnetic field multiplied by the velocity of light ($c\vec{B}$) would provide the same force magnitude. 1 T magnetic fields are more easily achieved than 300 MV/m. Therefore, magnetic fields are preferred to deflect or focus the beam.

Neglecting the electric field in Eq. 1.1, and only considering a transverse magnetic field, the particle will see a constant deflecting force with magnitude:

$$F = qvB. \tag{1.2}$$

To obtain a circular orbit the Lorentz force is equal to the centrifugal force:

$$qvB = \frac{\gamma m v^2}{\rho}, \tag{1.3}$$

with ρ being the local bending radius of the trajectory, m the mass of the particle and γ the relativistic factor: $\gamma = \frac{1}{\sqrt{1-(v/c)^2}}$. Dividing by the velocity and equating the momentum of the particle to $p = \gamma m v$, Eq. 1.3 can be expressed as:

$$B\rho = \frac{p}{q}. \tag{1.4}$$

Bρ is known as the beam rigidity. Eq. 1.4 can be expressed in terms of practical units:

$$\frac{1}{\rho[m]} \approx 0.2998 \frac{B[T]}{p[GeV/c]}. \tag{1.5}$$

With hard limits on the maximum dipole field achievable, Eq. 1.5 illustrates that a higher energy can only be achieved by increasing the radius of curvature of the accelerator.

1.1.1 Multipole Fields

Magnetic fields provide a suitable means to steer and focus a beam in an accelerator. Some types of magnet are particularly useful as they can be used to provide steering (dipole magnets) and focusing (quadrupole magnets).

Maxwell's equations in differential form can be written as [2]:

$$\nabla \cdot \vec{D} = \rho, \tag{1.6}$$

$$\nabla \cdot \vec{B} = 0, \tag{1.7}$$

$$\nabla \times \vec{H} = \vec{J} + \frac{\partial \vec{D}}{\partial t}, \tag{1.8}$$

$$\nabla \times \vec{E} = -\frac{\partial \vec{B}}{\partial t}, \tag{1.9}$$

where ρ is the electric charge density and $\vec{J}$ the current density.

The electric displacement $\vec{D}$ and the magnetic intensity $\vec{H}$ are related to the electric ($\vec{E}$) and magnetic ($\vec{B}$) fields as:

$$\vec{D} = \epsilon \vec{E}, \tag{1.10}$$

$$\vec{B} = \mu \vec{H}, \tag{1.11}$$

where the electric permittivity (ϵ) and the magnetic permeability (μ) depend on the medium through which fields are propagated.

The magnetic fields for various magnet types can be derived from Maxwell's equations in free space. In a vacuum, the following conditions must be satisfied:

$$\nabla \cdot \vec{B} = 0, \tag{1.12}$$

$$\nabla \times \vec{B} = 0. \tag{1.13}$$

A solution for $\vec{B} = (B_x, B_y, B_z)$ with constant B_z that satisfies these equations has the form [3]:

$$B_y + iB_x = C_n(x + iy)^{(n-1)}, \tag{1.14}$$

where C_n is a complex constant.

Fields of the form Eq. 1.14 are known as multipole fields. The value of n indicates the order of the multipole, so $n = 1$ is equivalent to the field of a dipole, $n = 2$ the field of a quadrupole, $n = 3$ of a sextupole and so on. By using the the principle of superposition, the fields can be added together to construct a single field that will still be a solution to Maxwell's equations 1.12 and 1.13:

$$B_y + iB_x = \sum_{n=1}^{\infty} C_n(x + iy)^{(n-1)}. \tag{1.15}$$

Expressing the magnetic field in polar coordinates gives:

$$\begin{pmatrix} B_r \\ B_\theta \end{pmatrix} = \begin{pmatrix} \cos\theta & \sin\theta \\ -\sin\theta & \cos\theta \end{pmatrix} \begin{pmatrix} B_x \\ B_y \end{pmatrix}. \tag{1.16}$$

Hence:

$$B_\theta + iB_r = B_y \cos\theta - B_x \sin\theta + iB_y \sin\theta + iB_x \cos\theta \tag{1.17}$$

$$= (B_y + iB_x)(\cos\theta + i\sin\theta) \tag{1.18}$$

$$= (B_y + iB_x)e^{i\theta}. \tag{1.19}$$

Using $x + iy = re^{i\theta}$, Eq. 1.15 can now be expressed in polar coordinates:

$$B_\theta + iB_r = \sum_{n=1}^{\infty} C_n r^{n-1} e^{in\theta}. \tag{1.20}$$

Using polar coordinates it can be seen that the strength of the field varies as r^{n-1}. Also from the angular component the symmetrical nature of the solution can be observed as for a rotation π/n the fields simply change sign.

Equations 1.15 and 1.20 can also be expressed in terms of the dimensionless parameters b_n and a_n, using a reference field B_{ref} and a reference radius R_{ref}:

$$B_y + iB_x = B_{\text{ref}} \sum_{n=1}^{\infty} (b_n + ia_n) \left(\frac{x + iy}{R_{\text{ref}}} \right)^{(n-1)}. \tag{1.21}$$

Equivalently in polar coordinates:

$$B_\theta + iB_r = B_{\text{ref}} \sum_{n=1}^{\infty} (b_n + ia_n) \left(\frac{r}{R_{\text{ref}}} \right)^{(n-1)} e^{in\theta}. \tag{1.22}$$

Conventionally the multipoles with $a_n = 0$ are called "normal multipoles" and those with $b_n = 0$ are called "skew multipoles". Figure 1.1 illustrates pure multipole fields with the corresponding symmetry for dipoles, quadrupoles and sextupoles with normal and skew fields.

The coefficients a_n and b_n can be determined by taking derivatives of the fields. For a normal multipole this is given by:

$$\frac{\partial^{n-1} B_x}{\partial y^{n-1}} = \frac{\partial^{n-1} B_y}{\partial x^{n-1}} = (n-1)! \frac{B_{\text{ref}}}{R_{\text{ref}}^{n-1}} b_n, \tag{1.23}$$

in the limit where $r \to 0$. Equivalently for a skew multipole:

$$\frac{\partial^{n-1} B_x}{\partial x^{n-1}} = -\frac{\partial^{n-1} B_y}{\partial y^{n-1}} = (n-1)! \frac{B_{\text{ref}}}{R_{\text{ref}}^{n-1}} a_n. \tag{1.24}$$

The field in a normal multipole can then be expressed in terms of the field derivatives:

$$B_y(x) = B_{y0} + \frac{\partial B_y}{\partial x} x + \frac{1}{2} \frac{\partial^2 B_y}{\partial x^2} x^2 + \frac{1}{3!} \frac{\partial^3 B_y}{\partial x^3} x^3 + ... \tag{1.25}$$

Normalising to the beam rigidity $B\rho$:

$$B_y(x) = \frac{B_{y0}}{B\rho} + \frac{1}{B\rho} \frac{\partial B_y}{\partial x} x + \frac{1}{2B\rho} \frac{\partial^2 B_y}{\partial x^2} x^2 + \frac{1}{3!B\rho} \frac{\partial^3 B_y}{\partial x^3} x^3 + ..., \tag{1.26}$$

$$= k_0 + k_1 x + \frac{1}{2!} k_2 x^2 + \frac{1}{3!} k_3 x^3 + ... \tag{1.27}$$

where $k_n = \frac{1}{B\rho} \frac{\partial^n B_y}{\partial x^n}$.

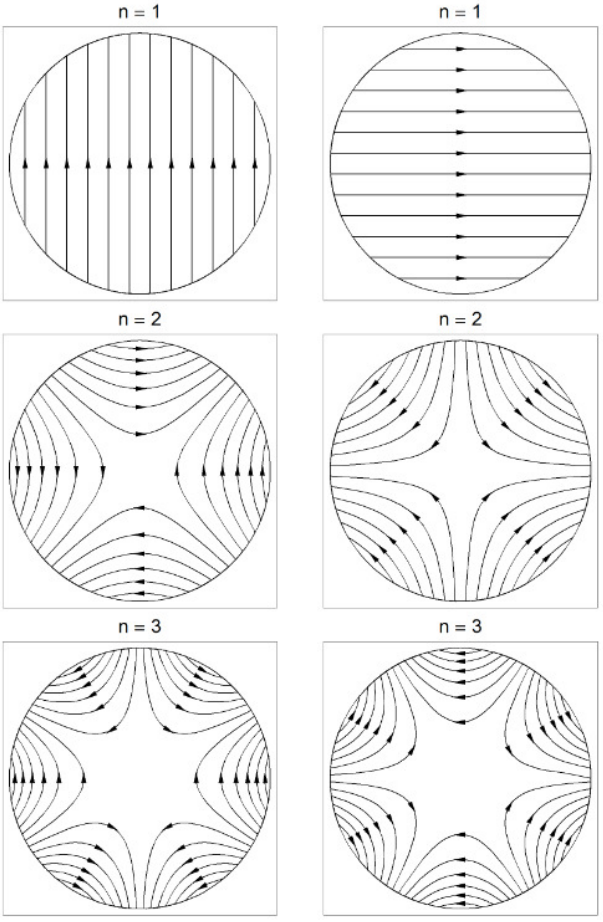

FIGURE 1.1: Pure multipole fields for a dipole (top), quadrupole (middle) and sextupole (bottom) for normal (left) and skew (right) fields [4].

This Taylor expansion gives a normal multipole expansion of a magnetic field with the right hand terms representing a dipole, quadrupole, sextupole, octupole, etc.

1.1.2 Dipoles

A dipole field is the simplest type of magnetic field. By comparison with Eq. 1.15 this refers to the field with $n = 1$. Dipoles are the commonly used elements in a beamline and are used to bend and steer a charge particle beam.

Dipoles provide a uniform field between two poles generated by a current circulating in the coils around them as illustrated in Fig. 1.2. Making use of Maxwell's equation (Eq. 1.8) and choosing the appropriate integral path the constant magnetic field between the poles (assuming permeability $\mu \to \infty$ in the poles and yoke) is given by:

$$B = \frac{\mu_0 NI}{h}, \tag{1.28}$$

where N is the number of turns in the coils carrying a current I and h is the distance of the gap between the poles.

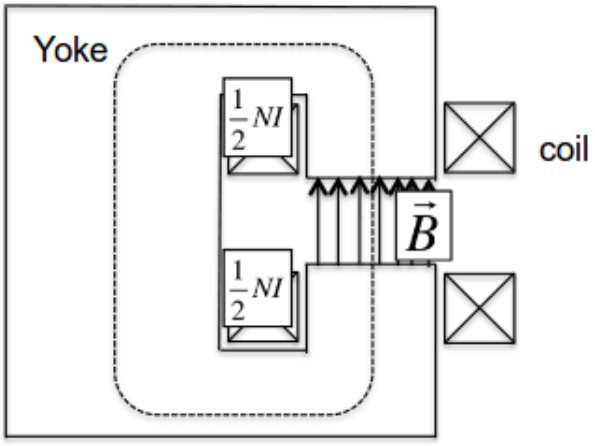

FIGURE 1.2: Illustration of a dipole with coils carrying a current of $\frac{1}{2}NI$. The dotted line illustrates the path integral loop [5].

Given a constant field in the vertical direction $\vec{B} = (0, B_y, 0)$ the corresponding Lorentz force for a particle travelling in the z direction is:

$$\vec{F} = q(0, 0, v_z) \times (0, B_y, 0) = -qv_z B_y \hat{x}. \tag{1.29}$$

Therefore, a force acts on a charged particle proportional to its velocity, and perpendicular to both the direction of the particle and the magnetic field.

In a superconducting magnet the field and geometry is given by the current distribution in the coils made of superconducting wire. In the LHC in particular two sets of coils create opposite fields, as illustrated in Fig. 1.3. The cosine field distribution in the magnet cross section generates a uniform dipole field [6].

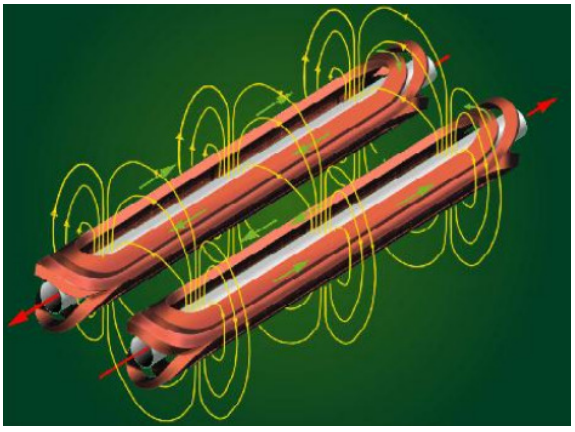

FIGURE 1.3: Illustration of coils-carrying tubes in the LHC, creating opposite fields in the neighbouring apertures [7].

1.1.3 Quadrupoles

Quadrupole magnets are used to keep the trajectory of the beam in the vicinity of the ideal orbit. Without focusing, the beam will naturally diverge.

Analogous to the dipole, wires carrying a current are wrapped around the 4 poles to create the quadrupole magnet, as illustrated in Fig. 1.4.

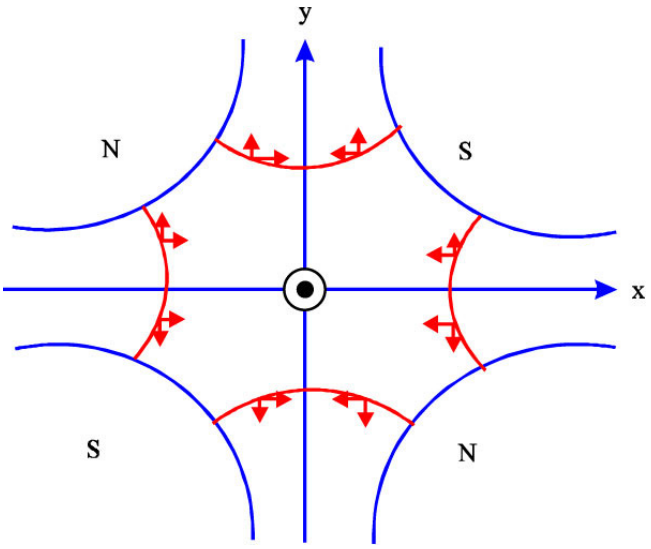

FIGURE 1.4: Illustration of a quadrupole. Current wires are wrapped around 4 poles (2 North and 2 South) arranged symmetrically to create the quadrupole. The direction of the force that the quadrupole field exerts on a particle is shown in (red arrows) [8].

The magnetic field generated by these quadrupoles, and consequently the corresponding Lorentz force, increases linearly with distance, written as:

$$\begin{aligned} B_x &= -gy \quad \therefore \quad F_x = -qvgx, \\ B_y &= -gx \quad \therefore \quad F_y = qvgy, \end{aligned} \tag{1.30}$$

the gradient g of the quadrupole magnet is given by:

$$g = 2\frac{\mu_0 nI}{r^2} = \frac{B_{\text{poles}}}{r_{\text{aperture}}}, \tag{1.31}$$

where r is the radius from the center, B_{poles} is the magnetic field at the pole tip at the point closest to the center of the magnet and r_{aperture} the radius of the aperture of the quadrupole. The focusing strength is given in terms of the gradient and the particle momentum as:

$$k_1 = \frac{g}{p/q} = g/B\rho. \tag{1.32}$$

Equation 1.30 shows that the Lorentz force derived from the quadrupole field has a different sign in the horizontal and the vertical direction. Thus, off-axis particles will be focused in one direction but defocused in the other. A way to overcome unwanted defocusing is to place two subsequent quadrupoles alternating in the focusing direction.

This will be explored in more detail in Section 1.2.5 where the equations of motion for particles passing through a quadrupole will also be presented.

1.1.4 Magnet Errors

Despite the best efforts to achieve ideal magnets, i.e. containing only one of the components of Eq. 1.27, real magnets consist of a superposition of an infinite number of multipole fields. The nature of these errors arise from fabrication limitations and from practical constraints that the design of the magnet has to obey. Some of these constraints are attributed to the finite dimensions of the magnet, the non-zero dimension of the wires and the finite permeability of the materials [3].

The higher-order multipole components of the magnetic field resulting from the practical limitations are known as systematic multipole errors, and are the same for all magnets of the same type. However, variations arise in the construction of each individual magnet, leading to random errors. Systematic errors are known from the design whereas random errors are not [9].

The symmetry of the magnetic field, expressed in terms of θ in Eq. 1.20, means that by design only the higher-order multipoles satisfying the same symmetry conditions will be present in a magnet. These multipoles are called *allowed* multipoles. The multipoles not satisfying the symmetry conditions, and hence not present in the magnet, are called *forbidden* multipoles.

Given a multipole of order n, the corresponding *allowed* multipoles of order m are the ones fulfilling the condition:

$$\frac{m}{n} = 3, 5, 7, ... \tag{1.33}$$

The presence of errors in the fields generated by the magnets in a beamline can have a significant impact on the beam dynamics. When tracking particles through a beamline using a dedicated accelerator code, it is important to consider both the systematic and random errors in magnets not only to obtain a realistic representation of the behaviour of the beam but also to determine whether under the consideration of these errors the stability of the beam can still be ensured.

1.2 Single Particle Dynamics

The study of beam dynamics aims to describe, as accurately as possible, the behaviour of particles passing through the electromagnetic fields of the elements along a beamline. Basic elements of a beamline consist of linear elements such as drifts, dipoles and quadrupoles. In real accelerators many more elements will need to be implemented. In this section, a description of individual particles passing through the linear elements will be given.

The equations of motion for particles travelling though fields from accelerator components may be derived using several methods. In the following sections both Newtonian

and Hamiltonian mechanics will be used. Solving the equations of motion, even for simple linear cases is not always a straightforward task, in most cases approximations need to be applied.

1.2.1 Newtonian Mechanics

Before solving the equations of motion an appropriate coordinate system must be chosen. Using a standard coordinate system in which time is the independent variable is not the most convenient system for an accelerator. This is because elements such as dipoles and quadrupoles are given at fixed positions and calculating the time at which particles pass through them would be a complicated task. Using the longitudinal position along the beamline as the independent variable is a more sensible choice along with a coordinate system that, rather than giving a global (x, y) coordinate position, has a local coordinate position with respect to the reference orbit at a certain point in the beamline, as shown in Fig. 1.5.

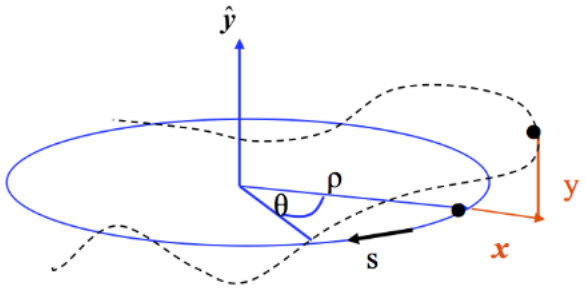

FIGURE 1.5: Local coordinate system with respect to the closed orbit [10].

In regions where the beam is bent by the magnetic field, the local coordinate system is adjusted accordingly. A general equation of particle motion can be derived in this coordinate system using Newtonian mechanics.

Substituting $\dot{\vec{p}} = \gamma m \ddot{\vec{r}}$ and the Lorentz force for a magnetic field given in Eq. 1.1 in Newton's second law $\vec{F} = \gamma m \ddot{\vec{r}}$ gives:

$$\ddot{\vec{r}} = \frac{q}{\gamma m}(\dot{\vec{r}} \times \vec{B}). \tag{1.34}$$

Now, consider a magnetic field with a dipole and a quadrupole component present. Assuming only vertical dipole fields and normal quadrupole fields, the resulting magnetic field in the horizontal and vertical direction is given by:

$$\frac{q}{p_0} B_y = \frac{1}{\rho} + k_1 x, \tag{1.35}$$

$$\frac{q}{p_0} B_x = k_1 y. \tag{1.36}$$

Inserting the magnetic fields given in Eq. 1.36 and making a linear approximation, after a series of approximations the equations of motion are given by the following expressions

[11]:

$$\begin{aligned} x''(s) + \Big(\frac{1}{\rho^2(s)} + k_1(s)\Big)x(s) = 0, \\ y''(s) - k_1(s)y(s) = 0. \end{aligned} \tag{1.37}$$

where $x'' = dx^2/dt^2$. These equations indicate the linear equation of motion for a particle travelling through a magnetic element of an accelerator with zero momentum deviation [11].

Assuming that particles have a momentum $p = p_0 + \Delta p$ (where p_0 is the reference momentum), the equations of motion in this case are given by:

$$\begin{aligned} x''(s) + \Big(\frac{1}{\rho^2(s)} + k_1(s)\Big)x(s) = \frac{1}{\rho(s)}\frac{\Delta p}{p_0}, \\ y''(s) - k_1(s)y(s) = 0. \end{aligned} \tag{1.38}$$

Equations 1.37 and 1.38 are known as Hill's equations, as they are very similar to the motion of particles in periodic external fields studied by the astronomer G.W. Hill [12]. The properties and solutions of these equations will be addressed in this chapter to understand the beam dynamics in periodic lattices.

1.2.2 Hamiltonian Formalism and Hamilton's Equations

In the last section Newtonian mechanics was used to derive an equation of motion. In this section Hamiltonian mechanics will be considered instead.

Hamilton's formalism is particularly useful given that it provides an elegant way to modify the equations to give the position along the beamline s as the independent variable. A further advantage of this formalism is that it makes use of conserved quantities to develop techniques to study particle dynamics in a beamline.

The Hamiltonian describes the mechanics of a system in the same way as the force in Newton's second law. The Hamiltonian is a function of the coordinates (x_i), the momentum (p_i) and an independent variable, which may be the time t:

$$H = H(x_i, p_i; t). \tag{1.39}$$

Hamilton's equations are given as [13]:

$$\begin{aligned} \frac{dx_i}{dt} = \frac{\partial H}{\partial p_i}, \\ \frac{dp_i}{dt} = -\frac{\partial H}{\partial x_i}. \end{aligned} \tag{1.40}$$

The Hamiltonian makes use of the momentum p_i rather than x_i', as was used for Hill's equations. However, these two values represent different physical quantities, in

particular:

$$x_i' = \frac{dx_i}{ds} = \frac{v_i}{v_s}, \tag{1.41}$$

while p_i is given by:

$$p_i = \frac{\beta\gamma m v_i + qA_i}{p_0}. \tag{1.42}$$

where q is the charge and A_i the component of the vector potential parallel to v_i. If the direction of motion makes a small angle with respect to the reference trajectory and if $\gamma \simeq \gamma_0$ then the approximation $x_i' \approx p_i$ can be taken.

The Hamiltonian for a relativistic charged particle moving in an electromagnetic field is [3]:

$$H = c\sqrt{(\vec{p} - q\vec{A})^2 + m^2c^2} + q\phi, \tag{1.43}$$

where ϕ and $\vec{A}$ are the scalar and vector potential respectively, related to the electric and magnetic fields as:

$$\vec{E} = -\nabla\phi - \frac{\partial \vec{A}}{\partial t}, \tag{1.44}$$

$$\vec{B} = \nabla \times \vec{A}, \tag{1.45}$$

and $\vec{p}$ is the canonical momentum.

As was the case for Newtonian mechanics, it is convenient to work in a system where the position along the beamline (s) is the independent variable and a local coordinate system is taken with respect to the reference trajectory. The Hamiltonian in terms of this new coordinate system with transverse positions x and y and canonical transverse momenta p_x and p_y is given by [3]:

$$H = \frac{\delta}{\beta_0} - (1+hx)\sqrt{\left(\delta + \frac{1}{\beta_0} - \frac{q\phi}{cp_0}\right)^2 - (p_x - a_x)^2 - (p_y - a_y)^2 - \frac{1}{\beta_0^2\gamma_0^2}} - (1+hx)\,a_s, \tag{1.46}$$

where δ is the energy deviation:

$$\delta = \frac{E}{cp_0} - \frac{1}{\beta_0}, \tag{1.47}$$

p_0 is the reference momentum and β_0 is chosen so that $p_0 = \beta_0\gamma_0 mc$ (with $\gamma_0 = 1/\sqrt{1-\beta_0^2}$). h is defined as the curvature of the reference trajectory ($h = 1/\rho$), and (a_x, a_y, a_s) are the scaled vector potentials in x, y and s directions, given by:

$$a_{x,y,s} = \frac{q}{p_0} A_{x,y,s}. \tag{1.48}$$

1.2.3 Matrix Formulation

The expressions given in Eq. 1.37 and the Hamiltonian in Eq. 1.46 both describe the system of a charged particle in an electromagnetic field in a local $x-y$ coordinate system relative to the reference trajectory.

In this section, the equations of motion are solved for some of the most common components of an accelerator beamline. It will be clear that even for the most simple cases, the equations of motion are not linear, however, a linear approximation can be made to a non-linear system to study certain aspects of the beam dynamics.

When obtaining the solutions to the equations of motion of different elements of the accelerator it is useful to present the final coordinates of the particle in terms of the initial coordinates using a transfer matrix such that:

$$\vec{x}_1 = M_{\text{element}}\vec{x}_0, \tag{1.49}$$

with $\vec{x}_0$ and $\vec{x}_1$ representing the initial and final phase space vectors respectively, both are constructed as:

$$\vec{x} = \begin{pmatrix} x \\ p_x \\ y \\ p_y \\ z \\ \delta \end{pmatrix}. \tag{1.50}$$

The matrix formalism makes it easier to follow a particle through a beamline consisting of linear elements such as drifts, dipoles and quadrupoles by multiplying the matrices in the appropriate order. As an example, supposing a beamline of three elements the total matrix will be given by:

$$M_{\text{Total}} = M_{\text{final}}M_{\text{middle}}M_{\text{start}}. \tag{1.51}$$

The final coordinates of the particles in such a beamline can be given in terms of the initial position as:

$$\vec{x}_1 = M_{\text{Total}}\vec{x}_0. \tag{1.52}$$

The transfer matrix for different elements can be obtained by solving the equations of motion, either by solving Eq. 1.37 or by using the corresponding Hamiltonian in 1.46 and making a linear approximation.

1.2.4 Drift

In this section the equations of motion of the simplest of elements, the drift, will be presented using the Hamiltonian formalism.

For a drift the potentials ϕ and A are set to zero in the Hamiltonian in Eq. 1.46 to obtain:

$$H = \frac{\delta}{\beta_0} - \sqrt{\left(\delta + \frac{1}{\beta_0}\right)^2 - p_x^2 - p_y^2 - \frac{1}{\beta_0^2\gamma_0^2}}. \tag{1.53}$$

Using Hamilton's equations (Eq. 1.40) the solutions to the equations of motion are:

$$\begin{aligned} x_1 &= x_0 + Lp_{x0} + O(2), && (1.54)\\ p_{x1} &= p_{x0}, && (1.55)\\ y_1 &= y_0 + Lp_{y0} + O(2), && (1.56)\\ p_{y1} &= p_{y0}, && (1.57)\\ z_1 &= z_0 + \frac{L}{\beta_0^2\gamma_0^2}\delta_0 + O(2), && (1.58)\\ \delta_1 &= \delta_0, && (1.59) \end{aligned}$$

where L is the length of the drift. Thus, even for the simplest of elements the equations are not linear and are expressed with a second order error. By making a linear approximation the matrix formalism can be used to express the final phase space vector in terms of the initial phase pace vector as:

$$\vec{x}_1 = M_{\text{drift}}\vec{x}_0, \tag{1.60}$$

where the corresponding matrix for the drift element is given by:

$$M_{\text{drift}} = \begin{pmatrix} 1 & L & 0 & 0 & 0 & 0 \\ 0 & 1 & 0 & 0 & 0 & 0 \\ 0 & 0 & 1 & L & 0 & 0 \\ 0 & 0 & 0 & 1 & 0 & 0 \\ 0 & 0 & 0 & 0 & 1 & \frac{L}{\beta_0^2\gamma_0^2} \\ 0 & 0 & 0 & 0 & 0 & 1 \end{pmatrix}. \tag{1.61}$$

1.2.5 Quadrupoles and Dipoles

In this section the equations of motion of the elements of the beamline that provide the particles with steering (dipoles) and focusing (quadrupoles) will be derived.

This time, Newtonian mechanics will be used to obtain the transfer matrix. A quadrupole magnet is equivalent to the system in Eq. 1.37 with $1/\rho = 0$, which gives:

$$\begin{aligned} x''(s) + k_1 x(s) = 0, \\ y''(s) - k_1 y(s) = 0, \end{aligned} \tag{1.62}$$

where k_1 is a constant. The sign of k_1 determines the focusing properties of the quadrupole, $k_1 > 0$ gives a horizontal focusing field, while $k_1 < 0$ gives a vertical focusing field.

Solving the differential equation 1.62 in the horizontal direction gives the solution:

$$\begin{aligned} x(s) &= A\cos(\sqrt{k_1}s) + B\sin(\sqrt{k_1}s), && (1.63)\\ x'(s) &= -\sqrt{k_1}A\sin(\sqrt{k_1}s) + \sqrt{k_1}B\cos(\sqrt{k_1}s), && (1.64) \end{aligned}$$

where A and B are constants of integration. Assuming the initial conditions $x(0) = x_0$ and $x'(0) = x'_0$ the values of the constants are $A = x_0$ and $B = x'_0/\sqrt{k_1}$, giving the solution:

$$x(s) = x_0 \cos(\sqrt{k_1}s) + \frac{x'_0}{\sqrt{k_1}} \sin(\sqrt{k_1}s), \tag{1.65}$$

$$x'(s) = -\sqrt{k_1}x_0 \sin(\sqrt{k_1}s) + x'_0 \cos(\sqrt{k_1}s). \tag{1.66}$$

A similar process can be carried out for the vertical direction which gives the solution:

$$y(s) = y_0 \cosh(\sqrt{k_1}s) + \frac{y'_0}{\sqrt{k_1}} \sinh(\sqrt{k_1}s), \tag{1.67}$$

$$y'(s) = \sqrt{k_1}y_0 \sinh(\sqrt{k_1}s) + y'_0 \cosh(\sqrt{k_1}s). \tag{1.68}$$

The transfer matrix for a quadrupole of length l and focusing strength k gives:

$$M_{\text{quad}} = \begin{pmatrix} \cos\phi & \frac{1}{\sqrt{k_1}}\sin\phi & 0 & 0 & 0 & 0 \\ -\sqrt{k_1}\sin\phi & \cos\phi & 0 & 0 & 0 & 0 \\ 0 & 0 & \cosh\phi & \frac{1}{\sqrt{k_1}}\sinh\phi & 0 & 0 \\ 0 & 0 & \sqrt{k_1}\sinh\phi & \cosh\phi & 0 & 0 \\ 0 & 0 & 0 & 0 & 1 & \frac{L}{\beta_0^2\gamma_0^2} \\ 0 & 0 & 0 & 0 & 0 & 1 \end{pmatrix}, \tag{1.69}$$

where $\phi = \sqrt{k_1}l$. If $k_1 > 0$ the particle will have an oscillatory motion in the horizontal direction, although within a magnet the particle will only perform a small fraction of the oscillation, resulting in a focusing force. In the vertical direction however, the force is defocusing. If $k_1 < 0$ the situation is reversed, and now the particle focuses in the vertical direction but defocuses in the horizontal direction.

The same technique can be used to obtain the solutions for a dipole field. This time $k = 0$ and $1/\rho \neq 0$ in Eq. 1.37, resulting in the following equation:

$$x''(s) + \frac{1}{\rho^2}x(s) = 0. \tag{1.70}$$

Solving the differential equation the solutions are given as:

$$\begin{aligned} x(s) &= x_0 \cos(s/\rho) + x'_0\rho \sin(s/\rho), \\ x'(s) &= -\frac{x_0}{\rho} \sin(s/\rho) + x'_0 \cos(s/\rho). \end{aligned} \tag{1.71}$$

Giving the equivalent transfer matrix as:

$$M_{\text{dipole}} = \begin{pmatrix} \cos(s/\rho) & \rho\sin(s/\rho) & 0 & 0 & 0 & 0 \\ -\frac{1}{\rho}\sin(s/\rho) & \cos(s/\rho) & 0 & 0 & 0 & 0 \\ 0 & 0 & 1 & L & 0 & 0 \\ 0 & 0 & 0 & 1 & 0 & 0 \\ 0 & 0 & 0 & 0 & 1 & \frac{L}{\beta_0^2\gamma_0^2} \\ 0 & 0 & 0 & 0 & 0 & 1 \end{pmatrix}. \tag{1.72}$$

Thin lens and small angle approximation

In the previous section linear transfer maps were defined for some of the most common elements of an accelerator. With these transfer maps it is possible to obtain the position of the particles after a series of components in a beamline. However, to simplify the analysis a 'thin lens' approximation can be made for the quadrupoles. This approximation is of relevance for symplectic tracking when an accurate description of the longitudinal dynamics needs to be included, as will be described in Section 2.6.1.

The thin lens approximation considers the following conditions:

$$\begin{aligned} l &\to 0, \\ k_1 l &\to \frac{1}{f}, \end{aligned} \tag{1.73}$$

where f is defined as the quadrupole focal length. This approximation is only useful for cases where the focal length is much bigger than the quadrupole length, i.e., $f \gg l$. The transfer matrix of a quadrupole focusing in the horizontal direction (and defocusing in the vertical direction) in the thin lens approximation is given by:

$$M_{\text{quad}} = \begin{pmatrix} 1 & 0 & 0 & 0 & 0 & 0 \\ -\frac{1}{f} & 1 & 0 & 0 & 0 & 0 \\ 0 & 0 & 1 & 0 & 0 & 0 \\ 0 & 0 & \frac{1}{f} & 1 & 0 & 0 \\ 0 & 0 & 0 & 0 & 1 & \frac{L}{\beta_0^2\gamma_0^2} \\ 0 & 0 & 0 & 0 & 0 & 1 \end{pmatrix}, \tag{1.74}$$

In the case of the dipoles a small-angle approximation can be made that gives a simplified linear matrix of a dipole of length l:

$$M_{\text{dipole}} = \begin{pmatrix} 1 & l & 0 & 0 & 0 & 0 \\ -\frac{l^2}{\rho^2} & 1 & 0 & 0 & 0 & 0 \\ 0 & 0 & 1 & L & 0 & 0 \\ 0 & 0 & 0 & 1 & 0 & 0 \\ 0 & 0 & 0 & 0 & 1 & \frac{L}{\beta_0^2\gamma_0^2} \\ 0 & 0 & 0 & 0 & 0 & 1 \end{pmatrix}. \tag{1.75}$$

FODO lattice

A system that is particularly useful in constructing accelerator beamlines is the FODO cell, which is composed of a focusing quadrupole and a defocusing quadrupole separated by a drift. Choosing the system to start in the middle of the focusing quadrupole, such that the system is periodic and symmetric, the transfer map for the combination of elements in matrix notation is written as:

$$M_{\text{fodo}} = M_{\text{QF}/2} M_{\text{Drift}} M_{\text{QD}} M_{\text{Drift}} M_{\text{QF}/2}. \tag{1.76}$$

Assuming the same focal length (f) for both quadrupoles, and the same length for both drifts (L), the transfer matrix of the FODO cell in the thin lens approximation for the horizontal direction is given by [14]:

$$M_{\text{fodo}} = \begin{pmatrix} 1 - 2\frac{L^2}{f^2} & 2L\left(1 + \frac{L}{f}\right) \\ -\frac{1}{f^*} & 1 - 2\frac{L^2}{f^2} \end{pmatrix}, \tag{1.77}$$

where, $f = f_f = -f_d$ (focusing and defocusing focal length respectively) and $1/f^* = 2(1 - L/f)L/f^2$.

1.2.6 Dispersion

In an ideal monochromatic beam all particles will travel along the design path for the reference momentum. In reality however, a momentum spread will be present. Since the bending and focusing systems of the accelerator have a dependence on momentum, this spread needs to be accounted for in order to give a realistic representation of the beam.

A particle with momentum $p = p_0 + \Delta p$ subject to a dipole field will satisfy the inhomogeneous Hill's equation:

$$x''(s) + \frac{1}{\rho^2} x(s) = \frac{1}{\rho} \frac{\Delta p}{p_0}. \tag{1.78}$$

The dispersion function $D(s)$ is defined as the solution for the trajectory of a particle with a fixed momentum deviation with $\Delta p/p_0 = 1$. The equation of motion now becomes:

$$D''(s) + \frac{1}{\rho^2} D(s) = \frac{1}{\rho}. \tag{1.79}$$

The general solution of this equation can be obtained by finding the homogeneous solution (D_h) plus a particular solution of the inhomogeneous equation (D_p). The solution to the homogeneous equation has already been given, since it has the same form as the equation of motion for a particle in a dipole field:

$$D_h(s) = A \cos\left(\frac{s}{\rho}\right) + B \sin\left(\frac{s}{\rho}\right), \tag{1.80}$$

where A and B are constants of integration. For the inhomogeneous equation, a particular solution that fulfills the conditions is given by:

$$D_p = \rho\left(1 - \cos\left(\frac{s}{\rho}\right)\right). \tag{1.81}$$

Hence, the general solution is given by:

$$\begin{aligned} D(s) &= A\cos\left(\frac{s}{\rho}\right) + B\sin\left(\frac{s}{\rho}\right) + \rho\left(1 - \cos\left(\frac{s}{\rho}\right)\right), \\ D'(s) &= -\frac{A}{\rho}\sin\left(\frac{s}{\rho}\right) + \frac{B}{\rho}\cos\left(\frac{s}{\rho}\right) + \frac{1}{\rho}\cos\left(\frac{s}{\rho}\right). \end{aligned} \tag{1.82}$$

Taking as initial conditions $D(s=0) = D_0$ and $D'(s=0) = D'_0$ the solutions to $D(s)$ and $D'(s)$ take the form:

$$\begin{aligned} D(s) &= D_0\cos\left(\frac{s}{\rho}\right) + \rho D'_0\sin\left(\frac{s}{\rho}\right) + \rho\left(1 - \cos\left(\frac{s}{\rho}\right)\right), \\ D'(s) &= -\frac{D_0}{\rho}\sin\left(\frac{s}{\rho}\right) + D'_0\cos\left(\frac{s}{\rho}\right) + \sin\left(\frac{s}{\rho}\right). \end{aligned} \tag{1.83}$$

The matrix formulation can be used to express $D(s)$ and $D'(s)$ in terms of the initial conditions D_0 and D'_0, however in this case, given the third term in both equations, a 3×3 matrix is required.

$$\begin{pmatrix} D(s) \\ D'(s) \\ 1 \end{pmatrix} = \begin{pmatrix} \cos\left(\frac{s}{\rho}\right) & \rho\sin\left(\frac{s}{\rho}\right) & \rho\left(1 - \cos\left(\frac{s}{\rho}\right)\right) \\ -\frac{1}{\rho}\sin\left(\frac{s}{\rho}\right) & \cos\left(\frac{s}{\rho}\right) & \sin\left(\frac{s}{\rho}\right) \\ 0 & 0 & 1 \end{pmatrix} \begin{pmatrix} D_0 \\ D'_0 \\ 1 \end{pmatrix}. \tag{1.84}$$

This solution can be added to the non-dispersive orbit to obtain the complete solution (x_T) representing the transverse position:

$$x_T = x(s) + D(s)\frac{\Delta p}{p_0}. \tag{1.85}$$

To propagate the dispersive orbit at the same time as the reference orbit, the 2×2 transfer matrices obtained previously can be converted into 3×3 matrices by adding a new row. So, for elements other than the dipole, with a transfer matrix of the form:

$$M = \begin{pmatrix} M_{11} & M_{12} \\ M_{21} & M_{22} \end{pmatrix} \tag{1.86}$$

the transformation for the dispersive beam becomes:

$$\begin{pmatrix} x(s) \\ x'(s) \\ \Delta p/p_0 \end{pmatrix} = \begin{pmatrix} M_{11} & M_{12} & 0 \\ M_{21} & M_{22} & 0 \\ 0 & 0 & 1 \end{pmatrix} \begin{pmatrix} x_0 \\ x'_0 \\ \Delta p/p_0 \end{pmatrix}. \tag{1.87}$$

This equation shows that even when dipoles are the only components generating dispersion, quadrupoles also affect the dispersive orbit, and hence, both can be used when trying to control the dispersion.

1.3 Particle Beam Dynamics

So far the study of single particle dynamics has been presented. However, in an accelerator, when dealing with bunches of many particles, considering the individual behaviour of every particle becomes impractical. Furthermore in most cases there is greater interest in the overall behaviour of the beam rather than the specific behaviour of the individual particles. As an example, in a collider it is necessary to specify the beam size at the interaction point.

In this section, rather than tracking each particle separately, mathematical tools are used that will help describe the behaviour of the whole particle beam assuming an uncoupled beamline, i.e. with the horizontal, vertical and longitudinal directions treated independently.

1.3.1 Courant–Snyder Parameters

Using Hill's equations (1.37) for a periodic beamline with focusing properties in the transverse direction assuming a monochromatic beam, i.e. $\Delta p = 0$ gives:

$$x'' + k_x(s)x = 0, \tag{1.88}$$

where k_x is a position dependent force.

Assuming that the solution forms an oscillation around the reference orbit, the proposed solution gives:

$$x(s) = A\sqrt{\beta(s)}\cos(\phi(s) + \psi), \tag{1.89}$$

where A and ψ are determined by the initial conditions.

Taking the derivative of x to obtain x'' and inserting it into Eq. 1.88 gives the equation:

$$\begin{aligned} -\frac{A}{\sqrt{\beta(s)}}\sin(\phi(s)+\psi)(\beta'(s)\phi'(s)+\beta(s)\phi''(s)) \\ -\frac{A}{4\beta(s)^{3/2}}\cos(\phi(s)+\psi)(-2\beta(s)\beta''(s)+\beta'(s)^2+4\beta(s)^2\phi'(s)^2) \\ = -k_x A\sqrt{\beta(s)}\cos(\phi(s)+\psi). \end{aligned} \tag{1.90}$$

Equating the cosine and sine terms on both sides of Eq. 1.90 we find that the sine term must always be zero, which is possible if the following condition is fulfilled:

$$\beta'(s)\phi'(s) + \beta(s)\phi''(s) = 0. \tag{1.91}$$

This results in the condition for $\phi(s)$:

$$\phi'(s) = \frac{1}{\beta(s)}. \tag{1.92}$$

The phase advance is defined as the change in the angle ϕ:

$$\mu = \phi(s_1) - \phi(s_0) = \int_{s_0}^{s_1} \frac{ds}{\beta(s)}. \tag{1.93}$$

Dividing the phase advance by 2π gives the number of transverse oscillations around a given reference trajectory of on-momentum particles travelling once around the ring (known as betatron oscillations). This quantity is called the tune. Since there are different β functions in the horizontal and vertical planes, a tune should be defined in each direction, and is written as:

$$Q_{x,y} = \frac{1}{2\pi} \oint \frac{ds}{\beta_{x,y}(s)}. \tag{1.94}$$

The tunes are an important design property of the accelerator. Choosing the appropriate values of the tunes is necessary to ensure the stability of the beam and avoid the excitation of resonances, as will be explained in Section 1.5.4. Also, a shift in tune may exist as a function of the amplitude of the particle or focusing errors: these effects will be further addressed in Section 1.5.3.

To develop further the significance of the β function, we introduce the following definition [14]:

$$\alpha(s) \equiv -\frac{\beta'(s)}{2}. \tag{1.95}$$

The derivative of x can be expressed in terms of the functions $\beta(s)$ and $\alpha(s)$ as :

$$x'(s) = -\frac{A}{\sqrt{\beta_x(s)}}(\alpha_x(s)\cos(\phi(s)+\psi) + \sin(\phi(s)+\psi)). \tag{1.96}$$

The expressions $\cos(\phi(s)+\psi)$ and $\sin(\phi(s)+\psi)$ can be given in terms of x and x' using Eqs. 1.89 and 1.96 as:

$$\cos(\phi(s)+\psi) = \frac{x}{A\sqrt{\beta_x(s)}}, \tag{1.97}$$

$$\sin(\phi(s)+\psi) = -\Big(\frac{\sqrt{\beta_x(s)}x'}{A} + \frac{\alpha_x(s)x}{A\sqrt{\beta_y(s)}}\Big). \tag{1.98}$$

Now, we introduce a third definition given as [14]:

$$\gamma_x(s) \equiv \frac{1+\alpha_x^2(s)}{\beta_x(s)}. \tag{1.99}$$

Then, using the identity $\cos^2\theta + \sin^2\theta = 1$, we find that:

$$A^2 = \gamma_x x^2 + 2\alpha_x x x' + \beta_x x'^2. \tag{1.100}$$

The set of functions $\beta_x(s), \alpha_x(s)$ and $\gamma_x(s)$ are known as the Courant–Snyder parameters [15] (also sometimes referred to as Twiss parameters).

For the case of individual particles a set of "action-angle variables" $(J_x(s), \phi_x(s))$ is introduced. In particular $J = A^2/2$. The original variables $x(s)$ and $x'(s)$ can be expressed in terms of these new variables as:

$$x(s) = \sqrt{2J_x\beta_x(s)}\cos(\phi_x(s) + \psi), \tag{1.101}$$

$$x'(s) = -\sqrt{\frac{2J_x}{\beta_x(s)}}\left(\sin(\phi_x(s) + \psi) - \alpha_x(s)\cos(\phi(s) + \psi)\right). \tag{1.102}$$

The variables J_x and ϕ_x can be expressed in terms of x and x' as follows:

$$J_x = \frac{1}{2}(\gamma_x x^2 + 2\alpha_x x x' + \beta_x x'^2), \tag{1.103}$$

$$\tan\phi_x = -\beta_x\frac{x'}{x} - \alpha_x. \tag{1.104}$$

The equation for the action J_x describes a parametric general equation of an ellipse in the (x, x') plane. The shape of this ellipse, along with the connection with the Courant-Snyder parameters is given in Fig. 1.6. The action J_x of the particle remains constant along the beamline, but the shape of the phase space ellipse will vary depending on the Courant–Snyder parameters.

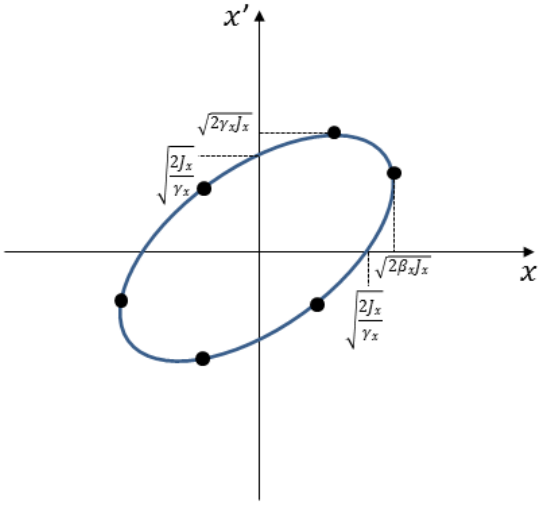

FIGURE 1.6: Phase-space ellipse in terms of the Courant-Snyder parameters.

Knowing the Courant–Snyder parameters at a given position in the beamline one can obtain the resulting Courant–Snyder parameters at any other point by knowing the

transformation of a single particle. At the starting point $s = 0$ (using Eq. 1.103) the action of a particle in the beam is given by:

$$\gamma_0 x_0^2 + 2\alpha_0 x_0 x_0' + \beta_0 x_0'^2 = 2J_x. \tag{1.105}$$

Assuming that the transformation from the starting point to a position $s \neq 0$ can be written using matrix notation, we introduce the functions C S C' and S', so that:

$$\begin{pmatrix} x_1 \\ x_1' \end{pmatrix} = \begin{pmatrix} C(s) & S(s) \\ C'(s) & S'(s) \end{pmatrix} \begin{pmatrix} x_0 \\ x_0' \end{pmatrix}. \tag{1.106}$$

Giving x_0 and x_0' in terms of the new position $x(s)$ and $x'(s)$, inserting them into Eq. 1.105 and rearranging the terms yields the result:

$$\begin{aligned} 2J_x = (C'^2\beta_0 - 2S'C'\alpha_0 + S'^2\gamma_0)x_1^2 \\ +2(-CC'\beta_0 + S'C\alpha_0 + SC'\alpha_0 - SS'\gamma_0)x_1x_1' \\ +(C^2\beta_0 - 2SC\alpha_0 + S^2\gamma_0)x_1'^2. \end{aligned} \tag{1.107}$$

Comparing with Eq. 1.105 new values of the Courant-Snyder parameters are obtained:

$$\gamma_1 = C'^2\beta_0 - 2S'C'\alpha_0 + S'^2\gamma_0 \tag{1.108}$$

$$\alpha_1 = -CC'\beta_0 + S'C\alpha_0 + SC'\alpha_0 - SS'\gamma_0 \tag{1.109}$$

$$\beta_1 = C^2\beta_0 - 2SC\alpha_0 + S^2\gamma_0. \tag{1.110}$$

If $CS' - SC' = 1$ Eq. 1.110 describes an ellipse of the same area (A=$2\pi J_x$) but the new parameters α_1, β_1 and γ_1 describe a ellipse with a different shape and orientation. This result can be written in matrix notation as:

$$\begin{pmatrix} \beta_1(s) \\ \alpha_1(s) \\ \gamma_1(s) \end{pmatrix} = \begin{pmatrix} C^2 & -2CS & S^2 \\ -CC' & CS' + C'S & -SS' \\ C'^2 & -2C'S' & S'^2 \end{pmatrix} \begin{pmatrix} \beta_0 \\ \alpha_0 \\ \gamma_0 \end{pmatrix}. \tag{1.111}$$

Courant-Snyder parameters also provide another way to describe the particle trajectories in periodic lattices. Assuming the initial variables x_0 and x_0', then the transport matrix for a single periodic structure in the horizontal direction will be given by:

$$\begin{pmatrix} x_1 \\ x_1' \end{pmatrix} = \begin{pmatrix} \cos\mu_x + \alpha_x \sin\mu_x & \beta_x \sin\mu_x \\ -\gamma_x \sin\mu_x & \cos\mu_x - \alpha_x \sin\mu_x \end{pmatrix} \begin{pmatrix} x_0 \\ x_0' \end{pmatrix}. \tag{1.112}$$

This result will be particularly useful for the case when the transfer matrix over a cell is known: this expression then allows for calculation of the Courant-Snyder parameters and the phase advance. As an example the phase advance can be easily obtained from the trace of the matrix as:

$$\mathrm{Tr}(\mathrm{M_x}) = 2\cos\mu_\mathrm{x}. \tag{1.113}$$

Hence, we require $|\mathrm{Tr(M)}| < 2$ for stable motion in a periodic lattice.

Courant–Snyder parameters for a bunch of particles

The Courant-Snyder parameters, under certain assumptions, describe also the distribution of particles within a bunch. Taking the statistical average of x^2 over all particles within a bunch at a particular point, using the definition given in Eq. 1.102 we obtain:

$$\left\langle x^2 \right\rangle = 2\beta_x \left\langle J_x \cos^2 \phi_x \right\rangle, \tag{1.114}$$

where the brackets $\langle \cdot \rangle$ indicate the mean of the enclosed quantity over all particles within a bunch. Assuming that the angles and action variables are uncorrelated and that the angles are uniformly distributed from 0 to 2π, we obtain:

$$\langle x \rangle = 0, \tag{1.115}$$

and the mean square value in Eq. 1.114 gives:

$$\left\langle x^2 \right\rangle = \beta_x \epsilon_x, \tag{1.116}$$

where the following definition has been introduced:

$$\epsilon_x = \langle J_x \rangle . \tag{1.117}$$

ϵ_x is called the horizontal emittance of the bunch. Following a similar procedure we obtain:

$$\left\langle x x' \right\rangle = -\alpha_x \epsilon_x, \tag{1.118}$$

$$\left\langle x'^2 \right\rangle = \gamma_x \epsilon_x. \tag{1.119}$$

Combining Eqs. 1.116, 1.118 and 1.119 with Eq. 1.99 we obtain the expression of the emittance in terms of the beam distribution:

$$\epsilon_x = \sqrt{\langle x'^2 \rangle \langle x'^2 \rangle - \langle x x' \rangle^2}. \tag{1.120}$$

Therefore, the emittance can be determined from the distribution of the beam at a particular point in the beamline, and consequently the values of the Courant-Snyder parameters are found from Equations 1.116, 1.118 and 1.119. A similar procedure can be followed to obtain the vertical emittance.

The emittance characterizes the phase space area occupied by the beam. Following from Eq. 1.116, for a Gaussian beam with standard deviation σ in a region of zero dispersion the beam size is given in terms of the emittance and the β function as:

$$\sigma_{x,y} = \sqrt{\epsilon_{x,y} \beta_{x,y}}, \tag{1.121}$$

The normalised emittance ϵ_N is defined by:

$$\epsilon_N = \beta\gamma\epsilon, \tag{1.122}$$

where $\beta = v/c$ and γ in this case is the relativistic factor (not the Courant–Snyder parameter). The normalized emittance is constant under acceleration.

Eq. 1.111 indicates that by knowing the initial Courant–Snyder parameters it is possible to obtain the Courant–Snyder parameters of the beam, and hence the shape and orientation in phase space, at any other point on the beamline by knowing the transformation of a single particle.

As an example consider a beam going through a drift of length l with initial conditions $\beta_0 = \beta^*$ and $\alpha_0 = 0$ and hence $\gamma_0 = 1/\beta^*$. Recalling the drift matrix given in Eq. 1.61 and comparing it with Eq. 1.106 the new Courant-Snyder parameters are:

$$\begin{pmatrix} \beta(s) \\ \alpha(s) \\ \gamma(s) \end{pmatrix} = \begin{pmatrix} 1 & -2l & l^2 \\ 0 & 1 & -l \\ 0 & 0 & 1 \end{pmatrix} \begin{pmatrix} \beta^* \\ 0 \\ 1/\beta^* \end{pmatrix}. \tag{1.123}$$

Hence, the new values of $\beta(s)$ and $\alpha(s)$ are given as:

$$\beta_x(s) = \beta^* + \frac{l^2}{\beta^*}, \tag{1.124}$$

$$\alpha_x(s) = -\frac{l}{\beta^*}, \tag{1.125}$$

$$\gamma_x(s) = \frac{1}{\beta^*}. \tag{1.126}$$

This example will be particularly useful to measure the size of the beam in the nearby zone of a collision point, and will be referred to later on.

1.3.2 Luminosity

The luminosity $\mathcal{L}$ is a key parameter in the design of a particle collider. The luminosity is the proportionality factor between the number of events per second (dR/dt) and the cross section (σ_p) [16]:

$$\frac{dR}{dt} = \mathcal{L}\sigma_p. \tag{1.127}$$

In particle physics, for rare events (such as the production of a Higgs particle) a high luminosity is essential to increase the number of events.

In a collider, the luminosity can be expressed as follows:

$$\mathcal{L} = \frac{N_1 N_2 N_b}{4\pi\sqrt{\epsilon_x\epsilon_y\beta_x^*\beta_y^*}}. \tag{1.128}$$

The luminosity is then given in terms of the number of particles per bunch (N_1, N_2), the number of bunches (N_b) and the emittance and beta functions in the horizontal and vertical directions.

In practice however, there are other factors to be considered that may affect the luminosity. The expression of the luminosity, considering some of these factors is given by:

$$\mathcal{L} = \frac{N_1 N_2 N_b}{4\pi\sqrt{\epsilon_x \epsilon_y \beta_x^* \beta_y^*}} W H_{\mathrm{hg}} F. \tag{1.129}$$

The factor W reduces the luminosity in the presence of beam offsets [16]. The hour-glass effect (H_{hg}) refers to the variation of the transverse beam size along the length of each bunch, occurring when the bunch lengths are comparable to or larger than β_x^* and β_y^* [17]. The factor F takes into account the geometric correction factor used for a crossing angle collision, this factor is given by [18]:

$$F = \frac{1}{\sqrt{1+\Phi_p^2}}, \tag{1.130}$$

where Φ_p is the Piwinski angle, obtained scaling the full crossing angle θ_c by the ratio of the longitudinal to transverse beam sizes σ_s and $\sqrt{\sigma_x \sigma_y}$:

$$\Phi_p = \frac{\theta_c}{2} \frac{\sigma_s}{\sqrt{\sigma_x \sigma_y}}. \tag{1.131}$$

In the case of head-on collisions the geometric factor becomes $F = 1$. Figures 1.7 and 1.8 illustrate head-on collisions and with a crossing angle respectively.

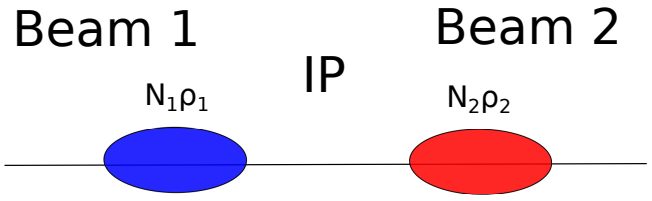

FIGURE 1.7: Head-on collision between beam 1 and beam 2.

Several parameters in the luminosity relate to the beam itself but the parameter that can be changed in the interaction region optics design is the β^*, which is proportional to the square of the size of the beam in the interaction point ($\sigma_{\mathrm{IP}} = \sqrt{\epsilon\beta^*}$). Greater luminosity can therefore be achieved by minimizing the value of β^*; however, following the result obtained in Eq. 1.126, minimizing β^* will result in an increase in the β function, and consequently the beam size, in the drift adjacent to the interaction point. If focusing quadrupoles are located at the end of this drift this may cause aperture issues.

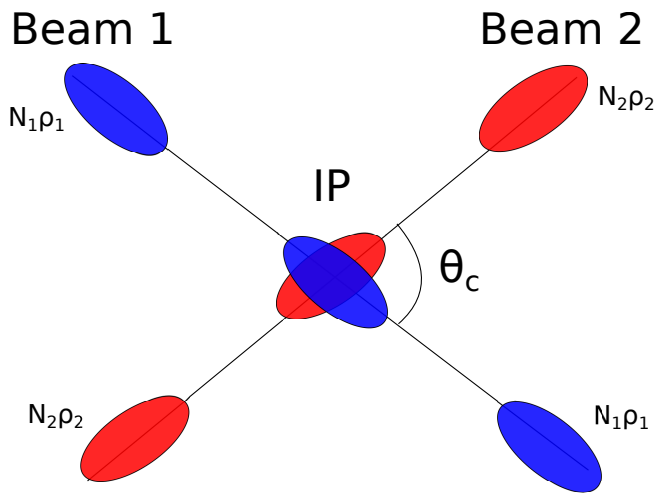

FIGURE 1.8: Collision between two bunches of Beam 1 and Beam 2 with a crossing angle θ_c. The overlapping area of the two beams is reduced in comparison with head-on collisions in Fig. 1.7. The factor by which this area is reduced is indicated in Eq. 1.130.

1.4 Linear Imperfections

Section 1.2.3 presented the description of transfer matrices for particles passing through linear elements of an ideal machine. In real life accelerators however, linear imperfections may occur in the magnets, such as a misalignment of magnets, or a variation in the focusing strength of the quadrupoles.

In an accelerator, an error in the misalignment or the focusing strength, however small, can have a considerable effect on the beam stability. Therefore, in the commissioning and running of any accelerator it is necessary to understand the source of the errors and how they may impact the beam dynamics.

The following sections will explain the effect of misalignment errors, studied in terms of the change in the closed orbit with respect to the reference orbit, and the impact of focusing errors, by calculating the change that these errors cause for the tune.

1.4.1 Dipole Alignment Errors

In the absence of any vertical steering, the vertical closed orbit will be the same as the reference trajectory. The effect of a field error can be evaluated by calculating the change in the vertical closed orbit, with respect the reference trajectory, that this error produces. For simplicity it will be assumed that the field error has only a horizontal field component, and that there is no coupling between the vertical, and either the horizontal or longitudinal motion.

Assuming a dipole field error at a position $s = s_0$, this will cause a change in momentum Δp_y in p_y when a particle reaches this point [3]:

$$\Delta p_y \approx \frac{q}{P_0} \int B_x ds, \tag{1.132}$$

where $\int B_x ds$ is the integrated strength of the horizontal dipole field along the reference trajectory and P_0 the reference momentum.

The conditions for a particle trajectory to close on itself are:

$$y(s_0 + C_0) = y(s_0), \tag{1.133}$$

$$p_y(s_0 + C_0) + \Delta p_y = p_y(s_0), \tag{1.134}$$

where C_0 is the circumference of the ring.

Expressing the previous conditions in action-angle variables and solving the equations, one obtains the action-angle variables for a particle in the closed orbit given as:

$$J_{y0} = \frac{\beta_y \Delta p_y^2}{8 \sin^2(\pi Q_y)}, \tag{1.135}$$

$$\phi_{y0} = -\pi Q_y. \tag{1.136}$$

where β_y is the β function in the location of the error and Q_y is the vertical tune.

Transforming back to Cartesian coordinates, the expression in the vertical direction at a location s, from the effect of a single dipole error at $s = s_0$ is given as [3]:

$$y_{co}(s) = \frac{\sqrt{\beta_y(s)\beta_y(s_0)}}{2\sin(\pi Q_y)} \Delta p_y \cos(\mu_y(s, s_0) - \pi Q_y). \tag{1.137}$$

Several conclusions can be drawn from these last results. First if the tune Q_y is an integer the action becomes infinite and therefore the closed orbit does not exist. On the other hand the effect of the dipole error is proportional to the β function at the location of the error and inversely proportional to $\sin(\pi Q_y)$. Thus, to reduce errors, the tune should be chosen to be far from integer numbers, and the β functions must be kept small in the location of errors. In some cases however, this is not possible: for example in the quadrupoles close to the interaction point in a collider where β functions reach very large values. Therefore, in these particular cases, special care must be put into the design, fabrication and installation of the magnets.

Considering a series of errors along the machine, if the perturbation is small enough linear superposition can be used, giving the position of the closed orbit as:

$$y_{co}(s) = \int_0^{C_0} \frac{\sqrt{\beta_y(s)\beta_y(s')}}{2\sin(\pi Q_y)} \frac{q}{p_0} B_x(s') \cos(\mu_y(s, s') - \pi Q_y) ds'. \tag{1.138}$$

The shape of the closed orbit when several errors are present along the ring is clearly more complicated. It should also be remember that certain approximations had to be taken into account to obtain this result, such as the fact that there is no coupling. However, some of the properties found under these assumptions still hold, such as the closed orbit is very sensitive to errors when the tune is close to an integer. This result will be considered further in Section 1.5.4 where the concept of resonances will be discussed.

1.4.2 Quadrupole Alignment Errors

The quadrupole field, as explained before, focuses particles to the reference trajectory in one direction while defocusing them in the other. In a perfectly aligned quadrupole the reference trajectory will pass through the middle of the quadrupole and a particle on this trajectory will not observe any field. However, if a misalignment occurs, a particle on the reference trajectory will receive a kick and consequently the closed orbit will no longer be exactly equal to the reference trajectory. In this case, the change in closed orbit can be calculated with respect to the reference trajectory assuming a vertical alignment error.

The calculation in this case will be performed for a vertical alignment error. Assuming that a quadrupole, of integrated gradient $k_1 L$ is moved a vertical distance Y_{quad} and letting y_{co} be the change in the closed orbit at the location of the quadrupole, a particle in the closed orbit passes through the quadrupole at a distance $y_{co} - Y_{\text{quad}}$ above the axis. Using the thin lens approximation the quadrupole field produces a change in p_y given by [3]:

$$\Delta p_y = k_1 L(y_{co} - Y_{\text{quad}}). \tag{1.139}$$

Inserting Δp_y into Eq. 1.137 at the location of the quadrupole ($s = s_0$), the expression for y_{co} of the closed orbit gives [3]:

$$y_{co} = \frac{\beta_y}{2} \cot(\pi Q_y) k_1 L(y_{co} - Y_{\text{quad}}), \tag{1.140}$$

where β_y is the vertical beta function at the location of the quadrupole. Solving for y_{co} this gives:

$$y_{co} = \frac{a}{a-1} Y_{\text{quad}}, \tag{1.141}$$

where:

$$a = \frac{\beta_y}{2} \cot(\pi Q_y) k_1 L. \tag{1.142}$$

The sensitivity of quadrupole errors can be given in terms of the ratio of $a/(a-1)$. If $a \ll 1$ the closed orbit will not be very sensitive to the quadrupole error, however if $a \gg 1$ then the error will be of the same order as Y_{quad}. On the other hand if $a \approx 1$ the quadrupole error will have a large effect on the closed orbit.

1.4.3 Quadrupole Focusing Errors

In the last section we presented the effects that a quadrupole misalignment has on the closed orbit. This section discusses the effects of another error that may arise in the quadrupoles: a change in the focusing strength.

Assuming that there is no coupling and in the case of no focusing errors, the transfer matrix for a single turn in the accelerator (given in Eq. 1.112) is:

$$M = \begin{pmatrix} \cos(2\pi Q_x) + \alpha_x \sin(2\pi Q_x) & \beta_x \sin(2\pi Q_x) \\ -\gamma_x \sin(2\pi Q_x) & \cos(2\pi Q_x) - \alpha_x \sin(2\pi Q_x) \end{pmatrix}. \tag{1.143}$$

where α_x, β_x and γ_x are the Courant–Snyder parameters, and Q_x the horizontal tune.

Now, considering an increase in the strength of a quadrupole given by ΔK, the focusing error can be represented by a transfer matrix in the same way as a normal quadrupole but for a focusing strength equivalent to ΔK, this is [3]:

$$M_{\text{err}} = \begin{pmatrix} 1 & 0 \\ -\Delta K & 1 \end{pmatrix}. \tag{1.144}$$

The complete transfer matrix along one turn of the storage ring including this focusing error is given by:

$$\bar{M} = M M_{\text{err}}. \tag{1.145}$$

The new transfer matrix $\bar{M}$ can be expressed in terms of the modified Courant–Snyder parameters ($\bar{\alpha}_x, \bar{\beta}_x$ and $\bar{\gamma}_x$) and the modified tune $\bar{Q}_x$ as:

$$\overline{M} = \begin{pmatrix} \cos(2\pi\bar{Q}_x) + \bar{\alpha}_x \sin(2\pi\bar{Q}_x) & \bar{\beta}_x \sin(2\pi\bar{Q}_x) \\ -\bar{\gamma}_x \sin(2\pi\bar{Q}_x) & \cos(2\pi\bar{Q}_x) - \bar{\alpha}_x \sin(2\pi\bar{Q}_x). \end{pmatrix} \tag{1.146}$$

Comparing the results between the multiplication of matrix $\bar{M}$ in Eq. 1.145 and the values given in the Matrix of Eq. 1.146, an approximate value of the change in tune ($\Delta Q_x = \bar{Q}_x - Q_x$) can be given as:

$$\Delta Q_x \approx \frac{\Delta K \beta_x}{4\pi}. \tag{1.147}$$

Hence, the change in tune will be proportional to the error in focusing and the value of the beta function at the location of the error. The value of the new beta function ($\bar{\beta}_x$) is given as:

$$\bar{\beta_x} = \frac{\beta_x}{1 + \frac{1}{2}\Delta K \beta_x \cot(2\pi Q_x)}. \tag{1.148}$$

From inspection of the denominator of this expression it is observed that, for integer and half integer tunes, the term $\cot(2\pi Q_x)$ becomes infinite and hence the β function vanishes. In reality the β function can not vanish. However, it does mean that, when the tune takes integer and half-integer values, the β function becomes very sensitive to the error. This effect will be seen again in Section 1.5.4 where resonances are explained.

1.5 Non-Linear Phenomena

Sections 1.2 and 1.3 described equations of motion for particles passing through the basic components of a beamline. These equations were obtained by making a linear approximation. In a real accelerator however, nonlinear elements will have to be introduced. In a realistic beamline for example, the incorporation of sextupoles becomes necessary to control the chromatic aberrations. On the other hand, nonlinearities can also have their source in the linear elements themselves; the presence of higher order multipole fields in the dipoles or quadrupoles (as explained in Section 1.1.4) is an example of this.

Since the presence of nonlinearities is unavoidable, the effects of nonlinear elements must be taken into account to make a truly accurate description of the beam.

1.5.1 Chromaticity and Chromaticity Correction

Even without the presence of magnetic errors, the particle beam is subject to a series of perturbations arising from momentum deviations. One of the most common consequences of a non-zero momentum deviation is the variation in focal length of a quadrupole with particle momentum. Particles with a change of momentum $\Delta p/p_0 > 0$ will have a longer focal length than those with no momentum deviation, and particles with $\Delta p/p_0 < 0$ will have a shorter one. This effect is illustrated in Fig. 1.9.

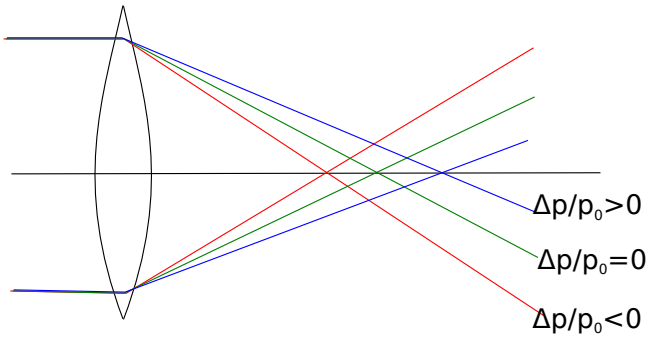

FIGURE 1.9: Chromatic aberrations produced by quadrupoles focusing particles at different lengths depending on their momentum.

The chromaticity is defined as the variation of the tunes with momentum:

$$Q' = \frac{\Delta Q}{\Delta p/p_0}. \tag{1.149}$$

The normalized chromaticity can be defined as:

$$\xi = \frac{Q'}{Q}. \tag{1.150}$$

The chromaticity in a circular accelerator can have undesirable consequences for two main reasons: First, a momentum deviation produces a tune spread in the beam and second, in the case of bunched beams, the chromaticity produces a transverse instability known as "head-tail instability" [19]. The following paragraphs will present the chromaticity due to the quadrupoles and the use of sextupoles as a way to compensate it.

Using the thin lens approximation, the transfer matrix in the horizontal direction of a quadrupole with integrated strength K is given as:

$$M_{\text{quad}}(k, p_0) = \begin{pmatrix} 1 & 0 \\ -K & 1 \end{pmatrix}. \tag{1.151}$$

Using the definition of the integrated quadrupole gradient we find that:

$$\frac{dK}{dp} = -\frac{K}{p_0}, \tag{1.152}$$

then, for a particle with momentum p, where $p = p_0 + \Delta p_0$, the transfer matrix is given as:

$$M_{\text{quad}}(K, p_0 + \Delta p_0) = \begin{pmatrix} 1 & 0 \\ -K\left(1 - \frac{\Delta p}{p_0}\right) & 1 \end{pmatrix}. \tag{1.153}$$

The effect of an increase in momentum can then be represented as a focusing error $\Delta K = -K\Delta p/p_0$. From Eq. 1.147, this corresponds to a contribution to the horizontal chromaticity in a storage ring of:

$$Q'_x = \frac{dQ_x}{dp/p_0} = -\frac{1}{4\pi}\oint_{\text{quads}} k_1(s)\beta_x(s)ds. \tag{1.154}$$

Similarly for the vertical direction:

$$Q'_y = -\frac{1}{4\pi}\oint_{\text{quads}} k_1(s)\beta_y(s)ds. \tag{1.155}$$

The expressions in 1.154 and 1.155 give the horizontal and vertical *natural* chromaticities. Given that the natural chromaticity is a function of the quadrupole strengths, focusing quadrupoles ($k_1 > 0$) will contribute to a negative value to the chromaticity, as for defocusing quadrupoles ($k_1 < 0$) will contribute with a positive value.

If not properly controlled, the chromaticity can have undesirable consequences on the stability of the machine. One way to control the chromaticity is to reduce the value of the β function at the location of the quadrupoles or reduce the quadrupole strengths. However, this is not always possible; as an example in a collider, such as the LHC, small beam sizes are required to achieve high luminosities, resulting in high β functions at the location of quadrupoles with high gradients, adjacent to the interaction points. Therefore, additional methods are required to control chromaticity. Fortunately, sextupole magnets provide the fields necessary to achieve the necessary control.

The magnetic field of a sextupole is given in Cartesian coordinates by [3]:

$$b_x = k_2 xy, \tag{1.156}$$

$$b_y = \frac{1}{2}k_2(x^2 - y^2), \tag{1.157}$$

$$b_z = 0, \tag{1.158}$$

where $(b_x, b_y, b_z) = \vec{b} = q\vec{B}/p_0$ and k_2 is the sextupole strength, related to the field of the sextupole as:

$$k_2 = \frac{q}{p_0}\frac{\partial^2 B_y}{\partial x^2}. \tag{1.159}$$

Applying the sextupole magnetic field for off-momentum particles (as given in Eq. 1.85):

$$x_t = x + D\frac{\Delta p}{p_0}, \tag{1.160}$$

the field b_y transforms as:

$$b_y = \frac{1}{2}k_2x^2 + k_2D\frac{\Delta p}{p_0}x + \frac{1}{2}k_2D^2\frac{\Delta p^2}{p_0^2} - \frac{1}{2}k_2y^2, \tag{1.161}$$

therefore, the second term is equivalent to a kick of a quadrupole with gradient $-k_2D\frac{\Delta p}{p_0}$, giving a tune shift from a short length ds of the sextupole:

$$\Delta Q_x = \frac{1}{4\pi}\beta_x(s)k_2(s)D_x(s)ds, \tag{1.162}$$

and a contribution to the horizontal chromaticity of:

$$Q'_x = -\frac{1}{4\pi}\oint_0^L \beta_x(s)k_2(s)D_x(s)ds. \tag{1.163}$$

where L is the length of the sextupole. Equivalently, for the vertical chromaticity:

$$Q'_y = -\frac{1}{4\pi}\oint_0^L \beta_y(s)k_2(s)D_y(s)ds, \tag{1.164}$$

The total chromaticity is the sum of the natural and the sextupole induced chromaticity, given in both directions this gives:

$$\begin{aligned} Q'_x &= -\frac{1}{4\pi}\oint \beta_x(s)(k_1(s) - k_2(s)D_x(s))ds, \\ Q'_y &= -\frac{1}{4\pi}\oint \beta_y(s)(k_1(s) + k_2(s)D_y(s))ds. \end{aligned} \tag{1.165}$$

Figure 1.10 illustrates the correction of the chromaticity by sextupoles located close to the quadrupoles. The sextupoles correct the chromaticity for particles with different momentum deviations resulting in the same focus length for all particles. The most efficient way to perform the chromaticity correction is to insert a sextupole at the same locations as each quadrupole (assuming non-zero dispersion) but often, fewer sextupoles with higher strengths are used instead [19]. In order to reduce the sextupole strengths it is also useful for the sextupoles to be placed in zones of high dispersion or high β function to maintain the same efficiency for the same strengths of the sextupoles.

The incorporation of sextupole families as a high order component has the disadvantage of introducing non-linear fields that can lead to chaotic motion. The effects of these nonlinearities must be considered to ensure that the required long term stability of the beam is still achieved.

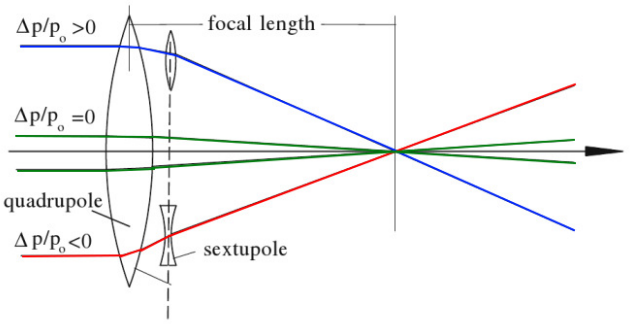

FIGURE 1.10: Chromaticity correction performed by the sextupoles for particles of different energies passing through a quadrupoles [14]

1.5.2 Montague Functions

Montague functions [20] describe how the Courant–Snyder parameters vary with momentum deviation. The Montague functions are defined for the horizontal and vertical directions as:

$$W_{x,y} = \frac{1}{2}\sqrt{A_{x,y}^2 + B_{x,y}^2}, \tag{1.166}$$

where:

$$A_{x,y} = \frac{1}{\beta_{x,y}}\frac{\partial \beta_{x,y}}{\partial \delta_p}, \tag{1.167}$$

$$B_{x,y} = \frac{\partial \alpha_{x,y}}{\partial \delta_p} - \alpha_{x,y} A_{x,y}, \tag{1.168}$$

and $\delta_p = \Delta p/p_0$ is the relative momentum deviation.

The variations of the Courant–Snyder parameters with respect to energy can be evaluated experimentally using observations made with beam position monitors [20]. In an idealised machine, where there is zero local chromaticity, W is equal to zero, in achromatic regions they are invariant. Therefore, by observing the behaviour the Montague functions one may determine the most critical regions for chromatic imperfections.

1.5.3 Amplitude Dependent Tune Shift

As previously stated when working with a real machine the implementation of nonlinear elements becomes necessary. Although higher-order multipoles may not be included in the lattice by design, errors in the magnets can lead to the presence of all orders. In this case the effect of another nonlinear element, the octupoles, is explored. First, consider the Hamiltonian of a beamline with only linear elements. In terms of the action-angle variables in one (horizontal) degree of freedom, this is given as:

$$H_0 = \frac{J_x}{\beta_x(s)}. \tag{1.169}$$

Canonical perturbation theory can be used to study the effects of non-linear elements. This is done by representing the complete Hamiltonian in the form [3]:

$$H = H_0(J_x; s) + \epsilon V(\phi_x, J_x; s), \tag{1.170}$$

where s is the independent variable, ϵ is a small parameter to keep track of the order of the perturbation and V is a function of the dynamical variables J_x and ϕ_x and the independent variables. For a beamline containing octupoles, the Hamiltonian in one (horizontal) degree of freedom is given as:

$$H = \frac{J_x}{\beta_x(s)} + \frac{1}{24}k_3(s)x^4, \tag{1.171}$$

which in action-angle variables corresponds to:

$$H = \frac{J_x}{\beta_x(s)} + \frac{1}{48}k_3(s)\beta_x(s)^2 J_x^2(3 + 4\cos(2\phi_x) + \cos(4\phi_x)). \tag{1.172}$$

Comparing with Eq. 1.170, we can identify:

$$H_0 = \frac{J_x}{\beta_x(s)} + \frac{1}{16}k_3(s)\beta_x(s)^2 J_x^2, \tag{1.173}$$

and

$$\epsilon V(\phi_x, J_x; s) = \frac{1}{48}k_3(s)\beta_x(s)^2 J_x^2(4\cos(2\phi_x) + \cos(4\phi_x)). \tag{1.174}$$

The change in phase advance through an octupole of length L located as $s = s_0$ is given by [3]:

$$\langle \Delta\phi_x \rangle = \int_{s_0}^{s_0+L} \left\langle \frac{\partial H}{\partial J_x} \right\rangle ds = \frac{1}{8}k_3 L\beta_x^2(s_0) \langle J_x \rangle . \tag{1.175}$$

Thus, creating a tune spread proportional to the integrated strength, the square of the β function and the emittance, since $\epsilon = \langle J_x \rangle$.

1.5.4 Resonances

A resonance is defined by any periodic motion with frequencies f_i that satisfy the following condition:

$$\sum_i n_i f_i = m_i, \tag{1.176}$$

where n_i and m_i are integers. These can occur in a perfect linear machine without any perturbations but perturbations can cause the resonances to become unstable. These section will refer to resonances in a circular machine.

An example of this is when a harmonic of the perturbation coincides with the eigenfrequency of the particle a resonance occurs and it may lead to the loss of the particle. Resonances normally appear in circular accelerators where the perturbation is added on every turn.

The study of resonances goes hand in hand with the presence of errors in the magnets of an accelerator. Section 1.4 has already illustrated how dipole and quadrupole errors require the tunes to be far from integer and half-integer values. This can also be understood by picturing a particle in phase space. In the case of ideal magnets if the tune is set to an integer number, for a point in an ellipse in Fig. 1.6 this will simply return to the same position after consecutive turns. If a dipole error is now introduced this will provide a kick to the particle in the p_x direction and, as the particle is returning to the same position in phase space, the kick will be given in the same direction every time and the kicks will therefore add coherently on every turn. At this point it can be seen that by choosing a half integer tune the particle arrives at the opposite side of the phase-space ellipse on successive turns, and hence the dipole kicks cancel. However, it is now the quadrupole errors that add on every turn. As it turns out this effect will not only occur for dipoles and quadrupoles but also for different order of errors in the lattice. The general effect of these errors can be studied using perturbation theory.

Making use of normalized coordinates, by making the transformation [14]:

$$w = \frac{z}{\sqrt{\beta_z}} \quad \text{where} \quad z = x, y. \tag{1.177}$$

Considering an nth order multipole perturbation, the equation of motion in normalized horizontal coordinates gives:

$$\ddot{w} + Q_x^2 w = \bar{p}_n(\psi) w^{n-1}. \tag{1.178}$$

Such a perturbation is periodic in φ and can be expanded into a Fourier series:

$$\bar{p}_n(\varphi) = \sum_m \bar{p}_{\mathrm{mn}} e^{-im\varphi}. \tag{1.179}$$

Expressing the amplitude factor $w^{n-1}(\phi)$ as a sum of exponential terms of the form:

$$w^{n-1}(\varphi) \approx w_0^{n-1}(\varphi) = \sum_{|q| \leq n-1} W_q e^{-iqQ_x \cdot \varphi}. \tag{1.180}$$

Inserting Eqs. 1.179 and 1.180 into Eq. 1.178 gives the expression:

$$\ddot{w} + Q_x^2 w = \sum_{q,m} W_q \bar{p}_{\mathrm{nm}} e^{-i(m+qQ_x).\varphi}. \tag{1.181}$$

The solution to this equation will include resonant terms whenever there is a perturbation term equal to the frequency Q_x. This resonance condition is therefore:

$$m + qQ_x = Q_x, \tag{1.182}$$

with $|q| \leq n - 1$.

When coupling is present, the equation of motion is given by:

$$\ddot{w} + Q_x^2 w = \bar{p}_{nr}(\varphi) w^{n-1} v^{r-1}. \tag{1.183}$$

The resonance condition in this case derived for horizontal motion gives:

$$m + lQ_x + qQ_y = Q_x, \tag{1.184}$$

where $|l| + |q| + 1$ dictates the order of the resonance. The same procedure can now be repeated for the vertical motion. The resonance condition for both directions can be expressed as:

$$kQ_x + lQ_y = hN, \tag{1.185}$$

where k, l and h are integers, and $|k| + |l|$ indicates the order of the resonance. Fig. 1.11 illustrates the lines that fulfill the condition in Eq. 1.185 for the fractional parts of Q_x and Q_y up to the 5^{th} order, that is for $|k| + |l| \leq 5$.

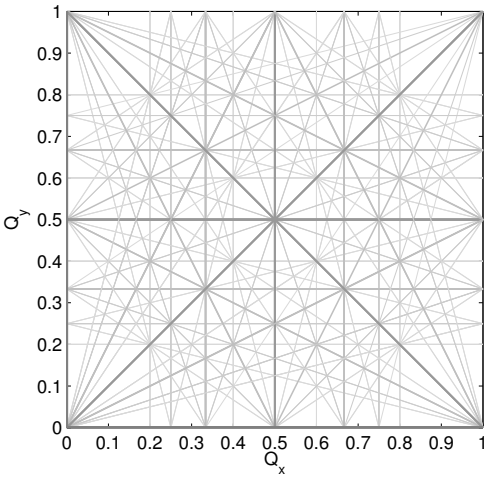

FIGURE 1.11: Resonance map up to 5^{th} order.

When particles tunes are close to one of these lines the resonance affects its trajectory and particles may be lost. Since there is an infinite number of resonance lines, choosing an appropriate reference tune can be difficult. However, the strength with which a particular resonance is driven is (usually) inversely proportional to its order. Thus, when designing an accelerator it is desirable to choose a working point as far away as possible from resonance lines of low order.

1.5.5 Dynamic Aperture

The dynamic aperture is defined as the maximum phase-space amplitude where the particle motion is stable over a certain number of turns. Stable motion is defined as bounded quasi-periodic motion over a given amount of time or, in the case of storage rings, the equivalent number of turns.

Dynamic aperture is generally determined by numerical particle tracking, using codes optimised for this task. In order to determine the dynamic aperture, a grid of initial coordinates is given for the particles which are then tracked in a model of the lattice. The model of the lattice may include systematic effects (such as fringe fields or beam-beam interactions) and random errors for the magnets, usually for several seeds [21].

The numerical approach to determine the dynamic aperture has an important drawback, since it is often necessary to track particles for very large rings, with thousands of elements, for a large number of turns: up to a hundred thousand turns for a storage proton ring for example. Furthermore, the tracking has to be repeated for several realisations of the random magnetic errors, resulting in a computationally expensive task.

A way to address the problem of the computational time needed to do the tracking is to detect the chaotic behaviour of the trajectory with fast indicators, such as the Lyapunov exponent [22]. The method of the Lyapunov exponents uses two particles with slightly different initial conditions in phase space. If the two particles reside in a region of phase space where the motion is regular (i.e. not chaotic), the distance between them will increase linearly with time, but if the particles are in a chaotic region, their separation will grow exponentially [21]. Chaos is detected by means of the computation of the maximal Lyapunov exponent. The maximum Lyapunov exponent at the nth turn is estimated as:

$$\lambda = \frac{1}{n}\ln\frac{|\vec{x}_2^{(n)} - \vec{x}_1^{(n)}|}{|\vec{x}_2^{(n)} - \vec{x}_1^{(n)}|}, \tag{1.186}$$

where $|\vec{x}_2^{(0)} - \vec{x}_1^{(0)}|$ is the (infinitesimal) initial phase-space distance, and $|\vec{x}_2^{(n)} - \vec{x}_1^{(n)}|$ is the phase-space distance between the two particles at the nth turn. If the particle is stable, then $\lambda(n)$ goes to 0 as $n \to \infty$, otherwise $\lambda(n)$ will reach a limit. This method has been used to determine the dynamic aperture for the LHC, as will be discussed in Chapter 5.

1.5.6 Frequency Map Analysis

The previous section presented the concept of dynamic aperture as an indicator of long term stability; the dynamic aperture calculation is normally carried out using numerical particle tracking. However, tracking studies for the required time of the simulation are extremely expensive. Moreover, the dynamic aperture does not provide information about the phase space structure of the system [23]. Frequency Map Analysis (FMA), originally used by Laskar [24] as a method to look at chaos in the orbits of planets and moons, has been proposed for use in accelerators to study the non-linear dynamics giving a global view of the phase space structure.

The synchrotron tunes are key parameters of a storage ring. In a system constructed of only linear elements, the tunes have a strong dependence on the particle energy, characterised by the chromaticity [3]. In order to control the chromaticity, the incorporation of nonlinear elements, such as sextupoles, becomes necessary as described in Section

1.5.1. The nonlinear elements introduce a dependence of the tunes on the betatron amplitudes. Moreover, in a system where nonlinearities are present, the amplitudes are not constant, so the tunes can vary over a certain number of turns [3]. Therefore, studying the variation of the tunes over a number of turns provides information about the stability of the system over some region of phase space. Moreover, FMA has the advantage that it can be applied to relatively short term tracking data, providing an early indicator of stability [23].

The first step of the process requires a high-precision calculation of the tunes. The discrete Fourier transform (DFT) provides a tool to obtain the frequencies of motion for a discrete set of samples. By simply applying the DFT and identifying the mode with the largest amplitude, the tune can be calculated with a precision inversely proportional to the number of samples (i.e. the number of turns, in the case of particle motion in a storage ring). For cases when the data is restricted, the DFT provides the tunes with limited accuracy. Therefore, the FMA makes use of an alternative technique known as numerical analysis of the fundamental frequencies (NAFF) algorithm [25].

The NAFF algorithm works as follows. First, the complex quantity w is constructed from the normalised co-ordinate x_{norm} and momentum p_{norm} as [3]:

$$w = x_{\text{norm}} - ip_{x,norm} = \sqrt{2J_x}e^{i\phi_{x,0}}e^{2\pi inQ_x}. \tag{1.187}$$

Taking the initial phase as ϕ_{x0} and the tune Q_x at the nth turn, w can be expressed as (in the absence of nonlinearities):

$$w_n = \sqrt{2J_x}e^{i\phi_{x0}}e^{2\pi inQ_x}. \tag{1.188}$$

Taking the Fourier transform of w_n gives:

$$\bar{w}_n = \frac{1}{N_t}\sum_{n=0}^{N_t-1} e^{-2\pi imn/N_t}w_n, \tag{1.189}$$

where N_t is the number of turns of tracking data and m is an integer between 0 and $N_t - 1$. Replacing Eq. 1.188 in Eq. 1.189 gives:

$$\bar{w}_n = \sqrt{2J_x}e^{i\phi_{x0}\frac{1-e^{2\pi i\Delta}}{1-e^{2\pi i\Delta/N_t}}}, \tag{1.190}$$

where:

$$\Delta = N_t\text{frac}(Q_x) - m, \tag{1.191}$$

$\text{frac}(Q_x)$ represents the fractional part of the tune. From the previous expression, we observe that if $\Delta = 0$, then the absolute value of $\bar{w}_m$ reaches a maximum. If m is restricted to be an integer, Δ will not be exactly zero unless $N_t\text{frac}(Q_x)$ happens to be an integer. But, if m is allowed to be any real number, then the m that maximizes $\bar{w}_m$ ($\hat{m}$) can be searched for numerically. From Eq. 1.191 the fractional part of the tune can

be found as:

$$\text{frac}(Q_x) = \frac{\hat{m}}{N_t}. \tag{1.192}$$

Hence, by allowing $\hat{m}$ to take on any value it is possible to find a more accurate estimation for the value of the tune. Once this $\hat{m}$ is identified it is subtracted from the original data. The process is repeated any number of times to find the subsequent m that produces the largest $\hat{w}_m$.

To minimise the effects of other frequency components a filter can be applied. For example a Hanning filter [26] can be used, which takes the form:

$$\chi(j) = 0.5\left(1 - \cos\left(2\pi\frac{j}{N_t}\right)\right), \tag{1.193}$$

where the length of the window is given by $L = N_t + 1$. The Hanning filter can then be applied to $\hat{w}_m$ as:

$$\hat{w}_m = \frac{1}{N_t}\sum_{n=0}^{N_t-1} e^{-2\pi imn/N_t} w_n \chi(n). \tag{1.194}$$

Without the use of any filters, this method gives the dominant frequency with an accuracy that scales as $1/N_t^2$. With the use of the Hanning filter described previously, this scaling can be improved to $1/N_t^4$, offering a much better result for a given number of samples than the one obtained by the DFT.

Using this method, the tune can be calculated for two equal and successive time spans for a grid of initial conditions. The diffusion factor gives the difference between the calculated tunes. This factor is defined as:

$$D = \log_{10}\sqrt{(\Delta Q_x)^2 + (\Delta Q_y)^2}. \tag{1.195}$$

The use of the diffusion factor plotted in the $x - y$ space gives an indication of stability. Three main features are expected to be seen in a frequency map [24]:

1. Regular areas. The tune space is regular, and the points associated with small tune shifts (small diffusion factors).

2. Resonances. Areas where tune shift is high and whose position can be associated with resonance lines, as dictated by Eq. 1.185.

3. Irregular areas. Regions where tune shift is very high and structure is lost. These regions correspond to highly non-linear or even chaotic motion.

The tunes found can also be plotted in the resonance diagram illustrated in Fig. 1.11. The presence of a strongly driven resonances will be characterized by lots of points

clustering around the corresponding line in tune space. By comparing these plots with the diffusion factor over the initial amplitudes, it is possible to identify the regions of instability, in terms of both the initial position and the resonances causing the disruption.

1.6 Synchrotron Radiation

The underlying principle behind synchrotron radiation production is that charged particles radiate when being accelerated. This radiation is a direct consequence of the fact that light travels at a finite velocity. Given this finite velocity, when a charged particle is accelerated, a re-arrangement of electric fields is required, causing a disruption in the field lines of the particles. This field perturbation travels away from the particle at the velocity of light and is what we know as radiation.

In the field of accelerators synchrotron radiation was often considered as a limitation to the energy of the particles in a storage ring as its emission could be very damaging to sensitive parts of the accelerator. It was later found that this radiation has a variety of useful properties in many different fields. This led to the development of a new kind of accelerator facility (light sources) dedicated to studies based on exploitation of synchrotron radiation.

The radiation power of a charged particle in the relativistic invariant form gives [27]:

$$P_{\mathrm{SR}} = \frac{q^2 c}{6\pi\epsilon_0 (m_0 c^2)^2}\left[\left(\frac{d\vec{p}}{d\tau}\right)^2 - \frac{1}{c^2}\left(\frac{dE}{d\tau}\right)^2\right], \tag{1.196}$$

where $d\tau = dt/\gamma$ with γ being the relativistic factor. The amount of synchrotron radiation produced will depend on the kind of accelerator. In the case of a linear accelerator, where the acceleration is parallel to the velocity, the radiated power is given as [27]:

$$P_{\mathrm{SR}} = \frac{q^2 c}{6\pi\epsilon (m_0 c^2)^2}\left(\frac{dE}{dx}\right)^2. \tag{1.197}$$

In modern accelerators $dE/dx \approx 15$ MeV/m giving the corresponding radiated power of $P_x = 4 \times 10^{-17}$ W. Hence, the power radiated in a linear accelerator can be considered negligible.

A circular accelerator presents a different scenario. In this case, the acceleration is perpendicular to the direction of motion, the corresponding radiated power for this case is [27]:

$$P_{\mathrm{SR}} = \frac{q^2 c}{6\pi\epsilon_0 (m_0 c^2)^4}\frac{E^4}{\rho^2}. \tag{1.198}$$

Thus, the synchrotron power is now proportional to E^4/ρ^2. For high energy accelerators, this radiation power can reach high values, but can be reduced by increasing the radius of curvature.

It can also be observed that the radiated power, in both a linear and a circular accelerator, is inversely proportional to m_0^4. This result has important consequences in

terms of which particle is being accelerated, this can be observed when comparing the radiation power between an electron and a proton, given as:

$$\frac{P_{\mathrm{SR,e}}}{P_{\mathrm{SR,p}}} = \left(\frac{m_p c^2}{m_e c^2}\right)^4 = 1.13 \times 10^{13}. \tag{1.199}$$

Hence, the radiation produced by an electron is 13 orders of magnitude larger than the one produced by the proton under the same system.

Another important aspect of the synchrotron radiation in a storage ring is the total energy loss per turn which is given by [27]:

$$\Delta E = \frac{e^2}{3\epsilon_0 (m_0 c^2)^4} \frac{E^2}{\rho}. \tag{1.200}$$

In an accelerator, this energy loss would have to be compensated by the RF system to keep the energy of the particles approximately constant. For electrons, the energy loss per turn can be expressed in practical units:

$$\Delta E[keV] = 88.5 \frac{E^4[GeV^4]}{\rho[m]}. \tag{1.201}$$

The results presented in this section will be useful in Chapter 4 when studying the synchrotron radiation power produced when bending an electron beam in the interaction region of the LHeC.

1.7 Conclusions

This chapter provided an overall description of the beam dynamics in an accelerator. The results for linear transfer maps, the impact of the chromaticity and its correction, as well as synchrotron radiation will be useful for discussion of lattice design in Chapter 4. The impact of nonlinearities and magnet errors (characterised in terms of the dynamic aperture and frequency map analysis) will be considered in Chapter 5. The simplifications used in this chapter do have limitations when solving particular kinds of problems, the development of tools to overcome these limitations will be addressed in Chapter 2.

Chapter 2

Transfer Maps and Symplectic Integrators

In Chapter 1 the development of transfer maps was presented for drifts, dipoles and quadrupoles. This was done by making a linear approximation to the solutions to the equations of motion resulting in a transformation matrix. For certain elements in an accelerator this approximation is not always possible, either because the nature of the element requires the expansion of the Hamiltonian to a higher order, such as the sextupole, or because the approximations no longer hold, such as the fringe fields of magnets. This chapter will study several techniques that have been developed to obtain transfer maps for these nonlinear elements.

2.1 Field Fitting Techniques

The multipole fields described in Chapter 1, and consequently the transfer matrices derived, made use of the approximation that the fields are only two-dimensional. This section addresses three-dimensional fields, explaining the accelerator elements for which this approach is relevant. The corresponding transfer maps for these types of elements can be obtained using techniques described later in this chapter.

In order to obtain the multipole magnetic fields satisfying Maxwell's equations (Eq. 1.14) we made use of the fact that the field does not change in the z-direction. Therefore, the results presented in Chapter 1 assume that the quadrupoles and dipoles have a magnetic field independent of z and consequently the change of magnetic field at the exit of the magnets is given as a step function. However, for a real multipole, the magnetic field changes smoothly at the boundaries, these zones are known as the fringe fields of the magnet. An illustration of the fringe fields is given in Fig. 2.1.

The two-dimensional magnetic fields, for which transfer maps were derived in Chapter 1, provide a good description of the dynamics in most accelerator magnets. For some cases however, the study of three-dimensional magnetic fields becomes desirable (when studying the effects of fringe fields on the beam dynamics for example) or necessary (such as when studying accelerator elements with an s-dependent field as in wigglers or

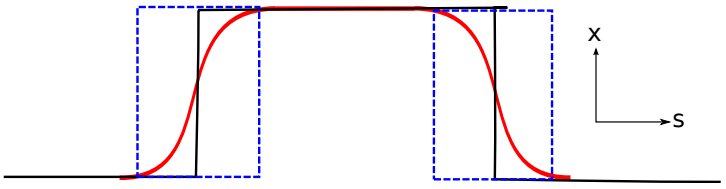

FIGURE 2.1: Illustration of the magnetic gradient in the quadrupole for the hard edge model (black) and the real magnet model (red). Blue squares illustrate the section of the magnet where the fringe fields are located.

undulators which consist of periodic magnetic structures of alternating polarity [28]). To study elements with s-dependent fields, further techniques will need to be developed, beyond the description of a field as a set of multipoles. In the following section a method to describe three dimensional fields, called generalised gradients, will be described.

Generalised gradients

This section describes the method of generalised gradients developed by A. Dragt [29].

Given a system with constant electric displacement and zero current density, the magnetic field can be expressed in terms of a scalar potential ϕ_{mag} as:

$$\vec{B} = -\nabla\phi_{\text{mag}}. \tag{2.1}$$

Using Eq. 1.8 the magnetic field for this system must satisfy Laplace's equation:

$$\nabla^2\phi_{\text{mag}} = 0. \tag{2.2}$$

The scalar potential can be expressed as [3]:

$$\phi_{\text{mag}} = \sum_{m=-\infty}^{\infty}\sum_{l=0}^{\infty}\frac{(-1)^l|m|!}{2^{2l}l!(l+|m|)!}C_m^{[2l]}(z)r^{2l+|m|}e^{im\theta}, \tag{2.3}$$

where $C_m^{[0]}(z)$ are called the generalised gradients. The integer m represents the order of the multipole and $C_m^{[n]}(s)$ is the nth derivative of $C_m^{[0]}(s)$.

The vector and the scalar potential are related as [2]:

$$\nabla\times\vec{A} = -\nabla\phi_{\text{mag}}. \tag{2.4}$$

The vector potential can then be derived from the scalar potential, resulting in the expressions:

$$A_r = \sum_{m=-\infty}^{\infty}\sum_{l=0}^{\infty}\frac{(-1)^{l+1}|m|!}{2^{2l}l!(l+|m|)!}C_m^{[2l+1]}(z)r^{2l+|m|+1}\frac{ie^{im\theta}}{m}, \tag{2.5}$$

$$A_\theta = 0, \tag{2.6}$$

$$A_z = \sum_{m=-\infty}^{\infty}\sum_{l=0}^{\infty}\frac{(-1)^l|m|!(2l+|m|)}{2^{2l}l!(l+|m|)!}C_m^{[2l]}(z)r^{2l+|m|}\frac{ie^{im\theta}}{m}. \tag{2.7}$$

when we choose a gauge in which A_θ=0. Also, using Eq. 2.1 and the expression of the scalar potential, the magnetic field components in terms of the general gradients can be written as:

$$B_r = \sum_{m=-\infty}^{\infty}\sum_{l=0}^{\infty}\frac{(-1)^{l+1}(2l+|m|)|m|!}{2^{2l}l!(l+|m|)!}C_m^{[2l]}(z)r^{2l+|m|-1}e^{im\theta}, \tag{2.8}$$

$$B_\theta = \sum_{m=-\infty}^{\infty}\sum_{l=0}^{\infty}\frac{(-1)^{l+1}|m|!}{2^{2l}l!(l+|m|)!}C_m^{[2l]}(z)r^{2l+|m|-1}ime^{im\theta}, \tag{2.9}$$

$$B_z = \sum_{m=-\infty}^{\infty}\sum_{l=0}^{\infty}\frac{(-1)^{l+1}|m|!}{2^{2l}l!(l+|m|)!}C_m^{[2l]}(z)r^{2l+|m|}e^{im\theta}. \tag{2.10}$$

Assuming that numerical field data are available for the field components B_r, B_θ and B_z for different values of r, θ and z it is possible to obtain the generalised gradients. This procedure is carried out by considering the component B_r for a particular longitudinal position $z = z_0$ and radius $r = r_0$.

Now, taking a Fourier transform of B_r as a function of θ, the coefficients $\tilde{B}_m(r_0, z_0)$ can be obtained such that:

$$B_r(r_0, \theta, z) = \sum_{m=-\infty}^{\infty}\tilde{B}_m(r_0, z_0)e^{im\theta}. \tag{2.11}$$

A comparison can now be made with Eq. 2.8 for specific values of r_0 and z_0 relating the coefficients $\tilde{B}_m(r_0, z_0)$ with the generalised gradients $C_m^{[2l]}$ as:

$$\tilde{B}_m(r_0, z_0) = \sum_{l=0}^{\infty}\frac{(-1)^{l+1}(2l+|m|)|m|!}{2^{2l}l!(l+|m|)!}C_m^{[2l]}(z_0)r_0^{2l+|m|-1}. \tag{2.12}$$

The same procedure can be repeated for different values of r_0 at a fixed z_0. A polynomial fit of $\tilde{B}_m(r, z_0)$ as a function of r can be applied up to a certain order $l_{\max}$ and expressed in terms of the coefficients $b_{m,l}(z_0)$ as:

$$\tilde{B}_m(r, z_0) = \sum_{l=0}^{l_{\max}} b_{m,l}(z_0)r^{2l+|m|-1}. \tag{2.13}$$

By comparing Eqs. 2.12 and 2.13 the generalised gradients can be given in terms of the coefficients of the fit $b_{m,l}$ as:

$$b_{m,l}(z_0) = \frac{(-1)^{l+1}(2l+|m|)|m|!}{2^{2l}l!(l+|m|)!}C_m^{[2l]}(z_0). \tag{2.14}$$

The generalised gradients can now be obtained for as many different longitudinal positions of z_0 as desired.

A similar procedure can be followed to obtain the generalised gradients $C_m^{[2l+1]}(z_0)$ by starting with the B_z component in Eq. 2.10 [3]. From the generalised gradients

analytical expressions for all the three field components can now be obtained by inserting the appropriate coefficients into Eq. 2.10 [3].

The generalised gradients approach, as oppose to using numerical data, has the advantage of providing an analytical representation of the fields, satisfying Maxwell's equations, in all variables. Furthermore, a controlled fit is made on the boundary, making the interior values (inferred from surface data) relatively insensitive to errors in surface data [29].

2.2 Transfer Maps

In Chapter 1, descriptions of transfer maps for linear elements of an accelerator were presented. In order to obtain the corresponding solutions, approximations were made in the Hamiltonians of the different elements, the resulting transfer maps were exact solutions of Hamilton's equations and therefore the representation is symplectic. However in the hope of representing a more realistic beamline incorporating further elements one may find beamline elements that will not admit exact solutions to Hamilton's equations. In the case of a sextupole for example, the important properties of these elements require the Hamiltonian to be expanded to the third order, or higher. For most of these cases however, the Hamiltonian will not admit exact solutions.

The symplectic nature of the dynamics, although not essential in all cases, becomes particularly important when tracking particles in a storage ring for thousands of turns without radiation damping, given that the loss of symplecticity can lead to inaccurate information on the stability of the beam. Therefore it is most important to provide the tools to construct symplectic transfer maps for the different elements whenever possible if one wishes to give a more realistic representation of the beam dynamics of a system. This will be more thoroughly described in Section 2.3.

In the next sections, the description of different techniques will be given aiming to obtain symplectic transfer maps for elements whose Hamiltonian does not admit exact solutions.

2.3 Symplecticity

For a dynamical system obeying Hamilton's equations, the transfer maps fulfill the property of symplecticity. The definition and relevance of this property will be described in this section.

The transfer map M that transforms the initial values of the dynamical variables $\vec{x}(s_0)$ to a new position $\vec{x}(s_1)$ can be expressed as:

$$\vec{x}(s_1) = M(\vec{x}(s_0)). \tag{2.15}$$

Expressing the components of the vector $\vec{x}$ as x_i, where $i = 1, ...2n$ and n is the number of degrees of freedom, Hamilton's equations can be written as:

$$\dot{x}_i = \sum_k S_{ik} \frac{\partial H}{\partial x_k}, \tag{2.16}$$

where $\dot{x}$ is the derivative of x with respect to the independent variable. S is the block-diagonal $2n \times 2n$ antisymmetric matrix given by:

$$S = \begin{pmatrix} s & 0 & \cdots & 0 \\ 0 & s & \cdots & 0 \\ \vdots & \vdots & \ddots & \vdots \\ 0 & 0 & \cdots & s \end{pmatrix}, \tag{2.17}$$

where each block s is given by:

$$s = \begin{pmatrix} 0 & 1 \\ -1 & 0 \end{pmatrix}. \tag{2.18}$$

This matrix fulfills the following properties:

$$\begin{aligned} S^{-1} &= -S, \\ S^2 &= -I, \\ \det(S) &= 1. \end{aligned} \tag{2.19}$$

Now, considering an infinitesimally small change in the independent variable s, the dynamic variables change as:

$$x_i(s_0 + \delta s) = x_i(s_0) + \dot{x}_i(s_0)\delta s. \tag{2.20}$$

In terms of the antisymmetric matrix this result can be expressed as:

$$x_i(s_0 + \delta s) = x_i(s_0) + \sum_k S_{ik} \frac{\partial H}{\partial x_k}\Big|_{s=s_0} \delta s. \tag{2.21}$$

The Jacobian of the transformation s_0 to $s_0 + \delta s$ is given by:

$$J_{ij} = \frac{\partial x_i(s_0 + \delta s)}{\partial x_j(s_0)}. \tag{2.22}$$

Using Eq. 2.21, the Jacobian can be expressed as:

$$J_{ij} = \delta_{ij} + \sum_k S_{ik} \frac{\partial^2 H}{\partial x_j \partial x_k}\Big|_{s=s_0} \delta s, \tag{2.23}$$

where δ_{ij} is the Kronecker delta function, i.e. $\delta_{ij} = 1$ if $i = j$ and $\delta_{ij} = 0$ if $i \neq j$. Expressing Eq. 2.23 in its matrix form gives:

$$J = I + S\tilde{H}\delta s, \tag{2.24}$$

where the entries of the $\tilde{H}$ matrix are given by:

$$\tilde{H}_{jk} = \frac{\partial^2 H}{\partial x_j \partial x_k}\Big|_{s=s_0}. \tag{2.25}$$

Given the previous result and the fact that $S^2 = 1$, the transpose of the Jacobian is given by:

$$J^T = I - \tilde{H}S\delta s. \tag{2.26}$$

Thus, we obtain that, to the first order of δ_s, the following condition is fulfilled [13]:

$$J^T S J = S. \tag{2.27}$$

A transformation whose Jacobian fulfils Eq. 2.27 is said to be symplectic.

It can be demonstrated that if two Jacobians J_0 and J_1 are both symplectic then its product $J_2 = J_1 J_0$ will also be symplectic. Thus, a transformation composed of a series of symplectic transformations will also be symplectic [3].

A further property of a symplectic transformation can be given in terms of the density of particles in phase space.

The volume element in phase space is given in terms of the dynamical variables as:

$$dv = \prod_{i=1}^{2n} dx_i. \tag{2.28}$$

Under a symplectic transformation where $\vec{X} = \vec{M}(\vec{x})$ the volume element in the new variables $\vec{X}$ is:

$$dV = \prod_{i=1}^{2n} dX_i = |\mathrm{det}J| \prod_{i=1}^{2n} dx_i, \tag{2.29}$$

where J is the Jacobian of the transformation from x_i to X_i. Using Eq. 2.27:

$$\mathrm{det}(J^T S J) = (\mathrm{det}J)^2 \mathrm{det}S = \mathrm{det}S. \tag{2.30}$$

Since det $S \neq 0$ it follows that:

$$|\mathrm{det}J| = 1. \tag{2.31}$$

And hence:

$$dV = dv. \tag{2.32}$$

Therefore, the volume element in phase space is conserved under a symplectic transformation.

Symplecticity has important consequences in beam physics, one of the most important is the conservation of the density of particles in phase space. Since both the number of particles and the volume in phase space are conserved in a transformation following Hamilton's equations it follows that the density of particles is also conserved. The conservation of density of particles in phase space is illustrated in Fig. 2.2.

The conservation of the density of particles in phase space in a system governed by a Hamiltonian is known as Liouville's theorem and can be written mathematically as [14]:

$$\frac{d\rho}{dt} = \frac{\partial \rho}{\partial t} + \sum_{i=1}^{2n} \frac{dx_i}{dt}\frac{\partial \rho}{\partial x_i} = 0. \tag{2.33}$$

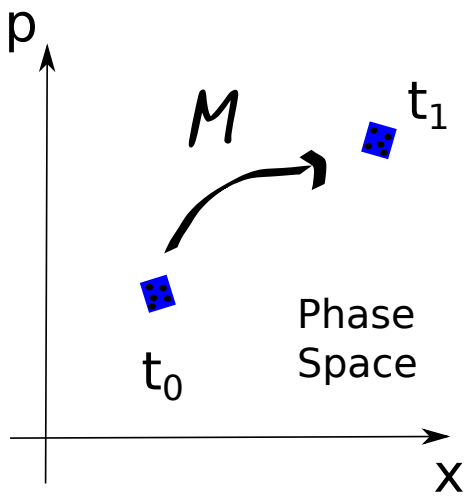

FIGURE 2.2: Illustration of Liouville's theorem dictating that for a dynamical system obeying Hamilton's equations the density of particles in phase space is conserved. The transfer map transports particles from t_0 to t_1 and, although the shape of the space occupied by the particles changes, the area and the number of particles, and consequently the density, remains constant.

As explained previously, the symplecticity is of particular importance when tracking particles in a storage ring for a large number of turns. The loss of symplecticity can lead to inaccurate calculation of the dynamic aperture.

2.4 Lie Transformations

Lie transformations can be used to represent transfer maps of different elements in a beamline and will be particularly useful when representing transfer maps of nonlinear elements.

First, the introduction of the so-called Poisson bracket is given as it will be useful in the representation of the Lie maps. A Poisson bracket is defined by [13]:

$$[f, g] = \sum_{i=1}^{n} \left(\frac{\partial f}{\partial x_i}\frac{\partial g}{\partial p_i} - \frac{\partial f}{\partial p_i}\frac{\partial g}{\partial x_i} \right), \tag{2.34}$$

where f and g are functions of x_i and p_i.

Giving f as the variables x_i and p_i, g as the Hamiltonian and making use of Hamilton's equations (1.40) the following expressions are obtained:

$$[x_i, H] = \frac{\partial H}{\partial p_i} = \frac{dx_i}{dt}, \tag{2.35}$$

$$[p_i, H] = -\frac{\partial H}{\partial x_i} = \frac{dp_i}{dt}. \tag{2.36}$$

Therefore, Hamilton's equations may be expressed in terms of Poisson brackets.

The Lie operator $: f :$ can be defined for a function $f(x_i, p_i)$ such that:

$$: f := [f, \quad] = \sum_{i=1}^{n} \left(\frac{\partial f}{\partial x_i} \frac{\partial}{\partial p_i} - \frac{\partial f}{\partial p_i} \frac{\partial}{\partial x_i} \right). \tag{2.37}$$

where n is the number of degrees of freedom.

Using the longitudinal positions as the independent variable and assuming that the Hamiltonian does not depend on s, the Lie operator for the Hamiltonian can be constructed as $: H :$. The equations of motion for a function $g(x_i, p_i)$ can be given as:

$$\frac{dg}{ds} = - : H : g. \tag{2.38}$$

The Taylor expansion of g at $s = s_0 + \delta s$ is given by:

$$g\big|_{s=s_0+\Delta s} = g\big|_{s=s_0} + \Delta s \frac{dg}{ds}\Big|_{s=s_0} + \frac{\Delta s^2}{2} \frac{d^2 g}{ds^2}\Big|_{s=s_0} + ... \tag{2.39}$$

$$= e^{\Delta s \frac{d}{ds}} g\Big|_{s=s_0}. \tag{2.40}$$

Replacing d/ds by the operator $- : H :$ gives:

$$g|_{s=s_0+\Delta s} = e^{-\Delta s : H :} g|_{s=s_0}. \tag{2.41}$$

The operator $e^{-\Delta s : H :}$ is known as a Lie transformation. The Taylor expansion of this transformation gives:

$$e^{-\Delta s : H :} = 1 - \Delta s : H : + \frac{\Delta s^2}{2} : H :^2 - \frac{\Delta s^3}{3!} : H :^3 + ... \tag{2.42}$$

Replacing the function g with the variable of motion x_i in Eq. 2.41 gives the transformation of variables:

$$x_i|_{s=s_0+\Delta s} = e^{-\Delta s : H :} x_i|_{s=s_0}. \tag{2.43}$$

Since the exponential can be expressed in terms of the power series given in Eq. 2.40, Lie transformations provide a way to obtain the transfer maps even for non integrable cases, as applying the operator just involves differentiation. Furthermore, given that

the system uses the Hamiltonian as a generator, the resulting transfer map of the Lie transformations is exactly symplectic. A drawback of this representation however, is that an exact explicit representation of the solution will normally require an infinite number of terms and hence, in order to obtain a practical solution, a truncation of the power series will be required. This truncation comes with a loss of symplecticity. The impact that such an error has on the dynamics depends on the problem in hand. For cases in which symplecticity is important, a modification of the technique is required in order to produce a symplectic map with a finite number of turns.

Lie transformations have the following properties [29]:

1. The series expression for a Lie transformation with generator f is:

$$e^{:H:}f = f + [H, f] + \frac{1}{2}[H, [H, f]] + ... \tag{2.44}$$

2. The Lie transformation of the product of two functions is:

$$e^{:H:}(fg) = (e^{:H:}f)(e^{:H:}g). \tag{2.45}$$

3. The Lie transformation of a function operating on a function is:

$$e^{:H:}f(g) = f(e^{:H:}g). \tag{2.46}$$

4. The Lie transformation of a Poisson bracket is:

$$e^{:H:}[f, g] = [e^{:H:}f, e^{:H:}g]. \tag{2.47}$$

5. The Lie transformation of a Lie transformation is:

$$e^{:e^{:H:}f:} = e^{:H:}e^{:f:}e^{-:H:}. \tag{2.48}$$

6. The combination of two Lie transformations, using the Baker–Campbell–Hausdorff formula (BCH) is given by:

$$e^{:A:}e^{:B:} = e^{:C:}. \tag{2.49}$$

   where

$$C = A + B + \frac{1}{2}[A, B] + \frac{1}{12}[A, [A, B]] + \frac{1}{12}[B, [B, A]] + ... \tag{2.50}$$

Some of these properties will be used to construct integrators to express solutions of the equations of motion for the dynamical variables, as will be discussed later on in Section 2.6.

2.5 Power Series Maps

A power series map expresses the final coordinates (x_j^f) in terms of the initial values (x_j^i) as:

$$x_k^f = f_k(x_1^i, ..., x_6^i), \tag{2.51}$$

where the functions $f_k(x_1^i, ..., x_6^i)$ are truncated power series of the form:

$$f_k(x_1^i, ..., x_6^i) = \sum_{i_1,...,i_6}^{\sum_j^6 i_j \leq \text{Order}} A_{k,i_1,...,i_6} \prod_{j=1}^{6} (x_j^i)^{i_j}. \tag{2.52}$$

The use of power series maps to represent sections of an accelerator beamline was proposed as an alternative to element-by-element tracking with the aim of reducing the amount of computing time required to perform a tracking simulation. However, in order to implement power series maps the power series has to be truncated at certain order.

Implementing the power series maps for tracking comes with some challenges. First given the number of coefficients to be calculated the generation of the power series map can become a computational expensive task; the use of Lie transformations (Section 2.4) and automatic differentiation (Section 2.5.1) have provided tools to address this challenge. Second, since a truncated power series map is not an exact solution to Hamilton's equations of motion, the map is in general not symplectic. If symplectic tracking is required the map must be first 'symplectified'. Different methods of symplectification are available, such as the use of a mixed-variable generating function [30], or the use of Cremona maps [31]. The mixed-variable generating function provides a way to obtain exactly symplectic transfer maps. Furthermore, it requires fewer coefficients to be specified than the power series map. A drawback of this method is that it is not explicit, and algebraic equations must be solved for each application of the map. Cremona maps [31] provide another method to symplectify the system. Procedures exists to convert a truncated power series map into a polynomial map with a finite number of terms (Cremona map) that is exactly symplectic. Cremona maps are constructed in such a way that their polynomial expansion agrees with the power series map up to the truncated order.

The feasibility of one-turn maps as a time-saving alternative to element-by-element tracking in long term stability studies was investigated for the LHC [32]. However, studies showed that discrepancies between the two methods of tracking grew with amplitude. Therefore power series maps were not guaranteed to give an accurate description of the stability of the beam without suitable symplectification [32]. Symplectification schemes were introduced in later studies for the LHC and HERA machines, however it was found that it could not be guaranteed that the use of one-turn power series maps would be accurate over long time scales, even after being symplectified, and therefore it cannot be assumed that one-turn power series maps will give an accurate prediction for the dynamic aperture [33].

Therefore, tracking in the LHC still makes use of the element-by-element method, explained in Section 2.6.1. However, the use of power series maps is still of value for certain aspects of accelerator physics, as will be the case in Chapter 6, where power series maps are used to represent the effects of fringe fields.

2.5.1 Differential Algebra

The use of truncated power series maps for particle tracking made a significant step forward when differential algebra tools began to be applied to the calculation of the maps [34]. Differential algebra reduces differential operations to algebraic operations. The principle relies on the fact that if the derivatives of two functions f_1 and f_2 (in variables x_i) are known, then the derivatives of the result of a combination of f_1 and f_2 are also known.

We start by giving a vector $\mathbf{F}(x_i)$, known as a 'DA vector', associated with a certain function $f(x_i)$ as [35]:

$$\mathbf{F}(x_i) = \begin{pmatrix} f \\ \partial f/\partial x_i \\ \partial^2 f/\partial x_i \partial x_j \\ \ldots \end{pmatrix} = \begin{pmatrix} f \\ f_{x_i} \\ f_{x_i x_j} \\ \ldots \end{pmatrix}. \tag{2.53}$$

Similarly, a second function $g(x_i)$ can be associated with a DA-vector $\mathbf{G}(x_i)$ such that:

$$\mathbf{G}(x_i) = \begin{pmatrix} g \\ \partial g/\partial x_i \\ \partial^2 g/\partial x_i \partial x_j \\ \ldots \end{pmatrix} = \begin{pmatrix} g \\ g_{x_i} \\ g_{x_i x_j} \\ \ldots \end{pmatrix}. \tag{2.54}$$

The DA-vectors $\mathbf{F}$ and $\mathbf{G}$ have the following properties:

1. The sum of the DA-vectors is given as:

$$\mathbf{F}(x_i) + \mathbf{G}(x_i) = \begin{pmatrix} f+g \\ f_{x_i} + g_{x_i} \\ f_{x_i x_j} + g_{x_i x_j} \\ \ldots \end{pmatrix}. \tag{2.55}$$

2. The product is given as:

$$\mathbf{F}(x_i) \cdot \mathbf{G}(x_i) = \begin{pmatrix} f \cdot g \\ f_{x_i} \cdot g + g_{x_i} \cdot f \\ f_{x_i x_j} \cdot g + f_{x_i} g_{x_j} + f_{x_j} \cdot g_{x_i} + g_{x_i x_j} \cdot f \\ \ldots \end{pmatrix}. \tag{2.56}$$

3. The multiplication of the vector with a constant c is given by the product of each component by the constant:

$$c\mathbf{F}(x_i) = \begin{pmatrix} cf \\ cf_{x_i} \\ cf_{x_i x_j} \\ \dots \end{pmatrix}. \tag{2.57}$$

4. Using the chain rule, a function $h(f)$ is represented by the DA-vector

$$\mathbf{H} = \begin{pmatrix} h(f) \\ h'(f) f_{x_i} \\ h''(f) f_{x_i} f_{x_j} + h'(f) f_{x_i x_j} \\ \dots \end{pmatrix}. \tag{2.58}$$

where $h'(f) = \partial h / \partial f$.

The DA-vector representing a variable x_i is:

$$\mathbf{F} = (x_i, 0, ..., 0, 1, 0, ..., 0). \tag{2.59}$$

Using these results, the computation of DA-vectors representing complicated functions can be achieved by algebraic operations easily implemented in a computer code. The use of differential algebra codes will be particularly useful in Chapter 6 to generate power series maps in a computationally efficient way.

2.6 Symplectic Integrators

Section 2.4 described the use of Lie transformations to obtain the equations of motion for the dynamical variables. Lie transformations can be used to construct solutions in the form of power series, even when the Hamiltonian is not integrable. However the often-needed truncation of the power series will come with a loss of symplecticity that, for problems such as particle tracking in storage rings, can have a considerable impact on the results. A possible way to correct the loss of symplecticity would be to represent a map in the form of a mixed-variable generating function [30]; however, as explained in Section 2.5, such a technique would involve solving algebraic equations for each application of the map which will impact the computational efficiency. This type of integration is known as implicit integration. On the other hand, an integrator whose solution at each consecutive step can be known from the solution at a previous step, and therefore requiring less time to perform the integration, is called an explicit integrator.

Therefore, it is of great interest to be able to express the transfer maps in a symplectic and explicit form. A method that fulfills both of these requirements is called an explicit symplectic integrator. In this section some symplectic integrators are described.

2.6.1 Splitting the Hamiltonian

Consider a Hamiltonian H, that can be given by the sum of two terms as:

$$H = H_d + H_k. \tag{2.60}$$

Making use of the BCH formula given in Eq. 2.49 it follows that:

$$e^{-\epsilon L:H_d:} e^{-\epsilon L:H_k:} = e^{-\epsilon L:H_d+H_k:+O(\epsilon^2)}, \tag{2.61}$$

where ϵ is a dimensionless parameter used to keep track of the order. If H_d and H_k are (separately) integrable, then the left hand side of Eq. 2.61 can be expressed in closed form; however there is an error of order ϵ^2 in the approximation that this closed form solution makes to the full Hamiltonian.

If the Hamiltonian is expressed as the sum of three terms:

$$H = \frac{1}{2}H_d + H_k + \frac{1}{2}H_d, \tag{2.62}$$

then, making use of the BCH formula and the bilinearity of the Poisson bracket, we obtain:

$$e^{-\frac{1}{2}\epsilon L:H_d:} e^{-\epsilon L:H_k:} e^{-\frac{1}{2}\epsilon L:H_d:} = e^{\epsilon L:H:+O(\epsilon^3)}. \tag{2.63}$$

This way, we still obtain a closed form solution, but the error is now of order ϵ^3. Thus a higher order approximation is made with this case in comparison with the Hamiltonian given by the sum of two terms. If H_d and H_k separately represent integrable Hamiltonians, then an expression for the map based on Eq. 2.63 does not require truncation of a power series, hence providing a second-order explicit symplectic integrator.

Kick codes

Kick codes make use of the principle of splitting the Hamiltonian to perform symplectic particle tracking through a beamline. The Hamiltonian is divided into a drift and a kick component of the form:

$$H_{\text{drift}} = \frac{\delta}{\beta_0} - \sqrt{\left(\frac{1}{\beta_0} + \delta - \frac{q\phi}{p_0 c}\right)^2 - p_x^2 - p_y^2 - \frac{1}{\beta_0^2\gamma_0^2}}, \tag{2.64}$$

$$H_{\text{kick}} = -a_s. \tag{2.65}$$

As an example, the transfer map of a sextupole (the hard edge model for which is illustrated in Fig. 2.3) can be approximated by expressing the Hamiltonian in terms of a drift, a sextupole "kick" and a second drift. This transformation is known as a *drift-kick-drift* approximation, illustrated in Fig. 2.4. The results expressed in Eq. 2.63 describe the benefits of this transformation over a *kick-drift* approximation (Eq. 2.61) illustrated in Fig. 2.5, although at the cost of making an extra transformation.

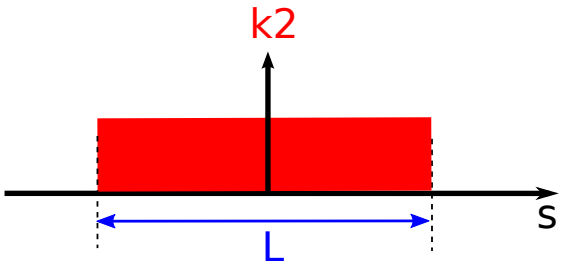

FIGURE 2.3: Schematic view of a sextupole of length L in a beamline.

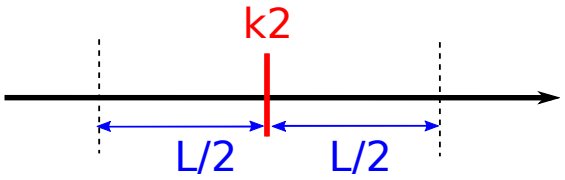

FIGURE 2.4: Schematic view of the drift-kick-drift approximation for a sextupole of length L.

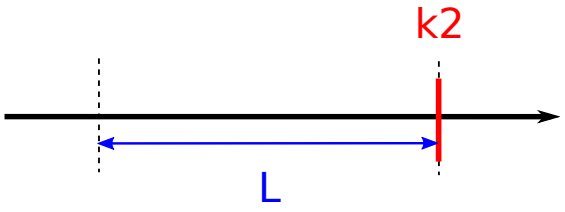

FIGURE 2.5: Schematic view of the drift-kick approximation of a sextupole for a sextupole of length L.

Splitting methods provide a very useful tool for long-term tracking studies since they provide integrators that are both symplectic and explicit (and can therefore be applied at relatively low computational cost). SixTrack [36] is an example of a kick-code and has been largely used for particle tracking in the LHC. The downside of this type of tracking is that the symplectification of the kicks given by the magnets comes with a loss of accuracy. In some cases a more detailed representation is needed, but this can be achieved by "splitting" the magnet into a larger number of slices [37].

2.6.2 Wu–Forest–Robin Integrator

The Wu–Forest–Robin integrator [38] provides an extension of the element-by-element tracking method for studying single particle nonlinear dynamics in magnetic fields that vary with the longitudinal variable s. The development of the Lie map is facilitated by the use of an extended phase space in which the variable s becomes a dynamical variable, and we introduce a canonical momentum p_s (conjugate to s), and a new independent variable σ. In this extended phase space and choosing a gauge for the vector potential

such that $A_x = 0$, the new Hamiltonian ($\tilde{H}$) is written as:

$$\tilde{H}(s_i, p_i, s, p_s; \sigma) = H(x_i, p_i; s) + p_s \tag{2.66}$$

$$= \frac{\delta}{\beta_0} - \sqrt{\left(\frac{1}{\beta_0} + \delta\right)^2 - p_x^2 - (p_y - a_y)^2 - \frac{1}{\beta_0^2\gamma_0^2}} - a_s + p_s. \tag{2.67}$$

The Lie transformation, given that the Hamiltonian has no explicit dependence on the new independent variable σ, can be written as:

$$M(\Delta\sigma) = e^{-\Delta\sigma:\tilde{H}:}. \tag{2.68}$$

Making use of the paraxial approximation and expanding the square root as a power series to second order, the Hamiltonian can be expressed in the form:

$$\tilde{H} = K_1 + K_2 + K_3, \tag{2.69}$$

where:

$$K_1 = \frac{\delta}{\beta_0} - D + \frac{p_x^2}{2D} + p_s, \tag{2.70}$$

$$K_2 = \frac{(p_y - a_y)^2}{2D}, \tag{2.71}$$

$$K_3 = -a_s, \tag{2.72}$$

and D is given by:

$$D = \sqrt{1 + \frac{2\delta}{\beta_0} + \delta^2}. \tag{2.73}$$

The terms K_1 and K_3 are integrable. Using the properties of Lie transformations the remaining term K_2 can be expressed as:

$$e^{-\Delta\sigma:K_2:} = e^{:I_y:} e^{-\Delta\sigma:\frac{p_y^2}{2D}:} e^{-:I_y:}, \tag{2.74}$$

for a function I_y that fulfills the condition:

$$e^{:I_y:} p_y = p_y - a_y. \tag{2.75}$$

A function that has this desired property is given by:

$$I_y = \int_0^y a_y(x, y', s) dy'. \tag{2.76}$$

The Lie transformation of the complete Hamiltonian in Eq. 2.69 can now be expressed as:

$$e^{-\Delta\sigma:K:} \approx e^{-\frac{\Delta\sigma}{4}:K_1:} e^{-\frac{\Delta\sigma}{2}:K_3:} e^{-\frac{\Delta\sigma}{4}:K_1:} e^{-\Delta\sigma:K_2:} e^{-\frac{\Delta\sigma}{4}:K_1:} e^{-\frac{\Delta\sigma}{2}:K_3:} e^{-\frac{\Delta\sigma}{4}:K_1:}. \tag{2.77}$$

The associated Lie transformation for each of these components is given as:

$$
\begin{aligned}
e^{-\frac{\Delta\sigma}{4}:K_1:}x &= x + \frac{p_x}{D}\frac{\Delta\sigma}{4}, && (2.78)\\
e^{-\frac{\Delta\sigma}{4}:K_1:}z &= z + \left(\frac{1}{\beta_0} - \left(\frac{p_x^2}{2D^3} + \frac{1}{D}\right)\left(\frac{1}{\beta_0} + \delta\right)\right)\frac{\Delta\sigma}{4}, && (2.79)\\
e^{-\frac{\Delta\sigma}{4}:K_1:}s &= s + \frac{\Delta\sigma}{4}, && (2.80)\\
e^{\pm:I_y:}p_x &= p_x \mp \int_0^y \frac{\partial a_y(x,y',s)}{\partial x}dy', && (2.81)\\
e^{\pm:I_y:}p_y &= p_y \mp a_y(x,y,s), && (2.82)\\
e^{\pm:I_y:}p_s &= p_s \mp \int_0^y \frac{\partial a_y(x,y',s)}{\partial s}dy', && (2.83)\\
e^{-\Delta\sigma:K_2':}y &= y + \frac{p_y}{D}\Delta\sigma, && (2.84)\\
e^{-\Delta\sigma:K_2':}z &= z - \frac{p_y^2}{2D^3}\left(\frac{1}{\beta_0} + \delta\right)\Delta\sigma, && (2.85)\\
e^{-\Delta\sigma:K_3:}p_x &= p_x + \frac{\partial a_s}{\partial x}\frac{\Delta\sigma}{2}, && (2.86)\\
e^{-\Delta\sigma:K_3:}p_y &= p_y + \frac{\partial a_s}{\partial y}\frac{\Delta\sigma}{2}, && (2.87)\\
e^{-\Delta\sigma:K_3:}p_s &= p_s + \frac{\partial a_s}{\partial s}\frac{\Delta\sigma}{2}, && (2.88)\\
& && (2.89)
\end{aligned}
$$

where $K_2' = \frac{p_y^2}{2D}$.

The transformations of the dynamical variables are then performed at each step of the integration, in terms of the new independent variable from σ_0 to $\sigma_0 + \Delta\sigma$. The extended phase space then allows us to compute the vector potential at different positions along the reference trajectory, which is precisely the task needed for s-dependent magnetic fields.

2.6.3 Runge–Kutta Integrator

The Runge–Kutta method provides schemes that, unlike some other methods, allows the integration of the equations of motion for a particle in an accelerator without the need for the paraxial approximation. Runge–Kutta methods are then particularly useful for cases where p_y and p_x can reach large values. Under certain conditions the integration will also be symplectic, however for this condition to be fulfilled requires the method to be implicit, which means that at each step of the integration a set of algebraic equations must be solved, which may increase the computational time needed to perform the integration. In this section both the implicit and explicit representation of Runge–Kutta integrators will be given.

We start by assuming that the variable $x(s)$ satisfies the differential equation:

$$\frac{dx}{ds} = f(x, s), \tag{2.90}$$

with initial conditions:

$$x(s_0) = x_0. \tag{2.91}$$

The principle of Runge–Kutta integration is to evaluate the function $f(x, s)$ at a series of intermediate points at each step and add the results in such a way that the value of variable x at the next step is accurate to a given order in the size of the step.

Given b and c as m-dimensional vectors and a an $m \times m$ matrix with real entries, the variable x can be expressed at the next interval of Δs (x_{n+1}) as:

$$x_{n+1} = x_n + \sum_{i=1}^{m} b_i k_i, \tag{2.92}$$

where at each step k_i is given as:

$$k_i = \Delta s f(x_n^{(i)}, s_n^{(i)}). \tag{2.93}$$

The intermediate steps $x_n^{(i)}$ and $s_n^{(i)}$ are given by:

$$x_n^{(i)} = x(s_n) + \sum_{j=1}^{m} a_{ij} k_j, \tag{2.94}$$

$$s_n^{(i)} = s_n + c_i \Delta s. \tag{2.95}$$

A particular Runge–Kutta method is specified by giving the values of the constants a_{ij}, b_i and c_i. Conventionally, these three sets of constants are written in a Butcher tableau, of the form:

$$\begin{array}{c|cccc} c_1 & a_{11} & a_{12} & \cdots & a_{1m} \\ c_2 & a_{21} & a_{22} & \cdots & a_{2m} \\ \vdots & \vdots & \vdots & \ddots & \vdots \\ c_m & a_{m1} & a_{m2} & \cdots & a_{mm} \\ \hline & b_1 & b_2 & \cdots & b_m \end{array}$$

The error of the Runge-Kutta integrator depends of the order of the method; for the second order Runge-Kutta integrator for example the error scales as h^2, where h is the step size in the integration.

Explicit scheme

As an example, the Butcher tableau for the explicit second order Runge–Kutta (RK2) scheme is:

The Butcher tableau for the third order Runge–Kutta (RK3) is given by:

$$\begin{array}{c|cc} 0 & 0 & 0 \\ \frac{1}{2} & \frac{1}{2} & 0 \\ \hline & 0 & 1 \end{array}$$

$$\begin{array}{c|ccc} 0 & 0 & 0 & 0 \\ \frac{1}{2} & \frac{1}{2} & 0 & 0 \\ 1 & -1 & 2 & 0 \\ \hline & 1/6 & 4/6 & 1/6 \end{array}$$

These Butcher tableaux have two distinct characteristics. The first one is that the vector c is related to the matrix a by:

$$c_i = \sum_{j=1}^{m} a_{ij}. \tag{2.96}$$

This is called the consistency condition and is generally required for all Runge–Kutta methods. The second characteristic is that the matrix a is strictly lower triangular. This feature is the condition that allows the scheme to be explicit as can be observed by calculating the corresponding k_i vectors:

$$k_1 = \Delta s f(x_n, s_n), \tag{2.97}$$

$$k_2 = \Delta s f(x_n + a_{21}k_1, s_n + c_1\Delta s), \tag{2.98}$$

$$k_3 = \Delta s f(x_n + a_{31}k_1 + a_{32}k_2, s_n + c_2\Delta s), \tag{2.99}$$

and so on. Thus, the vectors k_i are computable in terms of k_j with $j < i$. A downside of explicit Runge–Kutta schemes are that such schemes are not symplectic, but can still be of use if exact symplecticity, at least to numerical precision, is not required. If exact symplecticity is required one must make use of an implicit scheme.

Implicit scheme

An implicit method will have a vector in which (in general) all a_{ij} are non-zero and consequently a series of algebraic equations must be solved to obtain a solution. The corresponding Butcher tableau for an implicit second order Runge–Kutta, named the implicit midpoint rule, is given as:

$$\begin{array}{c|c} \frac{1}{2} & \frac{1}{2} \\ \hline & 1 \end{array}$$

It can be seen that this Butcher tableau has the following property:

$$b_i a_{ij} + b_j a_{ji} = b_i b_j, \tag{2.100}$$

which is the condition required for a scheme to be symplectic [39].

Application of Runge–Kutta integration in a Hamiltonian system

We shall explain the application of the Runge–Kutta integrator applied to Hamiltonian systems. Given the phase space vector $\vec{x} = (x, p_x, y, p_y, z, \delta)$, the corresponding Hamilton's equations are:

$$\frac{d\vec{x}}{ds} = S\nabla_{\vec{x}} H(\vec{x}, s), \tag{2.101}$$

where S is the antisymmetric matrix given in Eq. 2.17.

The same integration step used in Eq. 2.94 is used to give $\vec{x}_{n+1}$ as:

$$\vec{x}_{n+1} = \vec{x}_n + \sum_{i=1}^{m} b_i \vec{k_i}, \tag{2.102}$$

where $\vec{k_i}$ is given as:

$$\vec{k_i} = \Delta_s S\nabla_{\vec{x}} H(\vec{x}_n^{(i)}, s_n^{(i)}). \tag{2.103}$$

The intermediate values $\vec{x}_n^{(i)}$ and $s_n^{(i)}$ are given as:

$$\vec{x}_n^{(i)} = \vec{x}(s_n) + \sum_{j=1}^{m} a_{ij} \vec{k}_j, \tag{2.104}$$

$$s_n^{(i)} = s_n + c_i \Delta s. \tag{2.105}$$

Both the implicit and explicit Runge–Kutta methods can in principle be applied to integrate the Hamiltonian, although only the implicit scheme will be symplectic.

Applying an implicit midpoint rule on a Hamiltonian of the form $H(\vec{x}, s)$ gives:

$$\vec{x}_{n+1} = \vec{x}_n + \Delta s S\nabla_{\vec{x}} H\Big|_{\vec{x}=\vec{x}_n^{(1)}} \tag{2.106}$$

The intermediate values are given as:

$$\vec{x}_n^{(1)} = \vec{x}_n + \frac{1}{2}\Delta s S\nabla_{\vec{x}} H\Big|_{\vec{x}=\vec{x}_n^{(1)}} \tag{2.107}$$

Equation 2.106 hence provides an integration method for the phase space variables $\vec{x}$ that will be symplectic but, in general, will require a set of algebraic equations to be solved at each step to obtain the solutions.

2.7 Conclusions

In order to obtain transfer maps of linear elements discussed in Chapter 1 certain approximations needed to be taken into account. Accelerator beamlines require the implementation of more complicated elements for which the approximations will no longer hold. The goal of this chapter was to present additional tools to the ones presented in Chapter 1 to obtain transfer maps for nonlinear elements. First, the method of generalised gradients was presented; the generalised gradients provide a method to obtain an

analytical representation of a field that changes with longitudinal position, in terms of coefficients that can be computed from numerical field data. To obtain transfer maps for nonlinear elements it is desirable to maintain symplecticity. Although this is not essential in all problems, it is of particular importance when tracking particles in a storage ring without radiation damping. The method of power series was presented, as well as two different integrators: The Wu–Forest–Robin and the Runge–Kutta integrator. Both methods provide a way to obtain symplectic transfer maps, however the Wu–Forest–Robin integrator makes use of the paraxial approximation. On the other hand the Runge–Kutta method provides a symplectic transfer map only for implicit schemes, impacting the computational time needed to do the tracking.

The tools described in this chapter will be useful in Chapter 6 to study the effects of fringe fields in quadrupoles. In particular generalised gradients are used to provide an analytical representation of the fringe fields, and Wu–Forest–Robin and Runge–Kutta integrators can then be used (with the help of a differential algebra code) to obtain transfer maps in the form of power series. Also discussed was the use of kick codes in particle tracking: this type of tracking will be employed in Chapter 5 and again in Chapter 6 when the code SixTrack is used to study the stability of the beam in different lattices.

Chapter 3

LHC and its Upgrades

Accelerators have provided facilities for a large number of communities, not only to particle physics (which has been one of the main driving forces behind their development), but also joined by the growing users of synchrotron light and radiation therapy.

In this chapter a brief history of accelerators will be presented, along with a description of the fundamental physics that motivates the building of higher energy machines, and the evolution of technologies that allowed the construction of more powerful machines, in particular the LHC and its upgrades. An overall description of these upgrades along with the challenges encountered to increase the luminosity, which is the main motivation of this thesis, will also be presented.

3.1 The Standard Model

The many discoveries made in the last century have helped physicists acquire an incredible insight into the structure of matter. Largely developed in the 1970s, the theory of the Standard Model explains how all the known matter is made up of basic building blocks, consisting of fundamental particles which interact through fundamental forces. As it developed, the theory incorporated all the known subatomic particles discovered at the time and proposed the existence of others.

The Standard Model dictates that all known matter is made of fundamental particles divided in two groups: quarks and leptons. Each of these groups is classified into three different families, as illustrated in Fig. 3.1. The first family of the quarks is formed by the up and down quarks, followed by the strange and charm quarks in the second family and the top and bottom quarks in the third. Quarks also have a property called colour and only combine in a way to form colourless particles. In the case of the leptons, the families are given by a lepton and its corresponding neutrino, the electron and electron-neutrino in the first family, followed by the the muon and muon-neutrino and the tau and tau-neutrino in the second and third families respectively. The electron, muon and tau all have a given charge and a sizeable mass, as for the corresponding neutrinos they have a neutral charge and very small mass in comparison with the other particles of

the Standard Model. Each of these quarks and leptons of the three families also has a corresponding antiparticle with the same properties except for a charge of opposite sign.

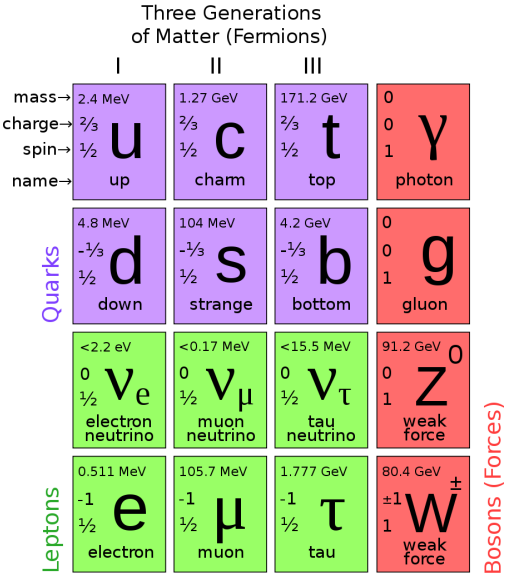

FIGURE 3.1: Fundamental particles and the force-carrier bosons of the Standard Model [40].

All stable matter that is known in the universe is made up of members of the first family. Combinations of up and down quarks make up protons and neutrons which form the nucleus of atoms, for example. The members of the second and third family quickly decay into more stable particles, increasing the difficulty of their detection.

The theory also describes the way in which these particles interact. The existence of four fundamental forces was proposed: the electromagnetic force, the strong force, the weak force and the gravitational force. Each of these forces has its own force carrier (known generally as bosons): the photon for the electromagnetic force, the gluon for the strong force, the $W^{\pm}$ and Z^0 boson for the weak force, and, although the evidence of its existence has not yet been found, the graviton for the gravitational force. The gravitational force however, is not part of the Standard Model, since the task of including this force into the same framework has not yet been achieved. The force carriers are also illustrated in Fig. 3.1. Finally, the Standard Model also describes the existence of the Higgs boson; more on the importance of this particle in the Standard Model theory will be given later on in Section 3.3.4.

Discovery of most of the particles was achieved with the use of particle accelerators, providing confidence in the results and establishing the Standard Model as a well-tested theory.

3.2 History of Accelerators

When considering the evolution of particle accelerators higher energy has always been a driving force for two main reasons. Firstly, higher collision energies means smaller objects can be probed. To probe an object the size of an atom a 10^3 eV (1 keV) energy probe is required. When studying the scale of the nucleus this energy should be increased to 10^6 eV (1 MeV) but reaching an energy of 10^9 eV (1 GeV) or higher allows the examination of the fine structure of the basic constituents of matter [41]. Secondly, the majority of particles are not stable and decay rapidly into more stable particles. To study these particles, the appropriate conditions have to be created. In general terms the famous formula $E = mc^2$ dictates the energy necessary to create a particle of mass m. However, to detect a fast decaying particle is more complicated than simply satisfying the energy requirement to create it.

The increasing need for higher energies in particle physics studies led to the development of higher energy accelerators. The following paragraphs will describe the evolution in technology that led to the development of accelerators from small and precarious machines to the large scale facilities that exist nowadays.

In 1896 J.J. Thomson [42] used a cathode ray tube to identify the first fundamental particle to be discovered, the electron. In this experiment a direct current was used to create a potential between an anode (A in Fig. 3.2) and a cathode (B in Fig. 3.2). The cathode rays produced were then passed between two parallel aluminium plates (C and D in Fig. 3.2) providing an electric field between them when connected to a battery. At the end of the tube the beam would impact the surface of a sphere coated in a fluorescent material, creating a glowing pattern. By measuring across the surface of the sphere the deflection of the beam due to the electric field could be calculated, providing a measurement of the charge to mass ratio, an important property of the electron.

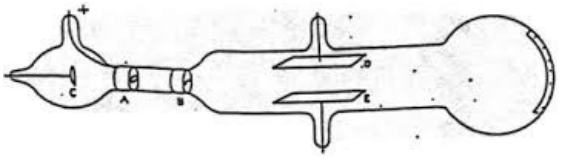

FIGURE 3.2: Schematic view of Thomson's cathode ray tube [42].

As the need for higher energies kept increasing, Ising proposed using alternating current in a series of drift tubes of increasing lengths, that would account for the increasing velocity of the particles, in a process known as resonant acceleration. Ising's principle was later developed and patented by Wideroe in 1928 [43]. Such was the significance of this idea that the invention was to provide the underlying principle of all of today's ultra high energy accelerators.

However, following this principle, increasing the energy would also require an increase in the length of drift tubes. To avoid the use of inconvenient large tubes, a solution would be to use a circular accelerator. Lawrence, inspired by Ising's principle conceived the cyclotron and Livingston demonstrated the principle by accelerating hydrogen ions to

80 keV in 1931 [44]. The main principle underlying the cyclotron is to use the same gap to accelerate the particles and use magnets to bend the path of the particles back to it. From Eq. 1.4 the radius of curvature of particles increases as:

$$\rho = \frac{\gamma m v}{qB}, \tag{3.1}$$

where γ is the relativistic factor, m is the mass, v is the speed, q is the charge and B is the magnetic field strength perpendicular to the plane of motion.

For further studies there was an inevitable need for higher energies but this was not possible until 1932 when an accelerator was built by Cockcroft and Walton [45]. The Cockcroft–Walton generator produces a high voltage direct current from a much lower voltage current with the aid of an arrangement of capacitors and diodes, as illustrated in Fig. 3.3. This type of accelerator used the idea of a fixed target whereby lithium nuclei were bombarded with accelerated protons to form two helium nuclei. However this technique reaches a limit at around 20 MV, beyond this point accelerating particles becomes harder due to electrical breakdown.

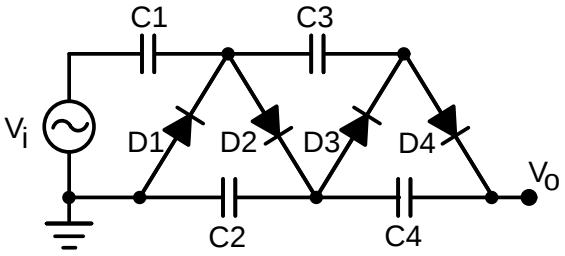

FIGURE 3.3: Illustration of the arrangements of capacitors and diodes of a Cockcroft-Walton generator [46].

Following the principle of the cyclotron, as the momentum increases (but assuming $v \ll c$), the radius grows larger by the same factor, keeping the orbit time constant, thus maintaining the same RF frequency of the gap voltage. The cyclotron however, is limited by relativity, which causes particles to lose synchronism with the RF field. The synchrocyclotron [47] was proposed to correct the relativistic effect, but it was a new type of accelerator, the synchrotron, that was used to achieve higher energies.

This new accelerator made use of varying magnetic fields, increasing the field with particle energy, keeping the orbit stationary. The acceleration is applied with an RF voltage via a gap or a cavity [48, 49]. The first proton synchrotron was proposed in 1947 by Oliphant, Gooden and Hyde [50], however the first one to be built was the 3 GeV cosmotron [51] at Brookhaven National Laboratory in 1952.

Up until this time, only dipoles had been used to provide focusing. In this case, the guide field decreases slightly with increasing radius and its gradient is constant all around the machine. Higher energies required larger apertures to contain the beam, making the magnets inconveniently big and costly. A breakthrough came in 1952 when strong focusing or alternating-gradient (AG) focusing using quadrupole magnets was proposed by Courant, Livingston and Snyder [52] and independently by Christofilos [53].

The quadrupoles, as explained in Section 1.1.3, focus the beam in one direction whilst defocusing in the other, but the combination of the two, a focusing and a defocusing quadrupole, leads to a focused beam in both directions with a much smaller and more convenient design than using dipoles. Strong focusing made it easier to reach higher energies.

A further development came with the proposal of radio frequency quadrupoles (RFQ). First proposed by Kapchinskij and Teplyakov [54] the RFQ proof-of-principle was done in Los Alamos laboratory in 1979 [55]. With this technique not only the focusing but also the bunching and acceleration are performed by the RF field of the quadrupole.

3.2.1 Particle Colliders

Particle colliders make for a distinct kind of accelerator, particularly useful for particle physics experiments. Such experiments can also be performed with fixed target accelerators. However, as will be shown in the next section, much higher centre-of-mass energies can be achieved by colliding two beams.

Energy

When colliding a moving particle with another one at rest, part of the available energy must go towards the kinetic energy of the system after the collision. However, when two particles of equal mass collide head on, the total momentum of the system after the collision is zero, meaning that all the energy from both particles is available for producing new particles. This is observed when calculating the center of mass energy for both cases.

The centre-of-mass energy for two particles colliding head-on with each other is given by [56]:

$$E_{cm} = \left(2E_1E_2 + (m_1^2 + m_2^2)c^4 + 2\sqrt{E_1^2 - m_1^2c^4}\sqrt{E_2^2 - m_2^2c^4}\right)^{1/2}, \tag{3.2}$$

where $m_{1,2}$ and $E_{1,2}$ are the masses and energies respectively of the two incoming particles. In most existing colliders $m_1 = m_2$ and $E_1 = E_2(= E)$, reducing the previous expression to:

$$E_{cm} = 2E. \tag{3.3}$$

For asymmetric storage rings, such as electron-proton colliders, the center-of-mass energy reduces instead to:

$$E_{cm} = \sqrt{2E_1E_2}. \tag{3.4}$$

For a fixed target collision, the equivalent centre-of-mass energy is given by [57]:

$$E_{cm} = \sqrt{m_1^2c^4 + m_2^2c^4 + 2E_1m_2c^2}, \tag{3.5}$$

where m_1 and E_1 are the mass and energy respectively of the incoming particle, and m_2 is the mass of the target particle. For most cases E_1 is much larger than the rest mass of the particles, under this approximation, the previous results gives:

$$E_{CM} \simeq \sqrt{2E_1 m_2 c^2}. \tag{3.6}$$

Taking the beam of the LHC as an example, colliding two proton beams at 3.5 TeV will result in a center-of-mass energy of 7 TeV, while for a fixed target collision (using protons as target) will result in a significant reduction, with a center-of-mass energy of ~ 80 GeV. Therefore, colliding beam machines have a great advantage over fixed target machines when pursuing high energies collisions.

Making use of this principle several colliders have been built colliding different types of particles, and can be divided into three general groups: hadron colliders, lepton colliders and lepton-hadron colliders.

Competing criteria arise for each of these different types of collisions. Hadron-hadron collisions have the advantage of providing a higher event rate than those using electrons, hence providing higher luminosity for the same conditions. On the downside hadrons are not elementary particles, therefore the data collected from collisions is harder to interpret. On the other hand, when we use electrons to collide with proton targets for example, the complex structure of the proton is explored using an elementary particle whose behaviour is well understood. When using electrons however, the synchrotron radiation produced when bending an electron beam is much larger than the corresponding radiation from a proton beam following the same path, as explained in Section 1.6. This radiation has to be controlled to avoid damage to the machine and to minimise the power needed to replace the energy lost through synchrotron radiation. Another option is to reduce the bending constructing a larger path, resulting in an increase in the cost of the machine.

Physicists benefit from having different kinds of collisions, each of them providing important advances in the understanding of matter and with complementary studies giving confidence in the results.

Figure 3.4 illustrates the centre-of-mass energy against the year of the first physics results for different accelerators. The linear increase of energy with the year of first physics is shown both for hadron colliders and e^+e^- colliders with an increase in energy of about a factor of 10 every 6-8 years, however a reduction is observed in the later years. This slower progress in pushing the energy frontier is due to the limit in technology. The latest energy achieved in the LHC in 2015 (indicated in the figure) is closer to the previous rate.

Luminosity

As discussed in Section 1.3.2 the luminosity, just as much as the energy, is a critical figure of merit of a particle collider since it provides the likelihood to observe a given

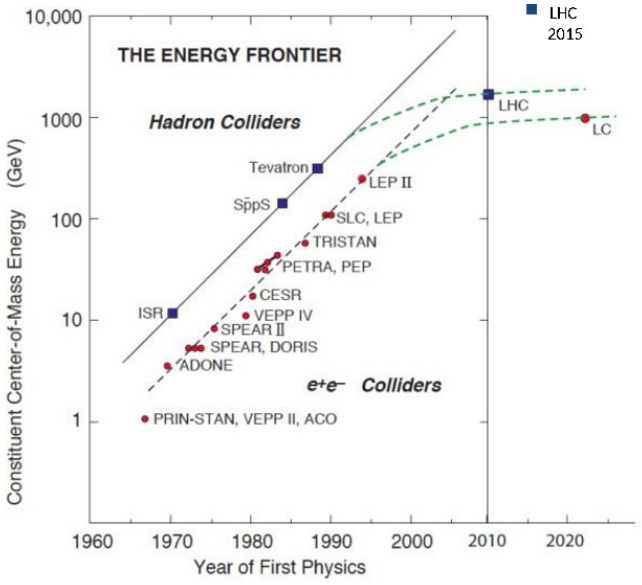

FIGURE 3.4: Centre-of-mass energy for different particle accelerators with respect to the year of first physics results [58]. Figure has been edited to include results from the LHC in 2015.

event; however, an increase of luminosity to more than $10^{34}\text{cm}^{-2}\text{s}^{-1}$ can lead to pile-up in the detectors. The luminosity of different particle accelerators with respect to its centre-of-mass energy is shown in Fig. 3.5. This is shown for different types of collisions.

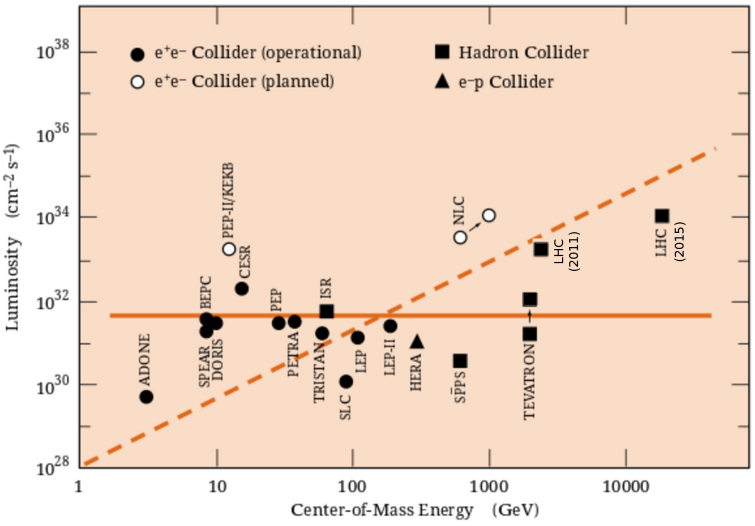

FIGURE 3.5: Luminosities for different particle accelerators with respect to their centre-of-mass energy [41]. Figure has been edited to include results from the LHC in 2011 and 2015.

3.3 Colliders Towards the LHC Era

Building higher energy accelerators often requires a significant development in technology that is not trivial to achieve. Even when the technology is available, the costs of the accelerator have to be controlled to justify its construction and operation. This is true especially in fundamental particle physics, as the benefits of the experiment might not be of direct economic benefit but rather of cultural and scientific value with the advancement of knowledge.

In this section, a description of four different accelerators will be given. These accelerators were chosen not only to illustrate the benefits of having different (complementary) types of collisions at high-energies (> 100 GeV as shown in Fig. 3.5), but also because these experiments had a significant impact in preparing the ground for the LHC to be constructed.

3.3.1 Hadron-Hadron Colliders

SPS

The Super Proton Synchrotron (SPS) [59] is located at CERN and measures almost 7 km in circumference. Starting operations in 1976 the SPS became the main driving force of CERN's particle physics program. This accelerator has been used to accelerate protons and antiprotons, electrons and positrons and heavy ions.

Investigations performed in the SPS are highlighted by the Nobel prize discovery of the $W^{\pm}$ and Z^0 bosons at the UA1 and UA2 [60, 61] experiments, when the SPS ran as a proton-antiproton collider at a collision energy of 400 GeV, reaching values of $10^{32}\text{cm}^{-2}\text{s}^{-1}$ for the luminosity [62]. The SPS also studied the inner structure of protons, investigated the preference in nature for matter over antimatter and searched for exotic forms of matter.

By accelerating electrons and positrons to sufficient energy, the SPS served as the injector for the Large Electron-Positron collider at CERN.

Currently it is used as the final injector for high-intensity proton beams for the LHC, accelerating particles from 26 to 450 GeV, whilst still performing fixed-target experiments on its own account, such as the experiments NA61/SHINE [63], NA62 [64] and COMPASS [65].

TEVATRON

Located at Fermilab, Illinois, USA, the TEVATRON [66], with a circumference of 6.4 km, was operational from 1983 until 2011 providing colliding beam experiments as well as fixed target experiments and test beam areas.

Before shutting down, the Tevatron was the world's highest-energy proton-antiproton collider, accelerating and storing beams of protons and antiprotons travelling in opposite directions colliding at the locations of the two detectors CDF and DØ, reaching a center-of-mass energy of up to 1.8 TeV and a peak luminosity of $10^{32}\text{cm}^{-2}\text{s}^{-1}$ [66].

The first collisions produced in the Tevatron were performed in 1985. Several advances in the study of the Standard Model were achieved thanks to this experiment, highlighted by the discovery of the top quark [67]. The Tevatron research program also provided countless achievements in the development of detector, accelerator design and computer technology.

3.3.2 Lepton-Hadron Colliders

HERA

HERA [68] was the largest particle accelerator at DESY [69]. This storage ring had an operational life from 1992 to 2007, with a total of 15 years working as the world's most precise electron-microscope for studies of the inner structure of the proton.

The total length of the accelerator was 6.34 km, providing electron-proton collisions at a centre of mass energy of 318 GeV and a luminosity of $3 \times 10^{31}\text{cm}^{-2}s^{-1}$ studied by four experiments: H1, ZEUS, HERMES and HERA-B [68].

Important results were found thanks to this accelerator. Among them, H1 and ZEUS discovered that the density of quarks and gluons inside the proton was unexpectedly high when they carry a small fraction of the proton momentum.

The same experiments also produced direct evidence that two of the fundamental forces, electromagnetism and the weak force, have the same strengths, providing a first step towards the unification of all forces.

The studies at HERA not only enabled more accurate predictions for particle collisions in the LHC, but also provided valuable knowledge for the construction and operation of an accelerator like the LHC and its experiments. HERA was also an example of international collaboration by having a total of 11 countries contributing to the project, not only to the detector but also the accelerator.

3.3.3 Lepton-Lepton Colliders

LEP

The Large Electron-Positron collider (LEP) [70] with a circumference of 27 km was the largest electron-positron accelerator ever built. The collider's initial energy was chosen to be 91 GeV, the center-of-mass energy of the Z bosson. Later on LEP was upgraded to the W production for the main program at an energy of 160 GeV. LEP was upgraded for a second operation phase, increasing the energy to 209 GeV in 2000. The corresponding luminosity was $1.6 \times 10^{31}\text{cm}^{-2}\text{s}^{-1}$ [70].

LEP was operational for 11 years, starting collisions in 1989. During these years LEP experiments provided a detailed study of the electroweak interaction. Thanks to these experiments it was also proved that there are three, and only three, generations of particles of matter.

LEP finished operations in 2000 to allow the construction of the LHC in the same tunnel.

3.3.4 Discovery of the Higgs Boson

During the 20th century, the collaboration of strong theoretical developments and outstanding experimental work has led to the proposal and following discovery of almost all the particles of the Standard Model. In particular, the high energy experiments described in the last section helped to achieve the challenging discovery of the heaviest quarks and the weak force carrier bosons.

However an important piece of the Standard Model remained missing until 2012. In order to explain the mass of some elementary particles an additional boson, named the Higgs boson, remained to be discovered. Even when the rest of the theory worked perfectly with the experimental observations, the potential non-existence of this boson implicated drastic changes to the way particle physicists understood the theory.

Confirming the existence of the Higgs boson was the main driving force behind a number of modern high-energy accelerators. It was initially expected that experiments such as the Tevatron or the SPS could provide information of its existence but the statistics and collision energy were not enough to confirm or refute the theory.

With a much higher energy and luminosity, the LHC was proposed to overcome these limitations; with the technology already developed by its predecessors, the LHC accelerator could be designed to have enough collision energy to create the Higgs boson. Furthermore, the experience gained from the previous experiments helped to better design high-luminosity detectors for its identification.

3.4 The LHC

The Large Hadron Collider [71] is located at CERN, in the border region between Switzerland and France. The accelerator tunnel has a circumference of 27 km making use of the previous LEP tunnel. First collisions were produced in this accelerator in March, 2010. In 2010 and 2011 the LHC operated at 3.5 TeV per beam providing proton-proton collisions at a centre-of-mass energy ($\sqrt{s}$) of 7 TeV. In 2012 the energy per beam was increased to 4 TeV resulting in $\sqrt{s} = 8$ TeV collisions. The energy per beam was once again increased to provide collisions at $\sqrt{s} = 13$ TeV. Lead-lead collisions have also been provided at an energy $\sqrt{s} = 2.76$ TeV/nucleon and proton-lead collisions at $\sqrt{s} = 5$ TeV/nucleon.

Among the experiments are ATLAS [72] at interaction point 1 (IP1) and CMS [73] at interaction point 5 (IP5) which are the general purpose experiments having the highest luminosity in the corresponding IPs. At the other interaction points the experiment LHCb [74] at interaction point 8 (IP8) studies the b quark and CP violation and operates at a luminosity $\approx$ 20 times lower than the luminosity in ATLAS and CMS. Finally ALICE [75] is located at interaction point 2 (IP2) operating at a luminosity $\approx 10^5$ times lower than that of ATLAS and CMS, and is optimised for Pb-Pb collisions for studies of the quark-gluon plasma. A schematic view of the LHC is shown in Fig. 3.6. Table 3.1

lists the main parameters of the LHC and the colliders listed in Section 3.3 to provide a comparison in circumference, energy and luminosity between these high-energy colliders.

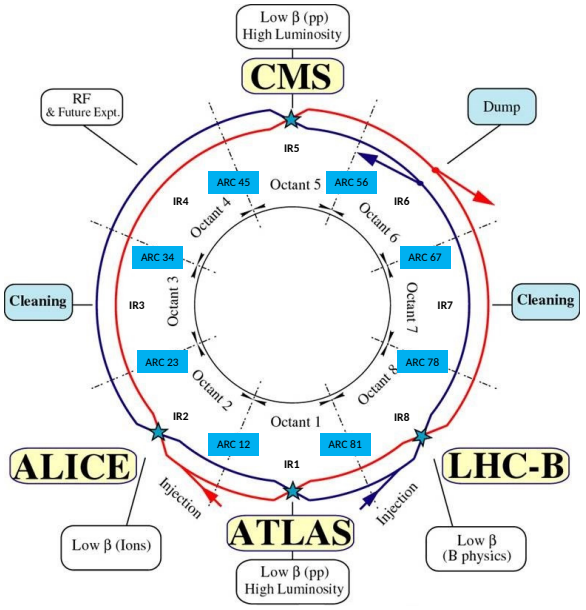

FIGURE 3.6: LHC schematic showing clockwise beam 1 colliding with counter-clockwise beam 2 in the 4 different experiments [71].

Accelerator	Types of collisions	Circumference	Ultimate Centre-of-mass energy (GeV)	Ultimate Luminosity ($cm^{-2}s^{-1}$)
LHC	$p-p$	27 km	13 TeV	10^{34}
SPS	$p-\bar{p}$	7 km	630	3×10^{30}
Tevatron	$p-\bar{p}$	6.3 km	1800	4×10^{32}
HERA	$e-p$	6.3 km	319	3×10^{31}
LEP	e^+-e^-	27 km	209	1.6×10^{31}

TABLE 3.1: Comparison between the main parameters of the high-energy colliders: LHC, SPS, Tevatron, HERA and LEP.

3.4.1 Structure of the LHC

The LHC consists of eight 2.45 km long arcs and eight 545 m long straight sections [76]. Each of the arcs contains 154 dipole magnets. The machine is sectorized with each octant acting in synchrony. The long straight sections between the arcs contain dispersion suppressors and the interaction regions (IR). The layout of each straight section is customised for its use. Interaction regions 1, 2, 5 and 8 (IR1, IR2, IR5, and IR8 respectively) accommodate the experiments, as explained previously. Collisions take place at the corresponding IP, in the middle of the IRs mentioned previously. IR2 and IR8 also accommodate the injection of the beam.

Collisions do not take place at the remaining IRs, interaction regions 3, 4, 6 and 7 (IR3, IR4, IR6 and IR7 respectively). IR4 houses the RF cavities while a beam dump is located in IR6.

The performance of the LHC, circulating beams at unprecedented energies, not only relies on the adequate storing, accelerating and colliding of the beams, but also on the appropriate protection of the machine from the beam. The LHC collimation system protects the accelerator from beam loss, that at such high energies can cause serious damage. Two straight sections, IR3 and IR7 are dedicated to beam cleaning. IR3 houses the momentum cleaning system of the beams, while IR7 houses the betatron cleaning system. These regions are equipped with 54 movable, two-sided collimators and an arrangement of magnets [77].

Each arc contains 23 arc cells, each arc cell has a 106.9 m long FODO structure, consisting of the main dipoles, quadrupoles and other multipole magnets.

The 1232 superconducting dipoles operate reliably at a nominal magnetic field of 8.33 T, this field strength corresponds to a centre-of-mass energy of 14 TeV. The superconducting magnet system must operate in superfluid helium at 1.9 K. During the first period of operation of the LHC the accelerator did not run with its nominal design energy but instead ran at a centre-of-mass energy of 7 TeV. In the case of lead-lead collisions this corresponded to a 2.76 TeV centre-of-mass energy per nucleon. The proton beam energy has now been increased to 13 TeV after Long Shutdown 1 as will be explained in Section 3.4.5.

3.4.2 The LHC Accelerator Complex

In order to reach the high collisions energies of the LHC a series of machines accelerates the particles to increasingly higher energies.

The process starts with the proton source, in which an electric field is used to strip electrons from hydrogen atoms to produce ions. Linac 2 takes these protons and accelerates them to 50 MeV. The beam is then injected into the Proton Synchrotron Booster (PSB), accelerating the beam to 1.4 GeV. The following element of the chain is the Proton Synchrotron (PS) pushing the energy to 25 GeV. Next, the beam is injected into the Super Proton Synchrotron (SPS) accelerating the beams to 450 GeV.

The protons are then finally injected into the two rings of the LHC, beam 1 circulates clockwise and beam 2 circulates anticlockwise. The energies of the beams are then ramped to reach the final collision energy. Because the currents in the superconducting magnets must be changed very slowly, the energy ramp takes about 4 minutes, 20 seconds. After reaching their ultimate energy the two beams are brought into collision at the 4 different interaction points. Figure 3.7 illustrates the LHC accelerator complex.

3.4.3 Long Straight Section Layout

IR1 and IR5, housing the ATLAS and CMS experiments respectively, are identical in terms of hardware and optics. IR2 (housing ALICE) and IR8 (housing LHCb) have

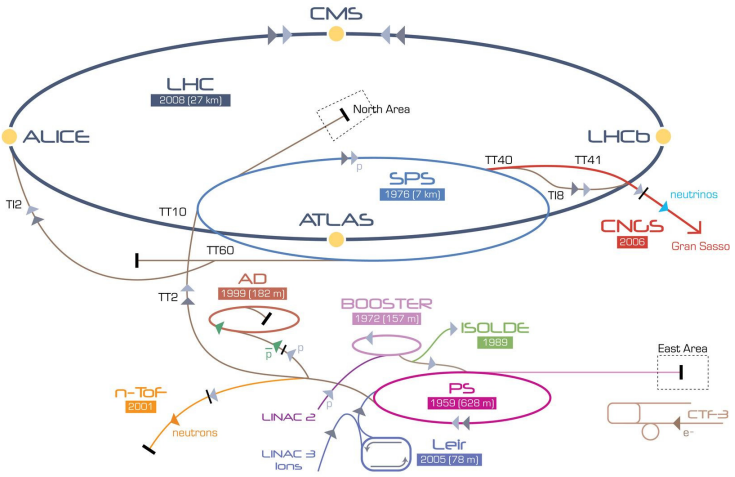

FIGURE 3.7: LHC accelerator complex [78]

slightly different layout and optics. However in general each of these IR layouts can be described in terms of the following sections, starting from the IP:

- The first magnets after the IP comprise a superconducting quadrupole triplet, called the inner triplet, named Q1, Q2 and Q3, located at a distance $L^* = 23$ m from the interaction point. At the location of the inner triplet both beams share the same vacuum chamber.
- A pair of separation/recombination dipoles (D1 and D2) bring the beams into collision and separate them afterwards. At the location of D1, both beams still share the same vacuum chamber but at D2, and the following sections, the beams are separated into different pipes.
- A matching section (MS), consists of 4 quadrupoles, named Q4 to Q7.
- A dispersion suppressor (DS), consists of 4 quadrupoles, named Q8 to Q11 and an arrangement of 8 dipoles. The first two quadrupoles of the first arc cell (QT12 and QT13) are also used for matching procedures in the IR.

The three first sections, the inner triplet, separation/recombination dipoles and the matching section are named the long straight section (LSS). This region comprises the full section between the arcs. A schematic view of its layout, up to the matching section, for IR1 is shown in Fig. 3.8.

3.4.4 Chromaticity Correction Scheme

In order to ensure the long term stability of the beam, an appropriate chromaticity correction must be adopted to control the focusing variation arising from the off-energy nature of the particles in the beam.

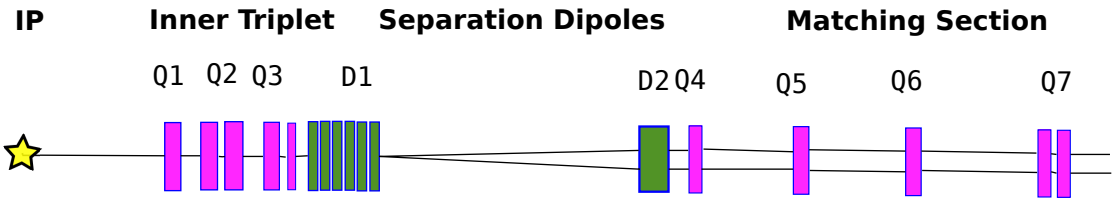

FIGURE 3.8: IR1 long straight section layout including the inner triplet and the matching section.

Making use of the principles described in Section 1.5.1 the correction system in the LHC is based on two families of focusing sextupoles (SFa, SFb) and two families of defocusing sextupoles (SDa, SDb) in each of the 8 arcs of the machine, accounting for a total of 32 families. For the nominal LHC optics, the horizontal and vertical betatron phase advances are close to π between two consecutive sextupoles of the same family. The LHC chromatic correction scheme is designed to correct the three types of chromaticity arising in the machine: the natural chromaticity from the quadrupoles, the chromaticity from the low β insertions quadrupoles and the non-linear chromaticity. A schematic view of the the sextuple powering scheme is shown in Fig. 3.9.

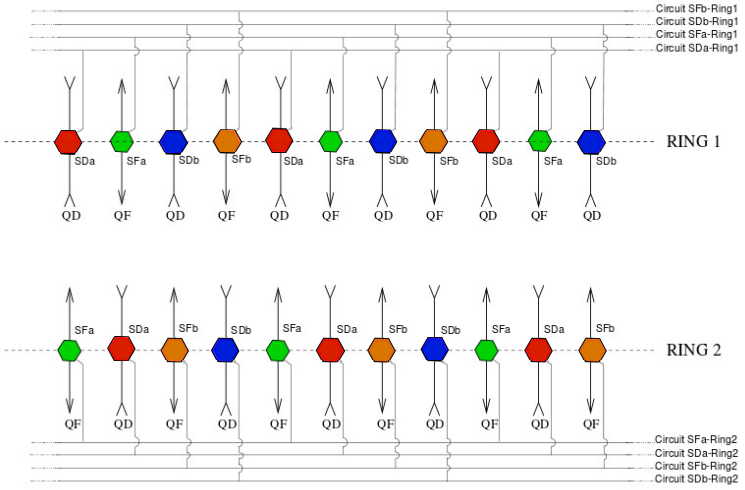

FIGURE 3.9: Chromaticity correction scheme in the LHC. The 2 focusing families (SFa and SFb) and the 2 defocusing families (SDa and SDb) are represented in different colors [71].

The two focusing and defocusing families are sufficient to correct the natural chromaticity of the whole ring including the contribution from the arcs and from the low β insertions. The scheme is also designed to correct the second order chromaticity by adjusting the phase advance per cell close to $\pi/2$ [79]. In the nominal LHC the focusing sextupole families and the defocusing sextupole families are set to the same value, such that the overall chromaticity, the addition of the natural chromaticity arising from the quadrupoles and the induced chromaticity from the sextupoles (Eq. 1.165), results in an absolute value of 2 [80]. Fig. 3.10 illustrates the Montague functions (described

in Section 1.5.2) after the chromaticity correction, and Fig. 3.11 illustrates the change in chromaticity for a δp in the range (-0.001, 0.001), where the linear behaviour the chromaticity is apparent.

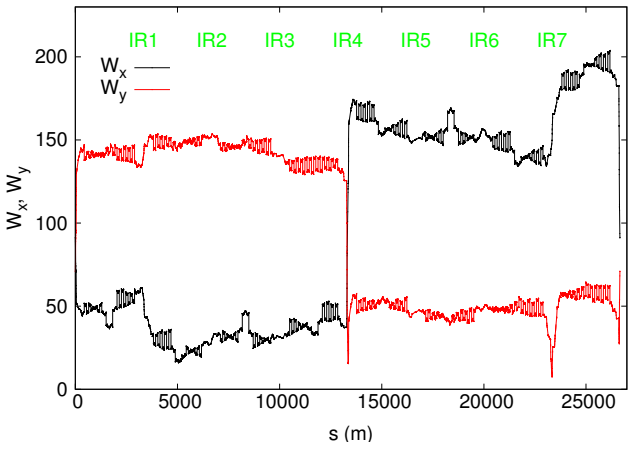

FIGURE 3.10: W_x and W_y functions for beam 1 along the LHC ring.

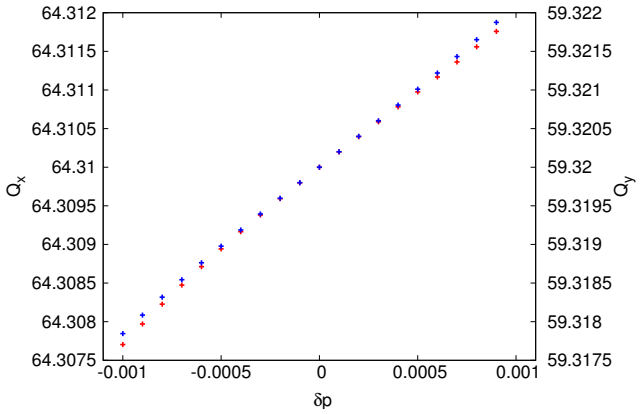

FIGURE 3.11: Tune vs δ_p in Beam 2 of the LHC.

3.4.5 Shutdowns and Upgrades

Two long shutdowns were planned over the full cycle of the LHC, the first one started in 2013 and finished in March 2015, the second one is planned to start in 2018.

The first shutdown was used to work on the superconducting interchanges of the magnets. A fault of such interchanges caused significant damage on a large section of the machine in 2008 during the first tests of the accelerator. The damaged section was repaired but in order to prevent further incidents the nominal field of the dipoles was limited below its full potential, and hence the energy was also prevented from reaching its nominal design value. During this shutdown the interchanges were repaired and the LHC is now running and producing collisions at 13 TeV, slightly below the nominal design energy of 14 TeV. At this stage, 13 TeV was the best chance to obtain new results quickly, the decision to go to higher energies will be taken later in the second run.

The main purpose of the second shutdown (to begin in 2018) is the upgrade of the injectors which includes the addition of Linac 4 into the machine sequence. Linac 4 will provide beams with twice the brightness of those provided with the currently used Linac 2. Furthermore the LHC will benefit from this period to perform full maintenance of the equipment.

3.5 Upgrades of the LHC

The discovery of a particle consistent with the Higgs boson was announced on July 4^{th}, 2012 by the CMS and ATLAS experiments [81, 82], with a mass of ~ 125 GeV/c^2 at a significance of over 5σ, reaching a milestone in particle physics and the understanding of nature.

This thesis concerns the development of two different upgrades for the LHC. Firstly the High-Luminosity LHC (HL-LHC) experiment aims to increase the luminosity of the pp collisions by a factor of ten. The second upgrade, the Large Hadron electron Collider (LHeC), aims to make use of the infrastructure of the LHC and take electron-proton collisions into the TeV era.

This section aims to describe the particle physics challenges that motivate the construction of both of these experiments following the discovery of a Higgs-like boson in 2012. The accelerator developments associated with these upgrades will be outlined in Section 3.6 and Section 3.7 for the HL-LHC and LHeC experiments respectively.

3.5.1 Particle Physics Motivation

Upgraded pp collisions

The discovery of the Higgs boson by the ATLAS and CMS experiments, given its low rate of production, was only achieved after two years of taking data, using datasets corresponding to an integrated luminosity of 4.8 fb^{-1} at $\sqrt{s} = 7$ TeV in 2011 and 5.8 fb^{-1} at $\sqrt{s} = 8$ TeV in 2012 [82]. However, to study its properties is still very challenging with the present LHC accelerator complex since the Higgs production rate is much lower than other Standard Model particles. Furthermore, certain aspects of particle physics cannot be described with the current Standard Model theory, such as dark matter, or the preference in nature for matter over antimatter. Several theories aim to explain new physics beyond the Standard Model. These include supersymmetry (SUSY), grand unification theories (GUTs) and string theory.

Increasing the luminosity of the collisions in the HL-LHC will improve the discovery potential of the LHC by enabling the observation of rare processes currently beyond the scope of any hadron collider. The challenges that must be addressed to increase the luminosity of such a complex machine in terms of the infrastructure of the accelerator will be explained further in Section 3.6.

Lepton-Hadron collisions

Lepton-hadron machines, as explained previously, provide a cleaner type of collision that uses the electron or positron as a probe to interact with a single constituent of the proton.

The so-called parton distribution functions (PDFs) express the probability of finding a parton with a particular fraction of the momentum of the hadron (x) and can only be obtained empirically. The current PDFs, used extensively for the proper design of the LHC, were obtained by HERA, but are now a limiting factor in systematic uncertainties for LHC research. The LHeC aims to address this issue and improve the current status of PDFs.

In the study of deep inelastic scattering (DIS), two variables are particularly useful, the four-momentum transfer (Q^2) and the so called Bjorken scaling variable (x), defined respectively as [83]:

$$Q^2 \equiv (\vec{p}_e - \vec{p}'_e)^2 - (E_e - E'_e)^2, \tag{3.7}$$

$$x \equiv Q^2/(M^2 + Q^2 - m_h^2), \tag{3.8}$$

where $\vec{p}_e$ and $\vec{p}'_e$ are the incoming and outgoing electron momenta respectively with the corresponding energies E_e and E'_e, m_H is the rest mass and M is the invariant mass, defined by the relationship $Mc^2 = \sqrt{E^2 - (\vec{p}c)^2}$.

The LHeC aims to provide opportunities for electron-proton collisions at a new scale of energy and luminosity, but also in a new kinematic range in Q^2 and $1/x$ increasing both by factors of about 20, as shown in Fig. 3.12, allowing a better precision in the PDF measurements and the study of a new area in deep inelastic scattering.

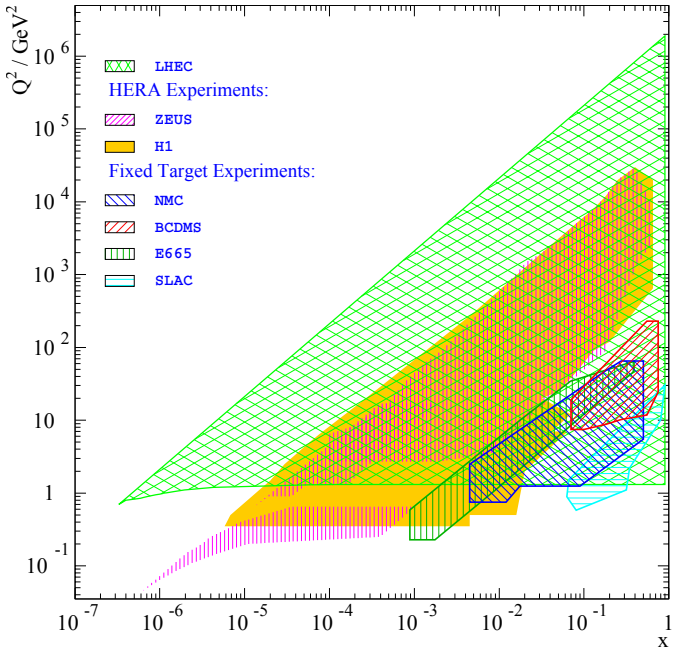

FIGURE 3.12: LHeC coverage in Q^2 and x in comparison with the previous deep inelastic scattering experiments [84].

The LHeC can also provide opportunities for further studies to complement the pp particle physics program. This includes Higgs studies, since with the absence of pile-up at high luminosity, the LHeC provides a better tool to study the Higgs particle coupling to the $b\bar{b}$, where b is the bottom quark, and other possible final states. The LHeC can also provide a strong reduction in the uncertainty of the strong coupling constant α_s, the most poorly constrained of the fundamental couplings [1].

3.6 The High-Luminosity LHC Experiment

The HL-LHC experiment is the first planned upgrade of the LHC, it aims to build on the success of the LHC and extend its discovery potential by increasing the luminosity by an order of magnitude.

This upgrade comprises different challenges such as the construction of 13 T superconducting dipoles, the development of compact and ultra precise superconductive cavities for precise beam rotation at the interaction point and high-temperature superconducting links with zero energy dissipation [85].

In this section the problem of increasing the luminosity by reducing the beam size at the interaction point in the ATLAS and CMS experiments is discussed.

3.6.1 Increasing the Luminosity

The luminosity and energy are key parameters to quantify the performance of any particle collider. In the case of accelerators dedicated to fundamental physics, where rare events with a small production cross section σ_p are studied, the luminosity measures the ability of the accelerator to produce the required number of interactions. An increase in the luminosity in the LHC is therefore desirable.

The peak luminosity of the present LHC is $10^{34}\text{cm}^{-2}\text{s}^{-1}$, providing an estimated integrated luminosity of 40 fb^{-1} per year, which means by 2020 the LHC is expected to achieve a total integrated luminosity between 200 and 300 fb^{-1}.

The European strategy for particle physics gave high priority to an increase in luminosity in the LHC to exploit fully the physics potential [86]. The HL-LHC project aims to increase the luminosity by an order of magnitude, to achieve values of $5 \times 10^{34}\text{cm}^{-2}\text{s}^{-1}$ with levelled luminosity, given that for the detection of events it is preferable for the luminosity to remain constant.

Referring back to the colliding beam luminosity in Eq. 1.129, it is clear that reducing β^* provides a mean to increase the luminosity. However, under the present layout and optics, a series of hard limits arise when reducing β^* beyond a certain value. In this section, these limitations and the proposals to overcome them will be explained.

3.6.2 New Insertions in IR1 and IR5

The upgrade plans for the HL-LHC project include the implementation of a new inner triplet of large-aperture quadrupoles. This inner triplet comprises three quadrupoles

(Q1, Q2 and Q3) to the left and right of IP1 and IP5 [87]. Table 3.2 specifies the changes to the magnets of the IR that will need to be made. This upgraded lattice configuration is called HLLHCV1.0 and will be referred to as such in future discussions.

Name	Type	HL-LHC Magnet characteristics	Changes with respect to LHC
Q1a/b, Q3a/b	Quadrupole	140 T/m, 150 mm aperture, 4.002 m length	instead of 70 mm aperture, 6.37 m length
Q2a/b	Quadrupole	140 T/m, 150 mm aperture, 6.792 m length	instead of 70 mm aperture, 5.50 m length
D1	Dipole	6.69 m long, 35 Tm, 160 mm aperture, cold magnets	instead of 6 warm modules
D2	Dipole	10 m, 35 Tm, 2-in-1 105 mm aperture moved 15 m towards the IP	instead of 80 mm aperture
Q4	Quadrupole	2-in-1 , 90 mm aperture, 160 T/m × 3.2 m	instead of 70 mm aperture
Q5	Quadrupole	2-in-1, 70 mm aperture, 160 T/m × 4.8 m moved 11 m towards the arc	instead of 55 mm aperture

TABLE 3.2: Changes to the IR magnets for the HLLHCV1.0 version of the HL-LHC [88].

Assuming the implementation of these magnets in the lattice a value of $\beta^* = 30$ cm is obtainable at IP1 and IP5 [89]. However, after this value, several limitations arise in terms of the strengths and apertures of the magnets. To achieve the luminosity goals a further minimization of the β^* is required. The limitations from the magnets are explained below.

Concerning the inner triplet, the aperture of these quadrupoles can in principle be increased with $1/g$, where g is the gradient of the quadrupole, so the maximum β function in the inner triplet is found to vary with the gradient as [89]:

$$\hat{\beta}_{\mathrm{IT}} \propto \frac{1}{\beta^* \sqrt{g}}. \tag{3.9}$$

Even when the inner triplet shows a flexibility in aperture, constraints in aperture do arise from the other quadrupoles in the IR (Q4-Q13). Furthermore the gradients of the quadrupoles Q6 and Q7 are pushed to very low and high gradients respectively. In terms of the chromaticity correction scheme, the lower β^* increases the β function in the location of the quadrupoles and, as a consequence, increases their contribution to the natural chromaticity. A third limitation then arises from the strength limits of the sextupoles in the chromaticity correction scheme.

To further reduce the β^* an option could be to make further changes in the lattice; such as changing the quadrupoles in the IR to increase the limits in aperture and/or gradients, or equipping the arcs with stronger sextupoles. However this would require extensive work and at a financial cost that can be avoided by finding an alternative solution.

3.6.3 Achromatic Telescopic Squeezing Scheme

The Achromatic Telescopic Squeezing (ATS) is a novel scheme proposed in the context of the HL-LHC [89]. This scheme allows the further reduction of β^* while controlling the chromatic aberrations, therefore providing a tool to overcome the limitations stated previously.

The scheme is implemented as follows. A standard matching procedure is performed in the interaction regions to obtain a value of β^* which is achievable in terms of the quadrupoles strengths and chromaticity correction efficiency, this β^* will be called the preesqueeze β^*. The value of β^* chosen at this step depends on the optics in use, which can provide flat ($\sigma_x > \sigma_y$ or vice versa) or round beams ($\sigma_x \sim \sigma_y$). In the case of round beams the presqueeze β^* is chosen to be 44 cm, which is within the limits. A further constraint is set at this point by matching the arc cells phase advance to exactly $\pi/2$.

For the following steps the quadrupoles of IR1 and IR5 are left unchanged. But now, the adjacent arcs to the low β insertions are allowed to contribute to the reduction of the β^*, that is arc 45 and arc 56 for IR5, and arc 81 and arc 12 for IR1.

This is possible given that the phase advance per cell of $\pi/2$ propagates any perturbation periodically creating β-beat waves in the arcs. If properly phased with the IP, these β-beat waves will reach their maximum at alternate sextupoles and the rate of increase of the β function at the sextupole locations will be proportional to the rate of decrease of β^* during the squeeze. This increase of the β function in the location of the sextupoles results in an increase of their efficiency to correct the chromatic aberrations produced by the high β functions in the inner triplet. A fundamental merit of the ATS is the boost of the chromatic correction scheme.

In this way, the ATS scheme overcomes the previous limitations not only to achieve a reduction of the β^* but also to provide the tools to correct the chromatic aberrations produced in the low β insertions.

The β functions along the HL-LHC ring with the implementation of the ATS are shown in Fig. 3.13. The high β functions at the location of the inner triplets is observed in IR1 and IR5, as well as the β-wave propagating in the arcs adjacent to those regions.

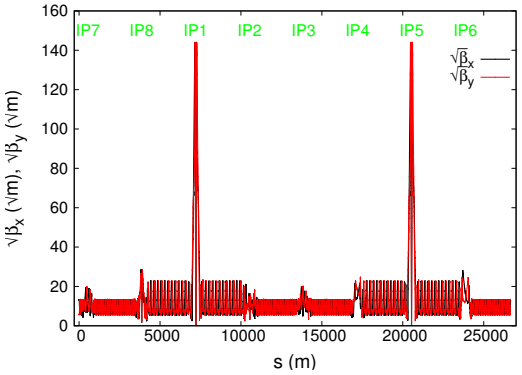

FIGURE 3.13: $\sqrt{\beta_x}$ and $\sqrt{\beta_y}$ along the HLLHCV1.0 lattice with round optics ($\beta^* =$ 15 cm in IP1 and IP5).

To perform the chromaticity correction the sextupole families are divided into different categories and are shown in Table 3.3.

Family	Sectors	Beam	Category
SF1, SD2	81, 45	B1	strong
SF1, SD2	12, 56	B1	strong
SF2, SD1	81, 45	B2	strong
SF2, SD1	12, 56	B2	strong
SF2, SD1	81, 45	B1	local
SF2, SD1	12, 56	B1	local
SF1, SD2	81, 45	B2	local
SF1, SD2	12, 56	B2	local
SF1, SF2, SD1, SD2	23, 34, 67, 78	B1, B2	weak

TABLE 3.3: Sextupole families regrouped in categories for the HLLHCV1.0 lattice configuration [90].

The families in the adjacent arcs to the low β insertions, that is arcs 81 and 12 for IP1 and arcs 45 and 56 for IP5 are divided into strong and weak families. As explained previously the ATS produces a β-beat wave in the arcs that peaks at the location of alternate sextupoles. These sextupoles correspond to the strong families. The sextupole families in the same arcs but not located at the peaks of the β-beating wave are called weak families. The local families correspond to sextupoles located in the arcs where there is no β beating (23, 34, 67 and 78).

Each of the the families in Table 3.3 performs a different task in the chromaticity correction [90]:

- **Strong:** These sextupoles correct the natural chromaticity induced by the new triplets and half of the natural chromaticity of the arc quadrupoles in the β-beating sectors (81, 12, 45, 56).
- **Local:** These sextupoles locally correct the remaining natural chromaticity of the arc quadrupoles in the β-beating sector.
- **Weak:** These sextupoles correct the natural chromaticity from the quadrupoles of the four arcs that do not participate in the squeeze (23, 34, 67, 78). They are used also for the global fine-tuning of the chromaticity.

The efficiency of the chromaticity correction provided by the ATS can be observed in the change of the tunes Q_x and Q_y for a momentum variation $\delta_p = \pm 0.001$, shown in Fig. 3.14. The Montague functions ($W_{x,y}$) along the HL-LHC ring are shown in Fig. 3.15. As shown in the figure Montague functions are confined in the adjacent arcs to IR1 and IR5 (in particular the value of the functions is close to zero in the collimation insertions IR3 and IR7), reaching their maximum at the location of the smallest betas in the arcs and negligible between the triplets [90].

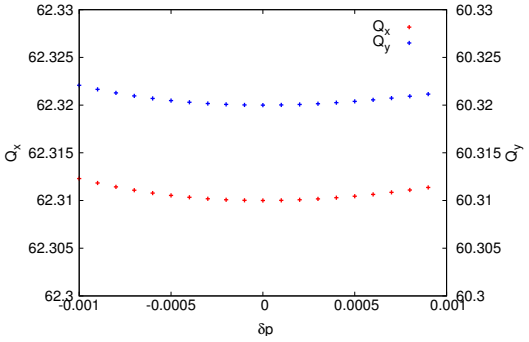

FIGURE 3.14: Change in the tunes Q1 and Q2 for beam 1 with collision optics (nominal values of $Q_x = 62.31$ and $Q_y = 60.32$) for the HL-LHC experiment with round beams ($\beta^* = 15$ cm at IP1 and IP5) for a maximum momentum deviation $\delta p = \pm 0.001$.

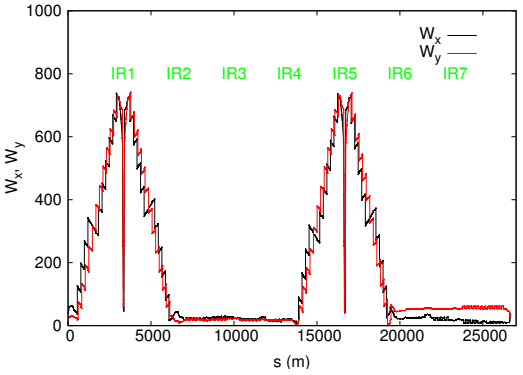

FIGURE 3.15: W_x and W_y functions along the HLLHCV1.0 lattice with a round optics ($\beta^* = 15$ cm at IP1 and IP5).

3.7 LHeC

The LHeC intends to make use of the infrastructure of the LHC to take electron-hadron collisions into the TeV regime, reaching 4 times the energy achieved by its predecessor HERA, and a 100 to 1000 times more luminosity. For this study the total power consumption of the lepton facility has been chosen to be below 100 MW. The LHeC would work alongside the HL-LHC and provide a complementary set of measurements.

Six dedicated LHeC workshops have been held between the years 2008 and 2015. The main focus of the workshop in 2012 was the presentation of the Conceptual Design Report (CDR) [1] which included a detailed description of the physics, the accelerator options and detector design comprising the LHeC project.

Two different options for the accelerator were initially proposed. The first option was based on a Ring-Ring (R-R) configuration, in which leptons are accelerated in a new electron synchrotron storage ring inside the LHC tunnel. The second option used a Linac-Ring (L-R) configuration featuring a 60 GeV Energy Recovery Linac (ERL) to accelerate the electron beam. Both designs have been found to be feasible but the R-R option installation would lead to significant disrupt of the LHC operation. Therefore the L-R option has been chosen as the design to follow.

The workshop in 2012 concluded with a mandate from CERN to carry out R&D on the following required systems:

- a superconducting RF system;
- superconducting magnet system;
- beamlines with large beam acceptance;
- the finalization of the ERL design for the LHeC, including optics design, beam dynamics studies and identification of potential performance limitations;
- the design and specification of an ERL Test Facility at CERN.

The overall design and the advances on these technical systems are summarised in this section.

3.7.1 Overview

The Linac-Ring option for LHeC was presented in the Conceptual Design Report [1] (CDR). This design proposes the construction of an Energy Recovery Linac (ERL) to accelerate the electrons up to 60 GeV and collide them with a proton beam at 7 TeV at IP2 of the LHC to achieve collisions with a luminosity of 10^{33} cm^{-2}s^{-1}. Motivated by the Higgs discovery the design also aims for a possible upgrade towards a luminosity of 10^{34} cm^{-2}s^{-1}. The parameters of both the CDR and the ultimate luminosity are shown in Table 3.4.

The overriding advantage of the ERL baseline design is that the energy of the spent beam, after collision, is recovered by returning the beam 180° out of phase through the same RF structure previously used for its acceleration (again with several recirculations). The energy recovery efficiency (η) reduces the electrical power required for RF power generation at a given beam current by a factor (1 - η). With an efficiency above 90% could be possible to reach the beam-current goal of 25 mA with less than 100 MW total electrical power.

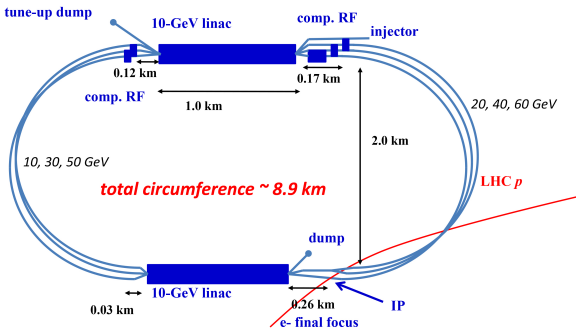

FIGURE 3.16: Schematic layout of the 60 GeV ERL option [1].

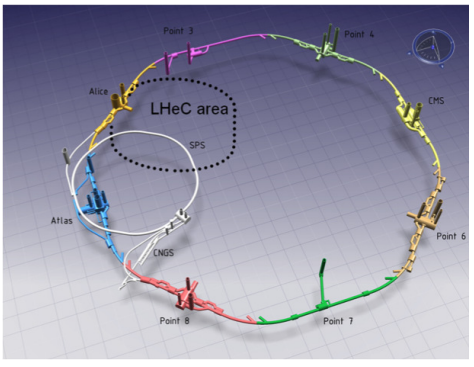

FIGURE 3.17: Integration of the ERL into the LHC configuration [91].

	CDR		Ultimate	
	p	**e**	**p**	**e**
Luminosity $[10^{33}\text{cm}^{-2}\text{s}^{-1}]$	1	1	10	10
Beam energy (GeV)	7000	60	7000	60
Normalized emittance $\gamma\epsilon_{x,y}$ (μm)	3.75	50	2.5	20
β^* (m)	0.1	0.12	0.05	0.10
Beam current (mA)	430(860)	6.4	1112	25
Bunch spacing (ns)	25 (50)	25 (50)	25	25

TABLE 3.4: Linac-Ring LHeC CDR and ultimate parameters [1].

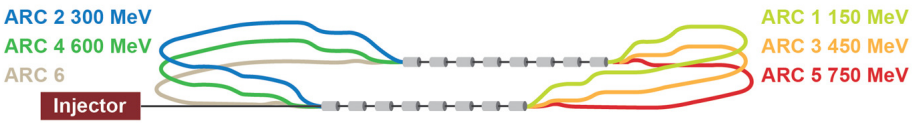

FIGURE 3.18: Complete configuration of the LHeC Test Facility (LTF) with 3 passes of 300 MeV per pass to deliver a 1 GeV electron beam energy [94].

A schematic view of the ERL is shown in Fig. 3.16. The integration of the ERL into the LHC configuration is shown in Fig. 3.17. The design of the ERL comprises four different sections: the linac, the arcs, the spreaders/combiners and the bypasses [92]. Each of the linacs is about 1 km long and provides an acceleration of 10 GeV. The electrons are injected at 500 MeV and then recirculate through the linacs three times to reach the ultimate collision energy of 60 GeV. The electrons are directed into the corresponding recirculating arcs with the aid of beam spreaders/recombiners located at the ends of each linac. The lattice cell provides a flexible momentum compaction factor that will allow a single combined design for the magnets [93]. The bypasses are built for the 20 GeV and 40 GeV beams to avoid the detector [92].

3.7.2 LHeC Test Facility

Several advances have been made towards the design of the LHeC Test Facility (LTF) [94]. Aside from various other technical and physics goals, this test facility will aim to investigate the multiturn high current demonstration, this includes the electron injector and return-arc magnets. It will also provide a test stand for superconducting RF cavity modules, as well as performing LHeC-related detector R&D. One possible application of the LTF beam is for generating controlled beam-induced quenches of superconducting magnets.

The LTF is designed to be constructed in stages. A first phase with beam recirculation would use just two 4-cavity cryomodules and single recirculation to reach 150 MeV. A second phase would feature multi-pass operation to reach 300 MeV (in 2 passes) or 450 MeV (in 3 passes). Adding two more cryomodules would boost the maximum achievable energy to 900 MeV. The final version is shown in Fig. 3.18.

Vertical spreaders/combiners separate the beams into as many as 3 vertically separated arcs, each of which is optimized for its nominal energy. The highest energy arc is adjusted in length to ensure that the beam arrives at the decelerating phase when next entering the linac.

The design comprises three different sections: the linac, the recirculation section and the merger. The lattice design, at present, is based on a Flexible Momentum Compaction (FMC) cell, that provides a minimization of the emittance blow-up when bending. A possible option for the magnets layout would consist of arcs with identical configurations in order to allow compact magnets to be stacked on top of each other in the same way as for the ERL [93].

A complete first-order layout for the arcs and linac-to-arc matching sections has been accomplished for the arcs on both sides of the ERL TF. The total beam path for a full three pass accelerating cycle is around 280 m. This would require $\sim$ 200 magnets.

3.7.3 RF Frequency

For the superconducting RF (SCRF) linac system a frequency of 801.58 MHz has been chosen as it is identical to the CERN SPS harmonic system and the LHC harmonic system presently under discussion. This is also one of the frequencies envisaged for the Future Circular Colliders study [95]. Strong synergy has been identified with the MESA project at Mainz University; help with the design and construction of the $\sim$ 802 MHz cavities and cryomodules will result from collaboration with JLAB; JLAB have relevant experience operating CEBAF and have also already contributed significantly to the lattice design.

3.7.4 Detector

The design of the baseline detector must not only satisfy the physics requirements but must also fit within the machine and interaction region constraints for running during phase 2 of the LHC. The detector should be able to run concurrently with other LHC proton-proton (pp) and proton-nucleon (pA) experiments to record the prospective ep and eA data. Furthermore, the detector must be flexible in design, able to accommodate different upgrade programs and must also be affordable [96].

Design

The present design of the detector has dimensions of 14 m $\times$ 9 m. Figure 3.19 shows a schematic view of the detector design where the following subsystems can be observed:

1. **Tracking**: The high acceptance compact tracking system is completely contained within the electromagnetic calorimeter (EMC) and uses pixel and strip silicon detectors.

2. **Calorimetry and magnets**: The main calorimeters of the system consist of the EMC and the baseline hadronic calorimeter (HAC) which uses steel absorber and scintillator sampling plates. The calorimeter structure provides support for inner detectors and return flux for the solenoid. Hadronic inserts in the forward and backward regions complement the main calorimeter system. The baseline magnet design is a small 3.5 T coil between the EMC and HAC, placing the solenoid and dipoles within the same cold vacuum vessel.

3. **Muon system**: The muon systems consist of 2-3 layers each with a double trigger layer and a further layer for measurements. In the current design the muon system does not provide an independent momentum measurement but rather the muon momentum is given in combination with the muon signal and the inner tracker.

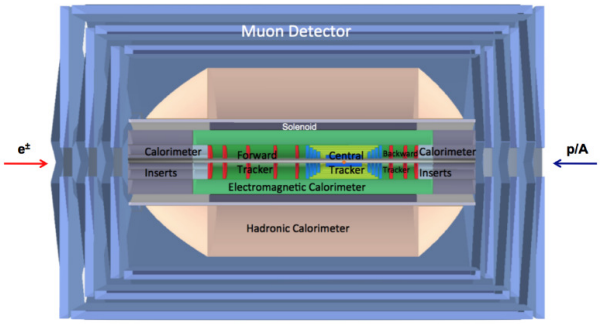

FIGURE 3.19: Schematic view of the detector design for the Linac-Ring LHeC option [1]. The figure indicates the location of the central, forward and backward trackers surrounded by the electromagnetic calorimeter and the muon detector on the outer layer.

3.8 Conclusions

In this chapter a summary of the history of the development of particle physics that led to the construction and development of high-energy accelerators has been given. At the end of this development so far is the current highest energy collider, the LHC. The recent discoveries made at the LHC have led to the exploration of future upgrades which may be implemented to improve the opportunities to discover new physics. Two upgrade plans for the LHC were presented: the HL-LHC, to increase the luminosity of hadron collisions, and the LHeC, to take electron-proton collisions into the TeV regime. The work in this thesis concerns the study of the effects of design features needed to achieve high luminosity collisions in both of these upgrades. Chapter 4 describes the integration of the LHeC IR into the HL-LHC lattice described in this chapter, using the tools developed in Chapter 1. Tracking studies of the proton beam with the LHeC lattice are presented in Chapter 5. The present chapter also discussed the challenges of achieving high-luminosity collisions through the use of stronger quadrupoles for the

inner triplet. Chapter 6 describes the effects of the fringe fields in the new inner triplet with studies based on the techniques described in Chapter 2.

Chapter 4

Flexibility of the LHeC Interaction Region Design

An optimised design for the interaction region (IR) is an important and challenging objective in the development of any particle collider. Challenges arise as a result of the beams being brought to a focus with small beam sizes and further restrictions from the detector layout also need to be considered to design the optics of the interaction region. In the case of the LHeC, the interaction region also needs to be integrated into the pre-existing LHC lattice which was designed for different ranges of energy and luminosity. Moreover, the LHeC is expected to work alongside the HL-LHC project to allow simultaneous proton-proton and electron-proton collisions. The complexity of designing the interaction region is hence greatly increased.

Given the challenges just listed, the goals of the LHeC interaction region design are to explore the flexibility of the integration of the LHeC interaction region into the HL-LHC lattice, and to find the best design that will achieve the greatest luminosity with the least impact on the accelerator in terms of the chromatic aberrations and synchrotron radiation.

This chapter first summarises the status of the LHeC IR presented in the LHeC CDR [1] (Section 4.1). The flexibility of this design is investigated to determine the limits on luminosity (Section 4.2). Then, the chromaticity correction scheme of the previous optical designs is considered and its limits explored (Section 4.3). Finally the synchrotron radiation is studied from the point of view of reducing the total synchrotron radiation power to avoid too large background in the detector (Section 4.4).

4.1 LHeC IR Implementation

To introduce the work done on the LHeC IR done in this thesis, this section summarises the previous studies carried out for the proton lattice design of the LHeC interaction region (LHeC IR). These studies comprise a first design for the layout and optics as presented in the LHeC CDR [1] and the implementation of the LHeC into the ATS, previously implemented in the HL-LHC (described in Section 3.6.3).

As described in Section 3.7.1, the LHeC Linac-Ring option proposed the electron beam to collide with one of the proton beams of the LHC in IR2, where ion-ion collisions currently take place in the ALICE experiment [75]. Therefore, the design of the LHeC IR aims to focus the counter-clockwise proton beam 2 and collide it with the electron beam while the clockwise proton beam 1 bypasses the interaction, keeping to a minimum the changes to the present corresponding interaction region (IR2). A configuration representing the aim of the design is shown in Fig. 4.1 where electrons are injected nearly parallel to the LHC beam 1 and are then collided head-on with beam 2.

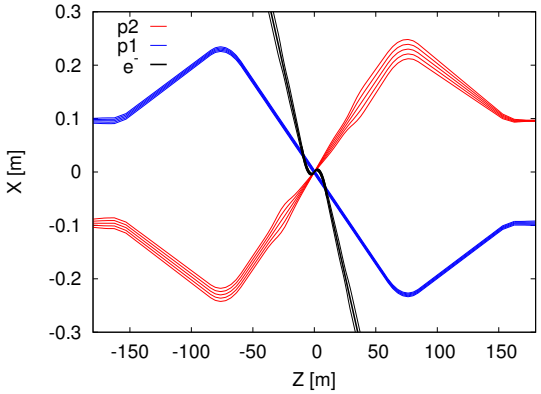

FIGURE 4.1: Schematic representation of the aim of the design of the LHeC IR. Proton beam 2 (red) is focused and collides head-on with the electron beam (black) while proton beam 1 bypasses the interaction. Envelopes with 5σ and 10σ are shown.

There were several challenges during the initial stages of the design. First, in order to achieve the luminosity goals, and with constraints regarding the electron beam current, it is essential to achieve the smallest proton beam size possible. Secondly, to avoid a reduction in luminosity due to a crossing angle between the beams, the design should aim for head-on collisions by means of dipoles around the IP: this presents challenges in terms of the synchrotron radiation produced when bending the electron beam. Finally, since the LHeC aims to work alongside the HL-LHC experiment producing proton-proton collisions in other interaction points, the second proton beam must be accommodated, and has to pass through the same interaction region [97].

The LHeC CDR presented a complete first conceptual design of the Linac-Ring LHeC IR, collecting together studies previously conducted [97, 98]. The merits of the IR presented in the CDR are a very low β^* of 0.1 m achieved by replacing the inner triplet (described in Section 3.4.3) and locating it at a new distance L^* of 10 m from the interaction point (IP). This new distance was chosen to allow enough space for the detector, but keeping the inner triplet as close as possible to minimize chromatic aberrations and avoid aperture limitations in the inner triplet while reducing β^*. The following section describes how this was achieved in terms of the optics and layout of the IR.

4.1.1 Layout and Optics

The nominal design requires the colliding beam triplet to start at a distance of 10 m from the IP. The magnet design for the first two quadrupoles is given in [1] and is illustrated in Fig. 4.2. Since only proton beam 2 needs to be focused, the design of both of these quadrupoles includes a field-free aperture for proton beam 1 and the electron beam to pass through. With the inner triplet located at an L^* of 10 m, bending the electron beam to the field-free aperture of the full-aperture quadrupole (left side of Fig. 4.2) would produce an excessive amount of synchrotron radiation power, so the design contemplates using a half-aperture quadrupole (right side of Fig. 4.2) which would allow a smaller spacing between the normal field and field-free apertures, reducing the bending of the electron beam and hence the synchrotron radiation produced.

The Nb_3Sn superconductor has been chosen for the proton inner triplet since it allows the largest gradient for a given aperture. However, this technology is not yet fully validated for use in an accelerator, but relies heavily on a magnet R&D plan [99]. If this technology proves not to be feasible in the timescale of the LHeC a new design of the IR may have to be investigated. Table 4.1 shows the parameters of the first two quadrupoles (Q1 and Q2) of the proton inner triplet for this initial design [1].

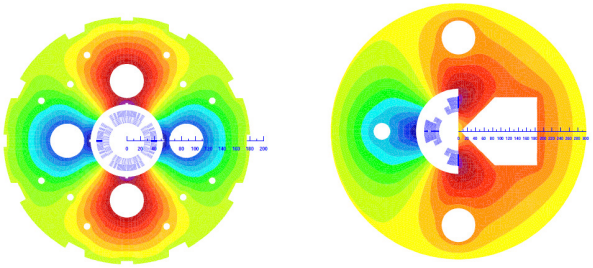

FIGURE 4.2: Design of the full-aperture quadrupole Q2 (left) and half-aperture quadrupole Q1 (right).

Name	Gradient (T/m)	Length (m)	Radius of aperture (mm)	p1-p2 Separation (mm)	"Radius" of field-free aperture (mm)
Q1	187	9	22	63	40
Q2	308	9	30	87	26
Q3	185	9	32	-	-

TABLE 4.1: Parameters of the design of the quadrupoles Q1, Q2 and Q3 of the proton inner triplet for the LHeC IR. [1].

A crossing angle of 6.8 mrad between the proton beams allows enough separation for each proton beam to go through its corresponding aperture in Q1 at $L^* = 10$ m. The polarity and strengths of the separation and recombination dipoles of the proton beams (D1 and D2) have to be changed to allow this crossing angle. The new D1 has one aperture per beam and it is stronger than the nominal LHC dipole by a factor of 3.43. The new D2 is stronger than the nominal LHC dipole by a factor of 1.21. Both

dipoles require a field of about 6 T. The lengths of the D1 and D2 dipoles have been left unchanged at 9 m. However, the final IR design will need to incorporate an escape line for neutral particles coming from the IP; this will probably make it necessary to split D1 into two parts separated by tens of meters.

Electron bending dipoles around the interaction point are envisaged to make the electrons collide head-on with proton beam 2 and to safely extract the electron beam. The required field of these dipoles is determined by the distance to the inner triplet (L^*) and the minimum separation of the electron and the focused beam p2 at the first quadrupole (Q1). A 0.3 T field extending over 9 m allows for a beam separation of 0.075 m at the entry of Q1. The electron beam will radiate 49 kW in the IR dipoles. A sketch of the 3 beams, the synchrotron radiation fan and the proton triplets is shown in Fig. 4.3.

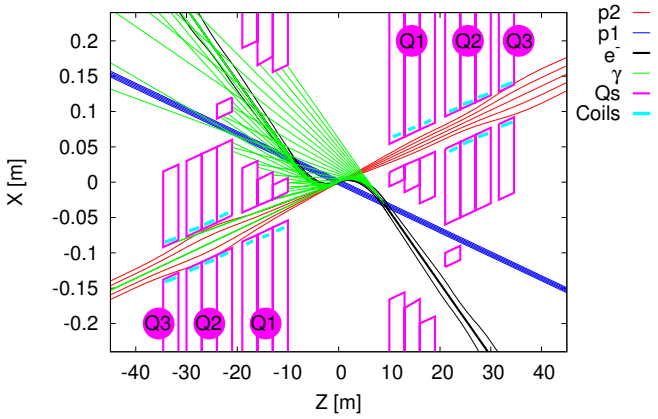

FIGURE 4.3: Focused proton beam 2 (red) colliding with electron beam (black) while unfocused proton beam 1 (blue) bypasses the interaction. Each proton and electron beam passes through its corresponding aperture in the inner triplet, shown in pink. The synchrotron radiation fan generated by the electron beam is shown in green [97].

It was initially hoped that a compact Nb_3Sn triplet with $L^* = 10$ m would allow for a conventional chromaticity correction using the arc sextupoles. However, it was found that after matching this triplet to the LHC and correcting the linear chromaticity, the chromatic β-beating with a momentum deviation $dp/p = 0.001$ was about 100%. This is intolerable regarding collimation and machine protection issues [1].

The challenge at this point relies on achieving an optics that would not only achieve a low β^* in the LHeC IR while keeping the HL-LHC insertions undisturbed, but would also provide a dedicated chromaticity correction scheme.

4.1.2 Implementation of the LHeC into the ATS

Following the experience whilst developing the HL-LHC project described in Section 3.6.3, the ATS scheme provides an optical tool for boosting the strengths of the chromatic correction. A proposal has been made to integrate the LHeC IR into the HL-LHC lattice [100]. The implementation of the LHeC into the ATS presents an extra challenge, as arc 23 is shared by both IR1 and IR2, and the ATS, as explained in Section 3.6.3,

makes use of the adjacent arcs of the low-β insertions for the telescopic squeeze. This further difficulty adds a constraint to be taken into account to achieve the reduction of the β^* in the three interaction points.

A first integration of the LHeC IR into the HL-LHC lattice using the ATS scheme for the nominal case with $\beta^* = 10$ cm and $L^* = 10$ m was presented in [101]. The proton optics in the LHeC IR with the new triplets was designed to extend the ATS scheme without modification of the HL-LHC optics [102] using the HLLHCV1.0 lattice configuration (described in Section 3.6.2) and round proton beams ($\beta^* = 15$ cm in IP1 and IP5). However, the chromaticity correction still needed to be addressed as well as the exploration of the flexibility on the β^* and the L^* .

In this procedure the arc cells in sector 23 are exactly adjusted to a phase advance of $\pi/2$. Then, the ATS matching conditions for proton beam 2 are imposed for the left and right phase advance of IR2. Following a standard matching procedure in MADX (further explained in Section 4.2.2) the quadrupoles of the IR2 are used to provide a presqueezed β^* of 30 cm. This value of β^* is achievable in terms of the quadrupole strengths and apertures, and within the limits of the conventional chromaticity correction scheme.

Transition from the presqueezed to the collision optics is performed by a telescopic squeeze using the quadrupoles in IR8, IR3, IR4 and IR6 with no variation of the quadrupole strengths in IR1, IR2 and IR5 at this stage. During the transition the phase advance in the arc cells matched to $\pi/2$ propagates an error in arc 23 in the same way as in the HL-LHC IR's adjacent arcs. β-waves in the sectors 45, 56, 81, 12, and 23 produce further reductions in β^* from 30 cm to 10 cm at IP2 and from 44 cm to 15 cm at IP1 and IP5. The $\sqrt{\beta}$ function along the ring with the HL-LHC and the LHeC optics is shown in Fig. 4.4. The peaks of the β functions are observed in the inner triplet of IR1, IR2 and IR5. The β-wave propagating in arcs 45, 56, 81, 12 and 23 can also be seen.

The β function is shown along IR2 in Figs. 4.5 and 4.6 for beam 1 and beam 2 respectively. The difference between the unfocused beam 1 and focused beam 2 is clear: in the latter the β function peaks in the inner triplet and reaches a minimum at the IP. For beam 1 this is not the case since the focusing is no longer necessary.

4.2 Flexibility of the Design

The extension of the LHeC into the ATS, described in last section, helped to achieve a nominal design for the LHeC lattice that provides a solution to obtain a β^* of 10 cm in the LHeC IP for Proton Beam 2 with the aid of a new inner triplet at $L^* = 10$ m. For these studies Proton Beam 2 has been chosen, but the final beam will depend on the orientation of the electron beam. In this section, the flexibility of the design is explored. This flexibility is studied via two methods: the first method looks at the feasibility of increasing L^* to minimize the synchrotron radiation power from the electron beam

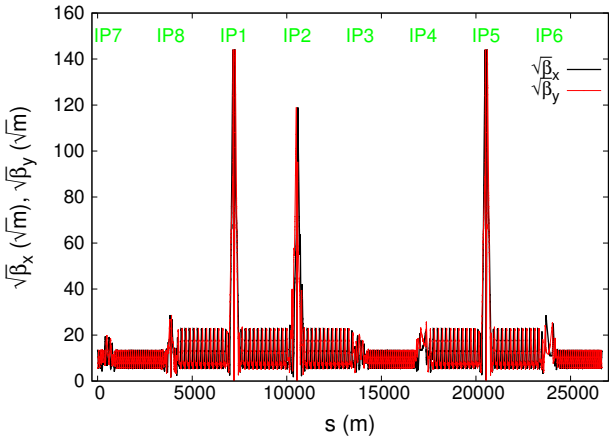

FIGURE 4.4: $\sqrt{\beta_x}$ (black) and $\sqrt{\beta_y}$ (red) functions for beam 2 for the LHeC nominal lattice with $\beta^* = 10$ cm and $L^* = 10$ m in IR2, and $\beta^* = 15$cm in IR1 and IR5. The β functions peak at the locations of the inner triplets in IR1, IR2 and IR5 and the β-beating wave is observable in arcs 81, 12, 23, 45 and 56.

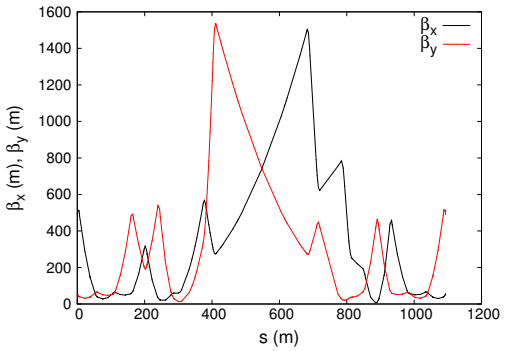

FIGURE 4.5: Horizontal (black) and vertical (red) β function along IR2 for the unfocused beam 1 for the LHeC nominal lattice ($L^* =$ 10 m and $\beta^* = 10$ cm in IR2).

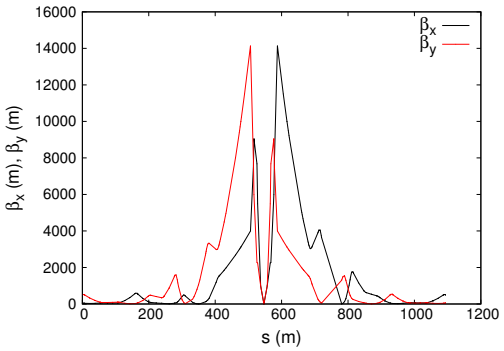

FIGURE 4.6: Horizontal (black) and vertical (red) β function along IR2 for the focused beam 2 for the LHeC nominal lattice ($L^* = 10$ m and $\beta^* = 10$ cm in IR2).

while the second investigates the minimization of β^* to obtain an upper limit on the luminosity.

Exploring different options for L^* and β^* is of great interest, not only because of the benefits in terms of increased luminosity and reduced synchrotron radiation power, but also because (given the tight constraints in the IR, both from the accelerator and the detectors) we want as much flexibility as possible in the parameters.

Before introducing the lattice configurations found with different L^* and β^* (Sections 4.2.3 and 4.2.4 respectively) an overview of the LHeC IR layout is given in Section 4.2.1 and the matching procedures and techniques to obtain solutions are described in Section 4.2.2.

4.2.1 LHeC IR Layout Overview

A general description of the IRs in the LHC was given in Section 3.4.3. This section presents a more detailed description of IR2 with the implementation of the new inner

triplet described in section 4.1.1. This modified version of IR2 will be named LHeC IR in future references.

Table 4.2 lists the names of each quadrupole in the LHeC IR along with the gradient name, which is the variable assigned to the strength of each quadrupole. The gradient names are a simplified version of the actual names given in the LHC optics files and will be used to refer to the quadrupoles in future discussions. Most of the quadrupoles have their own power supply so their gradients can be varied independently. The inner triplet has an antisymmetric structure so the gradients in the inner triplet quadrupoles are named accordingly. Some of the quadrupoles have different sections but the same gradients, in this table only the sector closest to the marker s.ds.l2.b2 (indicated in Table 4.2) is given. This table also gives the locations of some markers that will be used in descriptions and explanations of the matching procedures.

Element	**Type**	**Gradient name**
s.ds.l2.b2	Marker	NA
MQT.13L2.B2	Quadrupole	k13L
MQT.12L2.B2	Quadrupole	k12L
MQ.11L2.B2	Quadrupole	k11L
MQML.10L2.B2	Quadrupole	k10L
MQMC.9L2.B2	Quadrupole	k9L
MQML.8L2.B2	Quadrupole	k8L
e.ds.l2.b2	Marker	NA
MQM.B7L2.B2	Quadrupole	k7L
MQML.6L2.B2	Quadrupole	k6L
MQY.B5L2.B2	Quadrupole	k5L
MQY.B4L2.B2	Quadrupole	k4L
MQZ3.L2	Quadrupole	k3
MQZ2.L2	Quadrupole	-k2
MQZ1.L2	Quadrupole	k1
IP2	Marker	NA
MQZ1.R2	Quadrupole	-k1
MQZ2.R2	Quadrupole	k2
MQZ3.R2	Quadrupole	-k3
MQY.A4R2.B2	Quadrupole	k4R
MQM.A5R2.B2	Quadrupole	k5R
MQML.6R2.B2	Quadrupole	k6R
MQM.A7R2.B2	Quadrupole	k7R
s.ds.r2.b2	Marker	NA
MQML.8R2.B2	Quadrupole	k8R
MQMC.9R2.B2	Quadrupole	k9R
MQML.10R2.B2	Quadrupole	k10R
MQ.11R2.B	Quadrupole	k11R
MQT.12R2.B2	Quadrupole	k12R
MQT.13R2.B2	Quadrupole	k13R
e.ds.r2.b2	Marker	NA

TABLE 4.2: Quadrupoles and markers as arranged in IR2 from left to right. The recombination dipoles D1 and D2 are not shown in this table.

A schematic view of the layout of the LHeC IR is given in Fig. 4.7.

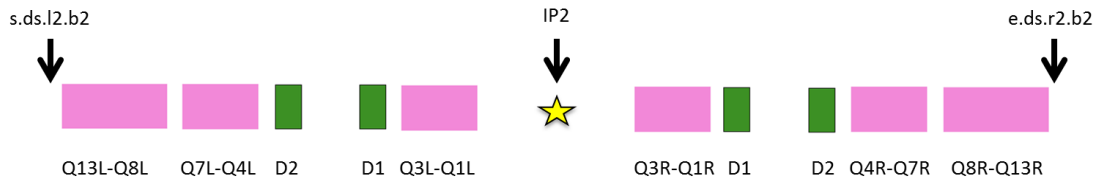

FIGURE 4.7: Schematic view of the LHeC IR showing the arrangements of quadrupoles, dipoles and markers around the IP: the inner triplet (Q1-Q3), the separation/recombination dipoles (D1 and D2), the matching section (Q4-Q7) and the dispersion section (Q8-Q13). A simplified name is given for the names of the quadrupoles.

4.2.2 Minimization Procedures

The values of the lattice functions at either end of IR2 are determined by the HL-LHC optics, which give a stable orbit outside the LHeC IR and provide the conditions to create the β-wave in arcs 12 and 23. Keeping these values at the ends of IR2 fixed, the gradients of the quadrupoles in IR2 can be used as variables to adjust to the new conditions that depend on the problem at hand.

In order to find solutions for a set of specified constraints, a matching procedure in MADX was used. A matching procedure in MADX requires the sequence of beamline components to be declared, followed by the initial conditions for transfer line matching, the constraints, the parameters to be varied and the method to be used. The constraints can be specified with a corresponding weight, the larger the weight, the more important a constraint becomes. Given a set of constraints and weights, MADX constructs a penalty function which is the sum of the squares of all residuals (i.e. difference between present and target values for the constraint parameters), each multiplied by the specified weight.

For the minimization procedure required in this case, either to increase L^* or reduce β^*, the sequence is the beamline along the LHeC IR and the initial conditions are the optical parameters at s.ds.l2.b2 for the solution with $L^* = 10$ m and $\beta^* = 10$ cm. The variables are the 26 quadrupole gradients in IR2 (23 independent variables). The constraints are given in Table 4.3. The minimization methods available in MADX will be described below.

To find solutions for different L^* and fixed β^*, the inner triplet was first located at the new desired distance, while the value of β^* in Table 4.3 was kept at 10 cm. To find solutions with different values of β^* and a fixed L^*, the corresponding desired value of β^* was added to the constraints in Table 4.3, while L^* was kept at 10 m.

Both cases then present a matching problem that requires the variation of 26 quadrupoles in the IR (reduced to 23 as a result of the antisymmetric structure of the inner triplet) to meet 14 constraints. Since there are more variables than constraints, there is no unique solution to this problem. However, obtaining a solution can still be difficult given the large number of elements involved.

Parameter	Value (m)	Location
$\beta_{x,y}$	0.05-0.1	IP2
$\alpha_{x,y}$	0	IP2
D_x	0	IP2
D_{px}	0	IP2
$\beta_{x,y}$	491.86/55.89	e.ds.r2.b2
$\alpha_{x,y}$	7.06/-2.19	e.ds.r2.b2
D_x	2.14	e.ds.r2.b2
D_{px}	-0.03	e.ds.r2.b2
μ_x	2.95	from s.ds.l2.b2 to e.ds.r2.b2
μ_y	2.7	from s.ds.l2.b2 to e.ds.r2.b2

TABLE 4.3: Constraints for the matching routine in MADX to find a stable optical solution for different L^* with a β^* fixed at 10 cm. The parameters $\beta_{x,y}$, $\alpha_{x,y}$, D_x and D_{px} at e.ds.r2.b2 correspond to the values of the optical parameters at such position for the nominal case with $L^* = 10$ m and $\beta^* = 10$ cm.

In order to solve this problem different techniques were applied. First, a combination of different matching procedures was used. Second, the quadrupoles in the IR which have the most impact on the optical parameters were identified. And finally, the LHeC IR was divided into different sections, with matching procedures then applied in each section with a fewer number of variables and constraints. A further description of these methods is given in the following sections.

Combination of methods

The first technique to solve the problem with a high number of variables and constraints is to use a combination of minimization methods available in MADX. A short description of each method is given below:

- **LMDIF**
  This method minimizes the sum of the squares of the differences (residuals) between the specified and current parameter values, using numerical derivatives. It has the advantage of being the fastest minimization method available in MADX, but is limited to problems where the number of variables is not greater than the number of constraints [103].

- **MIGRAD**
  The MIGRAD command minimizes the penalty function using the numerical derivatives of the sums of the squares of the differences between the specified and current parameter values [104]. It uses a minimization subroutine based on a variable metric method [105]. This method is particularly fast near a minimum or in a "nearly-quadratic" region but it can be slow when the function is badly behaved [106].

- **SIMPLEX**
  This method uses a minimization subroutine that implements the Simplex method

developed by Nelder and Mead [107]. The method is reasonably fast when far from a minimum and may also be used to converge to the exact minimum [106].

- **JACOBIAN**
  This method was developed to solve problems for an arbitrary number of variables and constraints. It proves to be particularly useful when the variables are already close to the solution [103]. The Jacobian method is based on the Newton-Raphson method, it minimizes the penalty function by calculating the Jacobian of the function relating variables and constraints, and solving the linear problem.

Using a combination of the previous methods proved to be useful when dealing with problems with a small number of variables and constraints. However, using this technique we failed to achieve a solution for a larger number of variables and constraints. The use of the two following techniques were found necessary to obtain a solution.

Optical sensitivity to quadrupole strengths

In the hopes of reducing the number of variables used in the matching routines, a study was made to find the quadrupoles that have the greatest impact on the optical parameters. To determine the impact, the gradients of the quadrupoles were changed in the range $\pm 10\%$ of their original values and the resulting change in the optical parameters at the interaction point was recorded. In this case only the quadrupoles on the left of the interaction point were changed (k1L-k13L in Table 4.2).

Fig. 4.8 shows the change in β^* when changing the quadrupoles with gradients k1L-k13L. It is clear from the figure that β^* is mostly sensitive to the inner triplet, with quadrupoles with gradients k4L-k13L having little impact on β^*. Removing the inner triplet from the results it is possible to see the impact of the remaining quadrupoles, as shown in Fig. 4.9. Results show that the quadrupoles with the greatest impact on the β^* are the inner triplet, followed by the quadrupoles with gradients k4L, k6L and k10L.

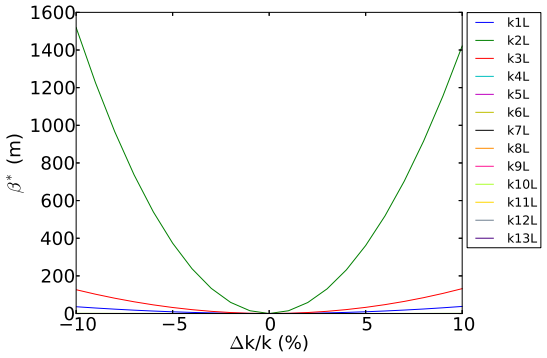

FIGURE 4.8: Change in β^* when the gradients of the quadrupoles to the left of the IP (MQZ1.B2 to MQT.13L2.B2 of Table 4.2) are changed in the range $-0.1 < \Delta k/k < 0.1$. The quadrupoles are represented by their gradients (k1L-k13L). Even though all the quadrupoles are plotted in the figure, only the effect of the inner triplet is visible.

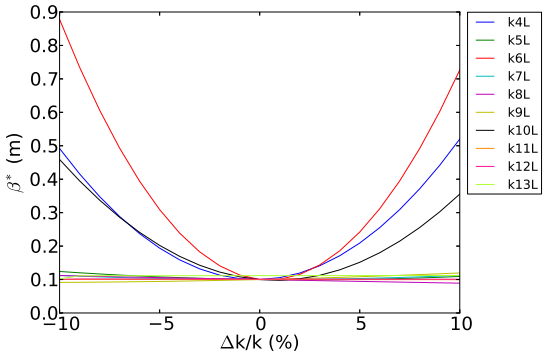

FIGURE 4.9: Change in β^* when the gradients of the quadrupoles to the left of the IP excluding the inner triplet (MQY.B4L2.B2 to MQT.13L2.B2 of Table 4.2) are changed in the range $-0.1 < \Delta k/k < 0.1$. The quadrupoles are represented by their gradients (k4L-k13L).

The same procedure was carried out for the α function. Fig. 4.10 shows the sensitivity of α^* to a change in the quadrupoles with gradients k1L-13L. Once again, the inner triplet shows the biggest sensitivity. Fig. 4.11 shows the results for the remaining quadrupoles. Both figures indicate that, as was the case for β^*, the quadrupoles with the greatest impact on α^* are the inner triplet, followed by the k4L, k6L, and k10L quadrupoles.

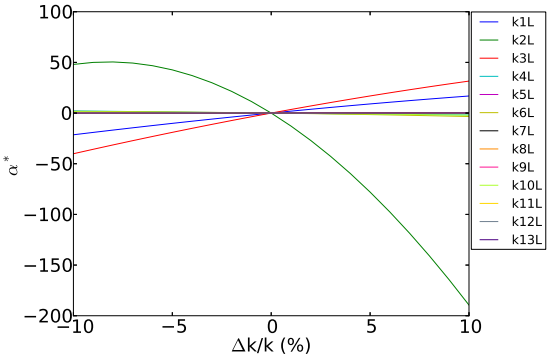

FIGURE 4.10: Change in α^* when the gradients of the quadrupoles to the left of the IP (MQZ1.B2 to MQT.13L2.B2 of Table 4.2) are changed in the range $-0.1 < \Delta k/k < 0.1$. The quadrupoles are represented by their gradients (k1L-k13L). Even though all the quadrupoles are plotted in the figure, only the effect of the inner triplet is visible.

The study was also performed for the dispersion at the interaction point (D^*). Fig. 4.12 shows that the dispersion at the interaction point is less sensitive to the change in the gradients of the quadrupoles and, unlike the case for β^* and α^*, the inner triplet quadrupoles do not have a greater impact than the other quadrupoles, since for this case the dispersion seems most sensitive to k10L and k6L.

The general study shows that the inner triplet along with the quadrupoles k4L, k6L and k10L have the biggest impact on the optical functions. This was taken into account when performing the matching to minimize the number of variables used.

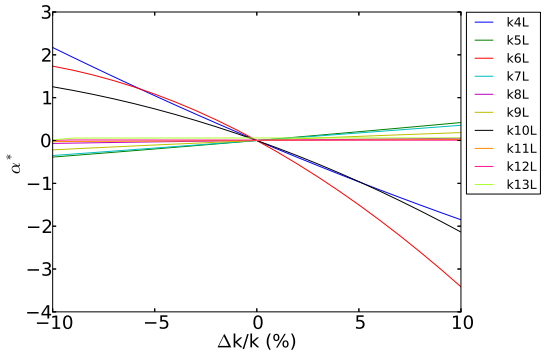

FIGURE 4.11: Change in α^* when the gradients of the quadrupoles to the left of the IP excluding the inner triplet (MQY.B4L2.B2 to MQT.13L2.B2 of Table 4.2) are changed in the range $-0.1 < \Delta k/k < 0.1$. The quadrupoles are represented by their gradients (k4L-k13L).

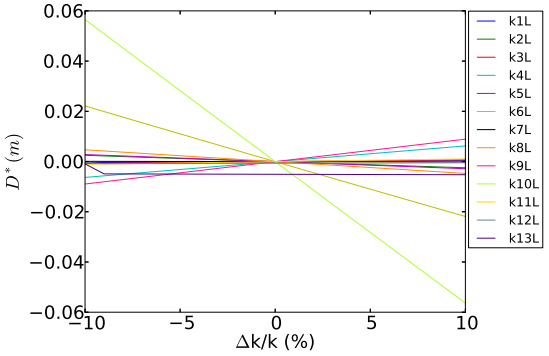

FIGURE 4.12: Change in D^* when the gradients of the quadrupoles to the left of the IP (MQZ1.B2 to MQT.13L2.B2 of Table 4.2) are changed in the range $-0.1 < \Delta k/k < 0.1$. The quadrupoles are represented by their gradients (k1L-k13L).

A matching procedure was tested using only the 13 quadrupoles with the greatest impact on the optical parameters, so that the number of variables was equal to the number of constraints. It was hoped that by setting up the matching procedure in this way, the matching routine would converge to a solution more quickly. However, although the final penalty function of the matching procedure was smaller than when using the whole range of quadrupoles, the result did not converge. A possible development of this idea is to use singular value decomposition of the response matrix, to study the effects of the combination of quadrupoles rather than the effects of individual quadrupoles. This approach however was not used in this study. Instead, in order to find solutions, the third and final technique, explained next, was implemented.

Matching by parts

The case described before, in which 23 variables were used to fix 13 constraints, proved to be ineffective with a direct minimization routine in MADX. To overcome this problem, a technique was implemented to perform the matching procedures in "blocks", such that

each block contains a small number of constraints and variables. This technique proved to be the most important in order to reach a solution. The matching problem was broken down into the following steps:

1. Right part of the interaction region, from IP2 to s.ds.r2.b2.
Initial values: $\beta_{x,y}$, $\alpha_{x,y}$, D_x and D_{px} at IP2.
Constraints: $\beta_{x,y}$, $\alpha_{x,y}$, D_x and D_{px} at s.ds.r2.b2.
Variables: quadrupoles from KQZ1.R2 to KQ6.R2B2.

2. Right part of the interaction region, from s.ds.r2.b2 to e.ds.r2.b2.
Initial values: $\beta_{x,y}$, $\alpha_{x,y}$, D_x and D_{px} at s.ds.r2.b2.
Constraints: $\beta_{x,y}$, $\alpha_{x,y}$, D_x and D_{px} at e.ds.r2.b2.
Variables: quadrupoles from KQ7.R2B2 to KQT13.R2B2.

3. Right part of the interaction region, from IP2 to e.ds.r2.b2.
Initial values: $\beta_{x,y}$, $\alpha_{x,y}$, D_x and D_{px} at IP2.
Constraints: $\beta_{x,y}$, $\alpha_{x,y}$, D_x and D_{px} at e.ds.r2.b2.
Variables: quadrupoles from KQZ1.R2 to KQT13.R2B2.

4. Left part of the interaction region, from e.ds.l2.b2 to IP2.
Initial values: $\beta_{x,y}$, $\alpha_{x,y}$, D_x and D_{px} at e.ds.l2.b2.
Constraints: $\beta_{x,y}$, $\alpha_{x,y}$, D_x and D_{px} at IP2.
Variables: quadrupoles from KQ4.L2b2 to KQ6.L2B2.

5. Left part of the interaction region, from s.ds.l2.b2 to e.ds.l2.b2.
Initial values: $\beta_{x,y}$, $\alpha_{x,y}$, D_x and D_{px} at s.ds.l2.b2.
Constraints: $\beta_{x,y}$, $\alpha_{x,y}$, D_x and D_{px} at e.ds.l2.b2.
Variables: quadrupoles from KQ7.L2b2 to KQ13.L2B2.

6. Left part of the interaction region, from s.ds.l2.b2 to IP2.
Initial values: $\beta_{x,y}$, $\alpha_{x,y}$, D_x and D_{px} at s.ds.l2.b2.
Constraints: $\beta_{x,y}$, $\alpha_{x,y}$, D_x and D_{px} at IP2.
Variables: quadrupoles from KQ4.L2b2 to KQ13.L2B2.

7. All interaction region, from s.ds.l2.b2 to e.ds.r2.b2.
Initial values: $\beta_{x,y}$, $\alpha_{x,y}$, D_x and D_{px} at s.ds.l2.b2.
Constraints: $\beta_{x,y}$, $\alpha_{x,y}$, D_x and D_{px} at e.ds.r2.b2.
Variables: quadrupoles KQ4.L2B2 to KQ13.L2B2 and KQ4.R2B2 to KQ13.R2B2.

This last method proved to be very useful in order to find a solution. Almost all the solutions for different L^* and β^*, presented in the following sections, were found by a combination of the matching by parts and by using different minimization procedures

(first method), but also providing appropriate initial values for the gradients of the quadrupoles. In the case of the iterative process it was useful to use as an initial estimate the values of the quadrupoles from the previously solved case. For example, the gradients of the quadrupoles for the case with a given L^* were used as an initial guess for the case with L^* increased by 1 m.

Fig. 4.13 illustrates this effect. The gradients of each of the 23 independent quadrupoles of IR2 are plotted against the value of L^* of the corresponding lattice. For most cases, the gradients of the quadrupoles varied slowly when increasing L^*. For some lattice configurations, such as the case with $L^* = 15$ m or the case with $L^* = 20$ m, the values of some of the quadrupoles gradients have a significant difference with respect to the previous cases. These cases coincide with the ones for which taking the initial solution of the previous case as the initial values for the new case did not work and other different techniques had to be implemented, such as using only certain quadrupoles, chosen with the second technique, or by using different initial values for the quadrupoles.

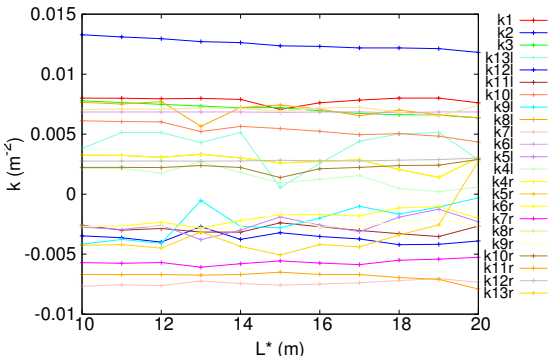

FIGURE 4.13: Strength of the 23 quadrupoles in the IR2 vs the value of L^* of the lattice it was computed for. All lattices have a β^* of 10 cm.

4.2.3 Increasing L^*

Following the techniques described in Section 4.2.2 stable solutions were found for the optical designs of the LHeC IR with L^* in the range from 10 m to 20 m (in 1 m steps) and β^* fixed at 10 cm.

There are several benefits of increasing L^*. The first and most important is the reduction of the synchrotron radiation power produced by the electron beam, since the bending required to direct the electron beam from the IP to the field-free aperture of the inner triplet reduces as L^* grows larger. This will be further discussed in Section 4.4.

Benefits also arise in terms of lattice design. As explained in Section 3.7.4, the detector is 14 m long: a larger L^* relaxes the space constraints. Locating the inner triplet inside the tunnel is preferable to avoid creating an extra system to support the quadrupoles. However the tunnel, and the current location of the inner triplet in IR2, is located at $L^* = 23$ m and optical solutions with the previous techniques were not achieved for $L^* > 20$ m.

Increasing L^* can also bring benefits in terms of magnet design. As explained in Section 4.1.1, a half-aperture quadrupole design (right side of Fig. 4.2) has been chosen for Q1 to allow a separation between the normal aperture and the field-free aperture at the entrance of this quadrupole to accommodate the beams, as illustrated in Fig. 4.14. Difficulties arise in the half-aperture quadrupole design since stray fields are present in the field-free aperture [108] increasing the difficulty to match the electron beam [109]. The cases with $L^* > 14$ m allow enough beam separation to use normal full-aperture quadrupoles (left side of Fig. 4.2) without the need to increase the strength of the dipoles. In full-aperture quadrupoles stray fields are not present in the field-free aperture and are therefore a preferable option.

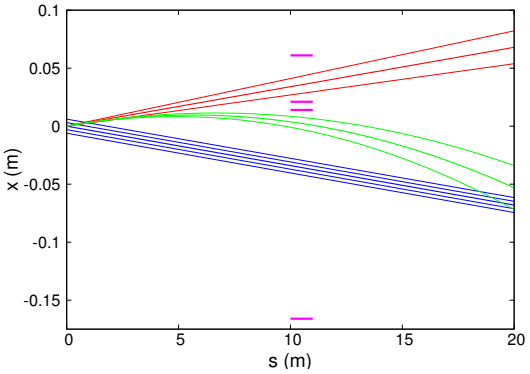

FIGURE 4.14: Proton beam 1 (blue), proton beam 2 (red) and electron beam (green) passing through the different apertures at the entrance of Q1. The apertures of the quadrupole are illustrated with pink horizontal lines with the top pair representing the normal field aperture and the bottom pair the field-free aperture.

Some drawbacks arise when increasing L^*. Recalling the result found in Eq. 1.123 the β function in the drift space next to the IP evolves as:

$$\beta(s) = \beta^* + \frac{s^2}{\beta^*} \tag{4.1}$$

where s is the longitudinal distance from the IP. Therefore, the β function at the location of the first quadrupole of the inner triplet ($s = L^*$) is expected to increase as L^* gets larger. This is illustrated in Fig. 4.15 where the β function in the LHeC IR is shown for the optical cases with $L^* = 10, 15$ and 17 m and a β^* fixed at 10 cm. The increase of the β function at the location of the inner triplet is clear from the figure.

If allowed to grow too large, the β function at the location of the inner triplet can cause aperture issues. Also, and most importantly, since the contribution to the chromaticity of an element is directly proportional to the β function at its location, the overall chromaticity is expected to increase with an increase in L^*.

4.2.4 Minimizing β^*

Using the same techniques discussed in Section 4.2.2, stable optical solutions were found for optical designs with $\beta^* = 5, 6, 7, 8, 9, 10$ and 20 cm with a fixed L^* at 10 m.

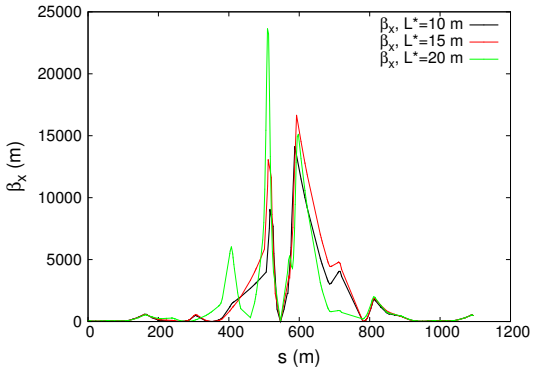

FIGURE 4.15: β_x function over the LHeC IR for the LHeC lattice configurations with $L^* = 10$ m (black), $L^* = 15$ m (red) and $L^* = 20$ m (green), all with a fixed β^* of 10 cm. The value of the β_x function at the location of the inner triplet grows as L^* increases.

Minimizing β^* has the clear advantage of increasing the luminosity. A particularly interesting case is the optical design with $\beta^* = 5$ cm, given that with this beam size in the IP, along with the other parameters shown in Table 3.4, a luminosity of $10^{34}\text{cm}^{-2}\text{s}^{-1}$ is achievable.

However, just as for the case of increasing L^*, the β function at the location of the inner triplet is expected to increase as β^* is reduced. This is illustrated in Fig. 4.16 which shows the β function in the LHeC IR for the optical cases with $\beta^* = 10$ cm, $\beta^* = 8$ cm and $\beta^* = 5$ cm, all with a fixed L^* at 10 m. The case with $\beta^* = 5$ cm and $L^* = 10$ m results in a larger β function at the inner triplet than the case with $\beta^* = 10$ cm and $L^* = 20$ m.

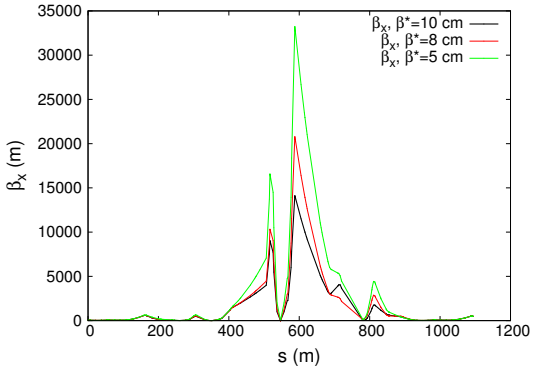

FIGURE 4.16: β_x function over the LHeC IR for the LHeC lattice configurations with $\beta^* = 10$ cm (black), $\beta^* = 8$ cm (red) and $\beta^* = 5$ cm (green), all with a fixed L^* of 10 m. The value of the β_x function at the location of the inner triplet gets larger as the value of β^* is reduced.

The effects that the increase in β function in the inner triplet has on the chromaticity for the optical cases with different L^* and β^*, along with the proposed chromaticity correction, will be discussed in Section 4.3.

4.3 Chromaticity Correction

In the previous section, different optics solutions were found in order to provide different L^* and β^*. In this section, we discuss the chromaticity correction for these configurations following the principles of Eq. 1.165.

While designing the LHeC IR competing criteria exist, and some drawbacks arise as the β^* and L^* parameters are changed. As previously stated, the benefits of increasing the luminosity by minimizing the β^* and reducing the synchrotron radiation by increasing L^*, come hand in hand with an increase of the β function at the location of the inner triplet. Recalling the result derived in Eq. 1.154 and Eq. 1.155 the natural chromaticity arising from the quadrupoles is proportional to the gradients of the quadrupoles and the β function at its location. The changes (with respect to the nominal values for $\beta^* = 10$ cm and $L^* = 10$ m) in the gradients of the inner triplet are kept in the range $-0.1 < \Delta k/k < 0.1$, as can be observed in Figs. 4.17 and 4.18 where the gradients of the inner triplet are plotted for different L^* and β^* respectively. The natural chromaticity arising from the inner triplet is then expected to be largely determined by just the β function at its location and therefore an overall increase of the natural chromaticity is expected for the new lattice configurations.

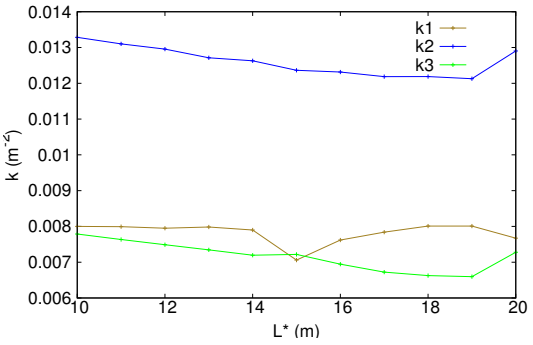

FIGURE 4.17: Gradients of the Q1 (k1), Q2 (k2) and Q3 (k3) quadrupoles in the LHeC IR as a function of L^*. All cases have a fixed β^* at 10 cm.

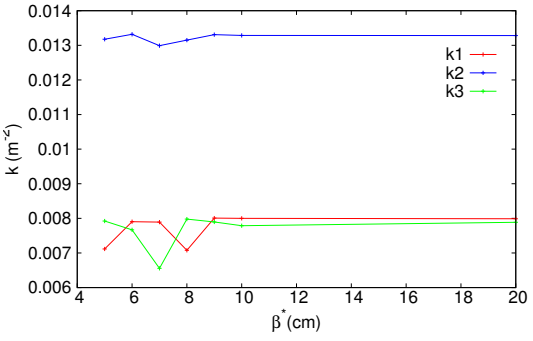

FIGURE 4.18: Gradients of the Q1 (k1), Q2 (k2) and Q3 (k3) quadrupoles in the LHeC IR as a function of β^*. All cases have a fixed L^* of 10 m.

By setting all the sextupole families to zero, the natural chromaticity was calculated. Fig. 4.19 shows the natural chromaticity for the lattice configurations with varying L^*; and Fig. 4.20 shows the natural chromaticity for varying β^* with L^* fixed at 10 m.

It is clear from the figures that the absolute magnitude of the natural chromaticity increases linearly as L^* grows larger, whereas minimizing β^* causes the absolute magnitude of the natural chromaticity to increase more rapidly.

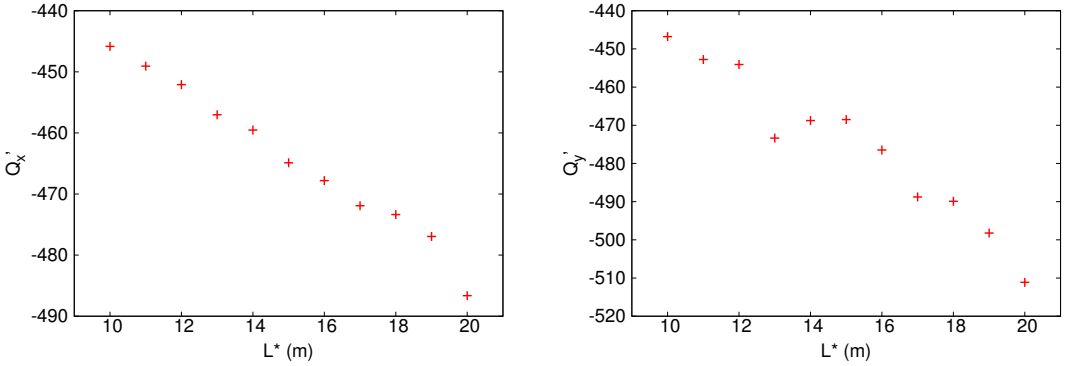

(A) (B)

FIGURE 4.19: (a) Natural horizontal (Q_x) and (b) vertical (Q'_y) chromaticity of the LHeC lattice as a function of L^*. All lattices have β^* fixed at 10 cm.

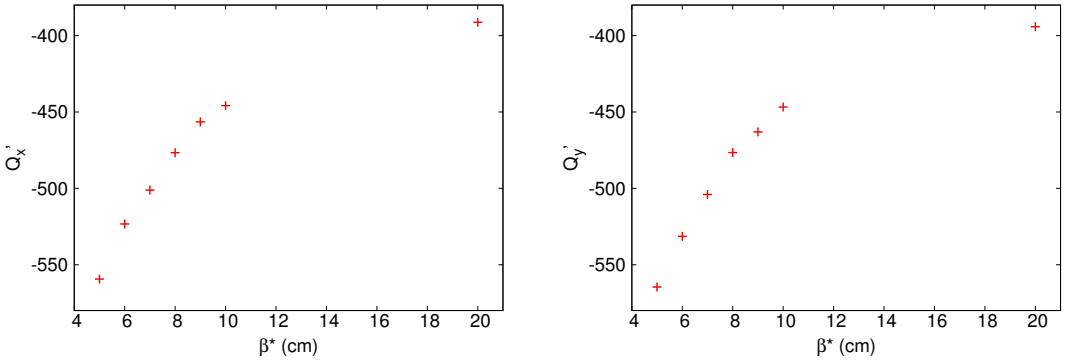

(A) (B)

FIGURE 4.20: (a) Natural horizontal (Q_x) and (b) vertical (Q'_y) chromaticity of the LHeC lattice as a function of β^*. All lattices have L^* fixed at 10 m.

At this point it is clear that a suitable chromaticity correction becomes significant, not only for the nominal case, which will now be addressed, but for all other cases, that have higher natural chromaticity.

4.3.1 Nominal Correction

As explained in Section 3.6.3, the ATS provides a local chromaticity correction of the inner triplet by using the sextupoles within the arcs on either side of IP1 and IP5. However, in the LHeC case, given that IR1 is adjacent to IR2, arc 12 can no longer

be used solely for IR1 since it is now used also for the extension of the ATS in IR2. Therefore, a new method to correct the chromaticity has to be adopted.

Three different chromaticity correction schemes have been proposed for beam 2 in LHeC: LHC-like, HL-LHC-like and LHeC-like. The chromaticity correction for beam 1 remains the same as for the HL-LHC. The different chromaticity correction schemes and the corresponding matching procedures in MADX are described below:

1. **LHC-like.** This correction, as the name indicates, performs the chromaticity correction in the same way as for the LHC, using all 32 families of sextupoles in the ring to achieve a global correction. The corresponding matching procedure uses two variables, the focusing and defocusing sextupole families, to meet the constraints $Q'_x = Q'_y = 2$.

2. **HL-LHC-like**. This procedure performs the chromaticity correction using a variation of the method used for the HL-LHC. As explained in Section 3.6.3 the HL-LHC chromaticity correction divides the sextupole families into three different groups: strong, weak and local as given in Table 3.3. In the case of the LHeC, given that a β-beating wave is now also produced in arc 23, the groups of families for beam 2 are adjusted accordingly and are given in Table 4.4.

Families	Sectors	Beam	Category
SF2, SD1	81, 45, 23	B2	strong
SF2, SD1	12, 56	B2	strong
SF1, SD2	81, 45, 23	B2	local
SF1, SD2	12, 56	B2	local
SF1, SF2, SD1, SD2	34, 67, 78	B2	weak

TABLE 4.4: Sextupole families grouped in the strong, local and weak categories for the HL-LHC-like chromaticity correction implemented in the LHeC lattice for beam 2.

   The strong families are allowed to vary independently. The members of the weak and local families are varied by the same amount but separated between focusing and defocusing, accounting for a total of 14 variables. The matching procedure then consists of 14 variables to adjust the horizontal (Q'_x) and vertical (Q'_y) chromaticities to a value of 2 in each case.

3. **LHeC-like**. The aim of this method is to try to achieve a global correction that might break the locality of the chromaticity correction but that will bring benefits in terms of controlling the chromatic aberrations.

   The optimization of the sextupole families strengths to control the chromaticity is performed by a matching procedure in MADX which takes as variables the strengths of all the families of sextupoles acting independently. The constraints are the reduction of the horizontal (Q'_x) and vertical (Q'_y) chromaticities to a value of 2 in each case and the reduction of the Montague (chromatic betatron

amplitude) functions in both transverse planes (W_x and W_y) below 200 in the collimation insertions IR3 and IR7. The Montague functions, as explained in Section 1.5.2, describe the variation of the Courant–Snyder parameters with respect to the energy.

For the nominal case ($L^* = 10$ m and $\beta^* = 10$ cm), where the natural chromaticities are $Q'_x = -445.83$ and $Q'_y = -446.77$, the matching procedures for the LHC-like and LHeC-like chromaticity corrections were achieved successfully. The HL-LHC-like correction, however, failed to converge.

Even when the corresponding constraints are met, the full effects of each chromaticity correction can be observed by studying its impact on the variation of the tunes as functions of the momentum deviation. This is illustrated in Fig. 4.21 where the horizontal tune Q_x (left) and vertical tune Q_y (right) are given as functions of the momentum deviation ($\delta p = \Delta p/p$) for the LHC-like and the LHeC-like chromaticity corrections.

The presence of nonlinearities in the horizontal and vertical chromaticities is observed for both correction schemes. The LHC-like scheme also presents a larger variation for large momentum deviations ($\delta p \approx 0.001$), with a change of horizontal and vertical tune of $|\Delta Q_x| \approx 0.025$ and $|\Delta Q_y| \approx 0.06$ over the range $-10^{-3} < \delta p < 10^{-3}$, compared to $|\Delta Q_x| \approx 0.002$ and $|\Delta Q_y| \approx 0.0009$ observed for the LHeC-like chromaticity correction.

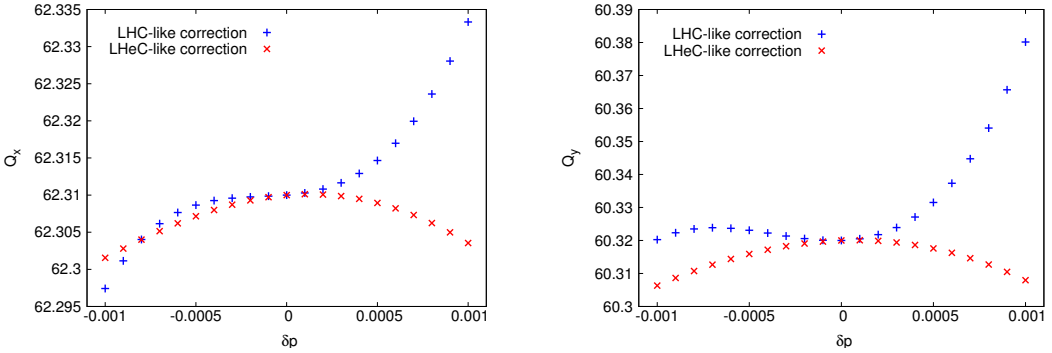

(A) (B)

FIGURE 4.21: (a) Horizontal (Q_x) and (b) vertical (Q_y) tunes as a function of a momentum deviation (δp). Markers show the results for LHC-like (blue) and LHeC-like (red) chromaticity correction schemes for the nominal LHeC lattice with $\beta^* = 10$ cm and $L^* = 10$ m. The momentum deviation is varied in the range $\delta p \pm 0.001$.

To study the possible impact of resonances, the tune variation with momentum can also be plotted on a resonance map, as described in Section 1.5.4. Fig. 4.22 shows the variation in tunes over the range of momentum deviation $-10^{-3} < \delta p < 10^{-3}$ for both chromaticity correction schemes. Resonances up to the 10^{th} order are shown. The difference between the two different chromaticity correction schemes can be seen clearly. The LHeC-like chromaticity correction scheme avoids resonances up to order 10 while the LHC-like chromaticity correction scheme fails to do so. In the LHeC-like chromaticity correction scheme; however, the tunes came closer to the second order resonance (-1,1)

which may affect stability. A more extended study of the effects of these resonances will be presented in Chapter 5 which gives the results of tracking studies.

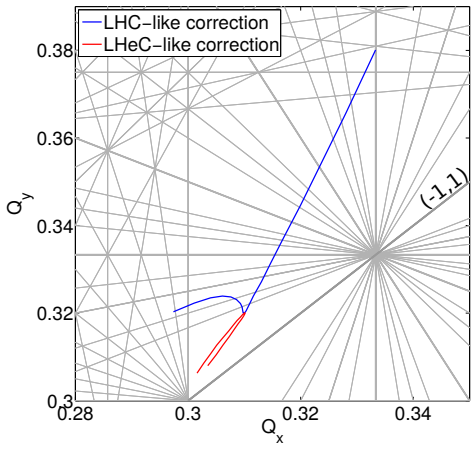

FIGURE 4.22: Horizontal (Q_x) and vertical (Q_y) tunes over the momentum range $10^{-3} < \delta p < 10^{-3}$ for beam 2, plotted on a resonance map up to 10th order. Lines show the results after an LHC-like (blue) and an LHeC-like (red) chromaticity corrections for the nominal LHeC lattice with $\beta^* = 10$ cm and $L^* = 10$ m.

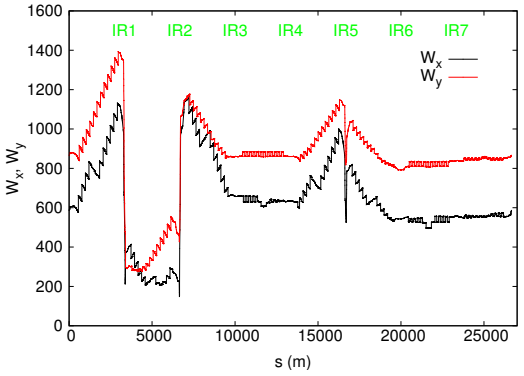

FIGURE 4.23: Horizontal (W_x) and vertical (W_y) Montague functions after the LHC-like chromaticity correction scheme for beam 2 (the machine starts in IP8) for the nominal LHeC lattice with $\beta^* = 10$ cm and $L^* = 10$ m.

The effects of the chromaticity correction can also be observed by the variation of the Courant–Snyder parameters via the Montague functions (Eq. 1.166). Montague functions along the LHeC IR are shown in Fig. 4.23 for the LHC-like chromaticity correction scheme. By setting constraints in the LHC-like chromaticity correction scheme only for the chromaticity, the Montague functions are free to vary and take values up to $W_x \approx 600$ and $W_y \approx 800$ in the collimation insertions IR3 and IR7. In the LHeC-like chromaticity correction scheme, because of the matching constraints used, limits of 200 on the values of W_x and W_y are observed in IR3 and IR7, as shown in Fig. 4.24. The merits of the LHeC-like chromaticity correction scheme are clear in comparison, not only because the Montague functions are controlled in the collimation insertions IR3 and IR7,

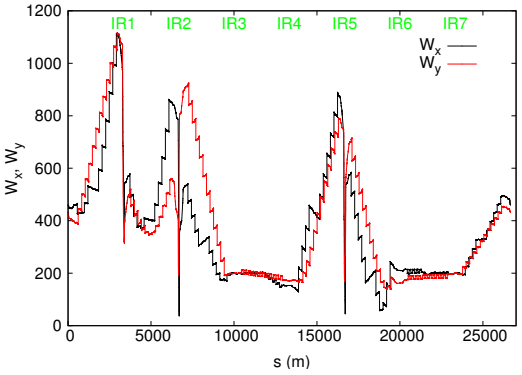

FIGURE 4.24: Horizontal (W_x) and vertical (W_y) Montague functions after the LHeC-like chromaticity correction scheme for beam 2 (the machine starts in IP8) for the nominal LHeC lattice with $\beta^* = 10$ cm and $L^* = 10$ m.

but also because the overall Montague functions are smaller along the ring (including a 20% reduction of the peak values of these functions).

4.3.2 Limits of the Chromaticity Correction Schemes

The chromaticity corrections found in Section 4.3.1 for the nominal lattice with $\beta^* = 10$ cm and $L^* = 10$ m are now applied for the different optical solutions found in Section 4.2.3 for different L^* and in Section 4.2.4 for different β^*. Given the results shown in Figs. 4.19 and 4.20 the natural chromaticity increases as L^* grows larger and β^* reduces. The aim of this section is to find the limit, if any, of the two different chromaticity correction schemes studied for the nominal case.

The LHeC-like chromaticity correction scheme has a limit for a maximum L^* of 19 m with β^* fixed at 10 cm, and a minimum β^* of 8 cm and with L^* fixed at 10 m. Considering the natural chromaticity shown in Figs. 4.19 and 4.20 we can set the limit of the LHeC-like chromaticity correction scheme for cases with an absolute value of the natural chromaticity ≈ 480 (Fig. 4.25).

An advantage of the LHC-like chromaticity correction scheme is that it is easier to obtain a solution, since the matching procedure not only has two constraints fewer to consider (limits on W_x and W_y in IR3 and IR7) but also has the same number of variables as constraints. Consequently the LHC-like chromaticity correction scheme was applied successfully for all the optical cases found previously.

The following sections will focus on the cases with β^* fixed at 10 cm and $L^* >10$ m since these values are sufficient to achieve a luminosity of 10^{33} cm^{-2}s^{-1}. Also, a larger L^* provides a way to minimize the synchrotron radiation. However, the case with $\beta^* = 5$ cm requires further study in order to explore the upgrade luminosity of 10^{34} cm^{-2}s^{-1} (Table 3.4).

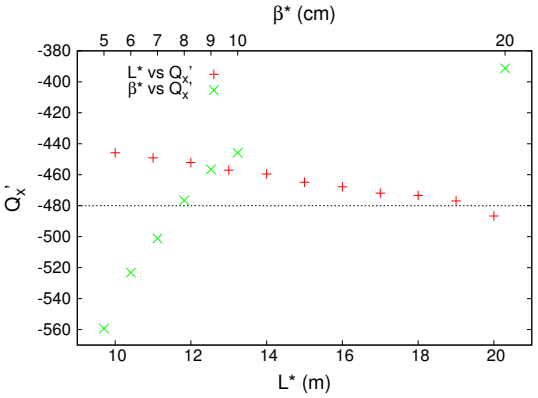

FIGURE 4.25: Limit of the chromaticity correction (black dashed line) using the LHeC-like scheme overlaid on a plot of Q'_x vs L^* (red) and Q'_x vs β^* (green). This limit was found around $Q'_x \approx$ -480 for a maximum of $L^* = 18$ m with $\beta^* = 10$ cm and a minimum β^* of 8 cm with $L^* = 10$ m.

4.3.3 Higher Order Chromaticity

The last section discussed the LHeC-like chromaticity correction scheme to achieve a global value of the chromaticity of 2 in the horizontal and vertical directions. By allowing the sextupole families to vary independently a limit was imposed on the Montague functions, which brought benefits in reducing the overall tune variation with momentum deviation.

In this section the non-linearity present in both the LHC-like and LHeC-like chromaticity correction schemes, observed in Fig. 4.21, will be addressed. A third type of chromaticity correction was carried out to address this problem. This correction which we refer to as "higher order", takes the same variables and constraints as the LHeC-like correction but adds as further constraints the second order variation of the tunes with respect to momentum $-10^{-3} < \delta p < 10^{-3}$ below a value of 7.

Figures 4.26 and 4.27 illustrate the change of tune over momentum for the three different chromaticity correction schemes for the nominal case with $L^* = 10$ m and $\beta^* = 10$ cm. As stated previously, the presence of nonlinearities is clear for the LHC-like and LHeC-like correction. After the higher order correction the variation of the vertical tune Q_y shows a nearly linear behaviour, but for the horizontal tune this linearity was not achieved for the whole momentum deviation, only for the range $\delta p = (-0.0005, 0.0005)$.

Figure 4.28 shows the tunes variation with momentum on a resonance map of order 10 for the three chromatic correction schemes for the nominal case with $L^* = 10$ m and $\beta^* = 10$ cm. The higher order correction shows similar benefits in comparison to the LHeC-like correction, in terms of the resonances crossed by the path of the tune variation. However, the tune variation once again comes close to the second order resonance line (-1,1).

The matching procedure for the higher order chromaticity correction was performed successfully for a maximum L^* of 18 m with a fixed β^* of 10 cm.

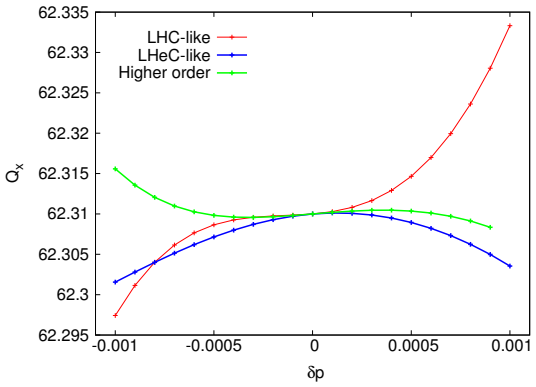

FIGURE 4.26: Horizontal tune (Q_x) for a momentum spread varying in the range $-10^{-3} < \delta p < 10^{-3}$ after the LHC-like (red), LHeC-like (blue) and higher order (green) chromaticity correction schemes for the nominal LHeC lattice with $\beta^* = 10$ cm and $L^* = 10$ m.

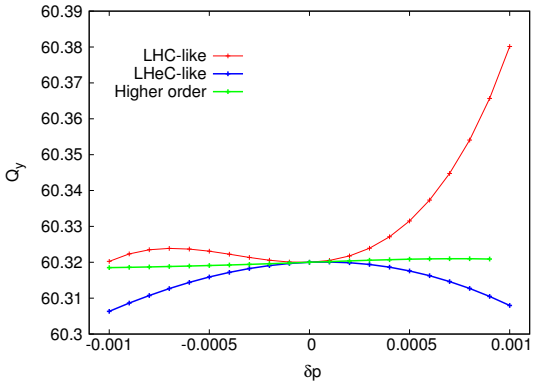

FIGURE 4.27: Vertical tune (Q_y) for a momentum spread varying in the range $-10^{-3} < \delta p < 10^{-3}$ after the LHC-like (red), LHeC-like (blue) and higher order (green) chromaticity correction schemes for the nominal LHeC lattice with $\beta^* = 10$ cm and $L^* = 10$ m.

Fig. 4.29 shows again the tunes variation over a momentum deviation but for the optical design with maximum L^* that each chromaticity correction scheme was able to correct, i.e. $L^* = 20$ m for the LHC-like case, $L^* = 19$ m for LHeC-like and $L^* = 18$ m in the case of higher order. All cases have a fixed β^* of 10 cm.

The comparison of Figs. 4.28 and 4.29 shows that even when the optical designs are stable and the corresponding chromaticity corrections are achieved, the effects of momentum deviation on the tunes calculation are different between lattices with different L^*. Tracking studies for dynamic aperture calculation (Section 1.5.5) and frequency map analysis (Section 1.5.6) are expected to provide more information about the effects of these nonlinearities and resonances, in order to compare in a quantitative way the benefits of each chromaticity correction scheme in the different lattices in terms of the stability of the beam. This will be addressed in Chapter 5.

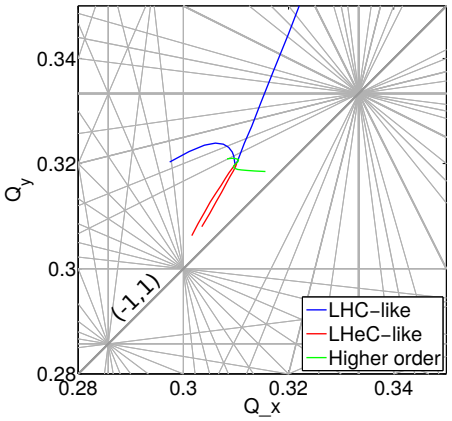

FIGURE 4.28: Tune variation over a resonance map of tenth-order for three different chromaticity correction schemes, LHC-like (blue), LHeC-like (red) and higher order (green) for the nominal LHeC lattice with $L^* = 10$ m and β^* =10 cm.

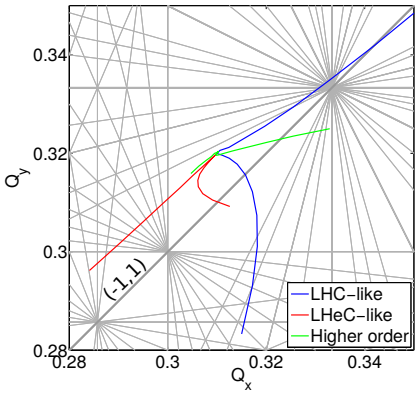

FIGURE 4.29: Tune variation over a resonance map of tenth-order for the limit of each chromaticity correction in terms of L^*. This limit corresponds to $L^* = 20$ m and $\beta^* = 10$ cm for the LHC-like chromaticity correction scheme (blue), $L^* = 19$ m and $\beta^* = 10$ cm for the LHeC-like chromaticity correction scheme (red) and $L^* = 18$ m and $\beta^* = 10$ cm for the higher order chromaticity correction scheme (green).

4.4 Synchrotron Radiation

The synchrotron radiation power produced by the electron beam while transporting it to and from the IP is a problem that has to be treated with great care in order to minimize the damage to the quadrupoles of the inner triplet and to the detector.

The total synchrotron radiation power in an electron storage ring as a function of the circulating particle current (I), the energy of the beam (E) and the bending radius (ρ_e) is given by [14]:

$$P = C_\gamma \frac{E^4}{\rho_e} I \tag{4.2}$$

where $C_\gamma = 8.85 \times 10^{-5} \mathrm{m/GeV}^3$.

For a single dipole with bending radius ρ_e and bending angle θ_e, the synchrotron radiation power will be:

$$P = C_\gamma \frac{E^4}{\rho_e} I \times \frac{\theta_e}{2\pi}. \tag{4.3}$$

For the separation dipoles in the LHeC IR, the bending radius and angle are given as functions of L^* and the separation Δ of the beams in the normal aperture and the field-free aperture in Q1 as [110]:

$$\rho_e = \frac{L^{*2}}{2\Delta}, \tag{4.4}$$

$$\theta_e = \arcsin\left(\frac{2\Delta}{L^*}\right). \tag{4.5}$$

From these equations it is clear that increasing L^* will result in an increase of the radius ρ_e and a decrease of the angle θ_e, both producing a reduction of the synchrotron radiation power produced in the separation dipoles. Studies have been done previously to investigate the effect of increasing L^*, but with a fixed beam separation Δ [101]. This section will refer to these previous results, increasing L^* without any change in the beam separation Δ, as "Scaling LHeC-CDR".

In the present work, we explore a possible way to reduce the synchrotron radiation power further via the reduction of Δ since this will result in a reduction of the synchrotron radiation power in the same way as increasing L^*.

In order to find the minimum value for the beam separation Δ between the focused proton beam and the electron beam, the following constraints are considered:

1. The distance between the beams has to be greater than 75 mm for $L^* < 14$ m (separation in half-aperture quadrupole design) and greater than 87 mm for $L^* \geq 14$ m (separation in full-aperture quadrupole design).

2. To keep the effects of parasitic beam-beam interactions (long range encounters) within tolerable limits, the separation at the first long-range encounter has to be at least 12σ (with σ being the rms beam size). The first long-range encounter occurs at a distance from IP2 of $s = 3.75$ m for 25 ns bunch spacing and a distance $s = 7.5$ m for 50 ns bunch spacing.

3. The proton and electron beams must physically fit inside the normal-field and field-free apertures respectively.

The sizes of the proton beam 2 and the electron beam σ were calculated at each L^*. Then, using the radius of the apertures, we calculated the number of beam σ that could be fitted in the corresponding aperture: the normal aperture for the proton beam and the field-free aperture for the electron beam. It was also considered that for an $L^* \geq 14$ m a full-aperture quadrupole was used for Q1. The resulting number of σ that could be fitted inside the corresponding aperture for each beam is shown in Table 4.5, along with the minimum separation required by the first and second constraints.

	1st constraint		**2nd constraint**		**3rd constraint**	
L^*	Minimum Δ_{25}	Minimum Δ_{50}	Minimum Δ_{25}	Minimum Δ_{50}	e-beam (σ)	p-beam 2 (σ)
10	0.075	0.075	0.023	0.011	41	32
11	0.075	0.075	0.027	0.014	38	29
12	0.075	0.075	0.033	0.016	34	27
13	0.075	0.075	0.038	0.019	32	24
14	0.087	0.087	0.044	0.022	27	23
15	0.087	0.087	0.051	0.026	25	21
16	0.087	0.087	0.058	0.029	24	20
17	0.087	0.087	0.066	0.033	22	19
18	0.087	0.087	0.073	0.037	21	18
19	0.087	0.087	0.082	0.041	20	17
20	0.087	0.087	0.091	0.045	19	16

TABLE 4.5: Minimum separation between beams (Δ_{25} for 25 ns bunch spacing and Δ_{50} for 50 ns bunch spacing) corresponding to a range of L^* and two different bunch spacings for the 1st and 2nd constraints. The number of sigmas that can be fitted inside the corresponding aperture for the electron and proton beam is also shown.

Results show that given the minimum separation distance Δ from the first constraint, the second constraint is automatically fulfilled, except for the case when $L^* = 20$ m with 25 ns bunch spacing, in which case the second constraint gives the minimum separation. For the third constraint the worst case scenario is the case with $L^* = 20$ m for proton beam 2: in this case 16σ can be fitted within the aperture, which is still an acceptable value.

Taking the maximum value from the first two constraints, Table 4.6 shows the minimum separation Δ for each L^* for both 25 ns and 50 ns bunch spacings, and the corresponding synchrotron radiation power produced.

	Bunch spacing 25 ns		**Bunch spacing 50 ns**	
L^*	Minimum Δ_{25}	P (kW) 25 ns	Minimum Δ_{50}	P (kW) 50 ns
10	0.075	49.29	0.075	49.29
11	0.075	37.03	0.075	37.03
12	0.075	28.52	0.075	28.52
13	0.075	22.43	0.075	22.43
14	0.087	24.17	0.087	24.17
15	0.087	19.65	0.087	19.65
16	0.087	16.19	0.087	16.19
17	0.087	13.50	0.087	13.50
18	0.087	11.37	0.087	11.37
19	0.087	9.67	0.087	9.67
20	0.091	9.07	0.087	8.29

TABLE 4.6: Minimum separation between beams (Δ) and the synchrotron radiation power produced corresponding to a range of values for L^* and two different bunch spacings.

Figure 4.30 shows the radiation power as a function of L^* and the beam separation for three cases: the first case illustrates the results of "scaling LHeC CDR" reported in [101], the second and third cases illustrate the minimum distance for the 25 ns and 50 ns bunch spacings. The reduction of the synchrotron radiation power for the cases $L^* > 10$ m is clearly observed already for the case of "scaling the LHeC CDR" (i.e. only increasing L^*); however, when considering also the minimum beam separation for each L^* we can observe further reduction of synchrotron radiation power.

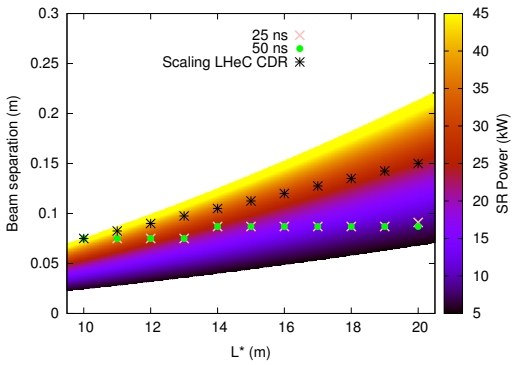

FIGURE 4.30: Synchrotron radiation power as a function of L^* and beam separation Δ in Q1. All LHeC lattices have a β^* of 10 cm. The black symbols show the cases for scaling the LHeC CDR reported in [101], the pink and green symbols (almost overlaid in the image) show the minimum beam separation for bunch spacings 25 ns and 50 ns respectively.

To better illustrate the synchrotron radiation power reduction with L^*, Fig. 4.31 shows the results presented in Fig. 4.30, but now the synchrotron radiation is given only as a function of L^*. This is presented again for the three different cases: scaling the values of the LHeC CDR, and finding the minimum separation for 25 ns and 50 ns bunch spacings. The reduction of the synchrotron radiation as L^* increases is clear for all three cases. For the cases when the minimum beam separation was found, we obtain a larger decrease. For an $L^* = 15$ m for example, we observe a decrease in synchrotron radiation power of over 50% when comparing it with the nominal case with $L^* = 10$ m.

In order to reduce the amount of synchrotron radiation hitting the inner triplet a new option with "sweet spot" magnets [111] has been proposed. These magnets provide a larger aperture for the same gradient, increasing the space for absorbers inside the aperture of the quadrupole [111]. The possible integration of this new magnet design may give additional flexibility to the final lattice design.

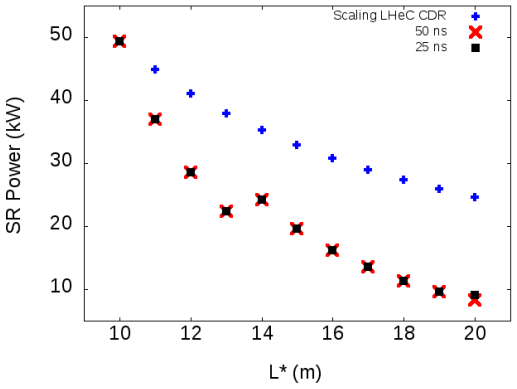

FIGURE 4.31: Synchrotron radiation power as a function of L^*. All lattices have a fixed β^* of 10 cm. The blue symbols show the cases for scaling the LHeC (reported in the LHeC CDR [101]), the black and red symbols (almost overlaid in the image) show the synchrotron radiation for the minimum beam separation for bunch spacings 25 ns and 50 ns respectively.

4.5 Conclusions

There were several challenges for the first design of the LHeC interaction region as presented in the CDR. Most importantly an optical design needed to be implemented that would have the appropriate parameters to achieve the desired luminosity while controlling chromatic aberrations. Furthermore, the synchrotron radiation generated when bending the electron beam has the potential to cause serious damage to the quadrupoles and other components in the IR.

In the present work we have explored the flexibility of the design to find the right balance between achieving the highest luminosity while controlling the chromaticity and minimizing the impact on the machine from the synchrotron radiation.

With the aid of the beam dynamics results obtained in Chapter 1 and the tools available in the MADX code, different lattice configurations were found, opening up possibilities to increase L^* up to 20 m with a fixed β^* at 10 cm, and reduce β^* to 5 cm with a fixed L^* of 10 m. Different chromaticity correction schemes were proposed to control the chromaticity, imposing new limits in the lattice configurations that should be considered. The LHeC-like chromaticity correction, with constraints on $Q'_{x,y}$ and the Montague functions $W_{x,y}$, is only achieved up to $L^* = 19$ m with $\beta^* = 10$ cm and for $\beta^* = 8$ cm with $L^* = 10$ m. Other chromaticity corrections schemes were considered. The LHC-like chromaticity correction scheme, with constraints only on $Q'_{x,y}$, has the advantage that chromaticity correction was achievable for all optical cases, but the Montague functions reached high values in the collimation insertions. Also considered was a higher order chromaticity correction, aiming to control the nonlinear order chromaticity by adding a constraint on the second derivative of the tune with respect to momentum. This chromaticity correction was achieved for cases with a maximum value of $L^* = 18$ m and $\beta^* = 10$ cm.

The minimization of synchrotron radiation is desirable to reduce the impact that this radiation may have on the machine. Increasing L^* and minimizing the separation between the electron beam and proton beam 2 at the entrance of the first quadrupole of the inner triplet results in a reduction of the dipole field strength required to bend the electron beam, and consequently the synchrotron radiation is also reduced. Results show a significant reduction in synchrotron radiation power as a result of applying these techniques. The case with $L^* = 15$ m and $\beta^* = 10$ cm for example, showed a reduction of synchrotron radiation power over 50% in comparison with the nominal case with $L^* = 10$ m and $\beta^* = 10$ cm.

Tracking studies in Chapter 5 aim to complement this work, and to analyse the impact of each scheme on the stability of particle trajectories in the LHeC.

Chapter 5

Tracking Studies in the LHeC Lattice

The development of different configurations for the LHeC lattice was presented in Chapter 4. In particular we explored the limits and feasibility of increasing L^* and minimizing β^* by adjusting the quadrupole strengths, using different chromaticity correction schemes and taking into account the corresponding synchrotron radiation. In this chapter, results are presented from particle tracking simulations for a range of initial conditions to complement the previous studies. The goal of the studies is to validate the extension of the ATS scheme to the LHeC IR for the different lattice configurations in terms of the particle trajectories in the proton storage ring.

This chapter first introduces previous particle tracking studies performed for the LHC (Section 5.1) because these techniques can be adapted for LHeC particle tracking. This chapter then presents particle tracking studies carried out for the LHeC lattice configurations, studying the stability of the beam in terms of the dynamic aperture and frequency map analysis (FMA).

Several considerations are taken when performing particle tracking to obtain the dynamic aperture. First, due to the computational cost required, particles are tracked only for a certain number of turns (10^5), the result is then extrapolated to the actual beam lifetime [112]. Also important is the consideration of different realisations of errors in the magnets (seeds). For dynamic aperture studies, 60 seeds are considered to be sufficient to provide enough confidence in the results [113].

5.1 Tracking Studies in the LHC

The concepts of dynamic aperture and FMA were previously explained in Sections 1.5.5 and 1.5.6 respectively. This section specifically focuses on how those techniques have been used in previous tracking studies for the LHC.

SixTrack [36] is a single particle 6D symplectic tracking code optimized for long term tracking in high energy storage rings, in particular it has been used in the LHC for dynamic aperture studies. SixTrack is a kick code (described in Section 2.6.1) that uses

a thin lens version of the lattice. SixTrack has been used to model particle dynamics in the LHC from the early stages of its design phase [114].

Particle tracking in SixTrack is carried out for a polar grid in the physical space in terms of the amplitude and angle. The amplitudes are given by:

$$I = \sqrt{I_x^2 + I_y^2} \tag{5.1}$$

and the angles by:

$$\theta = \frac{I_y}{I_x}. \tag{5.2}$$

where $I_x = x/\sqrt{\epsilon_x/\gamma_x}$ and $I_y = y/\sqrt{\epsilon_y/\gamma_y}$, ϵ is the geometric emittance and $\gamma_{x,(y)}$ the Courant–Snyder parameter in the horizontal (vertical) direction.

The initial conditions refer, in fact, to a pair of nearby particles ('Lyapunov pairs'). SixTrack determines the boundary between regular and chaotic motion by tracking two particles with slightly different initial conditions. The distance between these particles is then tracked and used to determine whether the motion is chaotic by means of the computation of the maximal Lyapunov exponent, as explained in Section 1.5.5. The greatest amplitude of a surviving particle $(I_{x,max}, I_{y,max})$, i.e. one that is not lost from the beam, is then considered to determine the dynamic aperture given as:

$$\text{DA} = \sqrt{I_{x,max} + I_{y,max}}. \tag{5.3}$$

At peak energy, the average lifetime of particles within the LHC is around 10 hours [115]. However, tracking particles over such time-scales is computationally expensive. For that reason, much shorter times are used in tracking studies, corresponding to an LHC time of around 10 seconds (10^5 turns). Based on the experience of SPS and HERA, a long term dynamic aperture of 6σ was set as a reasonable goal for the LHC [112]. Taking into account the expected reduction in computed dynamic aperture when extrapolating from several seconds (10^5 turns) to several hours, a target was set for dynamic aperture of 11σ for 10^5 turns at injection energy, and 10σ for 10^5 turns at collision energy [112, 114].

In order to run a tracking campaign, SixTrack requires a series of prerequisite steps. First, a SixTrack environment file is generated which contains beam properties (e.g. energy, chromaticity) and the tracking conditions (e.g. initial particle amplitudes and angles). Second, this file calls a MADX job, containing the lattice and optics files, which generates SixTrack input files.

As explained in Section 1.1.4 magnets have systematic and random errors. In the case of magnetic fields within the LHC, errors are applied in the form of magnetic multipoles up to the 15^{th} order. These errors are generated by the Windows Interface to Simulation Errors (WISE) [116]. Only a fraction of the LHC magnets were measured in cold (operational) conditions. The rest of the LHC magnets were measured instead in warm conditions, and therefore the use of warm-to-cold correlation was required [114].

In addition to this, WISE assumes that the measured magnet errors have a Gaussian distribution. To represent this behaviour, 60 different seeds are available, each containing a version of the magnetic multipoles up to the 15^{th} order. It is considered that 60 seeds are sufficient to provide a 95% confidence in the results; i.e. that only 5% of the total number of all possible LHC realisations have a dynamic aperture value lower than the lowest one found by particle tracking [113].

Fig. 5.1 shows the dynamic aperture for 25 angles over the 60 seeds for both beams at injection optics. Results show that the target dynamic aperture of 11σ was achieved for almost all angles apart for the single case with 25 degrees for beam 2 [114].

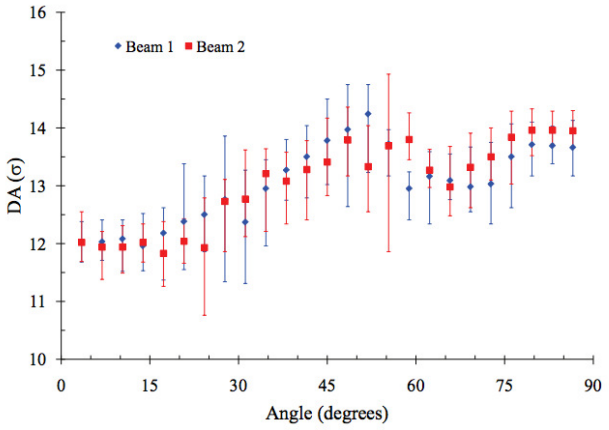

FIGURE 5.1: Dynamic aperture as a function of the angle for the nominal injection optics of the LHC over 10^5 turns. Both beam 1 and beam 2 values are shown for 25 different angles. Markers indicate the average over the 60 seeds, while the errors bars indicate the interval of variation over the seeds [114].

As mentioned in Section 1.5.6, another way to study the stability of particles within the beam is to study their frequencies of motion. For this reason, FMA studies have been performed for the LHC [23]. In those studies, particle tracking was again carried out using SixTrack, but this time for short-term tracking data (10^3 turns). In dynamic aperture studies, we were only interested in the conditions where motion becomes chaotic. In FMA studies, we are also interested in the overall behaviour in different regions of phase-space including effects such as diffusion in tune space. For that reason, a wider range of initial conditions, in particular small amplitudes, were also considered in the tracking.

The FMA studies for the LHC are illustrated in Fig. 5.2 where the computed horizontal tune (Q_x) and vertical tune (Q_y) are shown on a resonance map, with the colour scale representing the initial amplitudes of the particles. Also shown in the figure is the diffusion rate (explained in Section 1.5.6) as a function of initial positions of the particles.

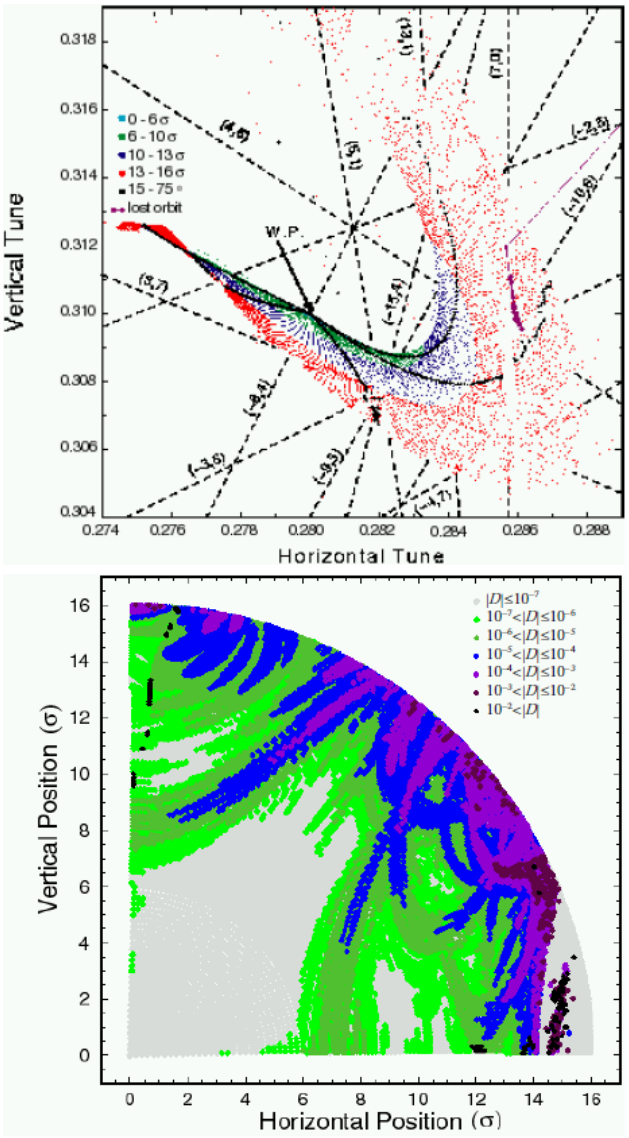

FIGURE 5.2: FMA studies for the version 5 of the LHC over 10^3 turns and for a grid of 10^4 different initial conditions. The computed horizontal and vertical tunes are shown in a resonance map with the colour scale indicating the initial amplitude of the tracked particles (top). Also shown is the variation of the computed tune via the diffusion factor, against the initial amplitudes of the tracked particles (below) [23].

5.2 Dynamic Aperture Simulations of the LHeC

A set of different lattice configurations was studied in Chapter 4 by making an extension of the ATS scheme into the LHeC IR (Section 4.2). Furthermore, different chromaticity correction schemes were proposed to overcome the large natural chromaticity introduced by the extension of the ATS into the LHeC IR, setting a limit on the lattice configurations that were feasible in terms of controlling the chromatic aberrations (Section 4.3.3). However, sextupoles have the drawback of generating nonlinear, geometric perturbations [14]. Even when the chromaticity corrections were achieved for a number of different lattice configurations, the tune variation for a given momentum deviation varied for each chromatic correction scheme, as illustrated in Section 4.3.3.

This section presents studies in which SixTrack was used to perform long-term tracking for the lattice configurations found in Chapter 4. Using the dynamic aperture obtained from these simulations, the stability of the beam can be calculated and used to validate the feasibility of each lattice configuration. In particular, we show the dynamic aperture achieved for different types of chromaticity correction (presented in Section 4.3.3), in order to obtain a more quantitative measure of the benefits of each chromaticity correction scheme.

The dynamic aperture was computed in SixTrack [36] over 10^5 turns, using a polar grid of initial conditions distributed in order to have 30 particles for each 2σ interval and five different values of phase angle. The momentum offset was set to 2.7×10^{-4} and the value of the normalized emittance was $\epsilon_N = 2.5$ μm, equivalent to a geometric emittance of $\epsilon = 0.335$ nm. For these studies the RF cavities are turned off so that particles do not perform synchrotron oscillations.

To account for the magnetic imperfections, just as for previous LHC studies, 60 different realisations (seeds) of the errors for the LHC magnets were assigned, generated by the program WISE. For these studies, the errors of the new inner triplet and recombination dipoles D1 and D2 for IR1, IR2 and IR5 were not considered, as well as the errors for the additional quadrupoles Q4, Q5 for the HL insertions IR1 and IR5. This is because, at the time that these studies were being performed, the values of these errors remained under study. The inclusion of these errors can contribute significantly to the degradation of the dynamic aperture, but several efforts have been made to measure and correct the nonlinear errors in the low-β insertions of the LHC, motivated in particular by the LHC second run and the luminosity upgrade [117].

5.2.1 Dynamic Aperture for the HL-LHC Lattice

Dynamic apertures studies have previously been performed for the SLHCV3.1b lattice version of the HL-LHC lattice for beam 1 [118] and for version HLLHCV1.0 [119]. This last study corresponds to the same version of the HL-LHC used for the LHeC IR integration; however, this last work includes the implementation of the error tables for the inner triplet which was still under development when this work was conducted. Furthermore,

the LHeC IR was implemented into beam 2 of the HL-LHC, for which studies had not yet been done. Therefore, in order to provide a fair comparison for the LHeC, we first perform studies for the HLLHCV1.0 version with round optics ($\beta^* = 15$ cm at IP1 and IP5) for beam 2 and with the conditions given in the last section.

Before performing dynamic aperture studies, a thin lens version of the lattice was constructed. Because SixTrack can only track particles moving in a clockwise motion, a workaround was developed. Tracking particles for beam 2 requires the use of the so called beam 4, which refers to a backwards beam 2. In principle, the direction of motion should have no effect, so the motion of particles in beam 4 should yield the same dynamic aperture as beam 2. Based on a thick lens model of beam 4 [120], we constructed the corresponding thin lens version of the lattice making use of the TEAPOT method [121]. In the case of beam 1, the pre-existing thin lens version of the lattice was used.

Tracking studies were carried out for beam 1 and beam 4 for 10^5 turns with the conditions given in last section. Fig. 5.3 illustrates the comparison between the two beams for round optics ($\beta^* = 15$ cm at IP1 and IP5 and $\beta^* = 10$ m at IP2) of the HLLHCV1.0 lattice. The points represent the average dynamic aperture over the 60 seeds while the error bars represent the lowest and highest value of the dynamic aperture over the 60 seeds.

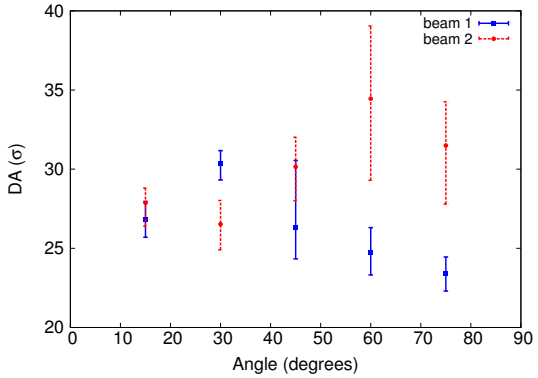

FIGURE 5.3: Dynamic aperture vs angle for the HLLHCV1.0 lattice version of the HL-LHC with round optics ($\beta^* = 15$ cm at IP1 and IP5 and $\beta^* = 10$ m at IP2) over 10^5 turns. Both beam 1 and beam 2 values are shown for 5 different angles. Markers indicate the average over the 60 seeds, while the errors bars indicate the maximum and minimum dynamic aperture value over the seeds.

Results show a similar behaviour for the two beams for small angles, however a disparity is observed at larger angles where beam 2 shows a larger dynamic aperture.

5.2.2 Dynamic Aperture Comparison Between the HL-LHC and the LHeC Nominal Case

In the previous section, the dynamic aperture was calculated for the most recently available HL-LHC lattice version; this provides the basis for a fair comparison with the same lattice but including the insertion for the LHeC IR. The implementation of the

LHeC IR is expected to have an impact on the dynamic aperture given the higher β functions in the new inner triplet.

Before performing the tracking studies in SixTrack, we made a thin lens version of the LHeC lattice for beam 2. Just as was done for the HL-LHC case, the thin lens version of the LHeC lattice was constructed using the beam 4 thick lens version of the HL-LHC as a base, but making the appropriate adjustments to implement the LHeC IR and using the TEAPOT method to make the thin lens version.

Using the same initial conditions for the beam and particles used for the HL-LHC studies, the dynamic aperture was computed for the LHeC nominal case ($\beta^* = 15$ cm at IP1 and IP5, $\beta^* = 10$ cm at IP2 with $L^* = 10$ m). The comparison of the dynamic aperture for this case with the results of beam 2 for the HLLHCV1.0 lattice with round optics (obtained in the previous section) is illustrated in Fig. 5.4. Both cases represent the average, minimum and maximum dynamic aperture found over the 60 seeds.

The implementation of the LHeC IR comes with a clear loss of dynamic aperture. Results show that the minimum value of the dynamic aperture for all angles and seeds for the LHeC nominal case is found to be around 18σ, this can be compared to the minimum value of 26σ found for the HL-LHC lattice. Further studies remain to be done considering the complete set of errors, to make sure the dynamic aperture is still above the minimum required to ensure stability.

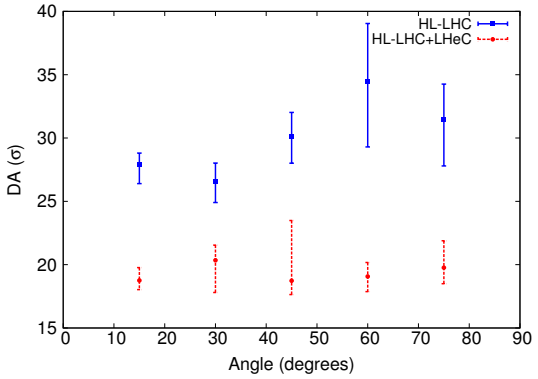

FIGURE 5.4: Comparison of the dynamic aperture as a function of the angle for beam 2 of the HL-LHC, using HLLHCV1.0 lattice version of the HL-LHC and round optics ($\beta^* = 15$ cm at IP1 and IP5 and $\beta^* = 10$ m in IP2) and the LHeC nominal lattice ($\beta^* = 15$ cm at IP1 and IP5, $\beta^* = 10$ cm at IP2 with $L^* = 10$ m) over 10^5 turns. Markers indicate the average over the 60 seeds, while the errors bars indicate the maximum and minimum dynamic aperture value over the seeds.

To better observe the dynamic aperture calculated for different angles in the LHeC nominal lattice ($\beta^* = 15$ cm at IP1 and IP5 and $\beta^* = 10$ cm at IP2 with $L^* = 10$ m), a larger sample of angles was chosen and is shown in Fig. 5.5. We observe that the minimum dynamic aperture found for all angles was 16.5σ.

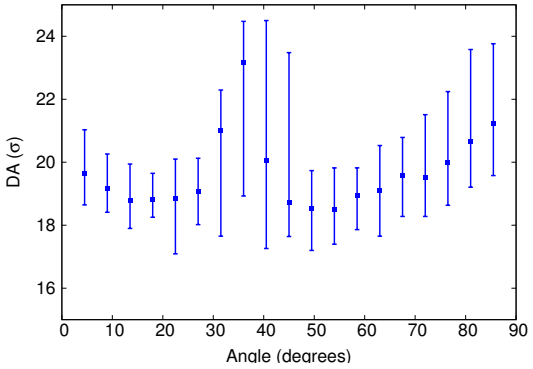

FIGURE 5.5: Dynamic aperture vs angle for beam 2 of the nominal LHeC lattice with collision optics ($\beta^* = 15$ cm at IP1 and IP5, $\beta^* = 10$ cm at IP2 and $L^* = 10$ m) over 10^5 turns. Markers indicate the average over the 60 seeds for 19 different angles, while the errors bars indicate the maximum and minimum dynamic aperture value over the seeds.

5.2.3 Dynamic Aperture Comparison for LHeC Lattices with Different L^*

In this section, we report the dynamic aperture for the different lattice configurations found in Section 4.2. By studying the stability of the beam for the different lattices, we can obtain information about possible tighter limits on the flexibility of the IR design that we were not able to determine just by considering correction of the chromaticity.

For the results presented in this section we concentrate on the optical configurations with a fixed β^* of 10 cm, which is necessary to reach a nominal luminosity of $10^{33}\text{cm}^{-2}\text{s}^{-1}$, but with different options of L^*. An LHeC-like chromatic correction scheme was used for all previous cases. The corresponding thin lens versions of the lattices and optics were made by repeating the same procedure as for the nominal case. For the tracking simulations, the initial conditions, number of turns, and the realisations of errors were the same as used in previous sections.

Figure 5.6 shows the average dynamic aperture for cases with an L^* of 10 m, 15 m, 16 m and 17 m over the 60 error seeds. The error bars indicate the maximum and minimum value found among the seeds. Results show a reduction of dynamic aperture as L^* increases. However, as shown in Fig. 5.6, the dynamic aperture for the lattice with $L^* = 15$ m is still very close to the value obtained for the nominal lattice with $L^* = 10$ m. At $L^* > 15$ m however, the dynamic aperture decreases more rapidly.

To better illustrate the reduction of dynamic aperture when increasing L^*, Fig. 5.7 shows the minimum dynamic aperture found for all seeds and angles as a function of L^*. From this figure a small reduction in the minimum dynamic aperture is observed between the case with $L^* = 15$ m and $L^* = 10$ m. A steep reduction is observed for the cases with $L^* > 15$ m.

With respect to beam stability, these results suggest that the largest possible value of L^* is 15 m, with a β^* of 10 cm. However, further studies are needed with the inclusion of

all errors to establish whether the minimum dynamic aperture required to ensure beam stability can be obtained for these lattices.

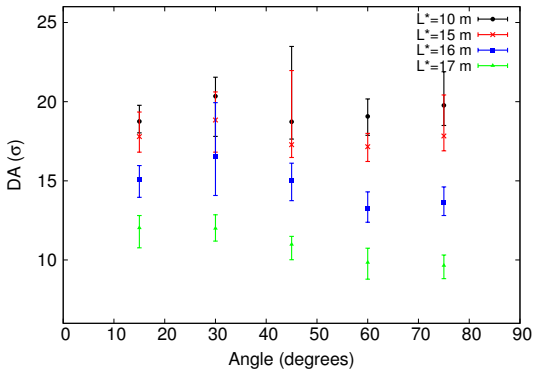

FIGURE 5.6: Comparison of dynamic aperture for LHeC lattices with different values of L^* and with collision optics ($\beta^* = 15$ cm at IP1 and IP5, $\beta^* = 10$ cm at IP2) over 10^5 turns. Markers indicate the average over 60 seeds for 5 different angles, while the errors bars indicate the maximum and minimum dynamic aperture value over the seeds, for lattices with L^* =10, 15, 16 and 17 m.

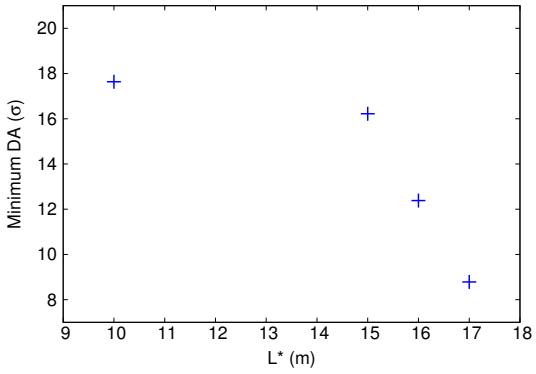

FIGURE 5.7: Minimum dynamic aperture over 60 errors seeds and 5 angles as a function of L^* for LHeC lattices with collision optics ($\beta^* = 15$ cm at IP1 and IP5, $\beta^* = 10$ cm at IP2) over 10^5 turns. Cases with $L^* = 10$ m, 15 m, 16 m and 17 m are shown.

5.2.4 Dynamic Aperture Comparison for LHeC Lattices with Different β^*

Up to this point, dynamic aperture studies were performed for a β^* fixed at 10 cm, required to achieve a luminosity of $10^{33}\text{cm}^{-2}\text{s}^{-1}$. However, in order to upgrade the luminosity by an order of magnitude to $10^{34}\text{cm}^{-2}\text{s}^{-1}$, and therefore increase the physics potential of the experiment, a β^* of 5 cm is required (Table 3.4).

Lattice configurations with varying β^* were presented in Section 4.2. An LHeC-like chromatic correction scheme was achievable for cases with a minimum β^* of 8 cm, according to the results presented in Section 4.3.2. For the case with β^* of 5 cm, an LHeC-like chromatic correction was no longer achievable, so, instead, an LHC-like chromaticity correction scheme (described in Section 4.3.1) was performed.

Fig. 5.8 shows a comparison of the dynamic aperture as a function of the angle over the 60 seeds for lattices with $\beta^* = 5$ cm, 8 cm, 9 cm and 10 cm, all with an L^* fixed at 10 m. Results show a reduction in dynamic aperture for cases with $\beta^* < 10$ cm, with similar results between the cases with $\beta^* = 9$ cm and $\beta^* = 8$ cm, but a clear reduction for the case with $\beta^* = 5$ cm. Fig. 5.9 shows the minimum dynamic aperture found for all angles and seeds. The steep reduction is observed for the case with $\beta^* = 5$ cm with the minimum dynamic aperture reaching values close to 7σ. This reduction may be due to the fact that not only are the β functions in the inner triplet the largest ones for all lattice configurations, but also there is a lack of control of the Montague functions in the collimation insertions, given the chromaticity correction scheme used.

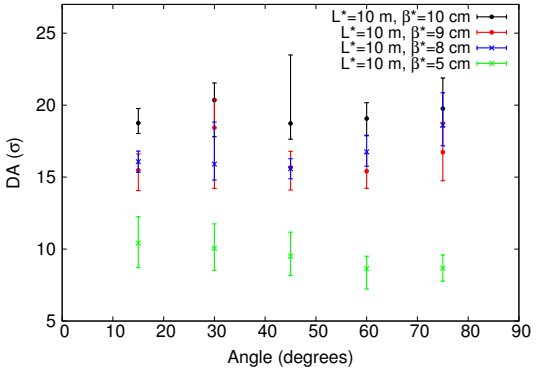

FIGURE 5.8: Comparison of dynamic aperture for the LHeC lattice with $\beta^* = 5$ cm, 8 cm, 9 cm and 10 cm at IP2 and L^* of 10 m over 10^5 turns. Markers indicate the average over the 60 seeds as a function of the angle, while the errors bars indicate the maximum and minimum dynamic aperture value over the seeds.

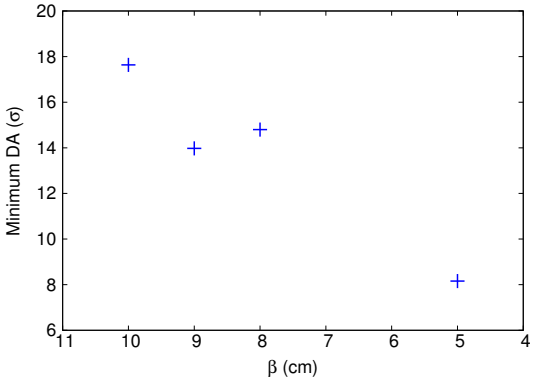

FIGURE 5.9: Minimum dynamic aperture over 60 errors seeds and 5 angles as a function of β^* for LHeC lattices with L^*=10 m over 10^5 turns. Cases with $\beta^* = 5$ cm, 8 cm, 9 cm and 10 cm are shown.

Results show that the dynamic aperture for the case with β^* of 5 cm is lower than the minimum target of the LHC even without the errors in the inner triplet. Furthermore, increasing L^* would be very challenging, given that this would result in an increase of the already large chromatic aberrations. The inability to increase L^* would result in the loss of benefits in terms of synchrotron radiation reduction and magnet design.

Therefore, if this value of β^* is necessary, further changes would need to be implemented to achieve it.

5.2.5 Dynamic Aperture Comparison Between Different Chromaticity Correction Schemes

Different chromaticity correction schemes were proposed in Sections 4.3.1 and 4.3.3. All three schemes aim to tune the sextupole families to adjust the chromaticity to a value of 2. The LHeC-like chromaticity correction scheme adds a further constraint to restrict the Montague functions in the collimation insertions. Further, the higher order correction aims to control the nonlinear chromaticity as well. The behaviour of the beam with a momentum deviation after each chromatic correction was shown in Figs. 4.26 and 4.27; however, the actual impact of each correction, to evaluate the importance of either controlling the Montague functions or controlling the chromaticity at higher orders, can be evaluated more accurately using particle tracking. In this section, the dynamic aperture is computed to determine the long term stability of the beam for each chromaticity correction scheme.

Figure 5.10 shows the computed dynamic aperture for each of the three different chromaticity correction schemes for the nominal lattice with $L^* = 10$ m and $\beta^* = 10$ cm. Results show that the higher order and the LHeC-like chromaticity correction schemes have very similar behaviour, overlapping in all angles when considering the variation over the 60 seeds. The impact can also be seen when we study the minimum dynamic aperture over all the 60 seeds; for the LHeC-like chromaticity correction scheme the minimum dynamic aperture was found to be 18.7σ, the higher order chromaticity correction scheme had a similar result with a minimum dynamic aperture of 17.4σ, while the LHC-like chromaticity correction scheme shows a reduction, with a minimum value of 14.5σ.

The implementation of the three different chromaticity correction schemes was only applied for the nominal case with $L^* = 10$ m and $\beta^* = 10$ cm, with the exception of the case with $L^* = 10$ m and $\beta^* = 5$ cm mentioned in last section, where the LHC-like chromatic correction scheme was implemented. For the rest of the lattice configurations only the LHeC-like chromatic correction scheme was used for tracking studies. This is because given the computational time required to perform each study, a single lattice was considered sufficient to provide a first comparison, although this is an area of possible further studies if a more thorough comparison is required.

In summary, a more refined chromaticity correction than the LHC-like scheme is needed. While differences arise for the LHeC-like and higher order corrections, they both present similar dynamic aperture and appear suitable to address the high chromatic aberrations resulting from the large β functions in the inner triplet.

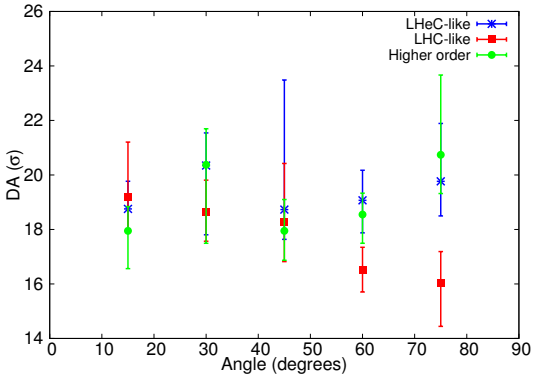

FIGURE 5.10: Comparison of dynamic aperture vs angle for different chromaticity correction schemes for the LHeC lattice with $\beta^* = 10$ cm and $L^* = 10$ m over 10^5 turns. Markers indicate the average dynamic aperture over the 60 seeds while the error bars indicate the minimum and maximum dynamic aperture value over the seeds. Results with an LHC-like (red), LHeC-like(blue) and higher order (green) chromaticity correction schemes are shown.

5.3 Frequency Map Analysis in the LHeC

FMA was performed using the program SUSSIX [122] applied to short term tracking in SixTrack. The same thin lens versions of the lattice configurations found in Section 5.2 were used but the tracking was performed for fewer turns (10^4). The grid of initial conditions was also changed, this time a larger sample of initial conditions was used, with initial amplitudes in the range $0 < I < 20\sigma$ and angles $0 < \theta < 90$ degrees. Unlike the dynamic aperture, these studies cover a wider range of amplitudes to be able to study the overall behaviour in phase space.

SUSSIX was used to perform a high-precision calculation of the tunes for the different particles at 5,000 and 10,000 turns. The calculation of the tunes was carried out using the principles explained in Section 1.5.6. The data were compiled with a Python script developed at CERN [123]. The diffusion factor, also described in Section 1.5.6, was calculated, giving the variation of the tunes for the different initial conditions.

5.3.1 Frequency Map Analysis for the LHeC Nominal Case

The diffusion rate in a frequency map with resonance lines up to order 12 is shown in Fig. 5.11 for the lattice with $L^* = 10$ m and $\beta^* = 10$ cm. The frequency maps also show the resonance lines $m_x Q_x + m_y Q_y = l$ where m_x, m_y and l are integers. The resonances causing a disruption are labelled with its corresponding values in the form (m_x, m_y). This type of plot, illustrating the frequencies over a diagram showing the resonance lines, will be referred to as "tune map" in the following discussion.

The effect of the various resonance lines can be observed from the figure. Particles close to the resonance lines (-4,7), (-3,6), (-2,5) and (-3,9) have an increase in their corresponding diffusion rate from -12 to approximately -8. For the higher-order resonances of (-1,1) and (-1,4), the effects on the particles appears to be stronger, with a corresponding diffusion factor close to -2.

To observe the effect that the reconstructed tune has on the amplitude of the particles, Fig. 5.12 illustrates the same tune map but now the colour scale represents the initial amplitude of the tracked particle. It is clear from the figure that the reconstructed tune diverges further from the original chosen working point as the amplitude increases.

The tune map can also be represented in terms of the initial angle, as shown in Fig. 5.13. We can observe from the figure that the highest order resonance causing a distortion (-1,1) is affecting particles close to the x axis, while the second higher order resonance (-1,4) affects particles close to the y axis.

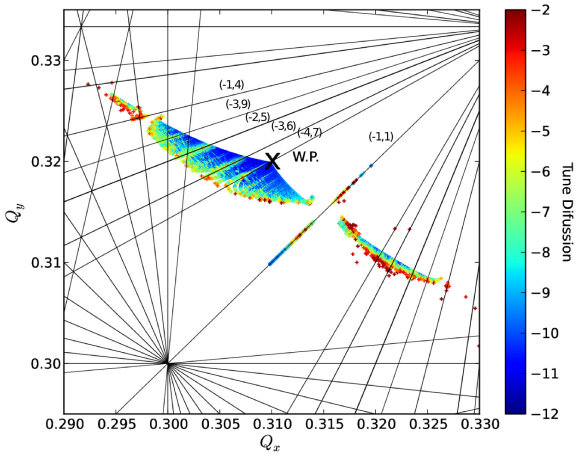

FIGURE 5.11: Diffusion factor on a tune map over a resonance diagram of order 12 for the LHeC lattice with $L^* = 10$ m and $\beta^* = 10$ cm. Tracking was done over 10^3 turns for a grid of initial angles varying from $0 < \theta < 90°$ and initial amplitudes $0 < I < 22\sigma$. The resonance lines causing a disruption in the diffusion factor are labelled in the figure.

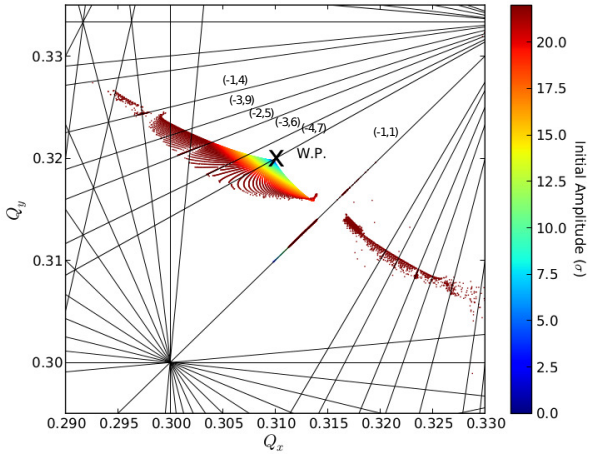

FIGURE 5.12: Initial amplitude plotted against the computed fractional parts of the horizontal (Q_x) and vertical (Q_y) tune over a resonance diagram of order 12 for the LHeC lattice with $L^* = 10$ m and $\beta^* = 10$ cm. Tracking was done over 10^3 turns for a grid of initial angles varying from $0 < \theta < 90°$ and initial amplitudes $0 < I < 22\sigma$. The resonance lines causing a disruption in the diffusion factor are labelled in the figure.

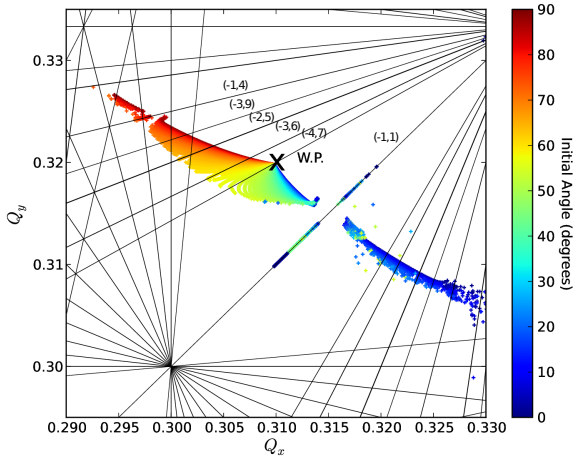

FIGURE 5.13: Initial angle plotted against the computed horizontal (Q_x) and vertical (Q_y) tune over a resonance diagram of order 12 for the LHeC lattice with $L^* = 10$ m and $\beta^* = 10$ cm. Tracking was done over 10^3 turns for a grid of initial angles varying from $0 < \theta < 90°$ and initial amplitudes $0 < I < 22\sigma$. The resonance lines causing a disruption in the diffusion factor are labelled in the figure.

The diffusion factor is plotted also for the different initial amplitudes and angles for the lattice with $L^* = 10$ m and $\beta^* = 10$ cm in Fig. 5.14. This type of plot, showing the diffusion factor over the initial amplitudes, will be referred to as an "amplitude map" in the following discussion. Also shown on the amplitude maps are the resonances causing a disruption in the diffusion factor. This identification was possible by restricting the ranges in amplitude and angle in both the amplitude and tune maps and then making a comparison between the two.

The amplitude map also shows, as expected, more stable motion for low amplitudes. For larger amplitudes, regions of instability are observed. A small region of stability, even at large amplitudes, is observed at an angle of $\approx 45°$. On closer inspection however, if the condition $|Q_x - Q_y| \leq 0.0001$ is imposed, the particles in the amplitude map lie within this apparently stable region, as illustrated in Fig. 5.15. Therefore, the particles in this apparently stable region lie on the resonance line (-1,1), and consequently their true stability cannot be ensured.

5.3.2 Frequency Map Analysis Comparison for LHeC Lattices with Different L^*

The dynamic aperture studies presented in Section 5.2 provided information about the long term stability of the beam for different lattice configurations. In this section, FMA studies are reported for some of the same lattice configurations to obtain further information about the nonlinear effects in particles with different initial conditions.

Figures 5.16 and 5.17 illustrate the diffusion factor plotted against the corresponding tunes in a resonance map for the lattice with $L^* = 15$ m and with $L^* = 17$ m respectively, both with a fixed β^* at 10 cm.

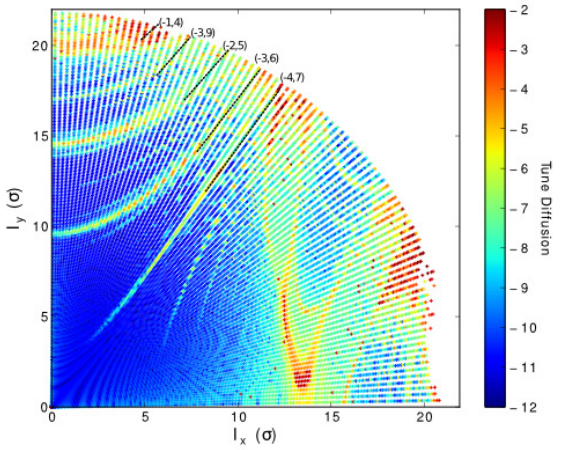

FIGURE 5.14: Diffusion rate as a function of the initial amplitudes for the LHeC lattice with $L^* = 10$ m and $\beta^* = 10$ cm. Tracking was done over 10^3 turns for a grid of initial angles varying from $0 < \theta < 90°$ and initial amplitudes $0 < I < 22\sigma$. The resonance lines causing a disruption in the diffusion factor are labelled in the figure.

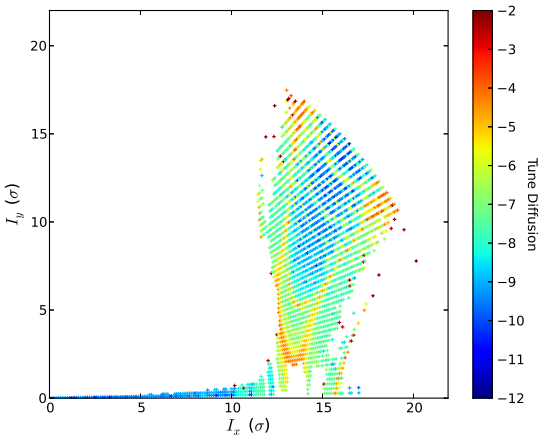

FIGURE 5.15: Diffusion rate as a function of the initial amplitudes for the LHeC lattice with $L^* = 10$ m and $\beta^* = 10$ cm. Tracking was done over 10^3 turns for a grid of initial angles varying from $0 < \theta < 90°$ and initial amplitudes $0 < I < 22\sigma$ for the region where $|Q_x - Q_y| < 0.0001$.

By making the comparison with Fig. 5.11 it is clear that the lattice with $L^* = 15$ m and $\beta^* = 10$ cm shows similar results as the nominal lattice with $L^* = 10$ m and $\beta^* = 10$ cm, while differences arise for the lattice with $L^* = 17$ m and $\beta^* = 10$ cm.

The corresponding amplitude maps are shown in Figs. 5.18 and 5.19. Just as for the nominal case we use the tune maps to match the resonances with the instability zones in the amplitude maps.

In conclusion, lattices with $L^* = 10$ m and $L^* = 15$ m, both with $\beta^* = 10$ cm, present a similar behaviour, except for the outer zones where the initial amplitudes I are closer to 20σ, however these amplitudes are already larger than the dynamic aperture. Both lattices present zones with a larger diffusion factor at lower angles and initial amplitudes close to 12σ.

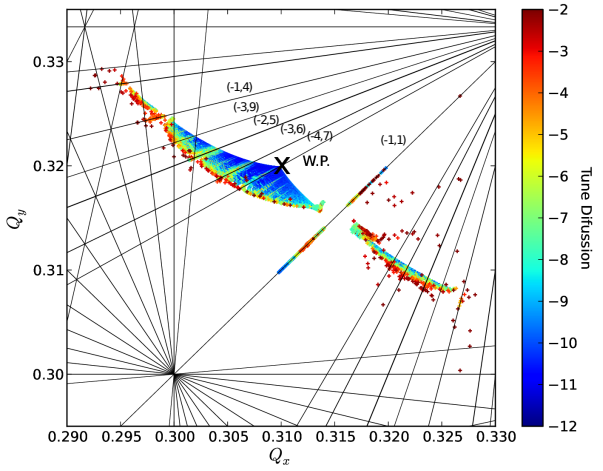

FIGURE 5.16: Diffusion factor on a tune map over a resonance diagram of order 12 for the LHeC lattice with $L^* = 15$ m and $\beta^* = 10$ cm. Tracking was done over 10^3 turns for a grid of initial angles varying from $0 < \theta < 90°$ and initial amplitudes $0 < I < 22\sigma$. The resonance lines causing a disruption in the diffusion factor are labelled in the figure.

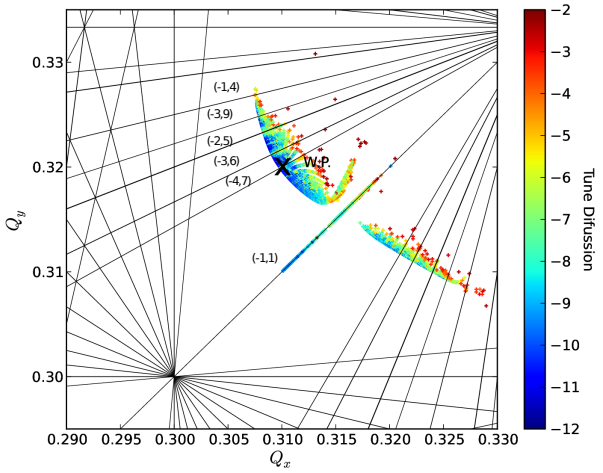

FIGURE 5.17: Diffusion factor on a tune map over a resonance diagram of order 12 for the LHeC lattice with $L^* = 17$ m and $\beta^* = 10$ cm. Tracking was done over 10^3 turns for a grid of initial angles varying from $0 < \theta < 90°$ and initial amplitudes $0 < I < 22\sigma$. The resonance lines causing a disruption in the diffusion factor are labelled in the figure.

A clear reduction of the stable region is observed for the lattice with $L^* = 17$ m and $\beta^* = 10$ cm as can be seen in Fig. 5.19. It is important to emphasize that this significant change in the frequency maps is observed for values of L^* where the dynamic aperture starts to collapse, as observed in Fig. 5.6 and Fig. 5.7. These results show that even though FMA does not necessarily provide a very accurate indication of the long-term dynamic aperture, given that it is computed for a different number of turns, these examples showed how both studies give consistent results in determining the point at which the stability of the beam can no longer be ensured, increasing the confidence in the results.

The collapse in both the dynamic aperture and the stability region indicated by FMA

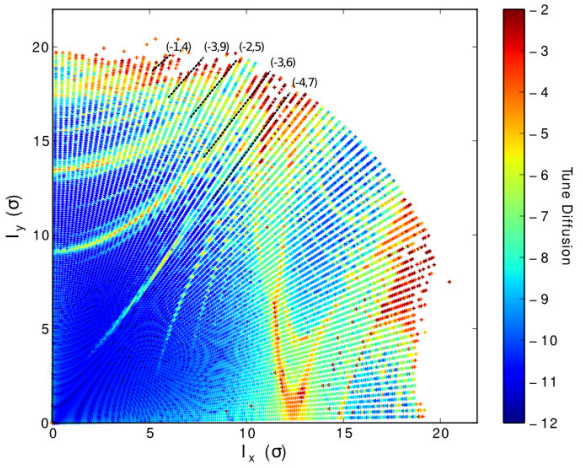

FIGURE 5.18: Diffusion rate as a function of the initial amplitudes for the LHeC lattice with $L^* = 15$ m and $\beta^* = 10$ cm. Tracking was done over 10^3 turns for a grid of initial angles varying from $0 < \theta < 90°$ and initial amplitudes $0 < I < 22\sigma$. The resonance lines causing a disruption in the diffusion factor are labelled in the figure.

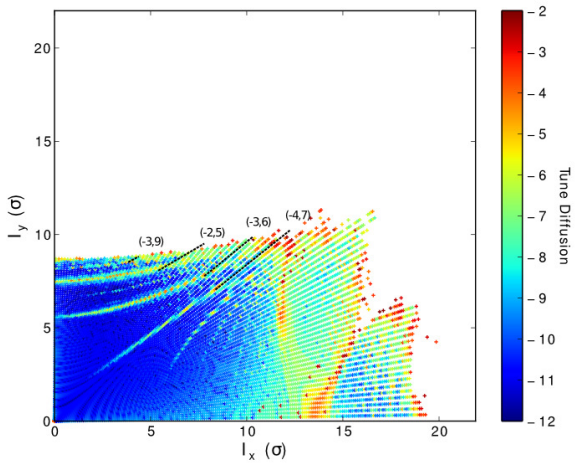

FIGURE 5.19: Diffusion rate as a function of the initial amplitudes for the LHeC lattice with $L^* = 17$ m and $\beta^* = 10$ cm. Tracking was done over 10^3 turns for a grid of initial angles varying from $0 < \theta < 90°$ and initial amplitudes $0 < I < 22\sigma$. The resonance lines causing a disruption in the diffusion factor are labelled in the figure.

at $L^* > 15$ m is possibly due the high β functions at the inner triplet. Furthermore, the configuration is at the limit where the chromaticity can be controlled with the sextupole correction scheme (see Fig. 4.25).

5.3.3 Frequency Map Analysis Comparison Between Different Chromaticity Corrections

FMA studies were carried out in the previous section to provide a comparison of the nonlinear effects on different lattice configurations. In this section, the same methods are used to study the effects of the different chromaticity correction schemes introduced

in Section 4.3.3. The dynamic apertures for these correction schemes were shown in Section 5.2.5.

The various chromaticity correction schemes were implemented in the nominal lattice with $\beta^* = 10$ cm and $L^* = 10$ m and using the same tracking conditions that were used for the previous studies. The tune maps for the higher order chromaticity correction scheme and the LHC-like chromaticity correction scheme are shown in Figs. 5.20 and 5.21 respectively. By comparing these plots with the LHeC-like chromaticity correction scheme in the nominal case (Fig. 5.11) it is clear that there are similarities between the LHeC-like and higher order chromaticity correction schemes. However, in the case of the LHC-like correction scheme the behaviour is different, with the "cone" formed by the particles folding to the other side.

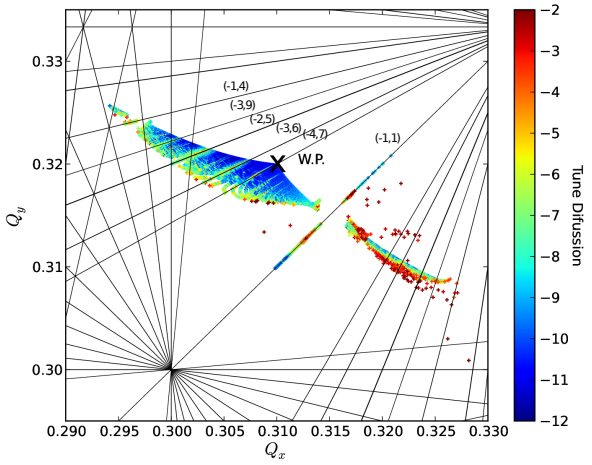

FIGURE 5.20: Diffusion factor on a tune map over a resonance diagram of order 12 for the LHeC lattice with $L^* = 10$ m and $\beta^* = 10$ cm using the higher order chromaticity correction scheme. Tracking was done over 10^3 turns for a grid of initial angles varying from $0 < \theta < 90°$ and initial amplitudes $0 < I < 22\sigma$. The resonance lines causing a disruption in the diffusion factor are labelled in the figure.

The amplitude maps are shown in Figs. 5.22 and 5.23 for the higher order and LHC-like chromaticity correction scheme respectively. These can be compared with the results obtained for the LHeC-like chromaticity correction scheme in Fig. 5.14.

The amplitude maps for the LHeC-like and the higher order chromaticity correction schemes look very similar (as was also the case for the tune maps), except for the small areas with $I_x \sim 14\sigma$ and $I_y \sim 2\sigma$, and $I_x \sim 4\sigma$ and $I_y \sim 20\sigma$ where instabilities observed for the LHeC-like chromaticity correction scheme are no longer present for the higher order correction scheme. Also, the "stable" region for $Q_x \approx Q_y$ observed in the LHeC-like chromaticity correction scheme is larger for the higher order chromaticity correction scheme. Just as was the case for the dynamic aperture, benefits do seem to arise from having a higher order correction in comparison with the LHeC-like chromaticity correction, although the differences are relatively small. Therefore we consider both corrections to have roughly the same effects.

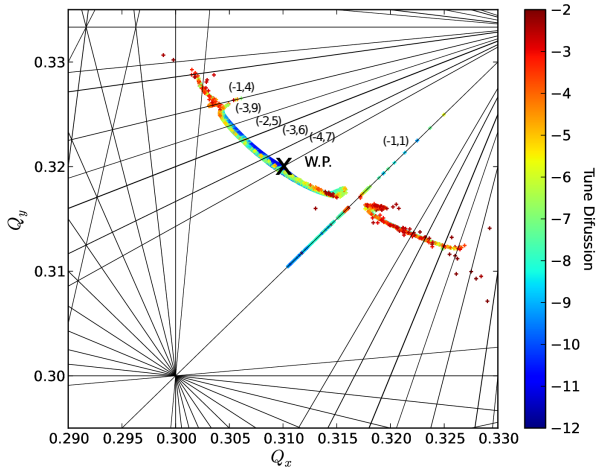

FIGURE 5.21: Diffusion factor on a tune map over a resonance diagram of order 12 for the LHeC lattice with $L^* = 10$ m and $\beta^* = 10$ cm using the LHC-like chromaticity correction scheme. Tracking was done over 10^3 turns for a grid of initial angles varying from $0 < \theta < 90°$ and initial amplitudes $0 < I < 22\sigma$. The resonance lines causing a disruption in the diffusion factor are labelled in the figure.

On the other hand, the amplitude maps for the LHC-like chromaticity correction scheme do not seem as drastically different from the other two corrections schemes, in contrast to the case with the tune maps. However, there are some differences in areas where the higher order correction has more stability, the area for large I_y and small I_x for example. The biggest difference is observed for the region $Q_x \approx Q_y$ which appears stable for both the higher order and LHeC-like chromaticity correction schemes, but appears less stable with the LHC-like chromaticity correction scheme.

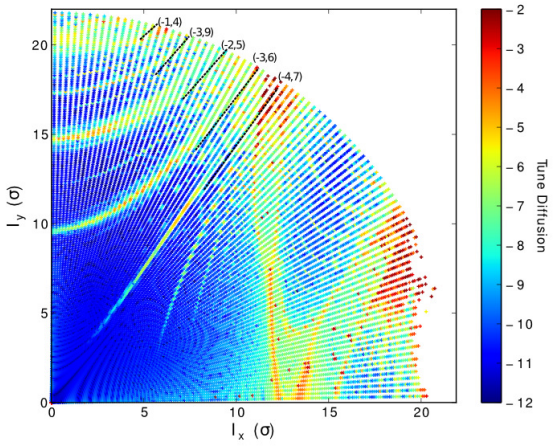

FIGURE 5.22: Initial amplitude plotted against the computed horizontal (Q_x) and vertical (Q_y) tune over a resonance diagram of order 12 for the LHeC lattice with $L^* = 10$ m and $\beta^* = 10$ cm using the higher order chromaticity correction scheme. Tracking was done over 10^3 turns for a grid of initial angles varying from $0 < \theta < 90°$ and initial amplitudes $0 < I < 22\sigma$. The resonance lines causing a disruption in the diffusion factor are labelled in the figure.

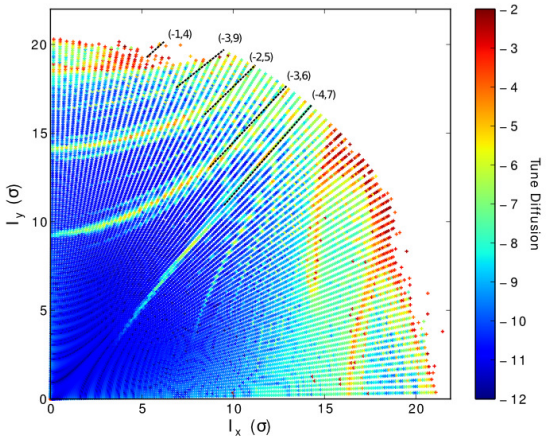

FIGURE 5.23: Initial amplitude plotted against the computed horizontal (Q_x) and vertical (Q_y) tune over a resonance diagram of order 12 for the LHeC lattice with $L^* = 10$ m and $\beta^* = 10$ cm using the LHC-like chromaticity correction scheme. Tracking was done over 10^3 turns for a grid of initial angles varying from $0 < \theta < 90°$ and initial amplitudes $0 < I < 22\sigma$. The resonance lines causing a disruption in the diffusion factor are labelled in the figure.

5.4 Conclusions

Tracking studies of the LHeC lattice configurations using different chromaticity correction schemes allows the study of long-term stability of the beam. Possible effects of nonlinearities can be compared, complementing the study presented in Chapter 4.

Following on from the work in Chapter 4, different lattice configurations provided possibilities to increase L^* up to 20 m, and minimize β^* to 5 cm. However, a chromaticity correction scheme with the specified constraints on $Q'_{x,y}$ and the Montague functions $W_{x,y}$ is only achieved up to $L^* = 18$ m with $\beta^* = 10$ cm and $\beta^* = 8$ cm with $L^* = 10$ m. In this chapter, we presented dynamic aperture studies in the presence of magnet errors for the different lattice configurations. Results show that a reasonable dynamic aperture is achieved for up to $L^* = 15$ m but significant reduction of dynamic aperture is observed for $L^* > 15$ m. Furthermore, FMA studies show that the two different lattices $L^* = 10$ m with $\beta^* = 10$ cm and $L^* = 15$ m with $\beta^* = 10$ cm present similar behaviour of the tune diffusion, but again several differences arise for the case with $L^* = 17$ m with $\beta^* = 10$ cm. Limitations are shown by both the dynamic aperture and the FMA studies: the dynamic aperture does not provide detailed information about the overall phase space behaviour while the FMA does not provide accurate information about the long term dynamic aperture; however, the consistency between the two studies in providing information at which point the stability of the lattices can no longer be ensured ($L^* > 15$ m) gives confidence in the results.

In terms of chromaticity correction, the LHeC-like and higher order schemes demonstrate very similar dynamic aperture and FMA. The higher order scheme shows slightly better results at large angles. On the other hand, the LHC-like correction shows the opposite effect for larger angles with a lower dynamic aperture and a larger diffusion

rate in the FMA. In summary, a more refined chromaticity correction scheme approach than the one currently used in the LHC is needed for the LHeC lattice, and either the LHeC-like scheme or the higher order scheme would provide sufficient dynamic aperture.

The complete study shows that the solution with $\beta^* = 10$ cm is sufficient to achieve the desired luminosity of the baseline version, but considerable benefits arise for the cases where $L^* > 10$ m, in particular for $L^* = 15$ m. For this value of L^* normal-aperture quadrupoles can be used, a proper chromaticity correction scheme can be achieved, there is a reduction of synchrotron radiation power, and there is a relatively small reduction in dynamic aperture with respect to the nominal case.

The more challenging parameters of the upgrade version to achieve a luminosity of $L = 10^{34}$ cm^{-2}s^{-1} with a $\beta^* = 5$ cm require further studies in order to provide a feasible design.

Chapter 6

Effects of Inner Triplet Quadrupole Fringe Fields in the HL-LHC and LHeC Lattices

The HL-LHC experiment aims to upgrade the luminosity of the LHC from $10^{34}\mathrm{m}^{-2}\mathrm{s}^{-1}$ to $10^{35}\mathrm{m}^{-2}\mathrm{s}^{-1}$ in IP1 and IP5. This increase of luminosity will be partly achieved with the reduction of the β^* at both interaction points. In practice this will involve the introduction of new quadrupoles in the inner triplets of the HL-LHC's interaction regions. These quadrupoles will not only have stronger fields but since a smaller β^* means a more rapid increase in beam size away from the interaction point, the new quadrupoles will need larger apertures. With these changes, the effects of the fringe fields of the inner triplet, described in Section 2.1, are expected to increase. Previous tracking studies for the LHC and HL-LHC, which used a hard-edge model for the magnets, do not account for these effects, so it was considered important to investigate possible impacts on machine performance, and in particular the effects on the dynamic aperture.

This chapter presents tracking studies based on a model of the HL-LHC that allows different representations of fringe fields to be included. Using this model, the impact of a variety of fringe field representations are studied via frequency map analysis.

6.1 Nominal Case Without Fringe Fields

Tracking studies have been previously performed using the HLLHCV1.0 lattice (described in Section 3.6.2), to obtain the dynamic aperture (described in Section 1.5.5) of the machine [124] and to study the effects of nonlinearities via Frequency Map Analysis (FMA) [125], described in Section 1.5.6. These studies have been performed using the kick code SixTrack [36] for a thin lens version of the lattice and without the consideration of the fringe fields.

Studies of the fringe fields in the following sections make use of an accelerator tracking code called SAMM [126]. This code enables the easy configuration of new component

types, which is useful when investigating fringe fields. In order to benchmark the code, FMA studies were first done without fringe fields and compared with the results obtained with SUSSIX [122], the standard code used in CERN for FMA studies.

6.1.1 SAMM Particle Tracking Code

The Simple Accelerator Modelling in Matlab (SAMM) code [126] is an accelerator tracking code developed at the University of Liverpool. It consists of a library of Matlab and C routines for modelling beam dynamics in particle accelerators.

The SAMM project directory comprises of the subdirectories that contain classes definitions for the beam and beamline, types of particles and accelerator components, as well as function definitions for the analysis of beam dynamics in a beamline.

A benefit of this structure is that user-defined components can be created easily by adding component class implementation files.

6.1.2 Comparison of SUSSIX with SAMM for the HL-LHC Nominal Case Without Fringe Fields

As illustrated in Chapters 4 and 5 MADX is the standard code used to perform optical studies in the LHC, tracking studies are done in SixTrack, and FMA studies are normally done with SUSSIX. In order to benchmark the SAMM tracking code, a comparison is made first between SAMM and the previous codes for the nominal case of HL-LHC without fringe fields.

Results show a good agreement between the β functions. This is illustrated in Figs. 6.1 and 6.2 where the β_x and β_y function are shown respectively along the HL-LHC ring computed with both MADX and SAMM. The difference in β_x and β_y functions between the two tracking codes scaled by the corresponding value of the beta function, is also shown in the figures.

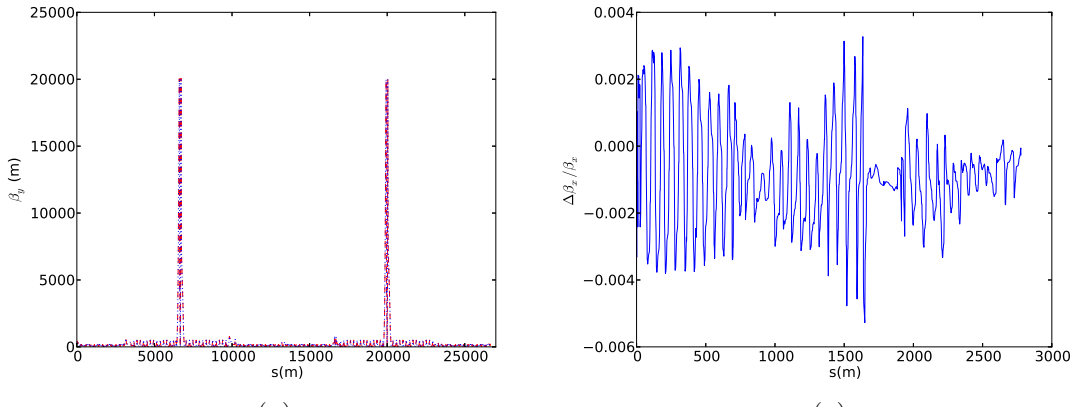

(A) (B)

FIGURE 6.1: (a) β_x function along the HL-LHC lattice with SAMM (red) and MADX (blue) tracking. (b) Difference between the β_x functions calculated with SAMM and MADX scaled by the β function.

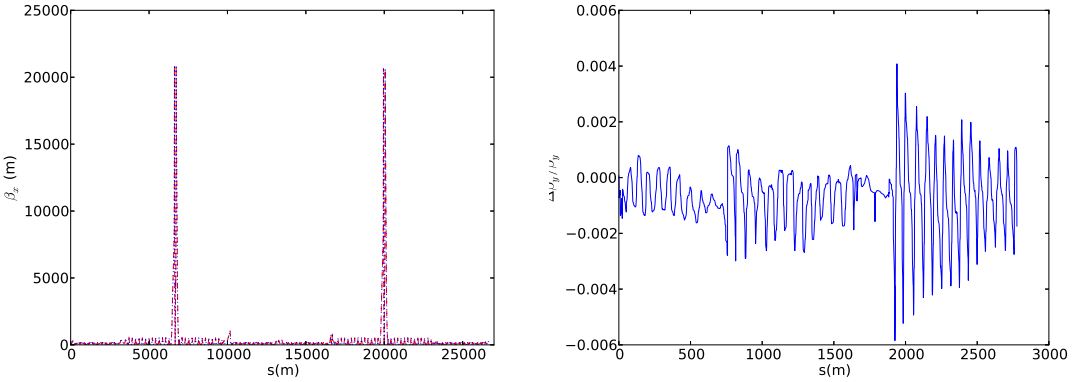

(A) (B)

FIGURE 6.2: (a) β_y function along the HL-LHC lattice with SAMM (red) and SixTrack (blue) tracking. (b) Difference between the β_y functions calculated with SAMM and SixTrack tracking scaled by the β function.

FMA studies, explained in Section 1.5.6 and previously done for the LHeC lattice in Chapter 4, were carried out for the nominal case with no fringe fields with tracking performed in both SUSSIX and SAMM. This comparison is illustrated in Fig. 6.3 where amplitude maps are shown using both particle tracking codes for the thin lens version of the HLLHCV1.0 lattice and the same seed of random errors. Particle tracking performed in SUSSIX was used to calculate the diffusion factor based on the variation of the tune over 1000 and 2000 turns. This was done for a range of initial conditions in the amplitudes varying from $0 < I < 20\sigma$, where $I = \sqrt{I_x^2 + I_y^2}$, and angles $\theta = I_y/I_x$ varying from $0 < \theta < 90°$. For SAMM the tracking was done for a similar number of turns, calculating the diffusion factor over 1028 and 2048 turns for a sample of initial conditions with a varying amplitude of $0 < I < 20\sigma$ in the x and y direction with a 0.2 resolution between the points. The amplitudes I_x and I_y give the amplitudes in the horizontal and vertical directions and are defined in terms of the emittance ($\epsilon_{x,y}$) and the Courant–Snyder parameter $\gamma_{x,y}$ as:

$$I_x = \frac{x}{\sqrt{\epsilon_x/\gamma_x}}, \tag{6.1}$$

$$I_y = \frac{y}{\sqrt{\epsilon_y/\gamma_y}}. \tag{6.2}$$

Tracking in both codes was done for a proton beam of 7 TeV and a normalized emittance of 3.75 μrad, corresponding to a geometric emittance of 0.502 nm. The observation point for both cases was chosen at IP3. Also, particle tracking in both SAMM and SUSSIX was performed with RF cavities in the ring turned off, thus the momentum deviation remained constant over the course of the tracking (i.e. there were no synchrotron oscillations). These conditions will be used for all following FMA studies.

The diffusion factor is also plotted against the corresponding tunes and over a resonance map of order 15. Fig. 6.4 shows the tune map with particle tracking performed

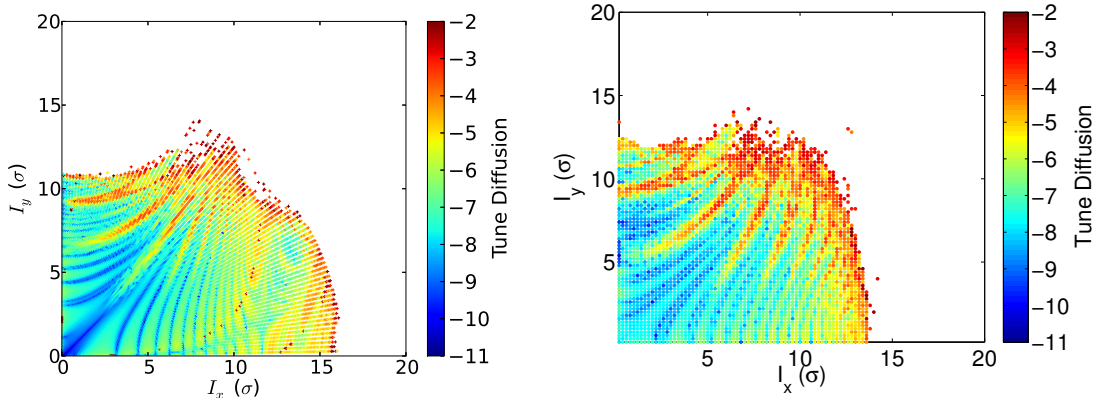

(A) (B)

FIGURE 6.3: Diffusion rate as a function of the initial amplitudes I_x and I_y with (a) particle tracking over 2000 turns in SUSSIX; and (b) 2048 turns in SAMM.

in SUSSIX and SAMM.

Results in both the tune and amplitude maps show reasonable agreement between the two codes, although some differences are found between the amplitude maps. In particular SUSSIX shows a larger range of stable particles in the horizontal direction. However, when looking more closely at this range of particles in the SUSSIX tune map, it is found that their positions lie close to the coupling resonance $Q_x = Q_y$, therefore their stability can not be ensured.

Despite the observed differences between the two different tracking codes, the overall behaviour of their amplitude maps in the stable zone is very similar. This gives confidence to perform further studies with SAMM for a model including fringe fields.

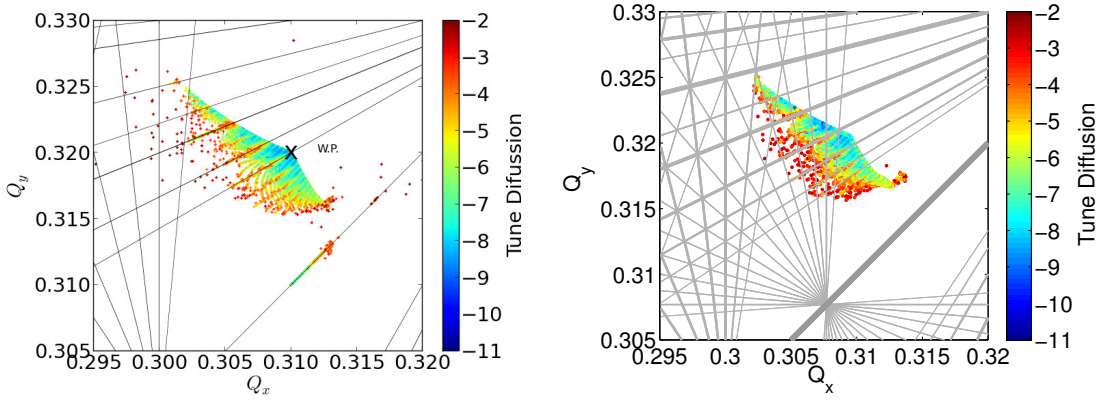

(A) (B)

FIGURE 6.4: Diffusion factor in a tune map for the initial angles over a resonance diagram of order 15 with (a) particle tracking over 2000 turns done in SUSSIX; and (b) 2048 turns done in SAMM.

6.1.3 Comparison of Matlab and C Tracking

The SAMM accelerator code provides two different ways to perform particle tracking. The first was a set of routines within Matlab, and the second uses a tracking library in C. C tracking was implemented to reduce the computational time required to do the tracking, although it requires separate tracking routines called from Matlab.

Figures 6.5 and 6.6 show the β_x and β_y function with tracking performed in Matlab and C. The difference along the ring scaled by the beta function is also shown in the figures. Table 6.1 shows the computed tunes for each method.

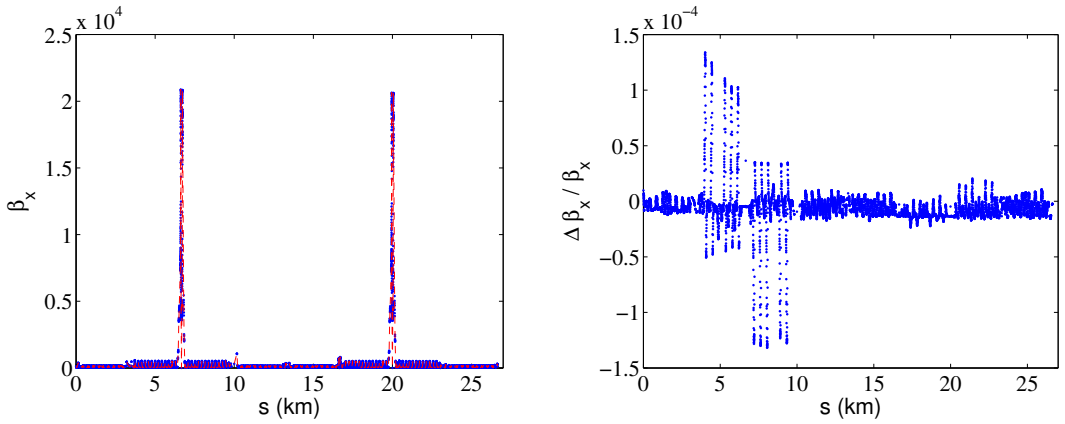

(A) (B)

FIGURE 6.5: (a) β_x function along the HL-LHC lattice with Matlab (red) and C (blue) tracking. (b) Difference between the β_x functions with Matlab and C tracking scaled by the beta function along the HL-LHC lattice.

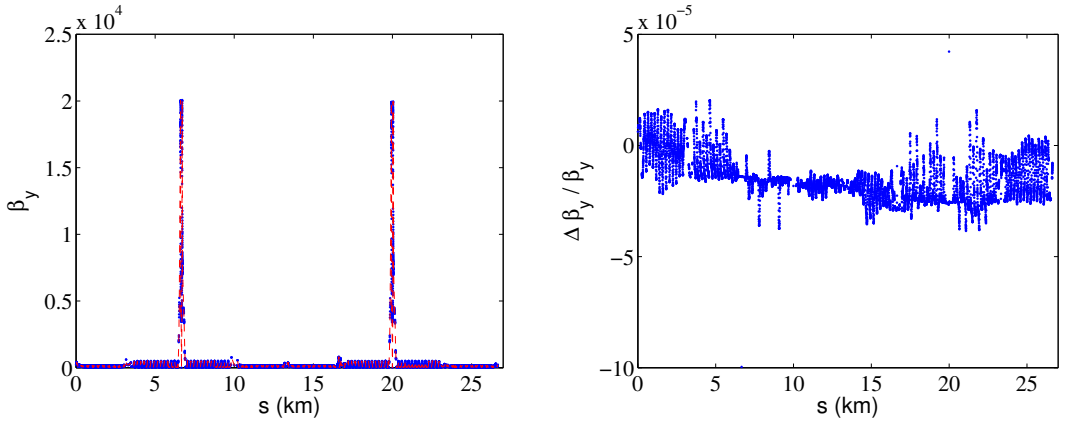

(A) (B)

FIGURE 6.6: (a) β_y function along the HL-LHC lattice with Matlab (red) and C (blue) tracking. (b) Differences between the β_y functions with Matlab and C tracking scaled by the beta function along the HL-LHC lattice.

Amplitude maps for both types of tracking are shown in Fig. 6.7. The diffusion factor in this case is given comparing the tune between 128 and 256 turns.

Tracking	Q_x	Q_y
Matlab	62.309462	60.320552
C	62.309463	60.320552

TABLE 6.1: Computed tunes for the nominal case with no fringe fields with seed #1 with Matlab (left) and C (right) tracking in SAMM.

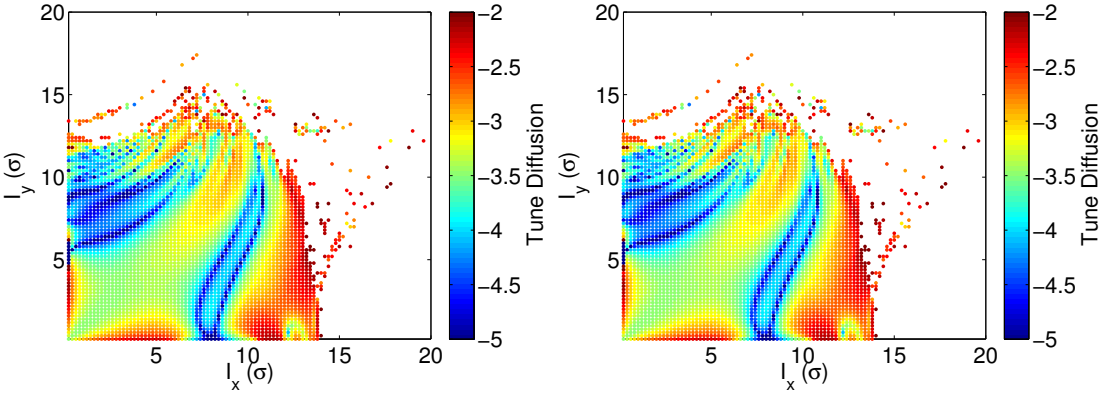

(A) (B)

FIGURE 6.7: Diffusion rate as a function of the initial amplitudes I_x and I_y over 256 turns in computed in SAMM with particle tracking performed in Matlab (a) and in C (b).

Results show that the difference between the β functions ($\Delta\beta/\beta$) from the different tracking routines in SAMM is less than 1.5 $\times 10^{-4}$ along the whole ring, and the computed tune is the same up to the 5th decimal place. Therefore, optics calculations show very good agreement between both methods. Furthermore, amplitude maps produced from both types of tracking show almost identical results.

The only difference between the two tracking methods is the computing time: the C tracking was almost twice as fast as Matlab tracking for the nominal case. C tracking is therefore recommended over Matlab tracking, specially for cases when longer tracking is expected. When tracking routines were available in this language, C tracking was used, otherwise tracking in Matlab was performed instead. The remainder of studies presented in this chapter use both tracking implementations interchangeably.

6.2 Fringe Field Studies

Given the good agreement between the SUSSIX and SAMM results in Section 6.1.2 we had a sufficient level of confidence to perform fringe field studies in SAMM to compare with the nominal model without fringe fields. This section explains how the fringe fields are modelled using the tools presented in Chapter 2 (Section 6.2.1). We then describe the implementation of the fringe fields in the HL-LHC lattice (Section 6.2.2) and, finally, we present the FMA studies with fringe fields (Section 6.2.3).

6.2.1 Modelling Fringe Fields

Modelling the fringe fields of the quadrupoles of the inner triplet of the HL-LHC involves three main steps: first, numerical field data for the fringe fields are obtained; second, analytical expressions for the fringe fields are constructed; and third, an appropriate integration method is used to obtain transfer maps for the fringe fields.

Obtaining numerical field data

The fringe fields were implemented in both the entrance and exit of the quadrupoles of the inner triplet. Each of these quadrupoles are divided into two sections: A and B. The gradients and lengths of each of the sections of the quadrupoles are shown in Table 6.2.

Quadrupole Name	Length (m)	Gradient (T/m)
MQXFA_B3L1/5	4.02	-139.46
MQXFB_A3L1/5	4.02	-139.46
MQXFB_B2L1/5	6.82	139.46
MQXFB_A2L1/5	6.82	139.46
MQXFA_B1L1/5	4.02	-139.46
MQXFA_A1L1/5	4.02	-139.46
MQXFA_A1R1/5	4.02	139.46
MQXFA_B1R1/5	4.02	139.46
MQXFB_A2R1/5	6.82	-139.46
MQXFB_B2R1/5	6.82	-139.46
MQXFA_A3R1/5	4.02	139.46
MQXFA_B3R1/5	4.02	139.46

TABLE 6.2: Characteristics of the new inner triplet quadrupoles in IR1 and IR5.

Numerical field data for the fringe fields were obtained using a computational electromagnetic model [127], shown in Fig 6.8. The numerical field data were obtained for the exit of a quadrupole with negative gradient ($dB_y/dx < 0$). The numerical field data were given on a rectangular grid in the transverse position (x, y) from the axis of the magnet to 75 mm in x and y, in steps of 3 mm. In the longitudinal direction the field was given over a range of 800 mm in steps of 5 mm.

The fringe fields at the entrance of the magnets were obtained by reversing the dependence of the field on the longitudinal position. Also, assuming the appropriate symmetry, fringe fields were obtained for the positive (horizontally focusing) quadrupoles by scaling the field by a factor of -1.

Obtaining an analytical field

Given that in the fringe field region fields change with longitudinal position the full three-dimensional nature of the fields needs to be properly included in any description of the fields. In this case, the technique of the generalised gradients, described in Section 2.1, was used.

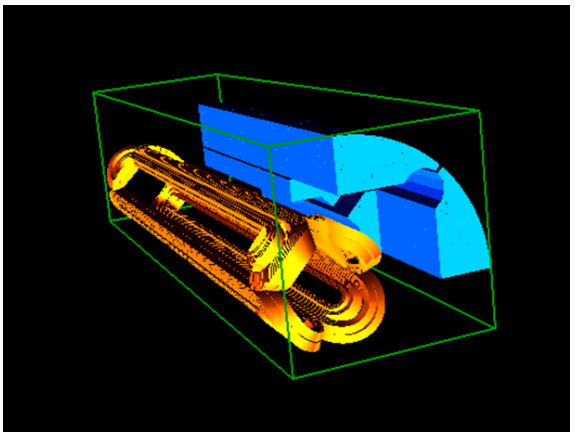

FIGURE 6.8: Computational model used to calculate the fringe fields numerical data at the exit of a quadrupole of the inner triplet with negative gradient [127].

Generalised gradients were calculated from the numerical field, as explained in Section 2.1. From the generalised gradients, an analytical description of the vector potential (Eq. 2.7) and the magnetic field (Eq. 2.10) at each longitudinal position was obtained.

Recalling the result obtained in Eq. 2.10, the components of the magnetic field in terms of the generalised gradients are given by an infinite sum in l and m. This summation must be truncated at some point. The sum over l was given from values $l = 0$ to $l = 4$. In the case of the multipoles, only the values $m = 2, 6$ and 10 were taken into account.

To avoid having to compensate for the linear focusing caused by the quadrupole component of the fringe fields, the generalised gradient component causing that effect ($m = 2$, $l = 0$) was set to zero. This way, both the effects of higher-order multipoles ($m = 6$, $m = 10$), and the variation of quadrupole effects with longitudinal position ($m = 2$, $l > 0$), are retained. This method provides a straightforward way to compensate for the linear focusing effect of the fringe field without the need to retune the lattice. A drawback of this approach is that by setting only this element to zero, the field no longer exactly satisfies Maxwell's equations.

An alternative way to obtain an analytical representation of the fringe fields has been found using Enge functions [128]. The present study, however, will only include the analytical field derived from the generalised gradients.

Integration

A number of different methods of integration can be used to transport particles through the fringe fields. Competing criteria must be considered when selecting a particular method, regarding symplecticity (described in Section 2.3), the approximations needed and the computational time. For this study, two different integration methods were used to model the fringe fields: a power series map and a Runge–Kutta integrator: both methods were described in Chapter 2. Below is the description of how these methods were implemented for the fringe field case.

1. **Power series map**. A Wu–Forest–Robin explicit symplectic integrator (described in Section 2.6.2) is used to generate the transfer map through the fringe field using Eq. 2.89. The analytical field given by the generalised gradients is used at each step to compute the variables at the next point. A differential algebra code (section 2.5.1) was used to generate a truncated power series map at certain order across the entire fringe field. Power series maps were also constructed with Mathematica up to the tenth order [129]. Power series maps of order $n < 10$ were constructed by truncating the tenth order map to the corresponding order n.

   Once power series maps have been computed for each quadrupole they can be included as a single element in the beamline, giving the values of the variables at the exit of the fringe field in terms of the initial values as described in Section 2.5. This single element implementation is expected to have relatively little impact in the computation time to do the tracking with respect to the nominal HL-LHC without fringe fields.

   However, power series maps have the disadvantage that, even when the original integrator used is symplectic, the final truncation gives a symplectic error. Techniques have been developed to compensate the symplectic error; however such techniques have not been included in this study. Furthermore, the Wu–Forest–Robin integrator makes use of the paraxial approximation. Even when this is a good approximation (as is hoped in the present case) it is sensible to compare it with an integrator that does not use the paraxial approximation and is also symplectic.

2. **Runge–Kutta**. The second method that we use is a Runge–Kutta integrator (described in Section 2.6.3). The algorithm chosen for this method was the second order Runge–Kutta implicit integrator, also known as the implicit midpoint rule. The error of this method scales as h^2, where h is the step size in the integration.

   The implementation of this method, in contrast to the power series map, cannot be given in terms of a single transfer map for the full fringe fields since the method is implicit and algebraic equations must be solved at each point during the tracking. This is expected to have a significant impact on the computational time needed for the tracking in comparison with the power series map method. The advantage of this method is that it provides symplecticity to numerical precision. Furthermore, the Runge–Kutta method does not require the use of the paraxial approximation as was the case for the Wu–Forest–Robin integrator.

6.2.2 Implementation of Fringe Fields in the HL-LHC Lattice

Fringe fields of the inner triplet quadrupoles can be implemented in the lattice model in several ways: the fringe field can be contained entirely within the hard edge model, half way out of the hard edge model or beyond the ends of the hard edge model. The three different configurations are illustrated in Fig. 6.9. Presumably, one of the options

will be a more accurate representation of the actual magnets, but for the present study, given the easy implementation and without any further information of the best model to be used, the third option (with the fringe fields located outside the hard edge model) was chosen.

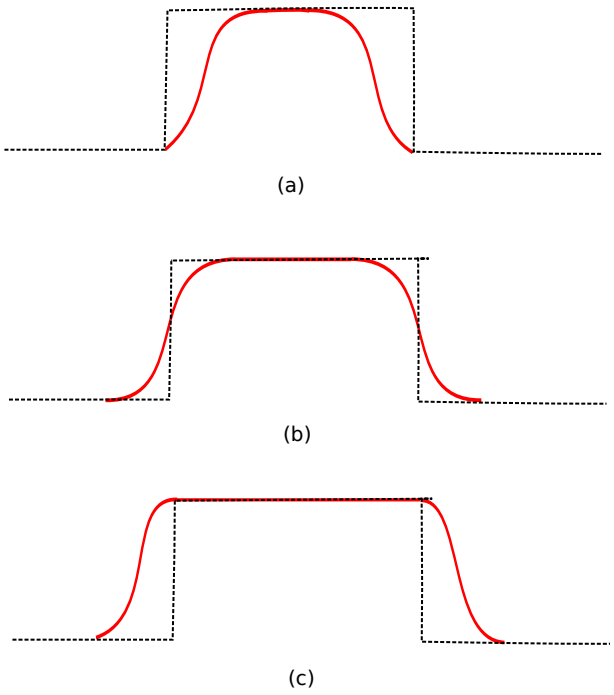

FIGURE 6.9: Possible configurations for the location of the fringe field of the inner triplet. The fringe fields can be implemented as (a) completely inside the hard edge model of the magnet, (b) half way out of the magnet or (c) completely outside the hard edge model. In each of the cases the black dotted line indicates the hard-edge model of the magnet, while the red lines indicate the fringe field model. The actual extent of the fringe fields with respect to the magnet is much smaller than represented in the figure, scaled for illustration purposes.

As a first step in the implementation, the thin lens version of the HLLHCV1.0 lattice (explained in Section 5.2.1) is imported from MADX to SAMM. This version represents the quadrupole field as a series of 16 kicks separated by drifts. Fringe fields were then added in the chosen form (power series map or Runge–Kutta) at the entrance and exit of each quadrupole of the inner triplet, as indicated in Table 6.2. To avoid double-counting the length of the fringe fields "negative drifts" were added next to each fringe field element. Fig. 6.10 illustrates schematically the original thin lens configuration and the model including the fringe fields.

The comparison of the β functions between the nominal case and the fringe field model using a power series map and a Runge–Kutta integrator is shown in Figs. 6.11 and 6.12 respectively. Results show that the difference between the nominal case and the fringe field model is very similar for both fringe fields models used. This difference however, is relatively small, reaching a maximum scaled difference of 3×10^{-3}. The

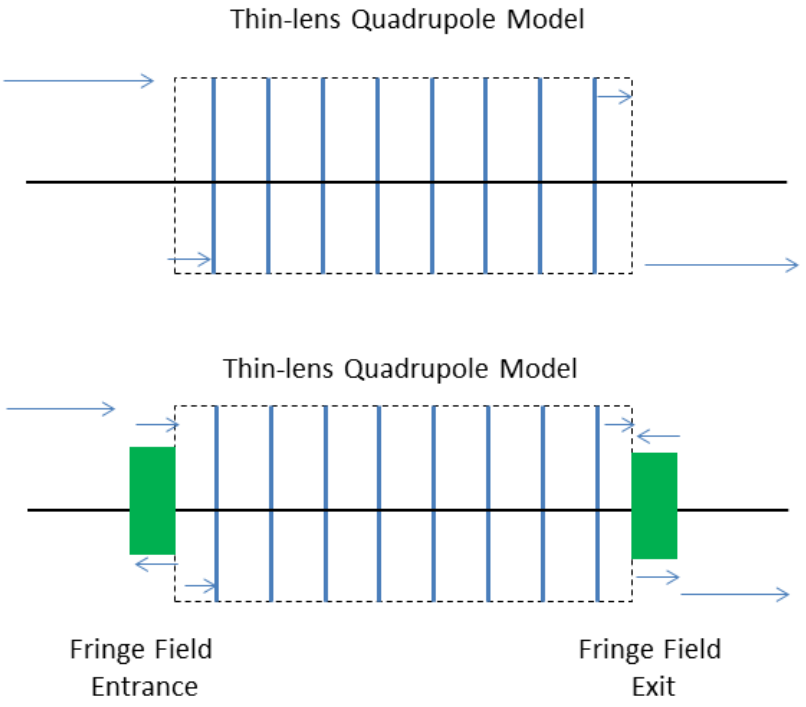

FIGURE 6.10: Schematic illustration of the thin lens model of a quadrupole in the inner triplet (top), where eight kicks are separated by drift sectors (in the actual thin lens model used for tracking 16 kicks are applied per magnet). Also illustrated is the implementation of the fringe fields (green) in the thin lens model (bottom).

computed tunes are also very similar, as can be observed in Table 6.3. Tracking studies will provide us with information on the nonlinear impact of the fringe fields.

Model	Q_x	Q_y
Nominal	62.309462	60.320552
Tenth order power series map	62.309948	60.320988
Runge–Kutta	62.309929	60.320992

TABLE 6.3: Computed tunes for the nominal case with no fringe fields, the fringe fields represented by a power series map of tenth order and the fringe fields represented by a Runge–Kutta integrator. The same random errors are applied to the lattice in each case (corresponding to the standard seed #1).

6.2.3 Results of Frequency Map Analysis with Lattices with Fringe Fields

The following sections present the results from FMA studies using the HL-LHC lattice including different representations (power series map or Runge-Kutta integrator) for the inner triplet quadrupole fringe fields. The studies aim to determine the effects of the fringe fields modelled with both a power series map and a Runge–Kutta integrator with

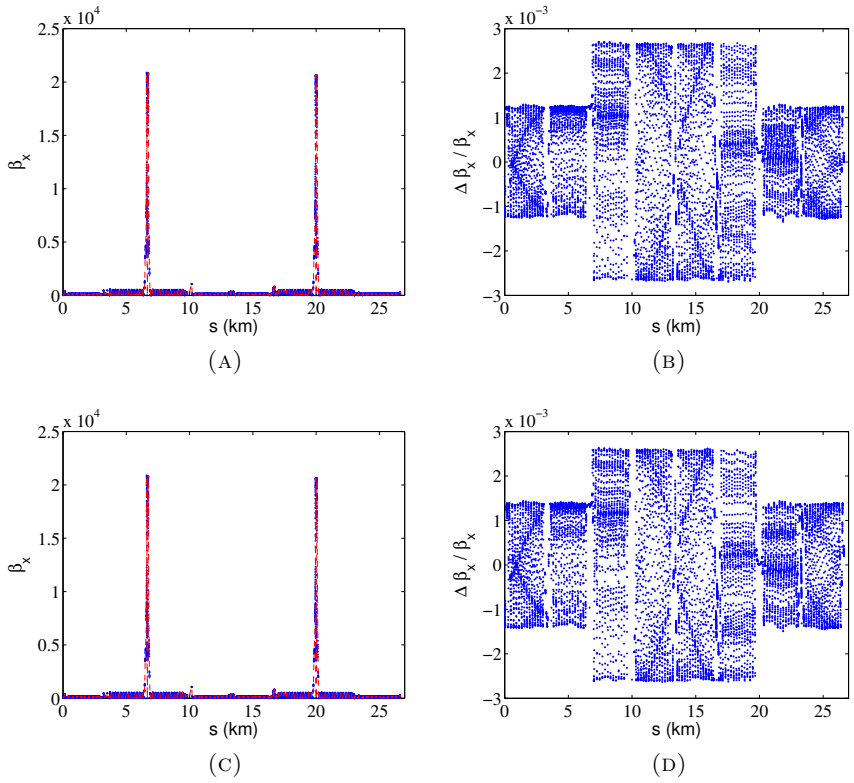

FIGURE 6.11: Comparison of β_x along the HL-LHC lattice between the nominal case without fringe fields (red) with the fringe field model (blue) using: (a) a tenth order power series map and (c) a Runge–Kutta integrator. Also shown is the difference in the β_x functions (scaled by the corresponding beta function) between the nominal case and the fringe field model with: (b) a tenth order power series map and (d) a Runge–Kutta integrator.

respect to the nominal lattice. In particular, FMA can be useful to give some indication of the dynamic aperture in the lattice.

Comparison between power series maps truncated at different orders.

As explained previously, one of the issues with using power series map is to choose an appropriate order of the map that would illustrate an accurate description of the dynamics. To determine whether the tenth order map chosen for the studies is of sufficiently high order, the results are compared with power series maps of different orders. Power series maps of fourth and sixth order were generated from the tenth order map by truncating this map at the corresponding order.

The tracking performed in this case used the same initial amplitudes as the nominal case without fringe fields, but here the tracking was performed over 256 turns. This smaller number of turns is less demanding in terms of the computational time in comparison with the previous cases; however, it does come with a loss of resolution as the instability zones are not as clearly defined, but for this case this number of turns seems sufficient to make a comparison. The diffusion rate for different amplitudes is shown in

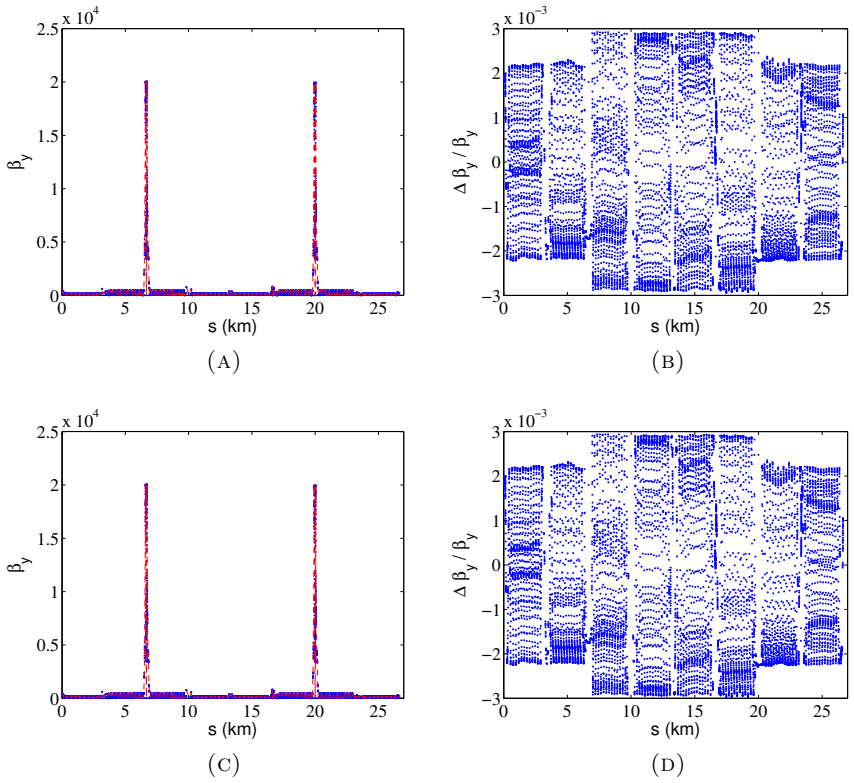

FIGURE 6.12: Comparison of β_y along the HL-LHC lattice between the nominal case without fringe fields (red) with the fringe field model (blue) using: (a) a tenth order power series map and (c) a Runge–Kutta integrator. Also shown is the difference in the β_y functions (scaled by the corresponding beta function) between the nominal case and the fringe field model with: (b) a tenth order power series map and (d) a Runge–Kutta integrator.

Fig. 6.13 (a), (b) and (c) for power series maps truncated at order 4, 6 and 10 respectively. The same seed of random errors was applied to the lattice in each case. Results

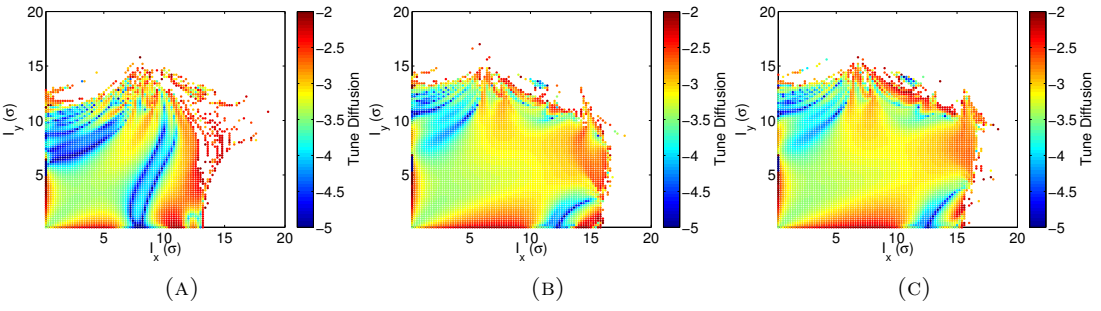

FIGURE 6.13: Amplitude map with fringe fields modelled with a power series map of order 4 (a), 6 (b) and 10 (c) for seed #1, with tracking performed in SAMM over 256 turns.

for the power series map of order 4 are very similar to the results for the nominal case. However, at order 6 differences arise, especially for amplitudes when $I_x > 8\sigma$ where a larger zone of instability appears, not observed in the nominal or the power series map

of order 4. Similarities between the results using power series maps of orders 6 and 10 are also observed, which leads to the conclusion that increasing the order of the map beyond 10 is unlikely to make any significant change in the results. The following studies will be done with a tenth order power series map.

Comparison with different representations for the fringe fields and different seeds

The results presented in this section compare the effect of the fringe fields modelled with a power series map and with the effects calculated using a Runge–Kutta integrator. Results were computed for different seeds of magnet errors. This will allow us to observe not only the impact of different seeds in the tracking but to check that the results are consistent between different realisations of the errors.

The tracking was done again for 256 turns in each case and for a sample of initial amplitudes from 0 to 20σ with a 0.2 resolution between the points. Results for seed #1 to #10 are shown in Fig. 6.14 to Fig 6.23. Each figure shows the amplitude plots for the nominal case without fringe fields, with a power series map of tenth order and with the Runge–Kutta integrator. The corresponding tune maps are shown in Fig. 6.24 to Fig. 6.33.

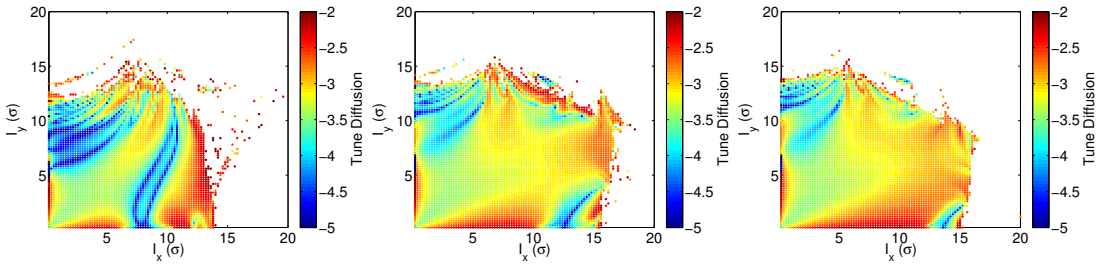

(A) (B) (C)

FIGURE 6.14: Amplitude maps for the HL-LHC lattice for (a) the nominal case with no fringe fields; (b) for the fringe field model with a tenth order power series map; and (c) with the fringe field modelbased on the Runge–Kutta integrator. Tracking was done in SAMM for 256 turns using error seed #1.

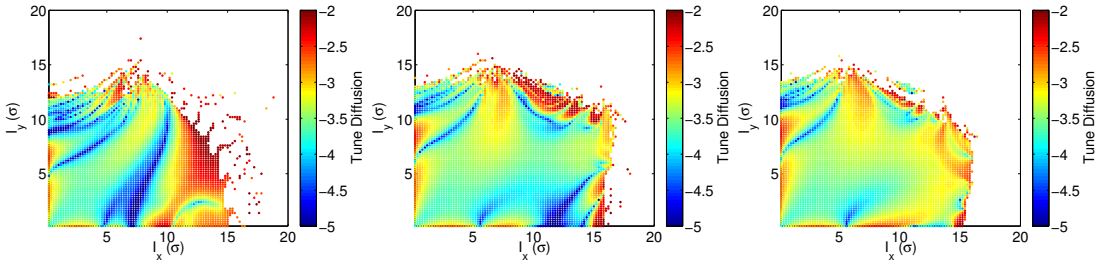

(A) (B) (C)

FIGURE 6.15: Amplitude maps for the HL-LHC lattice for (a) the nominal case with no fringe fields; (b) for the fringe field model with a tenth order power series map; and (c) with the fringe field model based on the Runge–Kutta integrator. Tracking was done in SAMM for 256 turns using error seed #2.

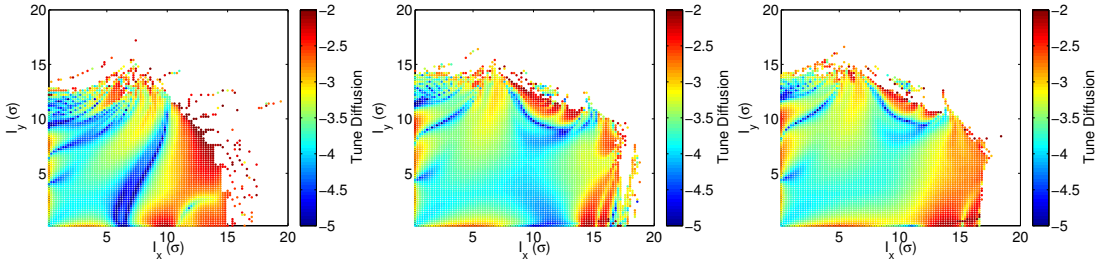

(A) (B) (C)

FIGURE 6.16: Amplitude maps for the HL-LHC lattice for (a) the nominal case with no fringe fields; (b) for the fringe field model with a tenth order power series map; and (c) with the fringe field model based on the Runge–Kutta integrator. Tracking was done in SAMM for 256 turns using error seed #3.

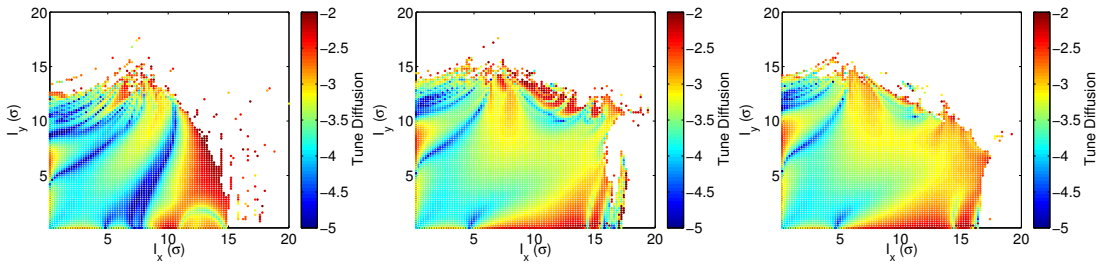

(A) (B) (C)

FIGURE 6.17: Amplitude maps for the HL-LHC lattice for (a) the nominal case with no fringe fields; (b) for the fringe field model with a tenth order power series map; and (c) with the fringe field model based on the Runge–Kutta integrator. Tracking was done in SAMM for 256 turns using error seed #4.

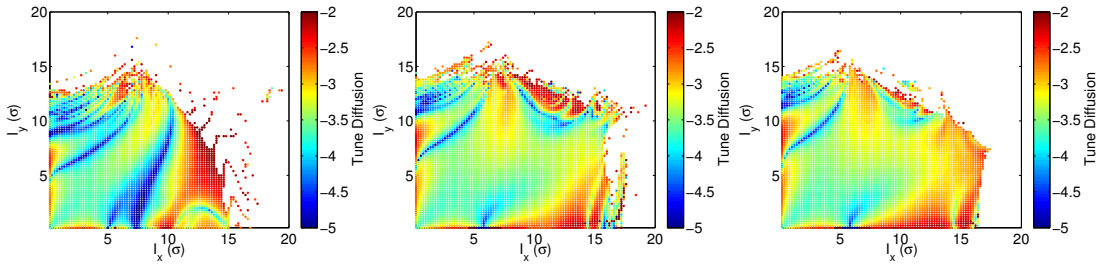

(A) (B) (C)

FIGURE 6.18: Amplitude maps for the HL-LHC lattice for (a) the nominal case with no fringe fields; (b) for the fringe field model with a tenth order power series map; and (c) with the fringe field model based on the Runge–Kutta integrator. Tracking was done in SAMM for 256 turns using error seed #5.

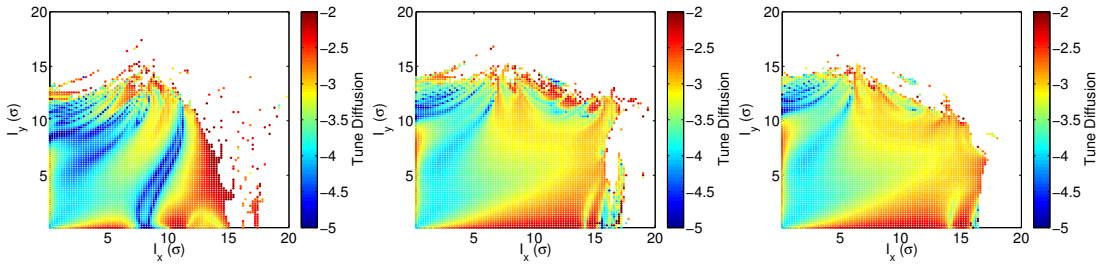

(A) (B) (C)

FIGURE 6.19: Amplitude maps for the HL-LHC lattice for (a) the nominal case with no fringe fields; (b) for the fringe field model with a tenth order power series map; and (c) with the fringe field model based on the Runge–Kutta integrator. Tracking was done in SAMM for 256 turns using error seed #6.

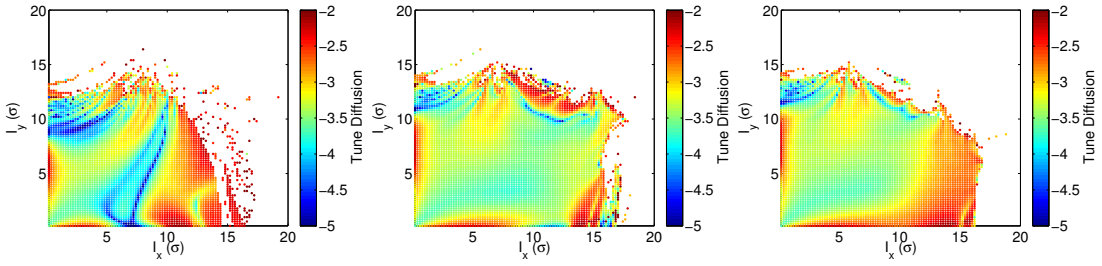

(A) (B) (C)

FIGURE 6.20: Amplitude maps for the HL-LHC lattice for (a) the nominal case with no fringe fields; (b) for the fringe field model with a tenth order power series map; and (c) with the fringe field model based on the Runge–Kutta integrator. Tracking was done in SAMM for 256 turns using error seed #7.

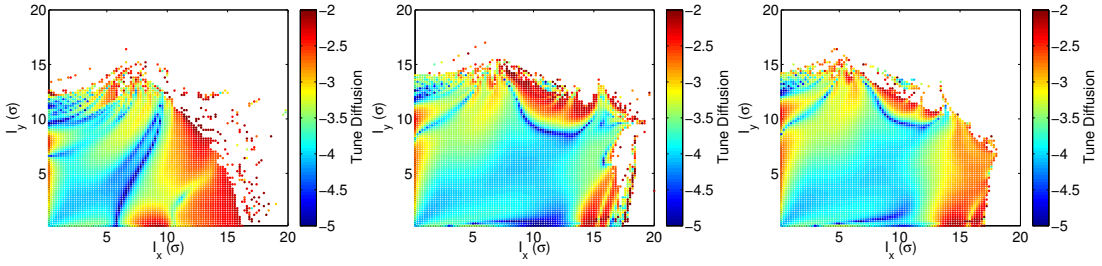

(A) (B) (C)

FIGURE 6.21: Amplitude maps for the HL-LHC lattice for (a) the nominal case with no fringe fields; (b) for the fringe field model with a tenth order power series map; and (c) with the fringe field model based on the Runge–Kutta integrator. Tracking was done in SAMM for 256 turns using error seed #8.

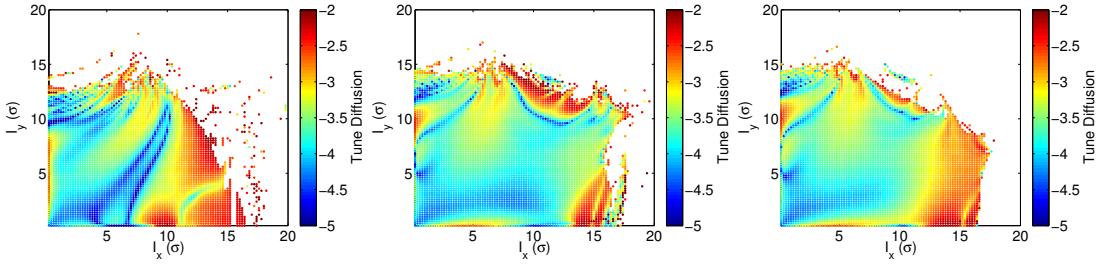

(A) (B) (C)

FIGURE 6.22: Amplitude maps for the HL-LHC lattice for (a) the nominal case with no fringe fields; (b) for the fringe field model with a tenth order power series map; and (c) with the fringe field model based on the Runge–Kutta integrator. Tracking was done in SAMM for 256 turns using error seed #9.

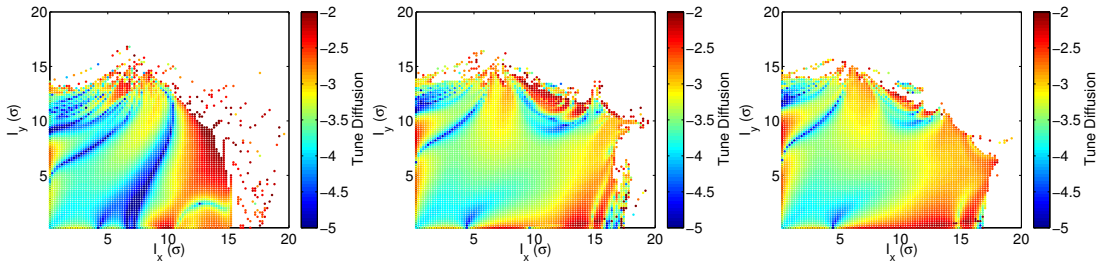

(A) (B) (C)

FIGURE 6.23: Amplitude maps for the HL-LHC lattice for (a) the nominal case with no fringe fields; (b) for the fringe field model with a tenth order power series map; and (c) with the fringe field model based on the Runge–Kutta integrator. Tracking was done in SAMM for 256 turns using error seed #10.

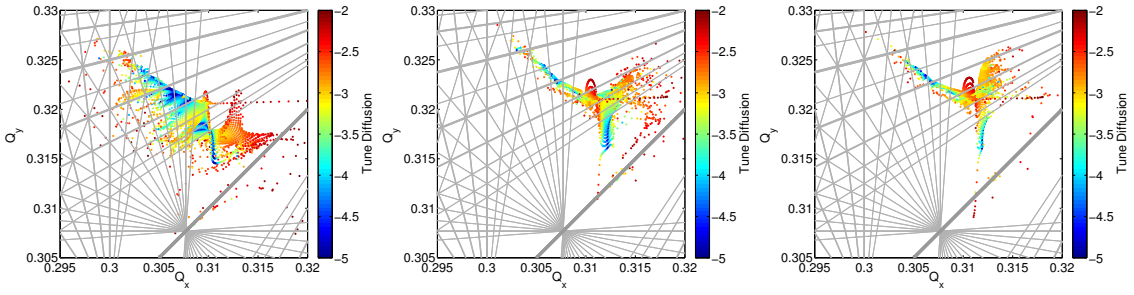

(A) (B) (C)

FIGURE 6.24: Tune maps for the HL-LHC lattice for (a) the nominal case with no fringe fields; (b) for the fringe field model with a tenth order power series map; and (c) with the fringe field model based on the Runge–Kutta integrator. Tracking was done in SAMM for 256 turns using error seed #1.

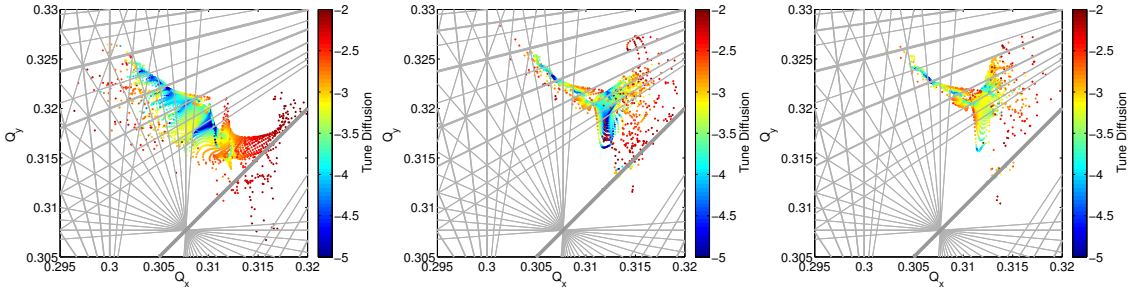

(A) (B) (C)

FIGURE 6.25: Tune maps for the HL-LHC lattice for (a) the nominal case with no fringe fields; (b) for the fringe field model with a tenth order power series map; and (c) with the fringe field model based on the Runge–Kutta integrator. Tracking was done in SAMM for 256 turns using error seed #2.

The nominal cases show consistent results between the different seeds with only minor differences in the region with $10\sigma < I_x < 15\sigma$. The fringe fields seem to have a bigger effect that any variation between the seeds of the nominal case. The amplitude maps modelled with the tenth order power series map and the Runge–Kutta integrator show similar results for each error seed, with minor differences for particles with large horizontal amplitude. Both cases show a variation with respect to the nominal case in the region $10\sigma < I_x < 15\sigma$. However, the dynamic aperture for the fringe field model does not seem to be significantly affected with respect to the nominal case.

The behaviour of the diffusion is less clear in the tune maps. There are significant differences between the case without fringe fields, and the cases with fringe fields; the two representations of the fringe fields (power series map and Runge-Kutta integrator) appear to give similar results. However, to understand better the behaviour of these tune maps in the fringe fields models, and to better compare them with the nominal case without fringe fields, a higher resolution is needed. This is achieved in the next section by increasing the number of turns.

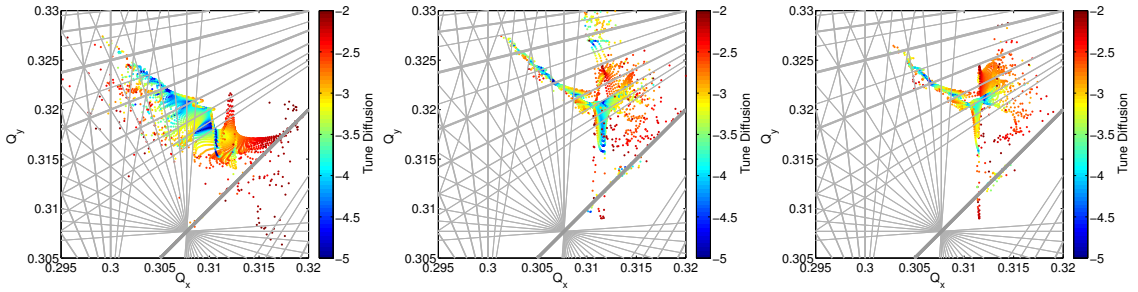

(A) (B) (C)

FIGURE 6.26: Tune maps for the HL-LHC lattice for (a) the nominal case with no fringe fields; (b) for the fringe field model with a tenth order power series map; and (c) with the fringe field model based on the Runge–Kutta integrator. Tracking was done in SAMM for 256 turns using error seed #3.

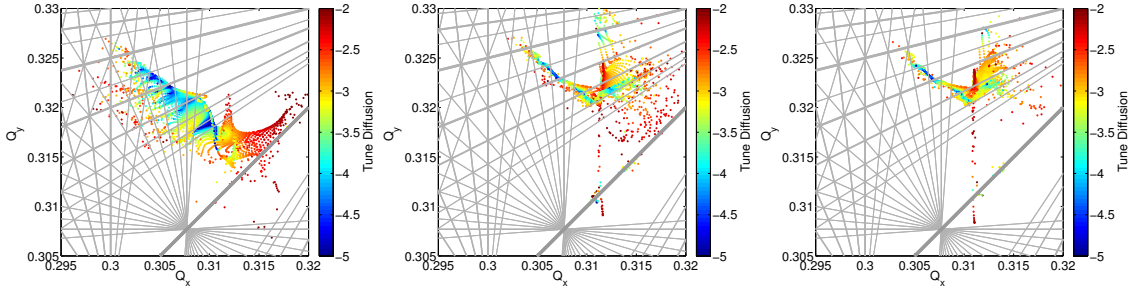

(A) (B) (C)

FIGURE 6.27: Tune maps for the HL-LHC lattice for (a) the nominal case with no fringe fields; (b) for the fringe field model with a tenth order power series map; and (c) with the fringe field model based on the Runge–Kutta integrator. Tracking was done in SAMM for 256 turns using error seed #4.

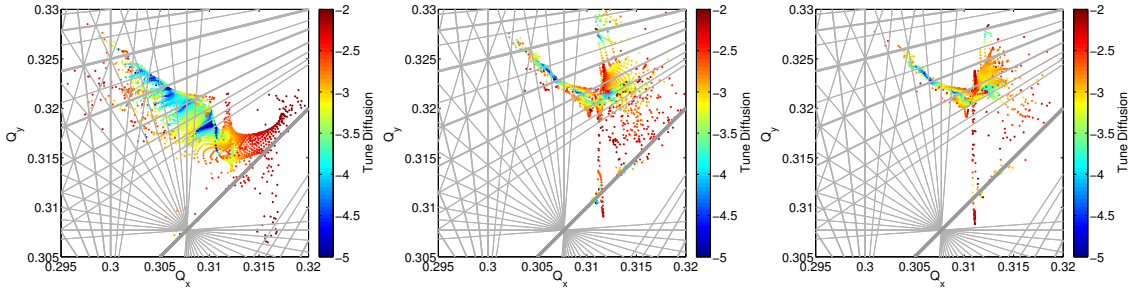

(A) (B) (C)

FIGURE 6.28: Tune maps for the HL-LHC lattice for (a) the nominal case with no fringe fields; (b) for the fringe field model with a tenth order power series map; and (c) with the fringe field model based on the Runge–Kutta integrator. Tracking was done in SAMM for 256 turns using error seed #5.

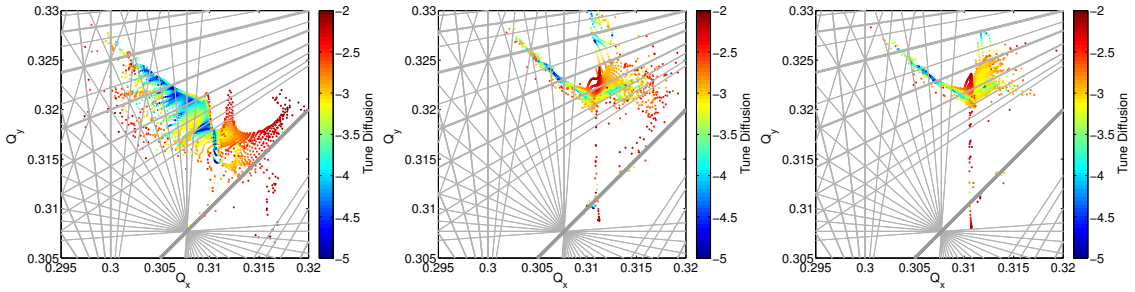

(A) (B) (C)

FIGURE 6.29: Tune maps for the HL-LHC lattice for (a) the nominal case with no fringe fields; (b) for the fringe field model with a tenth order power series map; and (c) with the fringe field model based on the Runge–Kutta integrator. Tracking was done in SAMM for 256 turns using error seed #6.

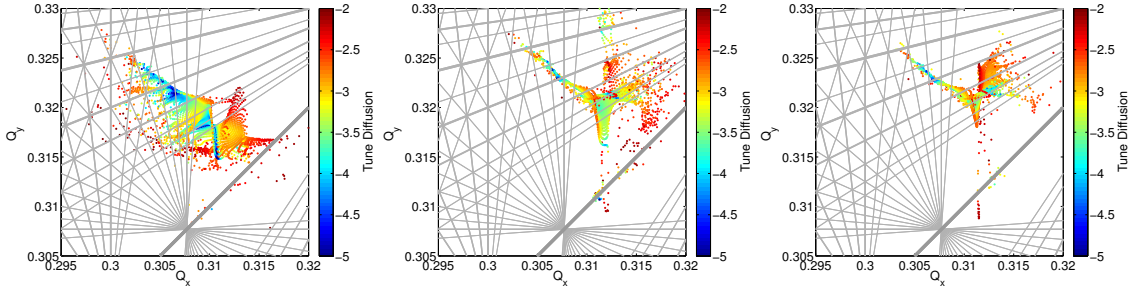

(A) (B) (C)

FIGURE 6.30: Tune maps for the HL-LHC lattice for (a) the nominal case with no fringe fields; (b) for the fringe field model with a tenth order power series map; and (c) with the fringe field model based on the Runge–Kutta integrator. Tracking was done in SAMM for 256 turns using error seed #7.

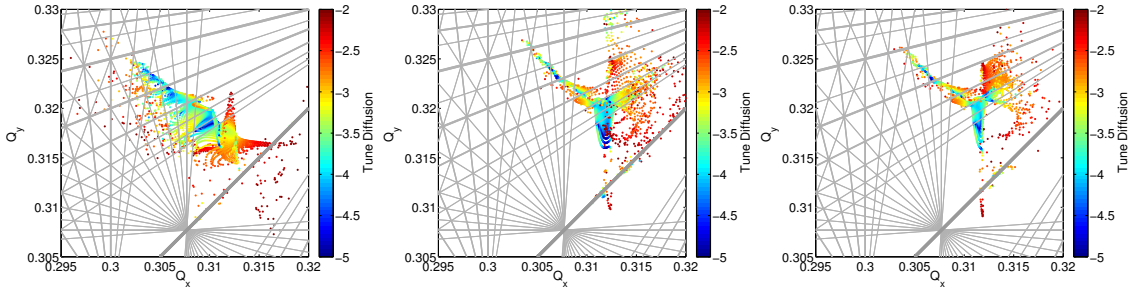

(A) (B) (C)

FIGURE 6.31: Tune maps for the HL-LHC lattice for (a) the nominal case with no fringe fields; (b) for the fringe field model with a tenth order power series map; and (c) with the fringe field model based on the Runge–Kutta integrator. Tracking was done in SAMM for 256 turns using error seed #8.

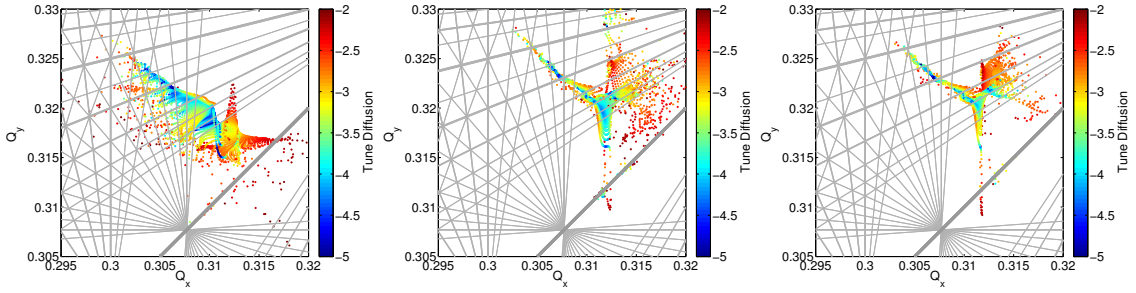

(A) (B) (C)

FIGURE 6.32: Tune maps for the HL-LHC lattice for (a) the nominal case with no fringe fields; (b) for the fringe field model with a tenth order power series map; and (c) with the fringe field model based on the Runge–Kutta integrator. Tracking was done in SAMM for 256 turns using error seed #9.

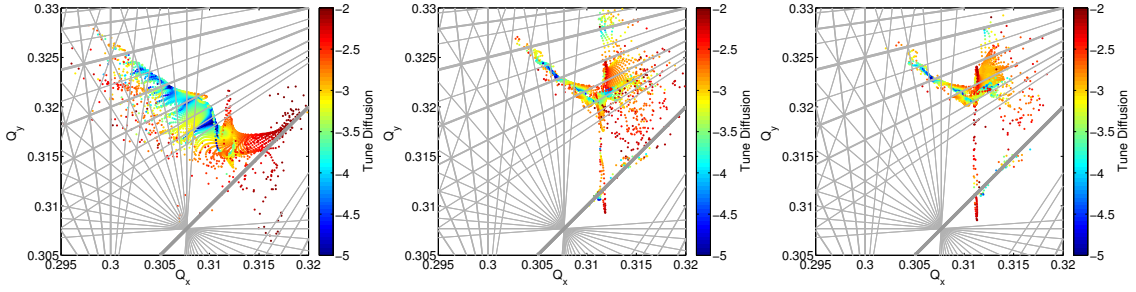

(A) (B) (C)

FIGURE 6.33: Tune maps for the HL-LHC lattice for (a) the nominal case with no fringe fields; (b) for the fringe field model with a tenth order power series map; and (c) with the fringe field model based on the Runge–Kutta integrator. Tracking was done in SAMM for 256 turns using error seed #10.

Implementation with a larger number of turns

So far the studies, except for the comparison between SUSSIX and SAMM, have been carried out using 256 turns. This number of turns was chosen given that it provided a good balance between the computation time required to perform the studies and the level of resolution required. A study with a higher number of turns will increase the resolution and will allow a better comparison of results between the nominal and the fringe field lattices.

Due to the high computational cost and the fact that in this case we are more interested in comparing the cases between lattices and less between the variations of the same lattices for different seeds, these studies were performed only for the error seed #1. The number of turns chosen for this case is 2048. FMA results are shown for the nominal case (Fig. 6.34 (a)) with fringe field modelled with a tenth order power series map (Fig. 6.34 (b)) and with a Runge–Kutta integrator (Fig. 6.34 (c)). Corresponding tune maps are shown in Fig. 6.35 (a), (b) and (c).

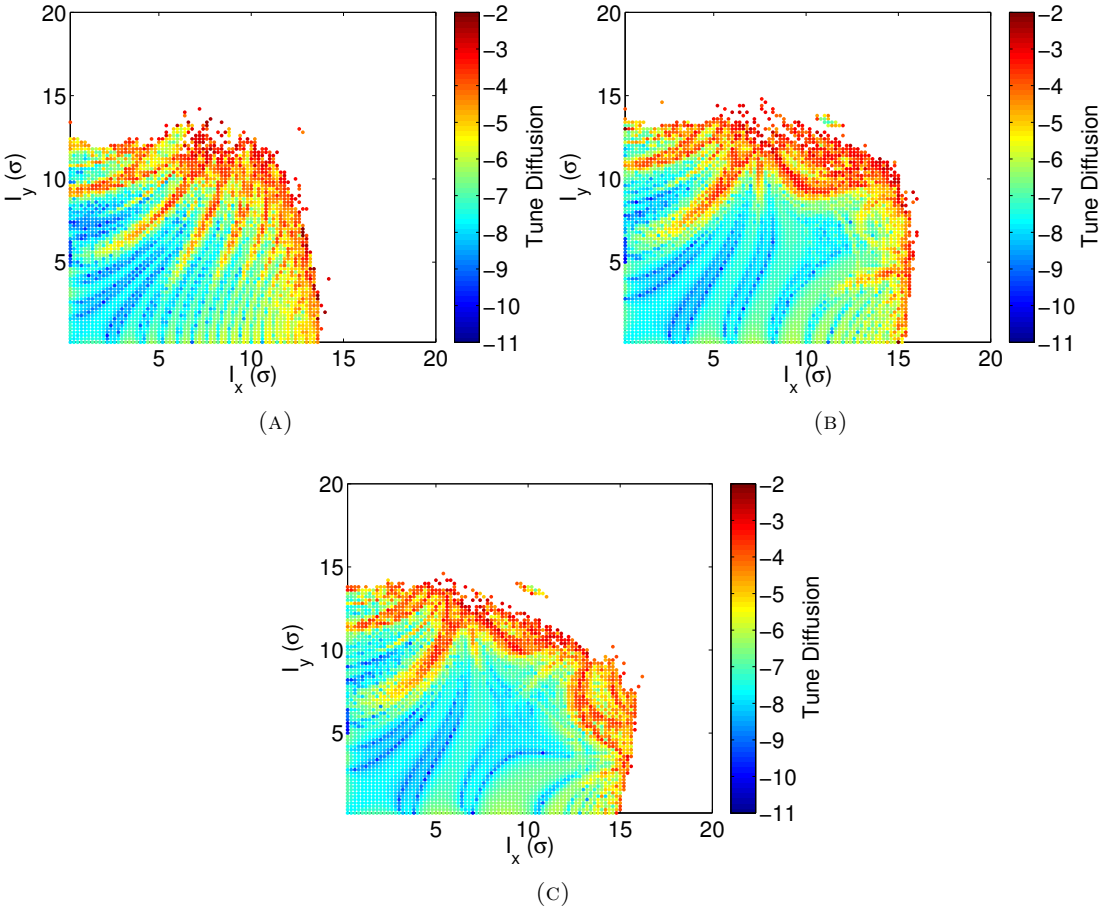

FIGURE 6.34: Amplitude maps for (a) the HL-LHC nominal lattice with no fringe fields; (b) with fringe fields modelled with a power series map of tenth order; and (c) with fringe fields based on the Runge–Kutta integrator. Particle tracking was carried out in SAMM over 2048 turns.

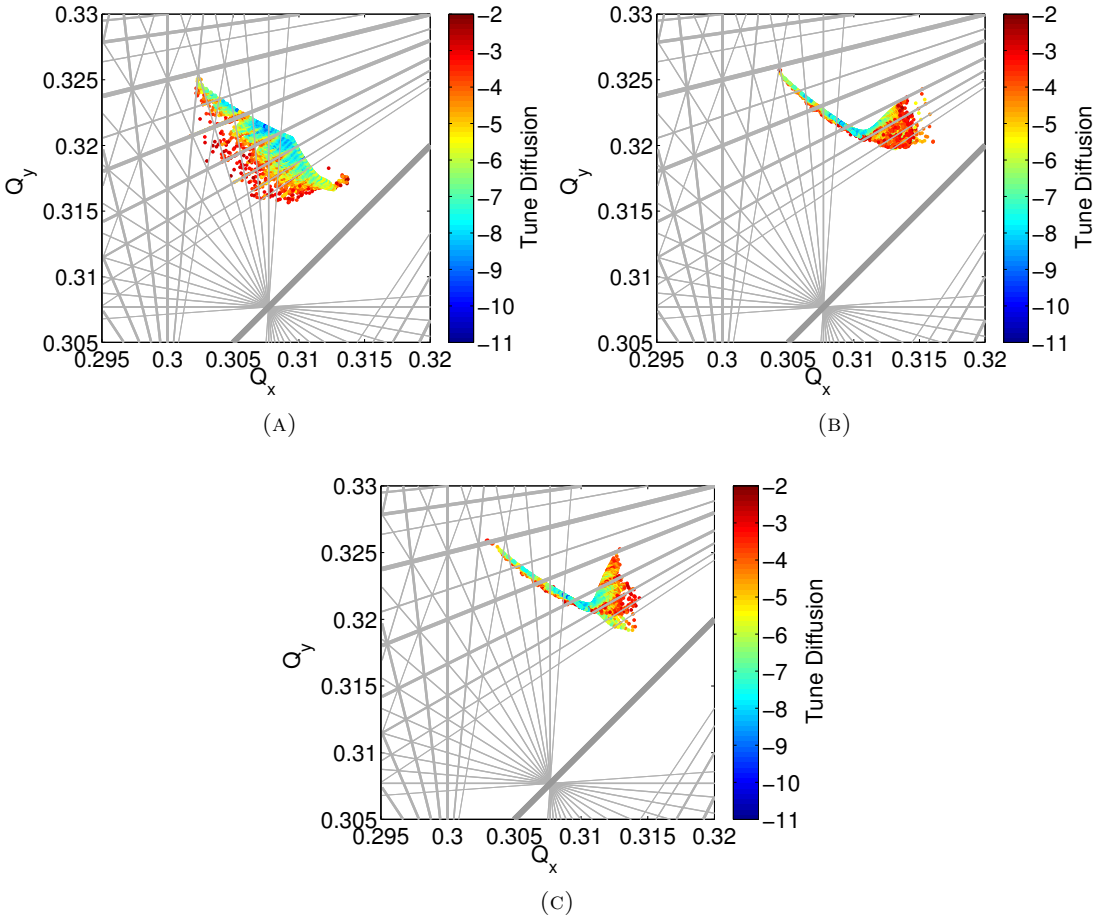

FIGURE 6.35: Tune maps for (a) the HL-LHC nominal lattice with no fringe fields; (b) with fringe fields modelled with a power series map of tenth order; and (c) with fringe fields based on the Runge–Kutta integrator. Particle tracking was carried out in SAMM over 2048 turns.

The higher resolution shows the similarities between the three cases when the amplitude $I_x < 7\sigma$. For higher values of I_x, specially for the zone $I_x \approx 10\sigma$ the fringe field models show a different behaviour. By comparing the tune maps we can observe the nature of this behaviour. For the nominal case the tune spread expands out of the working point as the amplitude $I = \sqrt{I_x^2 + I_y^2}$ grows larger. However, when fringe fields are included the vertical tune shift seems much less than for the nominal lattice. The horizontal tune shift on the other hand remains very similar, so that particles for the same amplitude cross the same resonances. However, at larger amplitudes ($I > 7\sigma$) the tune spread folds back on itself in the case of the lattice with fringe fields, in contrast to the case of no fringe fields where no "folding" of the tune shift is observed. In consequence, particles with amplitudes $I > 7\sigma$ encounter different resonances when fringe fields are included, compared to the case where there are no fringe fields.

The amplitude maps for the fringe field models with the tenth order power series map and the Runge–Kutta show the same overall behaviour and although differences

arise with respect to the nominal case, as was the case for the results with 256 turns, the dynamic aperture does not seem to be significantly affected.

Effect of momentum deviation.

To investigate the effects of chromaticity, studies were performed for particles with a fixed non-zero momentum deviation. Tracking was done for three different seeds and with a momentum deviation $\delta = \sigma_\delta$ and with $\delta = 3\sigma_\delta$, where the momentum deviation δ is defined:

$$\delta = \frac{E}{cp_0} - \frac{1}{\beta_0}. \tag{6.3}$$

Here, E is the particle energy, c is the speed of light, β_0 the velocity of a particle with the reference momentum divided by the speed of light and p_0 is the reference momentum. For these studies the rms momentum deviation was $\sigma_\delta = \sqrt{\langle \delta^2 \rangle} = 2.7 \times 10^{-3}$.

Results are shown comparing the frequency maps computed with non-zero momentum deviation for the nominal case, the tenth order power series map and the Runge–Kutta integrator for seed #1 in Fig. 6.36, seed #2 in Fig. 6.37 and seed #3 in Fig. 6.38.

As expected, the energy deviation has an impact on the dynamic aperture. This impact is noticeable in the same proportion for both the nominal case and cases with fringe fields for the three different seeds. There is good agreement between the cases with $\delta = 1\sigma_\delta$ for the power series map and the Runge–Kutta integrator; however, differences are noticeable in the case $\delta = 3\sigma_\delta$.

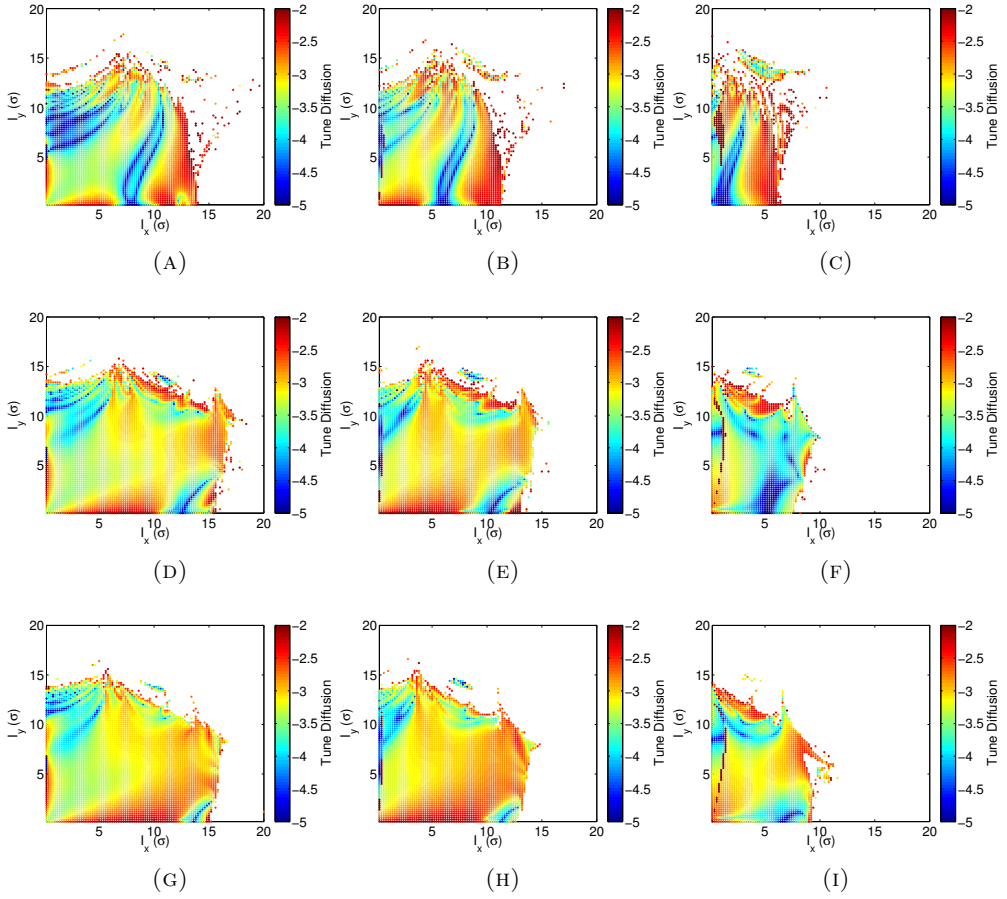

FIGURE 6.36: Amplitude maps for the nominal case without fringe fields (top), fringe field model with a tenth order power series map (middle) and with a Runge–Kutta integrator (bottom). Tracking is done in SAMM for seed #1 over 256 turns for particles with no energy deviation (left), energy deviation $\delta = 1\sigma_\delta$ (middle) and with energy deviation $\delta = 3\sigma_\delta$ (right).

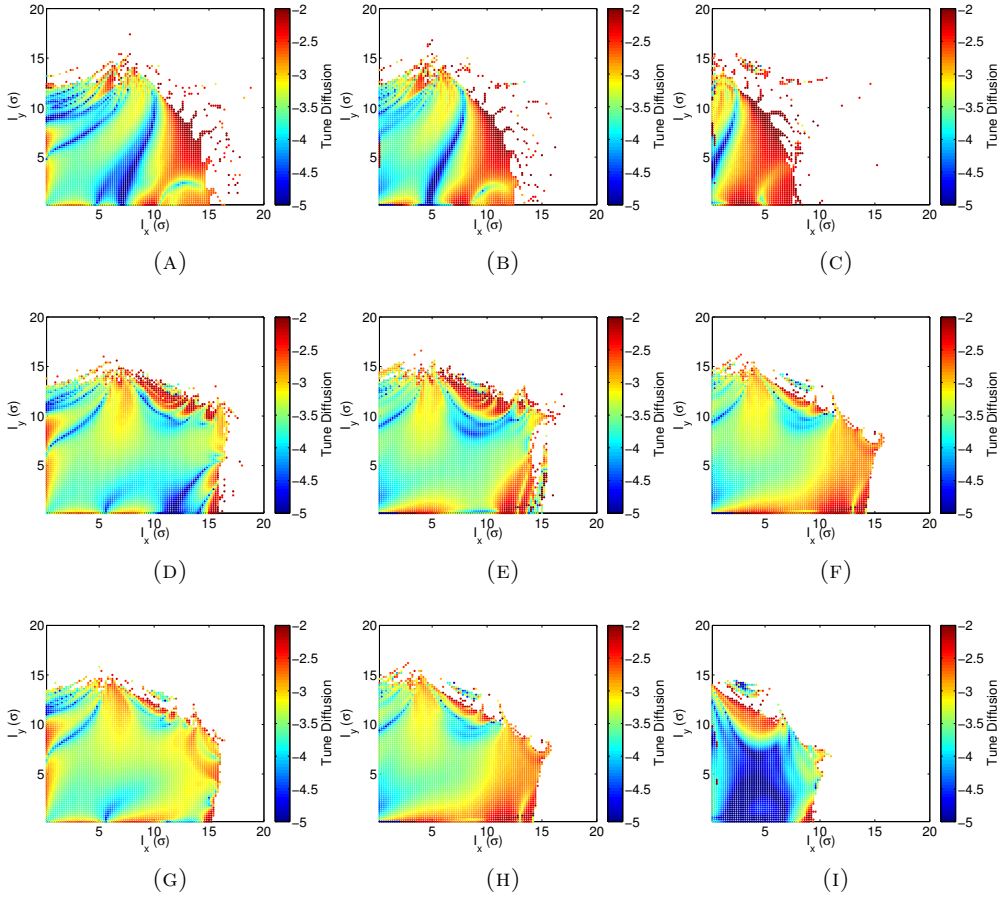

FIGURE 6.37: Amplitude maps for the nominal case without fringe fields (top), fringe field model with a tenth order power series map (middle) and with a Runge–Kutta integrator (bottom). Tracking is done in SAMM for seed #2 over 256 turns for particles with no energy deviation (left), energy deviation $\delta = 1\sigma_\delta$ (middle) and with energy deviation $\delta = 3\sigma_\delta$ (right).

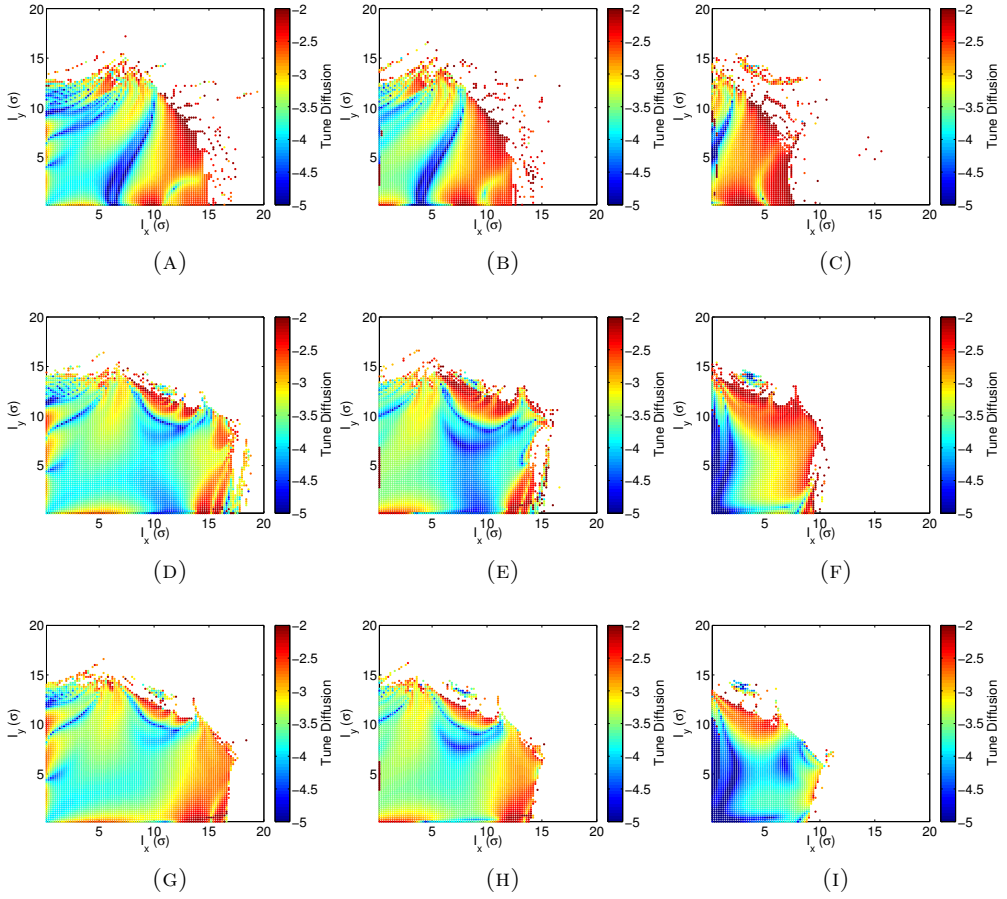

FIGURE 6.38: Amplitude maps for the nominal case without fringe fields (top), fringe field model with a tenth order power series map (middle) and with a Runge–Kutta integrator (bottom). Tracking is done in SAMM for seed #3 over 256 turns for particles with no energy deviation (left), energy deviation $\delta = 1\sigma_\delta$ (middle) and with energy deviation $\delta = 3\sigma_\delta$ (right).

6.3 Implementation of Inner Triplet Quadrupole Fringe Fields in the LHeC

This section presents a first study of the implementation of fringe fields in the inner triplet quadrupoles for the LHeC lattice introduced in Chapter 4 ($\beta^* = 15$ cm in IP1 and IP5, and $\beta^* = 10$ cm and $L^* = 10$ m in IP2). First, as in the HL-LHC case a comparison was made for the case without fringe fields between SAMM and SUSSIX. Using the same tools that were used for the HL-LHC case (see Section 6.3.2) fringe fields were implemented in the LHeC lattice. The implementation of fringe fields into the LHeC lattice was considered important to complement the work presented in Chapters 4 and 5, where the design of the LHeC interaction region and corresponding tracking studies were presented. However, since the designs for the inner triplet quadrupoles in IR2 are still being developed, for the present work we include only the fringe fields on the IT quadrupoles in IR1 and IR5.

6.3.1 Comparison of SUSSIX and SAMM for the LHeC Nominal Case

Amplitude maps for the nominal LHeC lattice without inner triplet quadrupole fringe fields are shown in Fig. 6.39. Tracking was performed in SUSSIX and SAMM (Fig. 6.39 (a) and (b) respectively). The corresponding tune maps are shown in Fig. 6.40 (a) and (b). In both cases, tracking was done for 2048 turns and with the same conditions used for the HL-LHC studies.

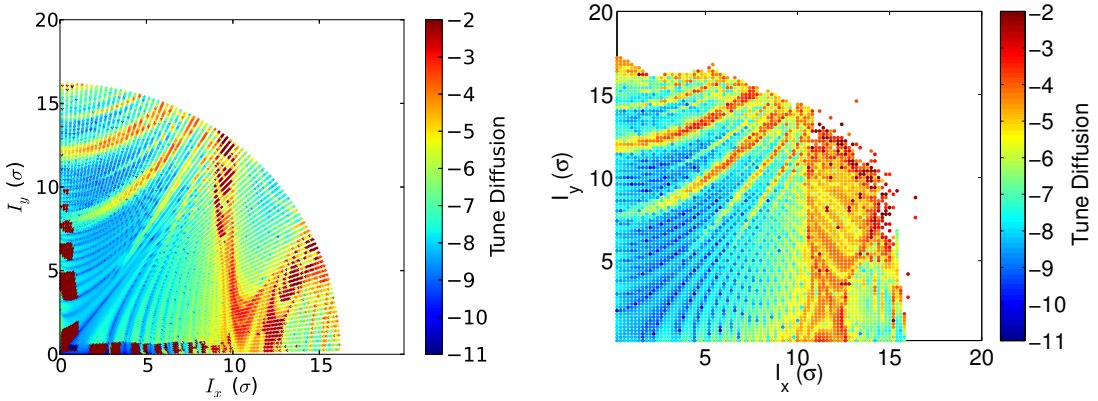

(A) (B)

FIGURE 6.39: Amplitude map for the LHeC lattice with no fringe fields. Particle tracking was performed in (a) SUSSIX, and in (b) SAMM over 2048 turns.

Both tracking studies show similar results for amplitudes $I_x < 10\sigma$. For larger amplitudes however, certain differences arise. In particular the apparently stable zone around 45 degrees observed in SUSSIX is no longer observed in SAMM. However, on closer inspection, this zone is within the region in tune space defined by: $|Q_x - Q_y| < 0.001$, i.e. particles within this region are close to the coupling resonance. This can be observed in Fig. 6.41, where the comparison between the amplitude and tune map is

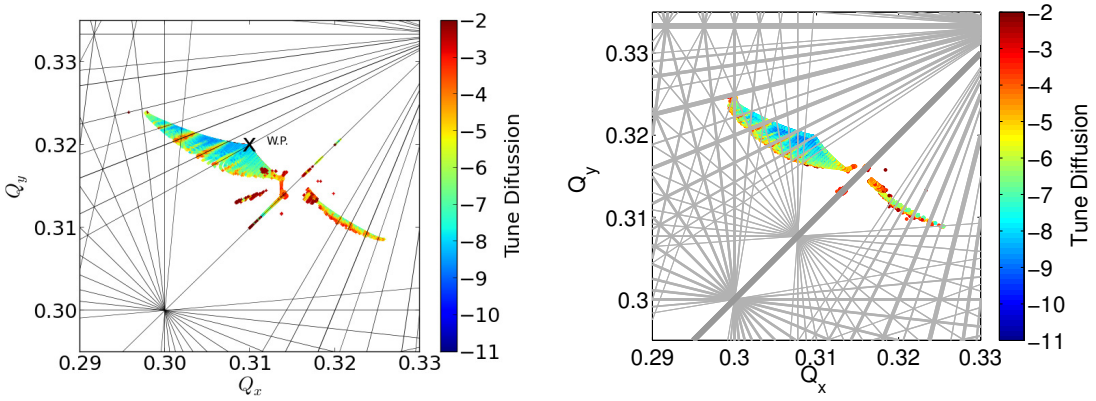

(A) (B)

FIGURE 6.40: Tune map over a resonance diagram of order 15 for the LHeC lattice without fringe fields. Particle tracking was performed in (a) SUSSIX and in (b) SAMM over 2048 turns.

made for particles fulfilling the condition $|Q_x - Q_y| < 0.001$ (with tracking performed in SUSSIX).

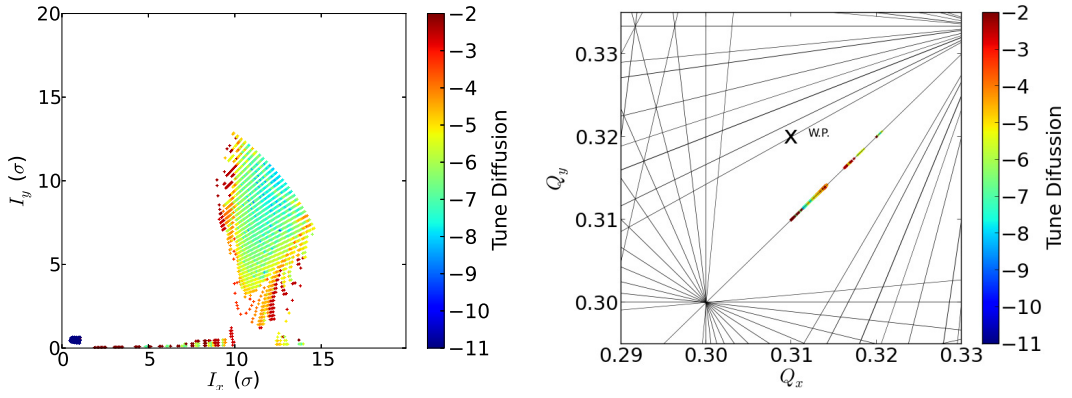

(A) (B)

FIGURE 6.41: (a) Amplitude and (b) tune map for the LHeC lattice without fringe fields with tracking performed in SUSSIX over 2048 turns. Only particles with tunes satisfying the condition $|Q_x - Q_y| \leq 0.0001$ are shown.

6.3.2 Fringe fields on the LHeC Lattice

Given the good agreement between SUSSIX and SAMM, at least for regions far from the coupling resonance, a first study is made to implement the fringe fields on the LHeC lattice. The fringe fields were implemented in the same manner as was described in the previous section (in the case of the HL-LHC for the inner triplet quadrupoles in IR1 and IR5). Given that the designs of the magnets for IR2 remain under study the fringe fields for these quadrupoles have not been included.

The integrator chosen for the fringe fields was the power series map of tenth order. Results are shown in the form of an amplitude map (Fig. 6.42 (a)) and a tune map (Fig. 6.42 (b)). The tracking, performed in SAMM, was done for 2048 turns to increase the resolution and allow a more detailed comparison with the nominal case with no fringe fields.

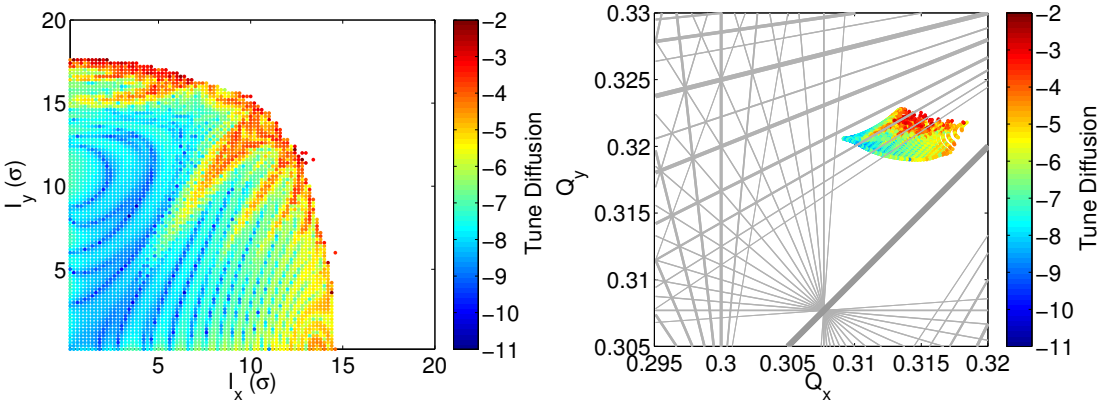

(A) (B)

FIGURE 6.42: Amplitude map (a) and tune map (b) for the LHeC lattice with fringe field implementation with a tenth order power series map with tracking performed in SAMM over 2048 turns.

The fringe fields in this lattice seem to have a bigger impact than the effects of fringe fields on the HL-LHC lattice. In particular, the fringe fields in HL-LHC did not seem to have an effect on the stability zone, around $I_x < 10\sigma$. For the LHeC case however, this is no longer the case and differences arise for the shape of resonance lines causing a disruption in the amplitude map. With respect to the tune map, when adding the fringe fields on the HL-LHC lattice we observe that the tune folds back on itself (Fig. 6.35) but only for a region of phase space with large amplitudes. For the LHeC however we observe that the tune maps folds on itself for all particles, therefore hitting different resonances than the nominal case.

When comparing the tune maps of the nominal lattices without fringe fields of the HL-LHC and LHeC lattices (Figs. 6.4 and 6.40) we observe that the LHeC lattice spreads out more, crossing the resonance (-1,1). The stronger effect of fringe fields for particles in the LHeC lattice in comparison with the HL-LHC lattice is possible due to the effect of this resonance line.

6.4 Summary and Conclusions

This chapter covered the studies of the effects of fringe fields of the inner triplet quadrupoles in the HL-LHC and LHeC lattices. Given the high β functions on the quadrupoles of larger aperture and higher strengths, the fringe fields are expected to have a bigger impact than for the LHC. The tracking code SAMM was used to perform fringe fields studies. This code allows new components to be easily incorporated into the beamline

and therefore makes it particularly useful when dealing with quadrupole fringe fields, which are not standard elements in most tracking codes.

Given the good agreement for the optics in the case without fringe fields between SUSSIX (the standard code used for FMA studies in CERN) and SAMM, there was enough confidence to use the latter to perform further studies including fringe fields. The study including fringe fields was carried out using the techniques developed in Chapter 2. The first step was to use numerical field data to obtain the generalised gradients, providing an analytical representation of the magnetic field and vector potential. The second step was to construct transfer maps for the fringe fields. Two different representations for the fringe fields were constructed, consisting of a power series map and a Runge–Kutta integrator.

Power series maps have the benefit that they can be written as a single beamline element in which the final values are written explicitly in terms of the initial values. This avoids the need to perform step-by-step integration through the fields during particle tracking. The truncation of the power series however, introduces a symplectic error that, although small, might have an impact on beam dynamics. Furthermore, the Wu–Forest–Robin integrator, used to obtain the power series, makes use of the paraxial approximation. The second technique, using an implicit Runge–Kutta integrator, provides symplectic tracking at least to numerical precision, and does not make use of the paraxial approximation; also, the error of this method scales with the square of the step size of the integration. However, this integrator is given in implicit form (so that algebraic equations have to be solved at each step) which has an impact on the computational time needed. Comparison between the two methods gives confidence in the results. By making use of transfer maps and integration techniques discussed in Chapter 2, fringe fields were modelled using both a power series map of tenth order and a Runge–Kutta integrator, and implemented at both the entrance and exit of each of the inner triplet quadrupoles in IR1 and IR5.

Results of FMA with the fringe fields show a change in the dynamics for particles with a large amplitude, especially in the horizontal direction of the coordinate space; however, no reduction in the dynamic aperture was observed. This was the case for both fringe field models (based on a power series map and the Runge–Kutta integrator) for 10 different error seeds and for particles with a given non-zero momentum deviation. These results however were obtained for a relatively small number of turns (2048). In order to provide a more detailed description of the impact of the fringe fields, long term tracking would need to be performed. Possible areas of development, apart from long term tracking, is the implementation of another way to represent the fringe fields using Enge functions [128].

Finally, a first study of the implementation of fringe fields into the nominal LHeC lattice was made. Results showed the impact of the fringe fields in the LHeC lattice was stronger than for the HL-LHC case. However, even when there were clear differences observed between the nominal and the fringe field models in both the amplitude and

tune maps, the dynamic aperture did not seem to be significantly affected. A possible area of development in this case is to apply the fringe fields in the different lattices options studied in Chapter 4.

Conclusions

Certain beam dynamics issues have been investigated for two of the proposed upgrades of the LHC: the flexibility of the design of the interaction region of the Large Hadron electron Collider (LHeC) has been explored, and the effects of fringe fields in the new quadrupoles to be implemented in the High-Luminosity LHC (HL-LHC) insertions have been studied.

Previous results demonstrated a design for the LHeC interaction region to achieve electron-proton collisions with a luminosity of $L = 10^{33}$ cm^{-2}s^{-1}, running alongside the HL-LHC experiment, by implementing the LHeC interaction region into the ATS scheme. However several challenges remained to be addressed, among them the exploration of the feasibility of the design and, most importantly, an appropriate correction of the chromatic aberrations.

The theory used for the results obtained in this thesis was given in Chapters 1 and 2. The first chapter covered the main concepts of beam dynamics with particular emphasis on the transfer matrices of the linear elements: drifts, quadrupoles and dipoles, as well as further concepts and techniques used in this thesis such as chromaticity, dynamic aperture and frequency map analysis. Different techniques however must be used when dealing with elements that do not fit within the criteria of the approximations used in Chapter 1, such is the case of elements where the field changes with the longitudinal position; the main objective of Chapter 2 is to provide transfer maps for such elements in a symplectic and explicit matter whenever possible.

Chapter 3 provides a brief history of the accelerators. The main developments, both in theory and technology breakthroughs, that led to the construction of high-energy accelerators are described. At the end of the this development so far is the LHC, also described in this chapter, as well as two of its possible upgrades that were studied in this thesis: the LHeC and the HL-LHC. Particular emphasis was given on the challenges to increase the luminosity in both of these upgrades.

Chapter 4 presented results from an investigation into the flexibility of the LHeC interaction region. This flexibility was explored in terms of reducing β^* to find the upper limits on the luminosity, and increasing L^* to reduce the synchrotron radiation. Different lattice configurations open up the possibility to increase L^* to 20 m with a fixed β^* at 10 cm, and to reduce β^* down to 5 cm, with a fixed L^* at 10 m.

A drawback of the new lattice configurations is that the β function at the location of the inner triplet of IR2, and consequently the chromatic aberrations grow larger as L^*

is increased and β^* is reduced. Different chromatic correction schemes were proposed: the LHC-like chromatic correction scheme made use of a global control on chromaticity, the LHeC-like chromaticity correction scheme added as a further constraint the control of the Montague functions in the collimation insertions, and finally, the higher order chromaticity correction scheme included the previous constraints plus a limit on the second order derivative of the tune with respect to momentum. The LHC-like chromatic correction scheme was achieved for all optical cases, the LHeC-like and higher order chromatic correction schemes had limits for an L^* of 19 m and 18 m respectively, both with a fixed β^* of 10 cm.

Studies were also performed to evaluate the possible reduction of synchrotron radiation in the LHeC IR. The reduction of the synchrotron radiation was explored by not only increasing L^*, but also by reducing, as much as possible, the bending of the electron beam. Significant reduction of synchrotron radiation power was found as a result of applying these techniques. The case with $L^* = 15$ m and $\beta^* = 10$ cm for example, showed a reduction of synchrotron radiation power of over 50% in comparison with the nominal case with $L^* = 10$ m and $\beta^* = 10$ cm. The high synchrotron radiation resulting from the nominal design (49 kW), even with the use of masks and absorbers, can cause serious damage, especially in the detector. These results show that a larger L^* contributes to the feasibility of the design with a significant reduction of the synchrotron radiation power, taking this radiation to safer margins.

Tracking studies reported in Chapter 5 complemented the studies described in Chapter 4, providing information about the stability of particle trajectories for the different lattice configurations and chromaticity correction schemes. Dynamic aperture calculations computed for the lattices with L^*=10 m and L^*=15 m, both with β^*=10 cm, gave very similar results. For $L^* > 15$ m however, a clear reduction in dynamic aperture was observed. This is consistent with the results found for frequency map analysis where for the lattice with $L^* = 17$ m and $\beta^* = 10$ cm particles were lost at much smaller amplitudes than those for lattices with $L^* \leq 15$ m. Even though frequency maps are computed for a smaller number of turns than the dynamic aperture, there is a consistency between the two methods in terms of the point at which the stability of the beam cannot longer be ensured. The agreement between the two methods gives confidence in the results.

For lattice configurations with varying β^* only dynamic aperture studies were performed. For these studies, a steep reduction was not observed at a given β^*, but instead a steady reduction was observed for values of $\beta^* < 10$ cm (although not always consistently, since the dynamic aperture for the lattice with $\beta^* = 8$ cm was larger than the one obtained for the lattice $\beta^* = 9$ cm). The more challenging case with β^*=5 cm to achieve a luminosity of $L = 10^{34}$ cm^{-2}s^{-1} had a very low dynamic aperture of 7σ, even without the complete set of errors. Therefore, if this luminosity is required, further studies will be needed to provide a feasible design.

In terms of the chromaticity correction schemes, the LHeC-like and higher order approaches demonstrate very similar dynamic aperture and FMA. The higher order chromaticity correction scheme gives slightly better results at large angles. On the other hand, the LHC-like correction showed the contrary effect for larger angles with a lower dynamic aperture and a larger diffusion in the FMA. In summary, a more refined chromaticity correction scheme approach than in LHC is needed for the LHeC lattice, and either LHeC-like or higher order would provide sufficient dynamic aperture.

The impact of fringe fields of the new quadrupoles with higher aperture in the HL-LHC interaction regions was presented in Chapter 6. For these studies, particle tracking was carried out in the tracking code SAMM, since it allows the easy implementation of new components (in particular, different models for the fringe fields) into the beamline.

First, a comparison was made for the nominal case without fringe fields between SAMM and SixTrack, the standard code used for tracking studies at CERN. Given the good agreement between the two codes for the nominal case, there was enough confidence to perform tracking studies in SAMM, including fringe fields.

Fringe fields were constructed using two different representations: a power series map and a Runge–Kutta integrator. The power series map had the benefit that it does not impact heavily on the computational time with respect to the nominal case without fringe fields; a drawback of this approach however is that the truncation of the power series map comes with a loss in symplecticity. The Runge–Kutta integrator, on the other hand, provides symplectic tracking; however, since the integrator is given in its implicit form, algebraic equations have to be solved at each step, increasing the computational time required to do the tracking.

The impact of fringe fields on the tune shifts and resonance strengths was evaluated using frequency map analysis. Results showed a difference in the dynamics for the fringe fields model, both for the Power series map and the Runge Kutta integrator, in comparison with the nominal case; but there was no indication of a significant reduction of the dynamic aperture. This effect was observed for ten different error seeds and for particles with a non-zero momentum deviation.

Also presented in Chapter 6 was a first study of the fringe fields of the inner triplet quadrupoles in IR1 and IR5, implemented into the LHeC lattice, to complement the work performed in Chapters 4 and 5. Results show a bigger impact of the fringe fields than those observed for the HL-LHC. Possible areas of development for these studies include FMA performed for a larger number of turns (to allow a more detailed representation of the dynamics) and implementation of the fringe fields for the different LHeC lattice configurations found in Chapter 4.

In conclusion, increasing the luminosity in the upgrades of the LHC, both in proton-proton and electron-proton collisions, comes with great challenges. Careful studies need to be performed to ensure the feasibility of the different lattices. Making use of the theory behind beam dynamics, and the tracking codes developed at CERN (MADX and SixTrack) we were able to make an extended study regarding the feasibility of

the integration of the LHeC IR into the HL-LHC lattice to achieve a luminosity of $L = 10^{33}$ cm^{-2}s^{-1}. The case of ultimate luminosity of $L = 10^{34}$ cm^{-2}s^{-1} might be within reach but further studies are required to produce a feasible design. For the case of fringe field studies, the benchmarking of a new tracking code (SAMM) was presented, and a combination of different techniques was used to produce accurate representations of the fringe fields of the inner triplet quadrupoles. The combination of a number of techniques, opens up not only opportunities for research into the effects of quadrupole fringe fields, but more generally studies that require the implementation of complex nonlinear elements in a beamline.

Bibliography

[1] LHeC Study Group. LHeC Conceptual Design Report. *J. Phys. G.*, 39(075001), 2012.

[2] D.J. Griffiths. *Introduction to Electrodynamics*. Addison Wesley, 1998.

[3] A. Wolski. *Beam Dynamics in High Energy Particle Accelerators*. Imperial College Press, 2014.

[4] A. Wolski. Maxwell's equations for magnets in CAS - CERN Accelerator School: Specialised course on magnets. CERN-2010-004, 2009.

[5] Y. Zhang J. Holmes, S. Henderson. Magnetic fields and magnet design. `http://uspas.fnal.gov/materials/09VU/Lecture2.pdf`, . Lecture in USPAS 2009.

[6] O. Bruening. Accelerators: Lecture v. `http://bruening.home.cern.ch/bruening/summer-school/lecture5`. Lecture for CERN summer students.

[7] Lyn Evans. The large hadron collider. `https://indico.cern.ch/event/145296/contributions/1381171/attachments/136930/194292/Kumasi2.pdf`. Presentation in ASP2012.

[8] S. Baird. Accelerators for pedestrians. *AB-Note-2007-014*, 2007.

[9] A. Wolski and J.Y. Jung. Effects of systematic multipole errors on the dynamic aperture of the NLC main damping rings. Technical Report LCC-0105 CBP Tec Note-266, SLAC, October 2002.

[10] A. Latina. Transverse dynamics course. Lecture in JUAS 2013.

[11] K. Wille. *The physics of Particle Accelerators An Introduction*. Oxford University Press, 2000.

[12] G. Hill. On the part of the motion of the lunar perigee which is a function of the mean motions of the sun and moon. *Acta Math*, 8:1–36, 1886.

[13] H. Goldstein, C.P. Poole Jr., and J.L. Safko. *Classical Mechanics*. Addison-Wesley, 2001.

[14] H. Wiedemann. *Particle Accelerator Physics*. Springer, 2007.

[15] E.D. Courant and H.S. Snyder. Theory of the alternating-gradient synchrotron. *Annals of Physics*, 3:1 – 48, 1958.

[16] W. Herr and B. Muratori. Concept of luminosity in CAS - CERN accelerator school: Intermediate course on accelerator physics. CERN-2006-002, 2003.

[17] M. Venturini and W. Kozanecki. The hourglass effect and the measurement of the transverse size of colliding beams by luminosity scans. Technical Report SLAC-PUB-8699, SLAC, 2000.

[18] J. P. Koutchouk and G. Sterbini. Increasing the integrated luminosity of SLHC by luminosity levelling via the crossing angle. In *Proceedings of EPAC08*, Genoa, Italy, 2008.

[19] S. Guiducci. Chromaticity. In *Proceedings of CAS-CERN Accelerator School: 5th General Accelerator Physics Course*, Jyvaskyla, Finland, 1992.

[20] W. Montague. Montague functions. Technical Report CERN-LEP-Note-165, CERN, 1979.

[21] Y.T. Yan J. Irwin. *Dynamic Aperture in Handbook of Accelerator Physics and Engineering*. World Scientific Singapore, 1998.

[22] Y. Papaphilippou. Detecting chaos in particle accelerators through the frequency map analysis method. *Chaos*, 24:024412, 2014.

[23] Y. Papaphilippou. Frequency maps of LHC models. In *Proceedings of PAC 1999*, New York City, USA, 1999.

[24] J. Laskar. The chaotic motion of the solar system: a numerical estimate of the size of the chaotic zones. *Icarus*, 88:266–291, 1990.

[25] H.S. Dumas and J. Laskar. Global dynamics and long-time stability in hamiltonian systems using lie algebraic methods. *Journal of Mathematical Physics*, 24:2734–2744, 1993.

[26] `http://uk.mathworks.com/help/signal/ref/hann.html?refresh=true`.

[27] K. Wille. Synchrotron radiation course. Lecture in JUAS 2013.

[28] J.A. Clarke. *The science and technology of undulators and wigglers*. Oxford University Press, 2004.

[29] A. Dragt. *Lie Methods for Nonlinear Dynamics with Applications to Accelerator Physics*. Springer, 2013.

[30] A. Wolski, J. Gratus, and R. Tucker. Symplectic integrator for s-dependent static magnetic fields based on mixed-variable generating functions. *Journal of Instrumentation*, 7(P04013), 2012.

[31] D. Abell. *Analytic Properties and Cremona Approximation of Transfer Maps for Hamiltonian Systems*. PhD thesis, University of Maryland, 1997.

[32] R. Kleiss, F. Schmidt, and F. Zimmermann. The use of truncated Power Series maps in dynamic aperture studies. *Part. Accel*, 41:117–132, 1993.

[33] E. Forest. Geometric integration for particle accelerators. *J. Phys. A*, 39:5321–5378, 2006.

[34] M. Berz. Differential algebraic description of beam dynamics to very high orders. *Part. Accel.*, 24, 1989.

[35] F. Willeke. Modern tools for particle tracking. In *proceedings of the CERN Accelerator School*, pages 215–218, 1995.

[36] E. McIntosh and R. de Maria. The SixDesk run environment for SixTrack.

[37] H. Burkhardt, L. Deniau, and A. Latina. Upgrade of slicing and tracking in madx. In *proceedings of IPAC2014*, Shangai, China, 2014.

[38] Y.K. Wu, E. Forest, and D.S. Robin. Explicit symplectic integrator for s-dependent static magnetic field. *Physical Review E*, 68, 2003.

[39] E. Hairer, C. Lubich, and G. Wanner. *Geometric numerical integration: structure-preserving algorithms for ordinadry differential equations*. Springer, Berlin, Germany, 2006.

[40] D. Fehling. The standard model of particle physics: A lunchbox's guide. John Hopkins University.

[41] W.K.H. Panofsky. The evolution of particle accelerators and colliders. *SPRING*, pages 36–44, 1997.

[42] J.J. Thomson. Xl. cathode rays. *Philosophical Magazine 5*, 4:293–316, 1897.

[43] R. Wideroe. Ber ein neues prinzip zur herstellung hoher spannungen. *Archiv fr Elektrotechnik*, 21:387–406, 1924.

[44] M.S. Livingston. The cyclotron. *J. Appl. Phys.*, 5, 1944.

[45] J. Cockcroft and E. Walton. Artificial production of fast protons. *Nature*, 129: 242, 1932.

[46] Chetvorno. Cockcroft walton voltage multiplier circuit. `https://commons.wikimedia.org/wiki/File:Cockcroft_Walton_voltage_multiplier_circuit.svg#/media/File:Cockcroft_Walton_voltage_multiplier_circuit.svg`. Licensed under CC0 via Commons.

[47] Y. Zhang J. Holmes, S. Henderson. Magnetic fields and magnet design. `http://uspas.fnal.gov/materials/09VU/Lecture2.pdf`, . Lecture in USPAS 2009.

[48] E. M. McMillan. Synchrocyclotron, 1952. US Patent 2615129.

[49] V. Veksler. *J. of Phys*, 9:153–8, 1945.

[50] M.L. Oliphant, J.S. Gooden, and G.S. Hyde. *Proc. Phys. Soc.*, 59:666, 1947.

[51] `https://www.bnl.gov/60th/cosmotron.asp`.

[52] E.D. Courant, M.S. Livingston, and H.S. Snyder. The strong-focusing synchrotron: A new high energy accelerator. *Physical Review 88 (5)*, pages 1190–1196, 1952.

[53] N.C. Christofilos. Focusing system for ions and electrons, 1950. US Patent No. 2736799.

[54] I.M. Kapchinskii and V.A. Teplvakov. *Prib. Tekh. Eksp*, 2(19), 1970.

[55] T.P. Wangler, A. Cimabue, J. Merson, R.S. Mills, R. Wood, and L. Young. Superconducting rfq development at los alamos.

[56] J. Rees. *Colliders in Handbook of Accelerator Physics and Engineering*, page 11. World Scientific Singapore, 1998.

[57] `http://astro.sunysb.edu/steinkirch/reviews/colliders.pdf`.

[58] Source (WP:NFCC4) Licensed under Fair use via Wikipedia. Particle accelerator Livingston chart 2010. `https://en.wikipedia.org/wiki/File:Particle_Accelerator_Livingston_Chart_2010.png#/media/File:Particle_Accelerator_Livingston_Chart_2010.png`.

[59] `http://home.cern/about/accelerators/super-proton-synchrotron`.

[60] G. Arnison et al. Experimental observation of isolated large transverse energy electrons with associated missing energy at s=540 GeV. *Physics Letters B*, 122: 103–116, 1983.

[61] M. Banner et al. Observation of single isolated electrons of high transverse momentum in events with missing transverse energy at the CERN pp collider. *Physics Letters B*, 122:476–485, 1983.

[62] P. Bryant. History of accelerators. `http://www.afhalifax.ca/magazine/wp-content/sciences/lhc/HistoireDesAccelerateurs/histoire1.pdf`.

[63] NA61 experiment. `http://shine.web.cern.ch/`, 2015.

[64] NA62 experiment. `http://na62.web.cern.ch/NA62/`, 2015.

[65] COMPASS experiment. `https://wwwcompass.cern.ch/`, 2015.

[66] http://www.fnal.gov/pub/tevatron/.

[67] F. Abe et al. *Physical Review Letters*, 74:2626–2631, 1995.

[68] M. Seidel. HERA. In *Proceedings of 1999 Particle Accelerator Conference*, page 34, New York City, USA, 1999.

[69] http://www.desy.de/.

[70] http://home.cern/about/accelerators/large-electron-positron-collider.

[71] O.S. Brüning, P. Collier, P. Lebrun, S. Myers, R. Ostojic, J. Poole, and P. Proudlock. LHC Design report. Technical Report CERN-2004-003-V-1, CERN, 2004.

[72] ATLAS Collaboration. The ATLAS experiment at the large hadron collider. *JINST*, 3(S08003), 2008.

[73] CMS Collaboration. The CMS experiment at the CERN LHC. *JINST*, 3(S08002), 2008.

[74] LHCb Collaboration. The LHCb detector at the LHC. *JINST*, 3(S08005), 2008.

[75] ALICE Collaboration. The ALICE experiment at the CERN LHC. *JINST*, 3 (S08004), 2008.

[76] http://www.lhc-closer.es/taking_a_closer_look_at_lhc/0.lhc_layout.

[77] L. Evans and P. Bryant. LHC machine. *JINST*, S08001, 2008. URL http://iopscience.iop.org/article/10.1088/1748-0221/3/08/S08001/pdf.

[78] http://te-dep-epc-oms.web.cern.ch/te-dep-epc-oms/operation-en/operation.stm.

[79] S. Fartoukh. Second order chromaticity correction of LHC V6.0 at collision. Technical Report LHC-Project-Report-308, CERN, 1999.

[80] E. Metral. Presentation at the LHC beam operation meeting. http://lhc-beam-operation-committee.web.cern.ch/lhc-beam-operation-committee/minutes/Meeting32-13_03_2012/LBOC_EM_13-03-12.pdf, 2013.

[81] CMS collaboration. Observation of a new boson at a mass of 125 GeV with the CMS experiment at the LHC. *Physical Review Letters B*, 716:30–61, 2012.

[82] ATLAS collaboration. Observation of a new particle in the search for the Standard Model Higgs boson with the ATLAS detector at the LHC. *Physical Review Letters B*, 716:1–29, 2012.

[83] B.R. Martin and G. Shaw. *Particle Physics*, chapter 7. John Wiley and Sons, 2006.

[84] P. Newman. Deep Inelastic Scattering at the TeV Energy Scale and the LHeC Project. In *Proceedings of RINGBERG08*, 2008.

[85] `http://hilumilhc.web.cern.ch/`.

[86] European strategy for particle physics. `http://cerncourier.com/cws/article/cern/54020`, 2013.

[87] S.D. Fartoukh and R. De Maria. Optics and layout solutions for the HL-LHC with large aperture Nb3Sn and Nb-Ti inner triplets. In *Proceedings of IPAC 2012*, New Orleans, US, 2012.

[88] R. De Maria, S. Fartoukh, A. Bogomyagkov, and M. Korostelev. HLLHCV1.0: The HL-LHC layout and optics models for 150 mm Nb3SN triplets and local crab cavities. In *Proceedings of IPAC 2013*, Shangai, China, 2013.

[89] S. Fartoukh. Achromatic telescopic squeezing scheme and application to the lhc and its luminosity upgrade. *Phys. Rev. ST Accel. Beams*, 16(111002), 2013.

[90] R. De Maria and S. Fartoukh. SLHCV3.0: Layout, optics and long term stability. Technical Report sLHC Project Report 50, CERN, 2012.

[91] O.S. Brüning. Overview of the LHeC Design Study at CERN. In *Proceedings of ERL2013*, Novosibirsk, Russia, 2013.

[92] D. Pellegrini, A.Latina, D. Schulte, and D. Alex Bogacz. Beam-dynamics driven design of the LHeC energy-recovery linac. *Phys. Rev. ST Accel. Beams*, 18(121004), 2015.

[93] A. Milanese. Warm magnets for LHeC/Test Facility arcs. url-https://indico.cern.ch/event/278903/session/6/contribution/41pdf. Presentation in the LHeC Workshop 2014.

[94] A. Valloni et al. Optics Design for the LHeC ERL Test Facility. In *Proceedings of IPAC 2014*, Shangai, China, 2013.

[95] E. Jensen et al. Design Study of an ERL test facility at CERN. In *Proceedings of IPAC 2014*, Dresden, Germany, 2014.

[96] P. Kostka, A. Polini, and D. M. South. The LHeC detector. In *Proceedings of DIS13*, Marseille, France, 2013.

[97] J. Abelleira, N. Bernard, S. Russenschuck, R. Tomás, and F. Zimmermann. Design status of the LHeC Linac-Ring interaction region. In *Proceedings of IPAC 2011*, San Sebastián, Spain, 2011.

[98] F. Zimmerman. Interaction region design options for a Linac-Ring LHeC. In *Proceedings of IPAC 2010*, Kyoto, Japan, 2010.

[99] L. Rossi. Superconducting magnet development for the LHC. *J.J. Cryo. Super. Soc. Jpn.*, 47(4), 2012.

[100] R. Tomás. Presentation in the meeting on LHeC with Daresbury group. `https://indico.cern.ch/event/207665/`.

[101] M. Korostelev, E. Cruz-Alaniz, D. Newton, A. Wolski, O.S. Brüning, and R. Tomás. The LHeC IR integrated into the HL-LHC lattice. In *Proceedings of IPAC 2013*, number MOPWO063, Shangai, China, 2013.

[102] R. De Maria, S. Fartoukh, A. Bogomyagkov, and M. Korostelev. HLLHCV1.0: HL-LHC layout and optics models for 150 mm Nb3Sn triplets and local crab-cavities. In *Proceedings of IPAC 2013*, number TUPFI014, Shangai, China, 2011.

[103] R. de Maria, F. Schmidt, and P. Krzysztof. Advances in matching with MAD-X. Technical Report CERN report WEPPP14, CERN.

[104] `http://madx.web.cern.ch/madx/`.

[105] R. Fletcher. *Practical Methods of Optimization*. John Wiley & Sons, 1987.

[106] F. James. MINUIT, A package of programs to minimise a function of n variables, compute the covariance matrix, and find the true errors. Technical Report Technical report, CERN, 1978.

[107] J. A. Nelder and R. Mead. A simplex method for function minimization. *Computer Journal*, 7:308–313.

[108] S. Russenschuck. Presentation in the 2012 CERN-ECFA-NuPECC Workshop on the LHeC. `https://indico.cern.ch/event/183282`.

[109] E. Cruz-Alaniz. Presentation in the EIC 2014 workshop. `http://appora.fnal.gov/pls/eic14/agenda.full`.

[110] A. Streun. Experimental methods and instruments of particle physics: Block3: Accelerators. `https://ados.web.psi.ch/empp-streun/`, 2013.

[111] B. Parker. Presentation at the LHeC 2014 workshop. `https://indico.cern.ch/event/356714/session/12/contribution/76`, 2015.

[112] J.P. Koutchouk. The LHC dynamic aperture. In *Proceedings of PAC99*, New York City, USA, 1999.

[113] H. Grote. Technical Report Beam Physics Note 34, CERN, 1999.

[114] S. Fartoukh and M. Giovannozzi. *Nucl. Instrum. Methods Phys. Res. A*, 671:10, 2012.

[115] M. Boge, A. Faus-Golfe, J. Gareyte, H. Grote, J.P. Koutchouk, J. Miles, Q. Qing, T. Risselada, F. Schmidt, and S. Weisz. Overview of the LHC dynamic aperture studies. In *Proceedings of Particle Accelerator Conference*, 1997.

[116] P. Hagen, M. Giovannozzi, J.P. Koutchouk, T. Risselada, F. Schmidt, E. Todesco, and E. Wildner. LHC project report 1123, 2008.

[117] E.H. Maclean, R. Tomás, M. Giovannozzi, and T.H.B. Persson. First measurement and correction of nonlinear errors in the experimental insertions of the CERN Large Hadron Collider. *Phys. Rev. ST Accel. Beams*, 18(121002), 2015.

[118] S. Fartoukh and M. Giovannozzi. Dynamic aperture computation for the as-built CERN Large Hadron Collider and impact of main dipoles sorting. *Nucl. Instrum. Methods Phys. Res. A.*, 671:10, 2012.

[119] R. de Maria, M. Giovannozzi, E. McIntosh, Y. Cai, Y. Nosochkov, and M-H. Wang. Dynamic aperture studies for the LHC High Luminosity Lattice. In *Proceedings of IPAC 2015*, number MOPMN003, Richmond, USA, 2015.

[120] R. de Maria. Private communication.

[121] H. Burkhardt, R. de Maria, M. Giovannozzi, and T. Risselada. Improved TEAPOT method and tracking with thick quadrupoles for the LHC and its upgrade. In *Proceedings of IPAC 2013*, number MOPWO027, Shangai, China, 2013.

[122] `http://cds.cern.ch/record/702438/files/sl-note-98-017.pdf`.

[123] J. Barranco. Private communication.

[124] R. De Maria et. al. Dynamic aperture performance for different collisions optics scenarios for the LHC luminosity upgrade. In *Proceedings of IPAC 2013*, number WEPEA047, Shangai, China, 2013.

[125] A. Valishev. Beam-Beam studies for HL-LHC. In *Proceedings of IPAC 2013*, number TUPB21, Shangai, China, 2013.

[126] A. Wolski. Simple accelerator modelling in matlab.

[127] S. Bermudez. Private communication.

[128] B.D. Muratori, J.K. Jones, and A. Wolski. Analytical expressions for fringe fields in multipole magnets. *Phys. Rev. STAB*, 18(064001).

[129] A. Wolski. Private communication.

Acknowledgements

I would firstly like to thank my first supervisor David Newton. David not only gave me the opportunity to join this community but provided me with guidance and support along the project. David lived life with such an intensity that I can only aspire to live by.

I will also like to thank Andy Wolski. Andy gave me the support I needed in difficult times and help me out through the last process of the PhD. He was an incredible mentor and I can only be grateful of the opportunity I had to work with him.

I would also like to thank Carsten Welsch. His initiative to create the OPAC network is the reason I'm here. He also always provided me with unquestionable support along this project.

To Rogelio Tomas, who provided me with guidance with incredible enthusiasm and always made me pushed results forward.

To all the members of the LHeC collaboration, in particular to Max Klein, Oliver Brüning and Frank Zimmerman who opened the doors for me to join this fantastic collaboration. I would also like to thank to the people of CERN that provided me with support in the use of CERN tracking codes. Special thanks to Javier Barranco, Ricardo de Maria and Massimo Giovannozzi.

To my dear family and their incredible support. To my mother who has guide me with her extraordinary example about the importance of education and the joy for the seek of knowledge. To my sister Yuria for sharing with me these last years and bringing with her the best piece of home. To my father "El brujo" for showing me to appreciate the unconventional joys of life. To Claudia for her care and support. To Paty and Matias, for their drive and determination that propels us around them to move forward. Thanks also to Guly for being an unconditional brother.

To the fantastic friends that proof read my thesis. Lee Devlin, whom I have also developed a great friendship, although only in real life. Adam Kewley, a once neighbour converted high-examiner, I can only be grateful for his hardness. And last but not least Louise Cowie, a great friend for whom I have great admiration for.

To all the Mexicans friends in Europe that have made me miss home a bit less. In particular to Bart and Memo that have not only been pillars in my life for several years now, but are always there to give me a Linux-helping hand.

To my fellow Cockcroft colleagues, that have decorated these three years of presentations, abstracts and stress, with laughters, jokes and overall fun. In particular to

Alexandra Alexandrova, a companion in evenings of tears and laughs. To Javier Resta Lopez, Chris Edmonds and Maxim Korostelev, whom endured me with (far too often) physics questions. And to the members of S.30, for filling the routine days with non-routine experiences. Special thanks to Sam Jones and his incredible ability to transform my bad mood with his unique charisma.

In general I would like to thank everyone who took part in this incredible experience. It was an emotional, challenging and fantastic journey. I will be forever grateful for the friendship and support that I received throughout this three years.